



**HAL**  
open science

# Ultrafast switching of semiconductor microcavities for quantum optics applications

Tobias Sattler

► **To cite this version:**

Tobias Sattler. Ultrafast switching of semiconductor microcavities for quantum optics applications. Materials Science [cond-mat.mtrl-sci]. Université Grenoble Alpes, 2017. English. NNT : 2017GREAY082 . tel-01788769

**HAL Id: tel-01788769**

**<https://theses.hal.science/tel-01788769>**

Submitted on 9 May 2018

**HAL** is a multi-disciplinary open access archive for the deposit and dissemination of scientific research documents, whether they are published or not. The documents may come from teaching and research institutions in France or abroad, or from public or private research centers.

L'archive ouverte pluridisciplinaire **HAL**, est destinée au dépôt et à la diffusion de documents scientifiques de niveau recherche, publiés ou non, émanant des établissements d'enseignement et de recherche français ou étrangers, des laboratoires publics ou privés.

## THÈSE

Pour obtenir le grade de

### **DOCTEUR DE LA COMMUNAUTÉ UNIVERSITÉ DE GRENOBLE**

Spécialité : **Nanophysique**

Arrêté ministériel : 25 mai 2016

Présentée par

**Tobias SATTLER**

Thèse dirigée par **Jean-Michel GÉRARD**

et codirigée par **Joël BLEUSE**

préparée au sein du **Laboratoire NanoPhysique & SemiConducteurs,  
INAC, PHELIQS**

et de l'École Doctorale **de Physique**

## **Commutation ultrarapide de micro- cavités semiconductrices pour des applications à l'optique quantique**

Ultrafast switching of semiconductor  
microcavities for quantum optics applications

Thèse soutenue publiquement le **28 novembre 2017**,  
devant le jury composé de :

**Jean-Philippe POIZAT**

CNRS – Institut Néel, France, Président

**Isabelle SAGNES**

CNRS - Centre de Nanosciences et de Nanotechnologies (C2N), France,  
Rapporteur

**Guillaume CASSABOIS**

Université Montpellier, France, Rapporteur

**Sylvain COMBRIÉ**

Thales Research and Technology, France, Examineur

**Jean-Michel GÉRARD**

Univ. Grenoble Alpes, France, Directeur de thèse

**Joël BLEUSE**

Univ. Grenoble Alpes, France, Co-Directeur de thèse





# Remerciements

Je commence ce manuscrit en remerciant toutes les personnes qui ont contribué à ce que ces trois années de thèse aient été une expérience scientifiquement enrichissante et productive. Grâce à eux, je pouvais acquérir tous les résultats et tout le savoir-faire ce qui m'a permis de rédiger ce manuscrit. Je tiens aussi à remercier les gens qui ont contribué à ces trois très belles années.

Tout d'abord, je voudrais remercier Jean-Michel Gérard, mon directeur de thèse. Grâce à sa conception, ce projet a pu avoir lieu. Pendant tout mon temps de stagiaire et thésard, son engagement et enthousiasme personnel pour le projet m'ont particulièrement motivé. Quand je ne savais plus comment améliorer mes expériences et évaluations, ses idées m'ont permis d'attaquer le problème différemment et d'arriver à un meilleur résultat. Ses explications illustratives des problèmes complexes de la CQED m'ont aidé à obtenir une bonne compréhension de ce champ de recherche et sont exemplaire pour une intuition énorme scientifique. Merci également pour sa disponibilité surtout pendant la fin de cette thèse.

Un grand merci également à mon codirecteur de thèse, Joël Bleuse. C'est lui qui m'a encadré afin de maîtriser le setup de microphotoluminescence en temps résolu. Merci pour sa patience et pour sa confiance qui m'ont permis d'utiliser ces appareils fortement sensitifs et fragiles. Grâce à cela et à l'aide que j'ai reçue, j'ai pu acquérir mes résultats en photoluminescence sur lesquels cette thèse se base. Merci aussi pour nos nombreuses et enrichissantes discussions sur des sujets scientifiques ou généraux.

Jean-Michel, Joël surtout merci beaucoup pour vos grands efforts qui ont énormément contribué à améliorer la qualité de ce manuscrit!

Côté fabrication, c'est Julien Claudon qui m'a enseigné pour la fabrication des nanostructures en salle blanche. Merci pour le temps consacré à mon projet, les lithographies électroniques et les "escapades salle blanche". Merci aussi pour beaucoup d'idées scientifiques et les discussions de sports de montagne.

Je remercie également les membres du jury qui ont accepté de corriger et évaluer mon travail : Jean-Philippe Poizat, le président du jury, Isabelle Sagnes et Guillaume Cassabois, les rapporteurs et Sylvain Combrié, examinateur.

Un grand merci à mon prédécesseur, Emanuel Peinke, qui m'a appris à mesurer le switch des micropiliers avec des boîtes quantiques intégrés. Je le remercie également pour son grand engagement avec les simulations FDTD qui m'ont beaucoup servi pour la compréhension des résultats sur le changement de couleur, et bien sûr pour les nombreuses sorties de vélo de route pendant la thèse.

Le début est toujours le plus difficile et c'est grâce à Petr Stepanov que je pouvais rapidement obtenir mes premiers résultats sur les résonateurs en forme d'anneau ovale. Merci de m'avoir accompagné et aidé pendant ces expériences. Merci aussi de m'avoir supporté pendant le temps qu'on a passé ensemble dans notre bureau et pour les nombreuses réponses à mes questions.

C'est Yann Genuist qui m'a formé sur la machine d'épitaxie: Merci beaucoup pour les explications qui m'ont aidé à comprendre et utiliser ce bâti, de sa patience et sa disponibilité.

Un grand merci à Gilles Nogues et Mathieu Jeannin pour l'introduction et l'aide pour les simulations COMSOL. C'est grâce à leur compréhension de l'électrodynamique que je pouvais mener les simulations. Merci également à Flora Gautheron d'avoir simulé des anneaux ovales.

Quand je parle des simulations, il ne faut pas oublier les simulations pour le switching différentiel: Merci à Luca Redaelli pour l'introduction à la simulation avec FEMSIM qui a assuré que je pouvais rapidement obtenir mes résultats.

Je tiens à remercier Eva Monroy qui m'a permis d'utiliser son setup de FTIR pour analyser les échantillons que j'ai sorti du bâti EJM, pour les nombreuses explications et sa disponibilité.

Malgré un bon équipement, même le CEA n'est pas parfait. Merci aux trois chercheurs côté Institut Néel, Jean-Philippe Poizat, Jacek Kasprzak et Maxime Richard de m'avoir prêté du matériel quand le nôtre était en panne ou quand le CEA ne disposait pas de ces équipements.

Je voudrais également remercier mes collègues du bureau Alice Bernard et Sirona Valdueza pour le temps qu'on a passé ensemble dans cette pièce C5-631. Merci à Alice pour le travail ensemble en salle blanche et pour m'avoir montré comment prendre de jolies photos avec le MEB.

Une mention spéciale pour les sorties de VTT et de ski de randonnée avec Tomek Jakubczyk et Quentin Mermillod, post-docs/doctorants à l'Institut Néel. Ce fût toujours un plaisir bien que je n'aie pas toujours eu le temps pour profiter des

bonnes conditions, hein Quentin? Merci aussi pour les soirées "Party like a Rockstar" qu'on a passé ensemble avec Manu.

En général, un grand merci à toute l'équipe NPSC pour le temps que j'ai pu passer avec les chercheurs, permanents ou non-permanents. Les conversations, sur des sujets scientifiques ou généraux m'ont toujours fait un énorme plaisir.

Merci également à l'équipe PTA de m'avoir formé sur les différentes machines de la salle blanche et merci pour l'aide et les explications.

Aucune recherche et aucune thèse sans administration: C'est pourquoi je tiens à remercier l'équipe administrative de l'INAC et de l'école doctorale, Céline Conche, Carmelo Castagna, Sarah Mauduit et Sandrine Ferrari qui m'ont énormément aidé pour les différentes démarches administratives.

Et maintenant dans ce dernier paragraphe, je voudrais remercier les gens, avec qui je n'ai pas travaillé mais sans qui je ne serais pas la personne que je suis maintenant: Merci à mes parents, mes grands-parents et ma sœur pour le soutien et la confiance que vous m'avez donné. Et un grand merci à ma chérie, Cristina qui m'a supporté (ce n'est pas toujours facile avec un thésard à la fin de sa thèse) et soutenu pendant les dernières années. Je vous embrasse très, très fort!!!



# Abstract / Résumé

## Abstract

The all-optical injection of free charge carriers into a semiconductor material can change the resonance frequency of an optical microcavity within few picoseconds and allows an ultrafast modulation of light-matter interaction. In this PhD thesis, we study the switching of different types of cavities based on GaAs/AlAs materials and explore possible applications. When the resonance wavelength of a cavity is shifted on a timescale shorter than its storage time, the frequency of the stored light is up-converted. In this work, we study this effect experimentally for high Q planar microcavities, able to store light during several tens of picoseconds. Upon ultrafast switching, we observe a large frequency shift (around 17 mode linewidths) of stored light. In agreement with numerical simulations, we evidence an adiabatic behaviour and an efficiency close to 100 % for this conversion process. When embedded in a cavity, quantum dots can serve as an internal light source for probing cavity modes and their switching dynamics. We use this approach to study two different kinds of microcavities. On one hand, we inject an inhomogeneous distribution of free charge carriers into micropillars, whose interest for quantum optics experiments is well recognized. We observe drastically different switching behaviors for their cavity modes, due to the different overlaps between free carriers and field intensity distributions. This behaviour is understood in a quantitative way on the basis of simulations taking into account the diffusion and recombination of electron-hole pairs. On the other hand, we explore the properties of a novel type of microcavity, oval ring resonators. We present a characterization of their optical properties, as well as first switching experiments. These objects offer appealing perspectives for the fabrication of microlasers, and for quantum optics experiments such as controlling the Purcell effect in real time.

## Résumé

L'injection toute-optique des porteurs de charge libres dans un matériau semi-conducteur peut changer la fréquence de résonance d'une cavité optique pen-

dant quelques picosecondes et permet une modulation ultra-rapide de l'interaction lumière-matière. Dans cette thèse, nous étudions la commutation de différents types de cavités basés sur les matériaux GaAs/AlAs et explorons des applications possibles. Quand la longueur d'onde de résonance est changée sur une échelle de temps inférieure à son temps de stockage, la fréquence de la lumière stockée est poussée vers des énergies plus hautes. Dans ce travail, on étudie expérimentalement cet effet pour des microcavités planaires à hauts facteurs de qualité, étant capable de stocker la lumière pendant plusieurs dizaines de picosecondes. Dans le cadre de cette commutation, on observe un décalage important (environ 17 largeurs de raie) de la lumière stockée. Conformément à nos simulations numériques, nous mettons en évidence un comportement adiabatique et une efficacité proche de 100 % pour ce procédé de conversion. Etant placées au sein d'une cavité, des boîtes quantiques (BQ) peuvent servir comme source de lumière interne pour sonder les modes de la cavité et la dynamique de la commutation. Nous utilisons cette approche pour étudier deux différents types de cavités. D'un côté, nous injectons une distribution inhomogène de porteurs de charge libres dans des micropiliers, dont l'intérêt pour des expériences d'optique quantique est bien reconnu. A cause des recouvrements différents entre les distributions des porteurs libres et des intensités des champs, nous observons des comportements de la commutation des modes drastiquement différents. Ce comportement est compris quantitativement sur la base des simulations prenant en compte la diffusion et la recombinaison des paires électron-trou. D'un autre côté, nous explorons les propriétés d'un nouveau type de microcavité, des résonateurs en forme d'anneau ovale. Nous présentons une caractérisation de leurs propriétés optiques et premières expériences de commutation. Ces objets présentent des perspectives prometteuses pour la fabrication des microlasers et pour des expériences d'optique quantique comme contrôler l'effet Purcell en temps réel.

# Contents

<b>Remerciements</b>	<b>i</b>
<b>Abstract / Résumé</b>	<b>v</b>
<b>Contents</b>	<b>vii</b>
<b>Introduction</b>	<b>1</b>
<b>1 Theoretical basics</b>	<b>5</b>
1.1 Optical cavities . . . . .	6
1.1.1 Properties of microcavities . . . . .	7
1.1.2 Geometries of microcavities . . . . .	10
1.2 Applications of optical cavities . . . . .	16
1.2.1 Cavity quantum electrodynamics . . . . .	17
1.2.2 Cavities as backbone of light emitters . . . . .	26
1.3 Ultrafast cavity switching . . . . .	33
1.3.1 Methods of ultrafast all-optical cavity switching . . . . .	33
1.3.2 Applications of ultrafast switching . . . . .	37
1.4 Conclusion . . . . .	38
<b>2 Experimental methods for sample fabrication and characterization</b>	<b>41</b>
2.1 Fabrication of the different samples . . . . .	41
2.1.1 Molecular beam epitaxy . . . . .	42
2.1.2 Cleanroom fabrication of the samples . . . . .	48
2.2 Optical characterization of semiconductor microstructures . . . . .	55
2.2.1 Photoluminescence spectroscopy . . . . .	55
2.2.2 Elements for time-resolved microphotoluminescence spectroscopy	57
2.3 Conclusion . . . . .	60
<b>3 Ultrafast color change experiments on planar cavities</b>	<b>61</b>
3.1 Adiabatic color conversion and planar semiconductor cavities . . . . .	61
3.1.1 Adiabatic color conversion: overview and basics . . . . .	62
3.1.2 An overview over planar cavities . . . . .	65

3.2	Characteristics of the planar cavities used for frequency conversion and the experimental setup . . . . .	69
3.2.1	Planar cavities designed for color change experiments . . . . .	69
3.2.2	Experimental setup . . . . .	74
3.2.3	Determining the quality factor of the cavity with a ring down experiment . . . . .	75
3.3	Changing the color of light in a planar cavity . . . . .	81
3.3.1	The color change experiment on a short time scale . . . . .	82
3.3.2	Longterm behaviour of the planar cavity . . . . .	89
3.3.3	Conversion efficiency . . . . .	91
3.3.4	Adiabaticity of the color change and comparison to simulations . . . . .	98
3.3.5	Perspectives for color change using cavity switching . . . . .	98
3.4	Conclusion . . . . .	101
<b>4</b>	<b>Differential mode switching in micropillar cavities</b>	<b>103</b>
4.1	Micropillar cavities - properties, modal structure and use of QDs as integrated probe . . . . .	104
4.1.1	Modal structure . . . . .	105
4.1.2	Probing micropillars with an internal light source . . . . .	109
4.2	The experimental configuration . . . . .	114
4.2.1	The Micropillar cavity . . . . .	114
4.2.2	Time-resolved microphotoluminescence using a two pulse system . . . . .	115
4.3	Differential switching of micropillars . . . . .	118
4.3.1	Characterization of switching events in micropillars . . . . .	118
4.3.2	Differential switching of micropillars . . . . .	125
4.4	Conclusion . . . . .	134
<b>5</b>	<b>Oval ring cavities: properties, lasing, emission behaviour and switching</b>	<b>137</b>
5.1	Principles of oval ring resonators . . . . .	137
5.1.1	Whispering gallery modes . . . . .	138
5.1.2	Ring microcavities . . . . .	139
5.1.3	Asymmetric microcavities . . . . .	141
5.1.4	Oval microcavities . . . . .	142
5.2	Design, fabrication and optical characterization of oval cavities . . . . .	146
5.2.1	Vertical structure of the substrate . . . . .	146
5.2.2	Setup for optical characterization . . . . .	147
5.2.3	Modal structure . . . . .	149
5.2.4	Quality factor . . . . .	153

5.2.5 Purcell factors of oval ring resonators . . . . .	159
5.3 Properties of active oval cavities . . . . .	161
5.3.1 Lasing in oval ring resonators . . . . .	161
5.3.2 Localized, directional emission . . . . .	164
5.3.3 Cavity switching . . . . .	173
5.4 Conclusion and outlook . . . . .	175
<b>Conclusion</b>	<b>179</b>
<b>Bibliography</b>	<b>A1</b>



# Introduction

Semiconductor microcavities have become a major research field since the end of eighties. These structures allow the three dimensional confinement of electromagnetic waves to small volumes of the order of few wavelengths by resonant recirculation. Because of the small confined volumes, the spectral spacing between the cavity modes is much larger than for macroscopic cavities.

Microcavities are used in already existing devices, e.g. for controlling laser emission spectra to enable data transmission by optical fibers and for ensuring narrow spot size laser beams in DVD devices [114]. Still, important research efforts are dedicated to a further improvement of existing experimental techniques by microcavities.

From a more fundamental side, microcavities are crucial for the solid state cavity quantum electrodynamics (CQED) experiments. Purcell predicted in 1946 that spontaneous emission properties of a two-level system can be modified by coupling it with a discrete mode of an electromagnetic resonator [87]. Experiments with Rydberg atoms in superconducting microwave cavities performed by Haroche confirmed these theoretical predictions [42]. Solid-state microcavities with embedded artificial atoms (quantum dots (QDs)) could reproduce these CQED experiments: during the last 20 years, the enhancement and inhibition of the spontaneous emission of QDs could be demonstrated with different cavity types [36, 31, 74, 65] as well as strong coupling between a cavity and a QD [89, 127, 84]. These effects are nowadays used for quantum devices such as single photon sources [19, 103] and low threshold microlasers [50].

Experimental techniques to tune resonance frequencies of solid state microcavities have been developed, too. In the case of semiconductor microcavities, the used techniques rely on the modification of the refractive index by an injection of free carriers into the cavity material [120]. In the case of all-optical injection by ultra short laser pulses, ultrafast switching speeds on the picosecond scale can be achieved. By shifting the resonance frequency, cavity-emitter-interactions can also be tailored. This can be exploited for controlling in real-time the Purcell effect [111] which recently has been demonstrated for a first time [54].

Ultrafast optical switching can also be used to induce a frequency shift of light which is stored in a microcavity. For well chosen switching parameters, it is possible

to ensure that the frequency of stored light follows the cavity mode adiabatically during the switching event. After the switch, the cavity releases a pulse whose frequency has been either up-converted or down-converted, depending on the switching mechanism. This effect has already been shown on different cavity types [85, 110].

The aim of this work was to study cavity switching effects and dynamics of different innovative microcavities. Time resolved optical spectroscopy - using a streak camera with picosecond resolution - was performed on empty cavities (for changing the color of light) and cavities with integrated QDs as an internal source. This allowed a study of cavity-photon-interaction as well as cavity-emitter-interaction. Furthermore, a novel cavity geometry - the oval ring resonator - was studied. The latter research axis is a follow-up of my master thesis. That is why this PhD thesis contains some similarities and already presented results on oval ring cavities.

During this PhD thesis, I contributed to research activities as follows:

**Epitaxy:** I performed the growth of planar structures based on  $\text{Al}_x\text{Ga}_{1-x}\text{As}$  materials as well as InAs-QDs with the molecular beam epitaxy (MBE) technique. Though, most samples which were used during this PhD thesis were grown by former group members Emmanuel Dupuy and Emanuel Peinke. The samples I grew myself will also be used for future projects on single photon sources and color change experiments.

**Microfabrication of resonators:** I was in charge of the fabrication of oval ring resonators and micropillars. I performed all the work steps which are explained in chapter 2 albeit the electron beam lithography process which was performed by Julien Claudon. The samples used in chapter 4 were fabricated by Jean-Michel Gérard.

**Simulations:** The codes for the FDTD simulation of color change and the free carrier distribution in micropillars were written by Emanuel Peinke. I performed FEM simulations with FEMSIM and COMSOL to calculate the energy of micropillars resonances and to simulate oval ring resonators.

**Optical characterization** was mostly done for studying planar cavities and samples with integrated emitters. I performed Fourier Transform Infrared (FTIR) spectroscopy

on planar cavities and was also in charge of the macroscopic analysis of grown samples containing QDs.

My main task was performing **time-resolved photoluminescence spectroscopy** based on a streak camera with picosecond resolution on different types of samples. I designed the optical setup for measuring the color change of planar cavities and for observing switching dynamics of micropillars. Furthermore, I performed experiments to measure the lasing behaviour of oval ring cavities and characterized their emission behaviour. Finally, I also was in charge of evaluating and documenting the experimental results.

This thesis is organized as follows:

**Chapter 1:** Optical solid-state microcavities are introduced. The figures of merit - quality factor  $Q$  and effective volume  $V_{\text{eff}}$  - are presented as well as different confinement principles and the corresponding experimental realizations. Atom-like solid state emitters and CQED basics are explained and an overview over devices which base on CQED effects are given. The principles of cavity switching and state-of-the-art experiments are described.

**Chapter 2:** The growth of bidimensional structures and QDs using the MBE technique is presented. I explain how these planar samples are processed and structured to form cavities capable to confine light in three dimensions. Furthermore, the experimental setup for time-resolved photoluminescence spectroscopy is explained and in particular the operation principle of the streak camera.

**Chapter 3:** We present a detailed experimental study of color change experiments using all-optical injection of free carriers into a high- $Q$  planar cavity. This experimental configuration allows the conversion of photons propagating in the free space. For a better understanding of the nature of the process, pump-probe experiments are performed to probe the switching dynamics. A novel approach for estimating the conversion efficiency is applied to our experiment. Finally, potential improvements for further frequency conversion experiments are discussed.

**Chapter 4:** A detailed experimental and theoretical study of the differential switching of micropillar cavity modes at low temperature is presented. An ensemble of embedded QDs serves as an internal light source and probes the micropillar mode

dynamics in real time. By all-optically injecting an inhomogeneous free carrier distribution into a micropillar, the cavity modes show different switching behaviours. For a better understanding, we develop a model for the dynamics of free carriers in a micropillar, taking into account diffusion and recombination. With the resulting refractive index profiles, we calculate the mode energies for different times after the switch and compare them to our experimental results.

**Chapter 5:** A new resonator geometry displaying an oval shape is introduced. Light is confined in a resonator of this geometry by total internal reflection. This structure combines potentially high quality factors with a large spatial extension which is favorable for future experiments on the real time control of the Purcell effect. Based on QDs as an internal light source, photoluminescence spectroscopy at low temperature was performed to study basic properties of the cavity, such as modal structure, quality factors and the effective volume. Furthermore, the behaviour of active oval cavities was studied. QDs show stimulated emission at higher pumping intensity and lasing can be observed. This property allows an investigation of the emission direction of the asymmetric oval cavities. Because of the varying curvature radii, the emission can be concentrated around specific directions, which presents an improvement compared to circular shaped cavities which show isotropic emission behaviour. By injecting free-carriers into the semiconductor material, the resonance frequency of oval ring cavities can also be switched. First results on such an experiment are presented and confirm the potential of future applications of ring cavities in experiments on controlling light-matter interaction in real time.

# Theoretical basics

Solid state cavity quantum electrodynamics (CQED) has become a major research domain during the last decades. It enables to engineer the optical properties of an emitter by placing it into a solid state optical resonator.

Depending on the quality and size of a microcavity, the spontaneous emission rate of an emitter into a cavity mode can be increased. For laser diodes, it is the spontaneous emission into the lasing mode that triggers stimulated emission. Photons emitted into other modes than the one of interest is in effect a loss which degrades the performance of the device. Therefore, control over spontaneous emission is a promising track for improving laser diodes. It is indeed interesting to know how one could act on this property or even control it dynamically.

In this chapter, an overview of the fundamental concepts of CQED and the requirements for experiments is given. Applications and recent experiments are described as well.

The first section deals with optical microcavities. These objects confine light in very small volumes during a finite time. An explanation about basic properties, figures of merit and experimental realizations is given.

Applications of optical cavities are presented in the second section. When microcavities are combined with integrated quantum emitters, solid state CQED experiments can be realized. I give an overview over recent experiments and highlight two promising devices based on CQED: single photon sources and low-threshold micro-lasers.

The third section handles all-optical switching of cavities. This technique allows an ultrafast modification of the resonance wavelength of cavities and, consequently, a modulation of light-matter interaction on a picosecond time scale.

## 1.1 Optical cavities

Optical cavities are objects which confine light in one, two or three dimensions. They are used in many devices which are part of our daily life (e.g. lasers, which are based on macroscopic cavities).

One speaks of a microcavity when the confinement of light is achieved on a scale comparable to the optical wavelength at least along one direction.

Let us consider a perfect, model microcavity which provides three-dimensional confinement using perfect mirrors with reflectivity  $R = 1$ : it would exhibit discrete modes and infinite storage time. The spectral position of the modes would depend on the dimensions of the cavity.

Actual cavities use mirrors which possess reflectivity  $R \neq 1$ . These cavities confine light for finite storage times, which result in a spectral broadening of the resonances of the cavity (see Figure 1.1).

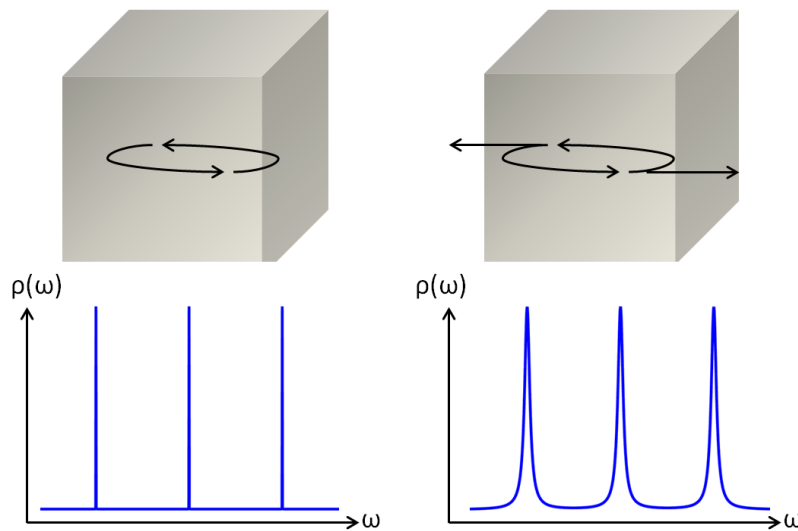


**Figure 1.1** Comparison of the density of states of an ideal cavity which confines light during an infinite time (left side) and a real cavity which emits light after a finite time (right side).

This finite temporal confinement, compared to an ideal cavity is described by the quality factor  $Q$ , while the effective volume  $V_{\text{eff}}$  quantifies the spatial confinement of the photons.

In the first part of this section, I define these two parameters and present different figures of merit of microcavities. These are decisive for evaluating the capability of microcavities to be used in applications or devices.

Then in the second part, I will give examples of different experimental realizations of optical semiconductor cavities. I will also provide state-of-the-art values for semiconductor microcavities based on GaAs.

### 1.1.1 Properties of microcavities

Two different parameters which characterize microcavity modes are defined in this section: The quality factor  $Q$  is directly related to the confinement time of photons (how long the photons are stored in the cavity), whereas the effective volume  $V_{\text{eff}}$  measures the spatial volume into which light is confined. Note that these two parameters are specific to a given cavity mode  $m$ .

#### 1.1.1.1 Quality factor

The quality factor  $Q$  is one of the most important parameters of a microcavity mode. It characterizes the temporal confinement of a photon in a microcavity, but also determines the properties of the emission spectrum of microcavities such as the linewidths of cavity modes. The general definition of the quality factor for the mode  $m$  is given as follows:

$$Q_m = 2\pi \cdot \frac{\text{Energy stored in the cavity}}{\text{Energy lost during one optical cycle}} \quad (1.1)$$

It is not easy to determine  $Q$  with this equation because of the difficulties to measure either the energy which is stored in the microcavity, or the energy that is emitted (lost).

In the low loss regime, the energy  $E$  of the light stored in the cavity decays exponentially as a function of time (see Figure 1.2)(a).  $\tau_m$  corresponds to the lifetime of a photon in a cavity or to the characteristic damping time of the energy stored in a cavity. If we consider the field amplitude  $\Psi(t)$  of the electromagnetic wave, we obtain:

$$E(t) \propto e^{\frac{-t}{\tau_m}} \propto |\Psi(t)|^2; t \in [0, +\infty] \quad (1.2)$$

It follows that

$$\Psi(t) \propto e^{\frac{-t}{2\tau_m}} e^{-i\omega_m t} \quad (1.3)$$

After applying a Fourier transformation, the field can be expanded in the frequency space:

$$\Psi(\omega) \propto \frac{1}{\frac{1}{2\tau_m} + i(\omega_m - \omega)} \quad (1.4)$$

The spectral density  $\rho$  associated with this discrete mode is given by  $|\Psi(\omega)|^2$ . It has a Lorentzian shape centered around the resonance frequency  $\omega_m$  and a FWHM  $\Delta\omega = 1/\tau_m$ :

$$\rho(\omega) = |\Psi(\omega)|^2 \propto \frac{1}{\frac{1}{4\tau_m^2} + (\omega_m - \omega)^2} \quad (1.5)$$

It is now possible to deduce the fraction of light which is lost during one period  $T = \frac{2\pi}{\omega}$ . The differential equation satisfied by  $E(t)$  is

$$\frac{dE}{dt} = -\frac{E}{\tau_m} \quad (1.6)$$

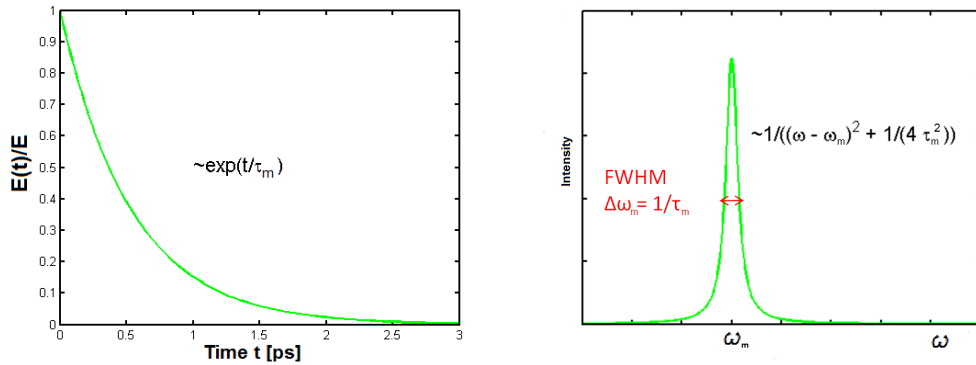
$\frac{E}{\tau_m}$  is the expression of the energy loss rate, therefore

$$\frac{E}{\tau_m} = \frac{E_{\text{loss}}}{T} = \frac{E_{\text{loss}}}{2\pi/\omega} \quad (1.7)$$

Equation 1.1 can now be written as

$$Q = \frac{2\pi E}{E_{\text{loss}}} = \omega\tau_m = \frac{\omega}{\Delta\omega} \quad (1.8)$$

It follows that the quality factor can be determined from the spectral response of a cavity by measuring the full width of half maximum (FWHM) of the Lorentzian curve, as shown on Figure 1.2(b).



(a) Time dependence of the electromagnetic energy stored in cavity mode  $m$ . (b) Spectral density for a cavity mode  $m$ .

**Figure 1.2** Graphs for a microcavity with resonance frequency  $\omega_m$  and  $Q_m = 1000$ .

### 1.1.1.2 The effective volume of a cavity

If light is confined by a cavity in all three dimensions, one can introduce the effective mode volume  $V_{\text{eff}}$ . This figure of merit describes the capacity of a cavity to confine light spatially.  $V_{\text{eff}}$  is the volume of a cavity defined by periodic boundary conditions, which would provide the same maximum field intensity than our actual cavity for a given amount of stored electromagnetic energy. It stores the same electromagnetic energy as the mode with a uniform energy density and refractive index, both equal to the values taken at the point in the mode where the electromagnetic field intensity is maximal (cf. Figure 1.3).

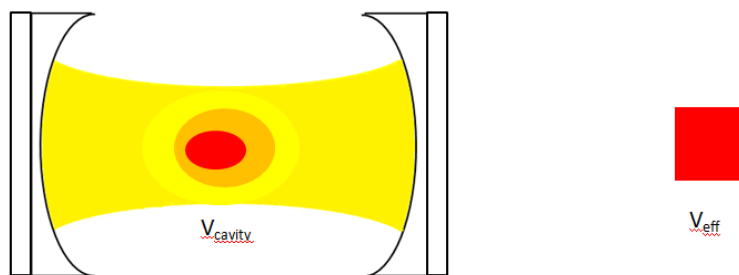


**Figure 1.3** Principle of the effective volume. On the left hand side the real volume of the cavity and its field distribution, on the right side the effective volume and its uniform field distribution (red: maximal intensity).

$V_{\text{eff}}$  can be calculated as:

$$V_{\text{eff}} = \frac{\int \int \int n^2(\vec{r}) |\vec{E}(\vec{r})|^2 d^3r}{n_{\text{max}}^2 |\vec{E}_{\text{max}}|^2} \quad (1.9)$$

$\vec{E}(\vec{r})$  and  $n(\vec{r})$  stand for the electric field and refractive index at position  $\vec{r}$ ,  $E_{\text{max}}$  and  $n_{\text{max}}$  are the values of the maximum field intensity and the refractive index at its corresponding position.

The numerator represents the whole energy stored in the cavity, whereas the denominator stands for the uniform energy density within the effective volume.

## 1.1.2 Geometries of microcavities

Different geometries based on different physical effects exist for confining light. In this chapter, I describe the geometries which can be fabricated from III-As-semiconductor materials.

### 1.1.2.1 One dimensional confinement: planar cavities

Planar cavities consist of two parallel flat mirrors separated by a spacer of a thickness of the order of magnitude of one optical wavelength. If experiments are done with atoms, the mirrors are usually separated by vacuum. In the case of a solid state cavity, the mirrors are separated by a dielectric layer. In the frame of this work, semiconductors are used. Planar cavities provide confinement in the direction normal to the mirrors. Photons can freely propagate in the other two dimensions.

The ideal planar cavity consists of two mirrors with reflectivity  $R = 1$  over an infinite spectral range. A standing wave forms between the mirrors, and photons are confined forever along the  $z$ -direction.

Actual planar cavities are of two different types: based on metallic mirrors or based on Distributed Bragg Reflectors (DBRs) (cf. Figure 1.4).

Cavities based on metallic mirrors consist of a metal-spacer-metal sandwich. Frequently used metals are silver, gold and aluminum. Metallic mirrors exhibit a reflectivity of  $> 0.95$  over a large spectral range in the visible and the infrared. The remaining light ( $< 0.05$ ) is absorbed.

The resulting low quality factors combined with bad extraction properties due to the absorption of light in the metal layer are a big drawback for planar cavities based on metallic mirrors.

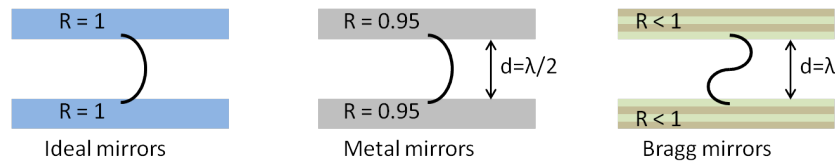
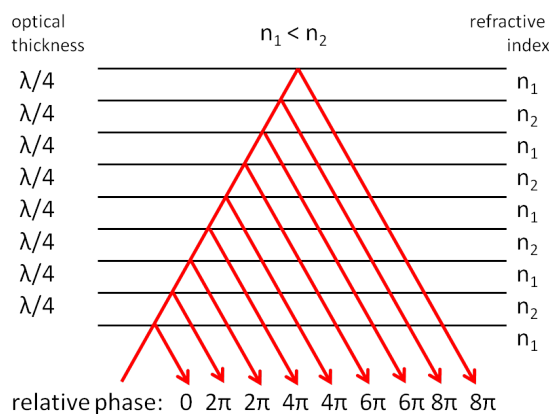
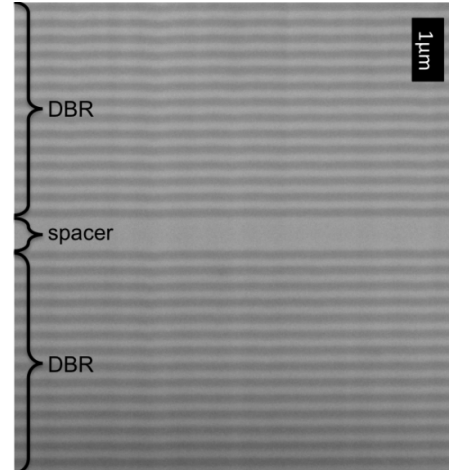


**Figure 1.4** Different models of planar cavities.

For these reasons, Bragg mirrors are mostly used nowadays. Bragg mirrors consist of periodically stacked layers of dielectric material having different refractive indices, and  $\lambda_B/4n$  optical thickness. For perpendicularly incident light at the  $\lambda_B$  wavelength, all rays subject to a single reflection emerge from the mirror with the same phase (modulo  $2\pi$ ). This is also true for any odd number of reflections. This implies equal phases of the reflected waves, which lead to constructive interference (note the phase shift of  $\pi$  which occurs when light coming from a material with lower refractive index is reflected at the interface to a material with higher refractive index). This principle is also depicted on Figure 1.5(a) (case of non-perpendicular incidence on the figure for a better understanding). The higher the number of Bragg pairs, the higher is the reflectivity of the Bragg mirrors.



(a) Reflection at a DBR: all reflected rays corresponding to  $\lambda_B$  are reflected and interfere constructively.



(b) Cross section of a planar cavity based on Bragg mirrors fabricated with GaAs/AlAs (taken from [82]).

**Figure 1.5** Principle and realization of a planar cavity based on Bragg mirrors.

With this method,  $R > 0.999$  can be obtained. This results in  $Q > 3000$  for planar cavities. There is in theory no upper limit to  $Q$  for this type of mirror. A

further advantage is that the growth of Bragg mirrors based on GaAs/AlAs-pairs which is well-mastered nowadays. A cross-section of a planar cavity is shown on Figure 1.5(b).

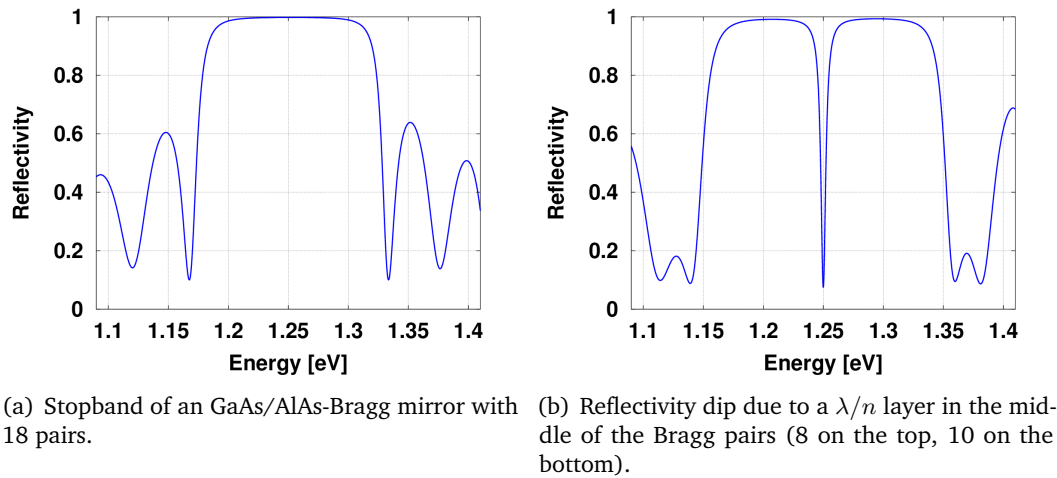


**Figure 1.6** Reflectivity bands of Bragg mirrors.

Figure 1.6(a) shows the reflectivity behaviour for a GaAs/AlAs Bragg mirror consisting of 18 DBR pairs which is optimized for operation at 1.25 eV. High reflectivities are observed for a 0.1 eV broad spectral range, the so-called stopband. For energies which do not lie in the stopband range, lower reflectivities are observed.

By putting a spacer with thickness of  $\frac{\lambda_m}{n}$  between two Bragg mirrors, we add a defect into the stopband. This breaks the periodicity of the dielectric layer, modifies the reflection pattern and allows the creation of a confined optical mode. A dip in the center of the stopband is visible (cf. Figure 1.6(b)). Its position corresponds to the energy of photons which can be confined in the cavity.

We use planar cavities in order to change the color of stored light. In chapter 3, these experiments are explained and a more detailed description of planar cavities is given, too.

### 1.1.2.2 Confinement based on total internal reflection

The possibility to confine light into a cavity is benefitting from total internal reflection at the interface of a material with high refractive index to a material with low refractive index  $n_c$ .

The light beam arriving from the medium with a higher optical density ( $n_{\text{Semiconductor}}$ ) obeys Snell's law. To observe total internal reflection, the incident light has to hit the interface with an angle  $\chi$  larger than

$$\chi \geq \arcsin(n_c/n_{\text{Semiconductor}}) \quad (1.10)$$

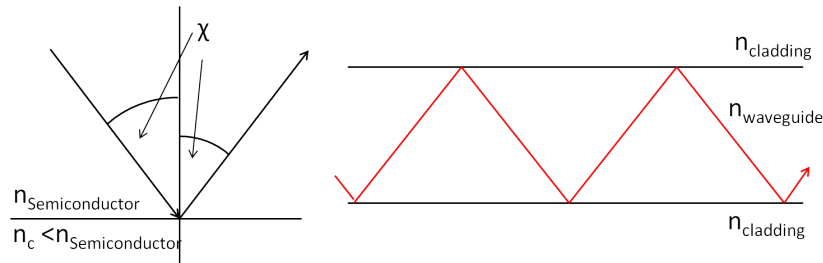


**Figure 1.7** Principle of total internal reflection at the interface of two dielectric materials (left side). Guiding of light based on total internal reflection (right side).

The principle of total internal reflection is illustrated on Figure 1.7. If the incident angle respects this limit, the light is reflected at the interface of the two dielectric materials.

This effect can be exploited for confining and guiding light. Optical fibers are based on this effect as well as waveguides and cavities based on total internal reflection such as microdisks.

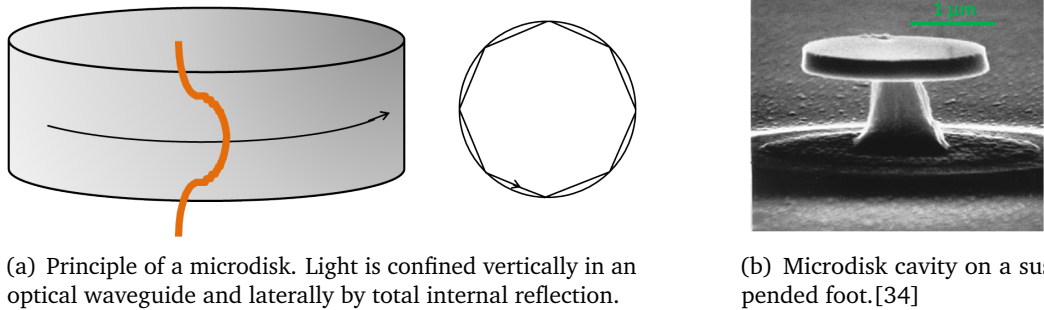
Total internal reflection also works well at curved interfaces if the curvature radius is much larger than the wavelength. The tangential line to the curved interface serves as a reference for the angles of incident waves.

### 1.1.2.3 Three-dimensional light confinement in semiconductor cavities

A short overview over cavities capable of confining light in three dimensions is given: microdisks, micropillars and photonic crystals.

**Microdisks** A resonator which provides this kind of confinement is a semiconductor microdisk (radius  $R_{\text{disk}}$ ) which is held by a small pedestal ( $R_{\text{pedestal}}$ ;  $R_{\text{pedestal}} \ll R_{\text{disk}}$ ) and depicted on Figure 1.8(b). The lateral confinement of the photons is provided by the dielectric structure in which waves are confined by total internal reflection at the curved interface between the semiconductor and the vacuum. Having a high refractive index contrast, the air-semiconductor-air sandwich serves as

a waveguide and confines the light vertically (cf. Figure 1.8(a)). If  $R_{\text{pedestal}} \ll R_{\text{disk}}$ , the pedestal does not introduce losses for the whispering gallery modes, for which light circulates close to the disk edge.



(a) Principle of a microdisk. Light is confined vertically in an optical waveguide and laterally by total internal reflection.

(b) Microdisk cavity on a suspended foot.[34]

**Figure 1.8** Physics and experimental realization of microdisk cavities.

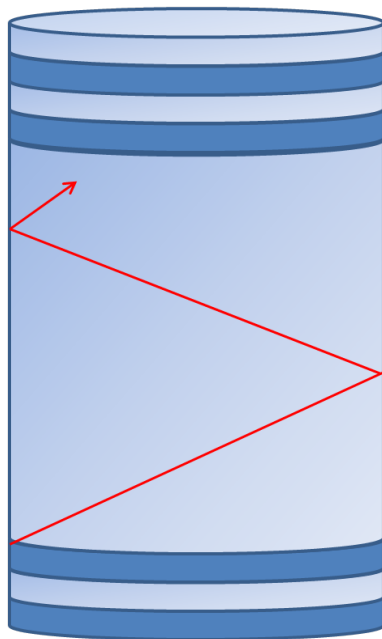
The first realization of this kind of cavity was achieved by S. L. McCall et al. in 1992 [68]. M. Borselli et al. measured  $Q$  factors up to  $5 \cdot 10^6$  for silicon disks in 2005 [13]. For AlGaAs, a  $Q = 3.6 \cdot 10^5$  was reported by the same group [105].

Parts of chapter 5 are dedicated to resonators based on this kind of confinement. A more detailed description is given there.

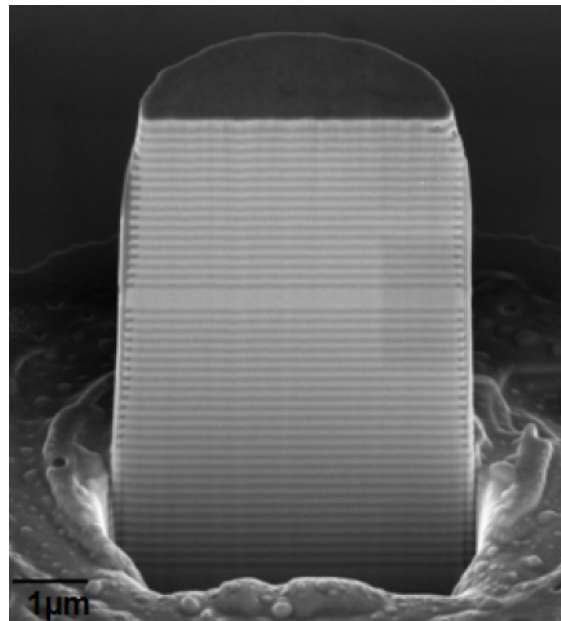
**Micropillars** One possibility to improve the planar cavity towards three dimensional confinement of light lies in the so-called micropillars. A micropillar is a cylindrical waveguide with DBRs at its top and bottom. The different refractive indices of air and the semiconductor material lead to the guiding of light (the configuration is similar to an optical fiber) and provides in-plane confinement. Additional vertical confinement is provided by the Bragg reflectors. Light is thus confined in all three dimensions (see Figure 1.9(a)).

Micropillars are fabricated by circularly etching planar cavities (cf. Figure 1.9(b)). Because of the non-zero electric field at the air-semiconductor interface, the guided light “feels” the roughness of the etched structure. It is important to avoid rough surfaces which decrease the quality factor.

Two different families of modes can exist in such a cavity: vertical modes that propagate parallel to the cylindrical axis and whispering gallery modes which propagate in the plane around the pillar axis. Because of their easier detection, the vertical modes are predominant in most experiments. C. Arnold et al. measured  $Q \approx 2 \cdot 10^5$  for vertical modes in AlGaAs/GaAs-micropillars in 2012 [4] and C. Schneider et al. reported quality factors of  $2.5 \cdot 10^5$  in 2016 [98].



(a) Principle of a micropillar. Light is confined laterally by total internal reflection and vertically by DBRs.



(b) SEM image of a cross section of a circular micropillar which was cut by a FIB[77].

**Figure 1.9** Physics and experimental realization of micropillar cavities.

In chapter 4, I provide a more detailed description of micropillars, their modes and results of experiments on micropillars.

**Photonic crystals** Cavities can also be formed by photonic crystals. I give here a short overview of their properties and different applications.

Photonic crystals are usually formed by holes which are periodically distributed over the material. An example for such a structure is shown on Figure 1.10. The distance between the holes must be in the same order of magnitude as the wavelength of the light which is confined. As described before, the periodic structure forms a stopband which depends on the distribution of the holes and has a reflectivity close to unity. The insertion of defects into photonic crystals results in cavities with ultra-high quality factors: H. Sekuguchi et al. measured  $Q \approx 9 \cdot 10^6$  for a silicon photonic crystal cavity in 2014 [99].

Photonic crystals have the advantage that their properties can be tailored depending on their application. It is possible to achieve one-, two- and three-dimensional confinement with differently arranged photonic crystals. Because of recent advances in fabrication and conceptions, photonic crystals now have the highest  $Q$ -factors and

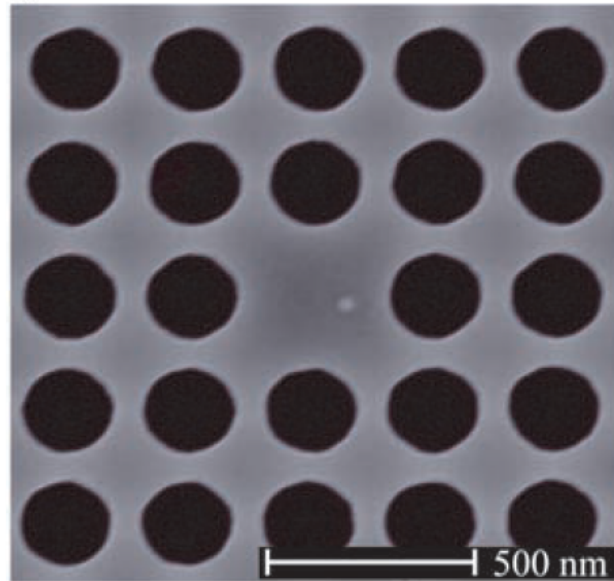


**Figure 1.10** A cavity formed by a photonic crystal [5].

lowest effective volumes of all III-V semiconductor cavities and proved their worth in many experiments.

However, the drawback of photonic crystals is their still difficult experimental handling as well as the complicated fabrication process.

## 1.2 Applications of optical cavities

A large number of applications of cavities exist and a detailed description of all of them is beyond the scope of this PhD thesis. In the following, I will concentrate on a description of a few of them involving optical semiconductor microcavities.

First, I give an overview over cavity quantum electrodynamics (CQED) which has become a major field of fundamental research during the last 40 years [47]. Understanding the fundamental mechanisms of CQED could greatly influence the design of devices used in daily life. And there is still a lot of research going on for further achievements. I give a description over cavity-emitter interactions and particularly the Purcell effect. I describe the properties of quantum dots (QDs) which are a well-suited solid state emitter for CQED. A description of CQED experiments based on QDs is also given.

In the second half of this section, I describe devices based on CQED: microlasers and single photons sources. Microlasers such as VCSELs are already used in existing

devices, but their performances could be significantly increased by exploiting CQED effects. On the other hand, single photon sources are not yet established and constitute still a hot research topic. But they look as promising candidates for future applications such as quantum computing [79] and quantum communication [38, 39].

## 1.2.1 Cavity quantum electrodynamics

CQED generally describes interactions between a photon emitter with quantum nature and light which is confined in a cavity mode. As a consequence, the properties of the emitter can be influenced by putting it into a cavity.

### 1.2.1.1 Emitter cavity interactions and the Purcell factor

Spontaneous emission describes the relaxation of a quantum system from its excited state to its ground state assisted by emission of a photon. In the quantum electrodynamics formalism, the emission is caused by the vacuum fluctuations of the quantized electromagnetic field of its environment. The emission rate depends thus on the local density of modes around the emitter. Properties of an emitter can be drastically modified by inserting it into a cavity.

Now, we consider a two level emitter (TLE) with states  $|g\rangle$  (ground state) and  $|e\rangle$  (excited state) and a cavity mode described by the number of photons stored in it:  $|n\rangle$ . In the spontaneous emission regime  $n = 0$ . We also consider that the emitter couples only to one mode of the cavity.

**Strong- and weak-coupling regime** Let us suppose a perfect, lossless cavity whose resonance has the same frequency as the emission line of the emitter. The coupling of emitter and cavity mode to the environment is supposed to be zero.

In this case, the emitter and the cavity form linear combinations of their states which are  $|e, 0\rangle$  and  $|g, 1\rangle$ . Photons are coherently exchanged between emitter and cavity. The population of the system shows undamped Rabi oscillations between both of the entangled states.

Actually, both cavity and emitter are coupled to their environment (see Figure 1.11(a)). It is possible to distinguish between two different regimes: the strong- and the weak-coupling regime.

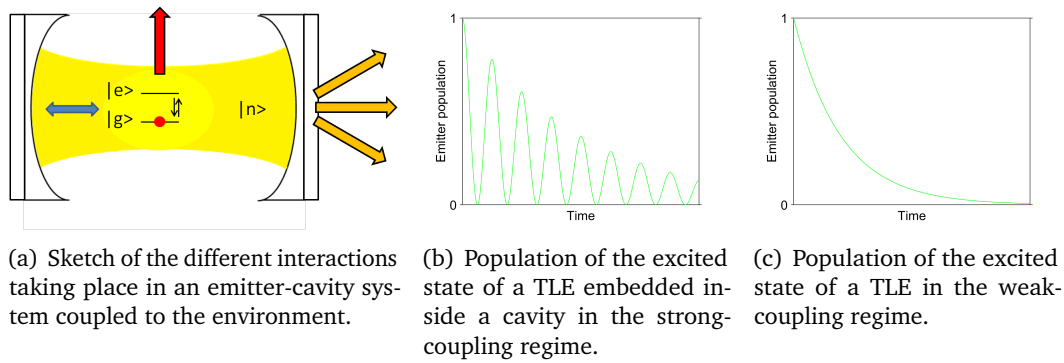


**Figure 1.11** A classical CQED system and its different behaviours.

The strong-coupling regime still shows Rabi oscillations between the emitter and the cavity population (see Figure 1.11(b)), but the oscillations are now damped. The emission of a photon by the emitter is still reversible. This is the case for a sufficiently high quality factor of the cavity and a small coupling of the TLE to the environment. This means that the photon has to stay long enough in the cavity for being reabsorbed by the emitter.

This behaviour has been observed for a first time back in 1996 with Rydberg atoms in microwave cavities defined by superconducting mirrors [14].

In the case of a lower  $Q$ , the photon does not stay long enough in the cavity to re-excite the emitter. The emission of a photon is therefore irreversible, as the system is overdamped. The emitter-cavity-mode system is in the weak-coupling regime.

This case results in an exponential decay of the population of the emitter, as can be seen on Figure 1.11(c). Qualitatively, this is similar to the decay of a TLE in a bulk material, but the cavity changes the quantitative behaviour of the emitter: depending on its environment, the decay rate is modified.

**The Purcell factor** When A. Einstein introduced his spontaneous emission coefficient, he supposed that an emitter would decay at a characteristic, constant rate.

In 1946, E. M. Purcell predicted that the spontaneous emission rate of an emitter can be drastically enhanced throughout its coupling to a mode of an electromagnetic resonator [87].

Fermi's Golden Rule states that the emission rate  $\Gamma$  of an optical emitter is proportional to the local density of optical states (LDOS) to which the emitter is coupled. The LDOS gives the number of modes, into which a photon can be emitted, and their

presence probability. In a QED picture, it can also be interpreted as the density of vacuum fluctuations at the position of the emitter.

$$\Gamma = \frac{1}{\tau} = \frac{2\pi}{\hbar^2} \left| \left\langle e, 0 \left| -\hat{d} \cdot \hat{E} \right| g, 1 \right\rangle \right|^2 \rho(\omega) \quad (1.11)$$

There,  $\tau$  is the lifetime of the emitter,  $\hat{d}$  the dipole operator,  $\hat{E}$  the corresponding electric field operator for the cavity mode at the location of the dipole and  $\rho(\omega)$  the density of modes at frequency  $\omega$ .

Now, we consider a single mode  $m$  with a quality factor  $Q_m = \frac{\omega_m}{\Delta\omega_m}$ . In this case, the density of states can be written as follows:

$$\rho(\omega) = \frac{2}{\pi\Delta\omega_m} \frac{\Delta\omega_m^2}{4(\omega - \omega_m)^2 + \Delta\omega_m^2} \quad (1.12)$$

In the case of an ideal emitter in perfect resonance with the cavity mode ( $\omega = \omega_m$ ), the density of state reduces to:

$$\rho(\omega) = \frac{2Q_m}{\pi\omega_m} \quad (1.13)$$

The amplitude of the electric field at the antinode of the cavity mode is given by:

$$E_{max} = \sqrt{\frac{\hbar\omega}{2\epsilon_0 n^2 V_{eff}}} \quad (1.14)$$

For an emitter with a dipole parallel to the electric field placed at the field maximum, we can write Equation 1.11 as follows:

$$\frac{1}{\tau} = \frac{2d^2 Q_m}{\hbar\epsilon_0 V_{eff} n^2} \quad (1.15)$$

We compare this emission rate to the spontaneous emission rate into free space [8]:

$$\frac{1}{\tau_0} = \frac{d^2 \omega^3 n}{3\pi \hbar \epsilon_0 c^3} \quad (1.16)$$

We obtain the so-called ‘‘Purcell factor’’  $F_p$ :

$$F_p = \frac{\Gamma_{\text{cav}}}{\Gamma_{\text{bulk}}} = \frac{\tau_0}{\tau} = \frac{3}{4\pi^2} \frac{Q \cdot (\lambda/n)^3}{V_{\text{eff}}} \quad (1.17)$$

$\Gamma_{\text{cav}}$  ( $\Gamma_{\text{bulk}}$ ) is the spontaneous emission rate of an emitter in a cavity (bulk material of refractive index  $n$ ).

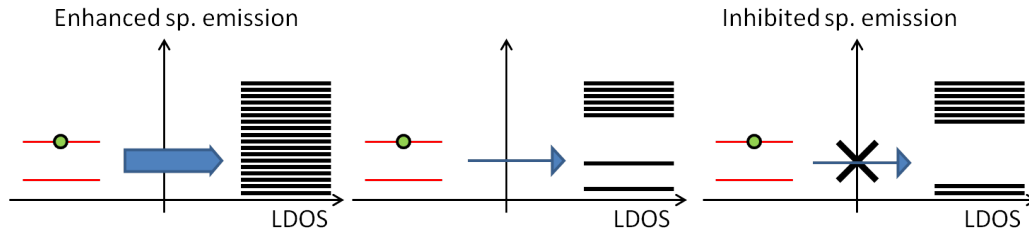


**Figure 1.12** Emission into different modes. The larger the mode density into which can be emitted the photon, the larger is the probability that emission would take place (the thickness of arrows stands for the probability of a spontaneous emission process).

The figure of merit of the exaltation or inhibition of spontaneous emission into cavity modes is the Purcell Factor  $F_p$ .

If we are using a cavity with a high quality factor and an effective volume whose order of magnitude is around several tens of  $\lambda/n$ , the ratio  $\Gamma_{\text{cav}}/\Gamma_{\text{free}}$  becomes  $\gg 1$  and the spontaneous emission rate can be drastically enhanced, as predicted by Purcell (cf. Figure 1.12). We see that high quality factors (which increase the spectral density of modes seen by the emitter) and low effective volumes (which increase the amplitude of vacuum field fluctuation) are favorable in that context.

Note that the Purcell factor is a figure of merit for the cavity alone. It describes the ability to increase the coupling of some ideal emitter with the vacuum field.

To observe Purcell enhancement, the following conditions have to be fulfilled:

- The linewidth of the emitter  $\Delta\lambda_e$  has to be inferior to the linewidth of the cavity  $\Delta\lambda_c$ . If the condition  $\Delta\lambda_c \gg \Delta\lambda_e$  is not fulfilled, the modification of the spontaneous emission is ‘‘washed out’’. This imposes a condition on the properties of emitters that have to show very small homogeneous transition linewidths compared to the cavity linewidth. One type of emitter which is well suited for observing the Purcell effect is described in the following section.
- The emitter is in perfect resonance with the cavity mode.

- The emitter is located at an antinode of the vacuum field and its dipole is parallel to the local polarization of the mode.

The Equation 1.17 is valid for a quantum emitter which is located at an antinode of the electric field and spectrally matches the cavity mode. In the case of a spatially and spectrally non-resonant quantum emitter,  $F_p$  writes

$$F_p = \frac{3}{4\pi^2} \frac{Q \cdot (\lambda_c/n)^3}{V_{eff}} \frac{\lambda_c^2}{\lambda_c^2 + 4Q^2(\lambda_e - \lambda_c)^2} \frac{|\vec{E}(\vec{r})|^2}{|\vec{E}_{max}|^2} \quad (1.18)$$

where  $\vec{E}(\vec{r})$  is the electric field at the emitter location and  $\lambda_e$  the emission wavelength.

In 1983, Purcell's prediction was confirmed experimentally for the first time by S. Haroche et al. They observed that the spontaneous-emission lifetime of Rydberg atoms is shortened by a ratio of 700 when these atoms are crossing a high-Q superconducting cavity tuned to resonance with a millimeter-wave transition between adjacent Rydberg states [42].

Beyond the enhancement of spontaneous emission, inhibition can also take place. An emitter whose transition energy corresponds to a low photonic LDOS will significantly slow down its spontaneous emission (cf. Figure 1.12).

### 1.2.1.2 Quantum dots: an atom-like photon source

Until now, I considered two level emitters as atoms or ions which are close to ideal TLEs. Despite their appealing properties and lots of striking experimental demonstrations of CQED effects with them, these photon sources are difficult to handle experimentally, because they have to be handled in vacuum [15]. This significantly complicates future applications and integration into future devices and systems.

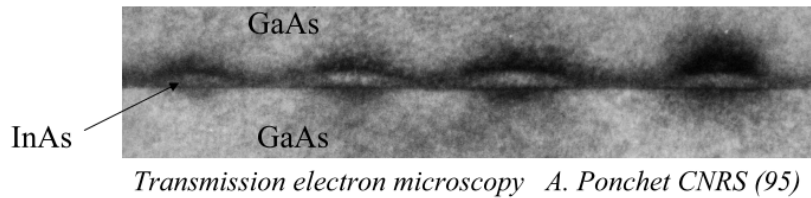


**Figure 1.13** TEM-image of a sidecut of InAs-QDs embedded in a GaAs-matrix.

To overcome this problem, many atom-like solid-state emitters have been developed during the last decades. The best known are color centers in 3D bulk crystals (diamond, SiC, YAG and ZnO), 2D materials (transition metal dichalcogenides, carbon nanotubes) and quantum dots (QDs) [1]. All of these emitters have advantages and disadvantages. In the following, I describe QDs, on which large parts of my work are based.

**Properties of single QDs** A quantum dot is a small nanostructure with sizes of a few nm in all three dimensions surrounded by a material of larger energy bandgap. A TEM-image of QDs is shown on Figure 1.13.

During this work, InAs QDs were used. The energy bandgap of these dots is smaller than the one of the surrounding material (GaAs). When excited, charge carriers like electrons and holes are captured by the potential well and confined by potential barriers of the QDs in all three dimensions to form excitons. The confinement can be described with the concept of three dimensional quantum mechanical potential wells, which cause the above-mentioned quantization of energy states.

The resulting energy states are sketched on the left side of Figure 1.14. In the QDs, discrete states are observed. Depending on the geometry of the QD, these states are separated by several meV. A continuum of states exists in the conduction and the valence band of the barrier material.

We first look at a single QD and concentrate on the ground state of the exciton (X) in the QD. It recombines under emission of a photon with energy  $h\nu_1$ . Back in 1994, photoluminescence of a single QD was observed for the first time by J.-Y. Marzin et al. [67]

Only one electron-hole pair is created in the QD after a weak enough excitation. The pair recombines and emits a single photon. At low temperatures, a discrete emission line showing a width in the few  $\mu\text{eV}$  range is observed. The linewidth is close to the lower limit defined by the radiative lifetime of the exciton [7] and the QD can be considered as an artificial atom because of its discrete transitions (see Figure 1.14). At 5 K, exciton lifetimes of about 1 ns are observed [36].

At stronger excitation energies, more than one electron-hole pair is created and captured by the QD. Following the Pauli principle, the discrete states of the QDs are populated. Of particular interest is the biexciton state (XX), for which two electrons (in the singlet spin state) occupy the first electron level of the QD, while two holes occupy the first hole level. Because of strong Coulomb interactions, it does not have the same energy as the exciton. This results in a different energy  $h\nu_2$  of the emitted

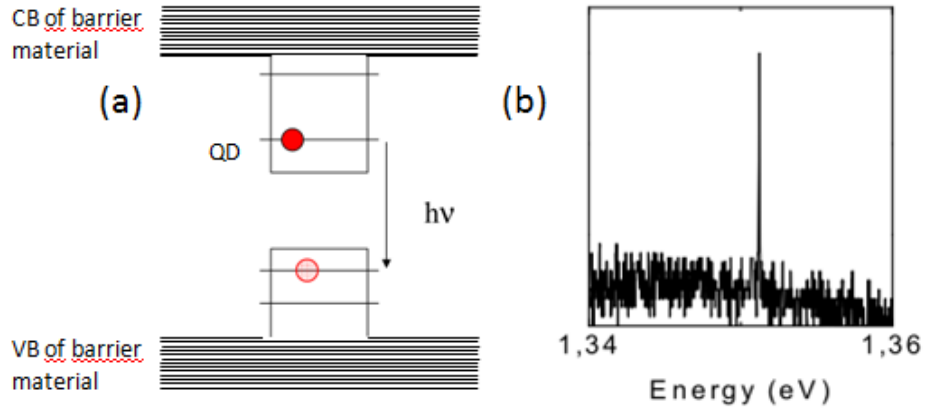


**Figure 1.14** (a) Sketch of the energy levels for a QD. The confinement in the potential well creates discrete energy levels. The discrete density of states  $\rho$  causes discrete spectral lines for the transitions between excited and ground states. At higher energies, a continuum of transitions between the CB and VB of the surrounding material can be observed. (b) Spectrum of a QD transition under weak excitation (taken from [67]).

photon when the first electron hole pair recombines. This leads to spectrally well separated emission lines of the recombinations of X and XX (see Figure 1.15).

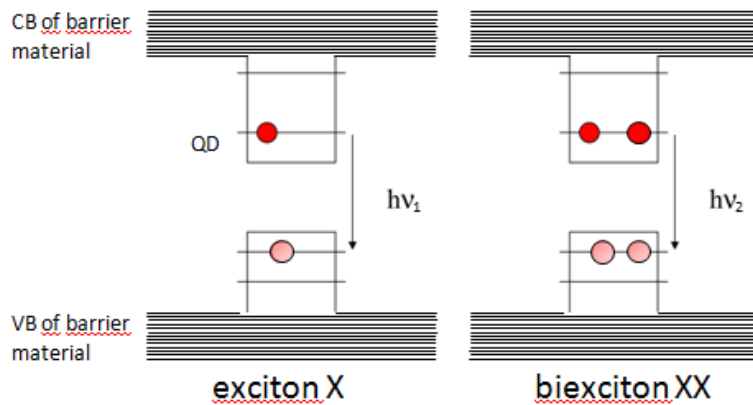


**Figure 1.15** Schematic picture of the energy levels in a QD. The filled dots represent electrons, the transparent dots represent holes. Each state of the QD (exciton (X) and biexciton (XX)) emits a photon at different energies. This appears because of the strong Coulomb interactions between excitons in the QD.

At higher temperatures, QDs start to couple to phonons. Figure 1.16 shows a significant broadening of the QD emission line for growing temperatures. This appears because the linewidth of a QD is defined by two contributions: its radiative lifetime  $T_1$  and dephasing time  $T_2^*$  [15]:

$$\Delta\nu_{QD} = \frac{1}{2\pi T_1} + \frac{1}{\pi T_2^*} \quad (1.19)$$

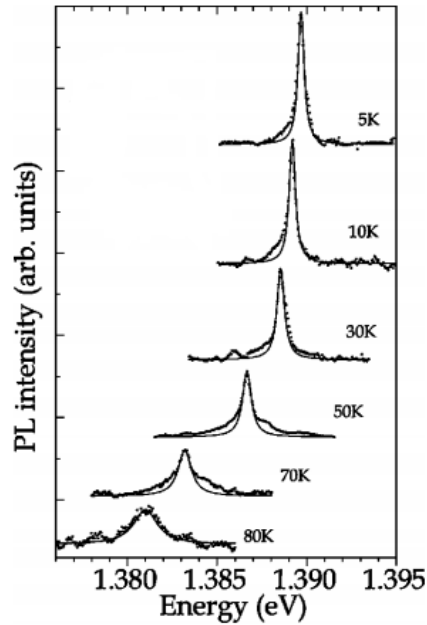


**Figure 1.16** Broadening of the emission line of a single QD with growing temperature (taken from [28]).

To become a lifetime-limited emitter,  $T_2^*$  must be infinite. In reality, the dephasing time results from interaction with phonons, the surrounding lattice and free carriers. At room temperature,  $\frac{T_1}{T_2^*} \approx 10^{-4}$  [43]. Upon cooling,  $T_2^*$  is reduced significantly because the phononic contributions to dephasing decrease.

It is also important to keep in mind that the capability of QDs to capture free carriers decreases when the sample is heated up. Free carriers can escape the potential and are no longer confined in the QD.

**Properties of an ensemble of InAs QDs** Semiconductor QD structures can be fabricated with many different materials (III-V and II-VI semiconductor structures) and a good overview about their properties is given in [15]. During this PhD thesis, I worked on InAs QDs embedded in a GaAs structure. This is the most common QD structure.

By epitaxial growth of InAs QDs in GaAs, a layer containing a large areal density of QDs is obtained. Luminescence thus consists of a superposition of the emission lines of this ensemble of QDs.

Due to a broad distribution of size, self-organized QDs cover a big spectral range. The average size of self-assembled QDs depends on the growth conditions (see chapter 2). Depending on their size, InAs QDs emit in a range from 900–1000 nm and can serve as a broadband source to probe optical structures from inside [33].

An ensemble of QDs has another positive effect: The QDs trap excitons and prevent further diffusion of excitons towards non-radiative recombination centers situated in the surrounding semiconductor or at its boundaries.

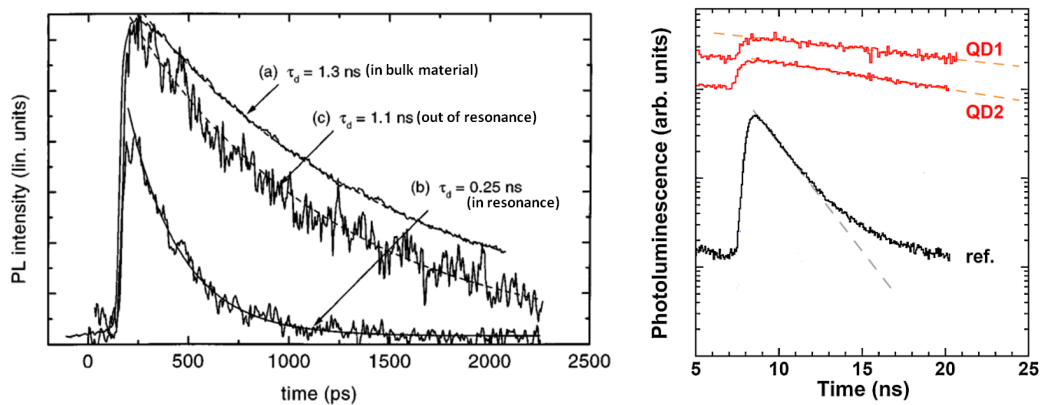
### 1.2.1.3 Experiments with quantum dots in cavities

The combination of cavities of a size of few  $(\frac{\lambda}{n})^3$  and InAs QDs which serve as quantum emitters opens the way for many experiments and applications.

It is possible to define semiconductor structures around the QDs after the growth by nanofabrication. All types of cavities described in section 1.1 can thus be fabricated with a layer of QDs, which is placed deterministically in the vertical direction.

Because of their small size and discrete resonances, QDs affect the photons which are stored in a resonator only slightly. With a collection of QDs which are distributed spectrally over a large range, it is possible to probe the cavity resonances from inside the cavity in a very easy way [33]. However, this method is limited to cavities whose intrinsic losses exceed the reabsorption of photons by QDs. For cavities with higher quality factors,  $Q$  spoiling appears and the cavity losses are dominated by the absorption of photons by QDs.

On the other hand, due to the appealing properties of InAs QDs as a quantum emitter and the well-understood nanofabrication processes of GaAs systems, many major solid state CQED experiments have been performed on these devices.



(a) Exaltation of the spontaneous decay rate of QDs at the center of a micropillar cavity compared to QDs off-resonance and in bulk material [36].

(b) Inhibition of the spontaneous emission of a QD integrated in a thin nanowire compared to a QD in bulk material [11].

**Figure 1.17** Modification of spontaneous emission rates of QDs in semiconductor structures.

In 1998, Gérard et al. observed Purcell enhancement for a collection of QDs in a micropillar [36]. Inhibition [26] and enhancement [102] have also been achieved for single QDs. Strong coupling of QDs to a cavity has been observed by Yoshie et al. on photonic crystals [127], by Reithmeier et al. on micropillars [89] and by Peter et al. on microdisks [84]. The inhibition of spontaneous emission has also been observed on QDs integrated in a photonic crystal [65, 74] and in nanowires [11]. Some experimental data are shown on Figure 1.17.

Showing very promising properties for serving as quantum emitters, QDs have also several drawbacks. The first problem results from the growth. QDs are randomly distributed over the sample and have size fluctuations which result in a large distribution of emission wavelengths, ranging over several tens of nanometers. It is possible to grow deterministically distributed QDs on the sample surface, but this requires a more complicated fabrication and degrades the QD properties [15].

However, it is also possible to deterministically fabricate cavities around single QDs [23]. Since CQED effects depend on the location and detuning of QDs with respect to cavity modes, this is an important step in view of practical implementation of CQED-based devices.

## 1.2.2 Cavities as backbone of light emitters

Many devices that are not yet commercially available are inspired by CQED. For example, the fabrication of microlasers with ultralow threshold and single photon sources was considered as a huge challenge 20 years ago. Great progress has been made during the last decades and the fabrication of these devices is now within reach.

In this subsection, I will describe their operating principle, the requirements and the work that has been done until now. I start with single photon sources, which are novel devices able to emit on-demand light pulses containing one and only one photon. As shown below, such sources rely on the spontaneous emission of a QD. To generate single photons in a well-defined mode, spontaneous emission control by photonic microcavities is mandatory. In the same spirit, single-mode spontaneous emission is extremely useful to realize ultralow threshold lasers, which are described in the second part.

### 1.2.2.1 Single photon sources

An ideal single photon source (SPS) should be able to emit a light pulse, which contains only one single photon in a well-defined optical mode after a precise trigger signal. Furthermore, it should have a high repetition rate and emit indistinguishable photons. For an actual implementation and easy handling, it should preferably be a solid state device that works at room temperature.

Two important figures of merit characterize the quality of single photon sources:

- The purity of the source: the emitted light pulses should contain one and only one photon. This corresponds to an ideal source. Deviations are measured by the second order intensity correlation function  $g^{(2)}(0)$  which describes the probability that several photons arrive at the same time. For an ideal source,  $g^{(2)}(0) = 0$ .
- The extraction efficiency  $\epsilon$  of the source: it describes the average number of photons per excitation emitted into a mode. In the case of an ideal source,  $\epsilon = 1$ .

As mentioned before, SPS have many potential applications: They could be used in quantum cryptography for securing communication [38, 116] as well as in quantum computing [57] and quantum metrology [101].

Besides the figures of merit named before, both quantum cryptography and computing also require a high indistinguishability of the photons.

Up to now, two standard approaches exist for creating single photons.

One approach is spontaneous parametric down-conversion [81]. This method provides reliable pairs of single photons and is already used in commercial single-photon applications at room temperature. The drawback of this method is a very low  $\epsilon \approx 0.05$ .

Besides efforts on SPS based on a single artificial atom like color centers in diamond or single molecules, approaches based on single QDs are investigated. Single InAs QDs have an excellent purity with a  $g^{(2)}(0) < 0.01$ . A drawback for QDs is the absence of directivity of the emission (solid angle  $4\pi$ ) and the complicated extraction of the emitted light from the surrounding material. Due to its high refractive index, most of the light stays confined in GaAs. Only 2% of light emitted by a QD embedded in GaAs, below a planar air-GaAs interface, can escape. An ideal single photon source should emit photons into a single mode which would then be collected with, e.g. a single-mode optical fiber.

The aim is thus to create monomodal emission. For achieving this, two different CQED-based strategies can be used.

Let us first consider an emitter coupled to a single cavity mode. Its ratio of spontaneous emission into a mode  $m$  to the full emission  $\beta$  is given by

$$\beta = \frac{\Gamma_m}{\Gamma_m + \gamma\Gamma_0} \quad (1.20)$$

where  $\Gamma_m$  is the spontaneous emission rate into the mode  $m$ ,  $\Gamma_0$  the spontaneous emission rate of the emitter into infinite bulk material and  $\gamma\Gamma_0$  the spontaneous emission rate into leaky modes, i.e., modes which are not confined in the cavity. In a microdisk or a micropillar for instance,  $\gamma \approx 1$ . In the weak coupling regime, we can now write  $\Gamma_m = F_m\Gamma_0$ . If the emitter is ideally positioned spectrally and spatially in a 0D cavity,  $F_m = F_p$ . Equation 1.20 becomes:

$$\beta = \frac{F_m}{F_m + \gamma} \quad (1.21)$$

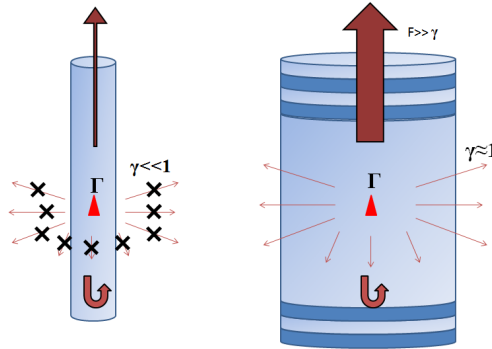


**Figure 1.18** Two possible approaches for funneling spontaneous emission into a cavity mode: inhibition of leaky modes (left side) and enhancement of emission into the cavity mode (right side).

For a single photon source,  $\beta$  must be close to unity. Otherwise, a large part of the created photons are emitted into leaky modes.

This aim can be realized by two ways:

- $F_m \gg 1$ : Enhancement of spontaneous emission into mode  $m$ , realized by putting the emitter into a cavity with a high Purcell factor.
- $\gamma \ll 1$ : Suppression of spontaneous emission into leaky modes, realized by inserting the emitter in, e.g., a photonic wire [19] or a photonic crystal [123].

These two approaches (also shown on Figure 1.18) based on III-V solid state devices with InAs QDs as emitters are currently investigated.

**Single photon sources based on spontaneous emission enhancement** The first approach is based on a high- $Q$  micropillar system and enhancement of the emission of photons into a single cavity mode by the Purcell effect [69, 83]. To maximize the Purcell enhancement, micropillars with ultrahigh  $Q$ -factors could be precisely positioned around a single QD and optimized for a precise resonance frequency corresponding to the QD emission line [23] (see Figure 1.19(a)). A higher number of Bragg pairs at the bottom ensures the unidirectional emission of photons towards the top direction.

To reduce charge fluctuations around the QD which decrease the indistinguishability of the emitted photons, a circular post is fabricated around the micropillar and an electric field is applied.

With this approach,  $\epsilon = 0.65$  and  $g^{(2)}(0) = 0.003$  have been achieved by two independent research groups [22, 103]. An indistinguishability of 0.996 has also been reported [103].

In another experiment based on micropillars, an ultrabright source of entangled photon pairs was demonstrated [24].

Despite these appealing performances, micropillar-based SPSs suffer several disadvantages: the fabrication process is complicated for creating a large number of emitting devices and micropillars only have a small spectral bandwidth because of the sharp cavity resonances.

**Single photon sources based on spontaneous emission inhibition** This bandwidth problem is solved by the second possible approach, the photonic nanowire. It is based on a semiconductor nanowire with a very small radius close to the QDs, with a tapered radius. A layer of QDs is inserted at the vertical position where the wire is the thinnest (see Figure 1.19(b) and (c)). The low diameter at the QD position induces an inhibition of the spontaneous emission into other modes. Photons are thus preferentially emitted into the guided modes. A reflector made of gold and silica positioned at the bottom of the wire ensures unidirectional emission of photons. In the case of the photonic trumpet [71], a  $\text{Si}_3\text{N}_4$  antireflection coating is deposited on the top of the wire in order to ensure an efficient outcoupling of the photons out of the wire. The conical taper expands the guided mode adiabatically and ensures excellent coupling to a Gaussian beam [71]. Coupling of this photon source

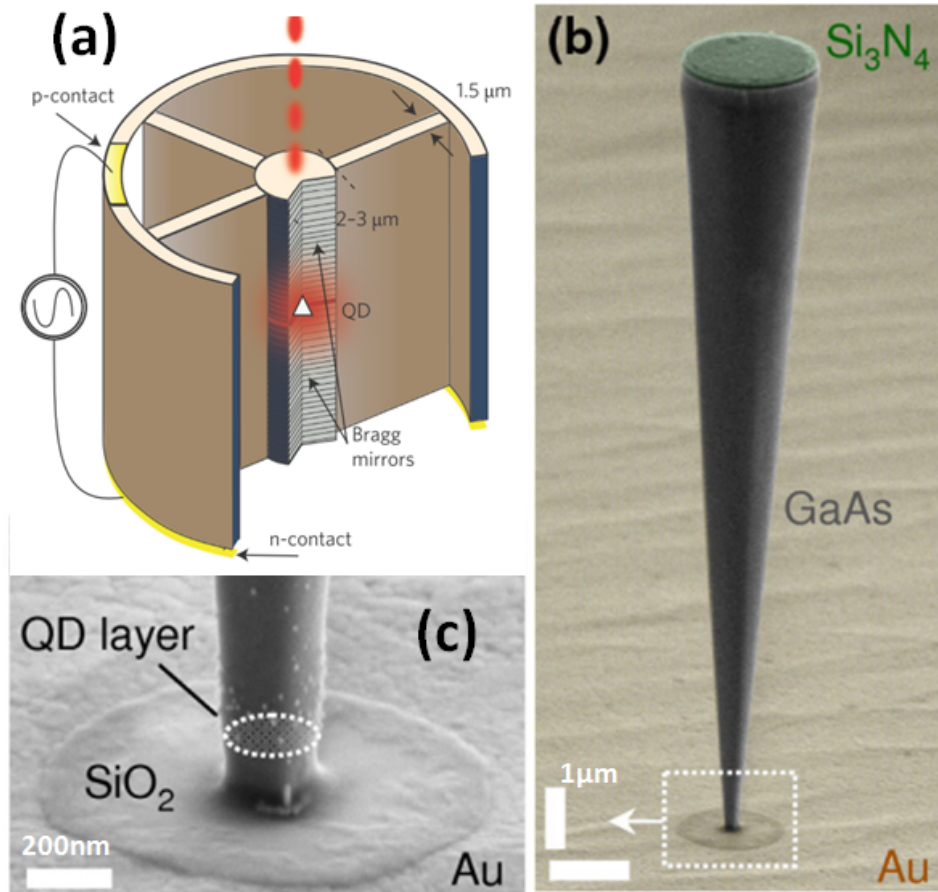


**Figure 1.19** (a) Sketch of a QD-micropillar SPS: A QD is positioned at the center of a micropillar in order to benefit from a high Purcell enhancement. The construction around the micropillar is used for eliminating charge fluctuation and increase the indistinguishability of the emitted photons (taken from [103]). (b) SEM image of a photonic trumpet. The inset (c) shows the exact position of the QDs and the bottom mirrors [71].

to an optical fiber has already been demonstrated [16]. It is also possible to use needle-like photonic wires to observe similar behaviour [19] but at the expense of worse coupling to fibers.

With this approach,  $\epsilon = 75\%$  and  $g^2(0) = 0.02$  have been observed [19, 71]. In contrast to micropillars, photonic nanowires can be used for broadband single photon emission. They are also not as sensitive to QD positioning as micropillars which facilitates the fabrication process.

The drawback of photonic nanowires is that no emission of indistinguishable photons has yet been observed, albeit theoretical proposals based on the integration of a low  $Q$  cavity in a photonic wire have recently been published [44]. Photonic wires emitting indistinguishable photons would still operate over a relatively large bandwidth ( $\approx 20$  nm).

Nevertheless, great progress has been made on single photon sources (also with photonic microstructures such as photonic crystals) and it only seems to be a question of time as to when single photon sources become a commercial product.

### 1.2.2.2 Microlasers with ultralow thresholds

Lasers have experienced a drastic reduction of size since their inception: from several centimeters around 1960 down to sub-micrometer sizes nowadays. It is indeed now possible to miniaturize laser cavities down to the diffraction limit. Examples for microlasers are vertical cavity surface emitting lasers (VCSELs) (of geometry very similar to micropillars) [41], microdisks [68], microspheres [94] and two-dimensional photonic crystals [58].

The small size strongly reduces the gain length of the resonators. This has to be compensated by many roundtrips in the cavity and thus requires high  $Q$  modes. The gain medium for microlasers consists usually of one or several quantum wells (QW).

By confining photons in a small space, CQED effects become increasingly important and could be potentially exploited if the emitters linewidth is sufficiently small. This could be realized by using QDs instead of QWs as emitter.

QDs provide a better confinement, a higher quantum efficiency and a narrower gain profile (in the case of uniform QD size and low temperature).

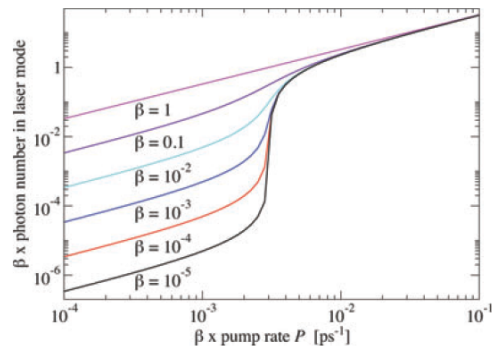
In reality, QDs are randomly positioned and have randomly distributed sizes. This results in lower modal gain than for QWs. Furthermore, even isolated QDs broaden at elevated temperatures and lose their atom-like emitting behaviour. This is why QD-microlasers (such as QD-VCSELs) do not outperform QW-based microlasers yet.

However, looking just at one single QD placed in a cavity, interesting experiments can be performed.

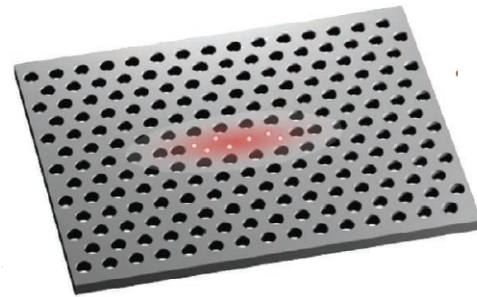
The threshold of a laser is defined as the input current (or optical pump power) for which the average photon number in the lasing mode of a cavity is equal to one. From this limit on, stimulated emission becomes predominant.

The widely used semiconductor laser diodes generally emit large amounts of spontaneous emission in leaky modes before entering into the lasing regime. This is a drawback for their efficiency and performance. It is thus strongly desirable to

fabricate laser diodes whose spontaneous emission is efficiently funneled into the laser mode [73].



(a) Plot of photon numbers emitted into a laser mode against the pump rate (attention, both axis are normalized to  $\beta$ ). For  $\beta = 1$ , no threshold behaviour can be observed. With decreasing  $\beta$ , the threshold behaviour becomes more significant and is shifted towards higher values (taken from [107]).



(b) A possible experimental realization of low-threshold microlaser: Single emitters are embedded into a low volume cavity (in this case a photonic crystal cavity). By placing the emitters at field maxima, their coupling to the lasing modes becomes maximal (taken from [73]).

**Figure 1.20** Threshold behaviour and realization of such a microlaser.

The ultimate achievement for a laser would be thresholdless lasing, obtained in the  $\beta \rightarrow 1$  limit.

Figure 1.20(a) shows input-output power curves (normalized with  $\beta$ ) for different  $\beta$ -values. Lower values result in significantly higher thresholds and a more striking threshold behaviour. The intensity jump at the threshold usually scales with  $1/\beta$ ; it is thus important to increase  $\beta$  towards unity.  $\beta = 1$  results in a curve which shows no more a threshold behaviour. By using CQED effects, it is possible to create lasers whose  $\beta$  is very close to unity.

As mentioned before, the source of this threshold behaviour is spontaneous emission into non-lasing modes. In analogy to single photon sources, CQED provides three possibilities to prevent this:

- Inhibition of emission into the non-resonant leaky modes
- Exaltation of emission into resonant modes
- Combination of 1) and 2)

With the second strategy, a record threshold of 287 nW was achieved at 150 K with electrically pumped InAs QDs in a GaAs-photonic crystal cavity [25]. A sketch of such a laser is shown on Figure 1.20(b). With a monolayer semiconductor as emitter,

this value was lowered to 27 nW [119]. These are remarkable values, because the lasing threshold for VCSEL lasers is of the order of 10  $\mu$ A. Edge-emitting diode lasers have thresholds of several mA.

More information and a review over microlasers is given by [50].

To sum this up, the research field of microlasers has seen significant advances concerning key parameters as size and threshold. In the future, the energetic consumption of small lasers could be decreased and applications on fields like biomedicine become imaginable [50].

## 1.3 Ultrafast cavity switching

Large parts of this PhD thesis are dedicated to cavity switching experiments. Cavity switching is a promising research area for improving performances of different devices and to go beyond existing limits of CQED.

“Cavity switching” refers to a transient and reversible modification of properties of a cavity. Usually, the resonance frequency is changed. But other properties could also be modified, such as the loss behaviour of the cavity. Different pulsed lasers are based on this “Q-Switching” [93].

An ultrafast cavity switch describes a modification of at least one cavity parameter on a time scale which lies at the same order of magnitude as the time constants which are characteristic of a cavity. Examples are the storage time and the period of a Rabi oscillation (in the case of strong coupling) or the emitter lifetime (in the case of the Purcell regime), when the cavity contains emitters.

This section is dedicated to a description of cavity switching by all-optical means, as well as related potential applications.

### 1.3.1 Methods of ultrafast all-optical cavity switching

Let us first consider a planar cavity with length  $L_{cav}$ . The resonance condition can thus be written as

$$k_m L_{cav} = m\pi; \quad m \in \mathbb{N} \quad (1.22)$$

$k_m$  is the set of wavevectors fulfilling the condition of Equation 1.22 ( $k_m = 2\pi n/\lambda_m$ ; where  $\lambda_m$  designs the wavelength in vacuum).  $m$  is an integer number that represents the order of the resonance.

This leads to

$$\lambda_m = \frac{2nL_{cav}}{m} \quad (1.23)$$

Switching a cavity means switching its resonance wavelength by an external perturbation (see Figure 1.21(a)). As can be read from the equation above, one possibility that can easily be achieved for macroscopic cavities is changing the length of the cavity (for example, in the case of a simple Fabry-Perot cavity: changing the distance between the mirrors).

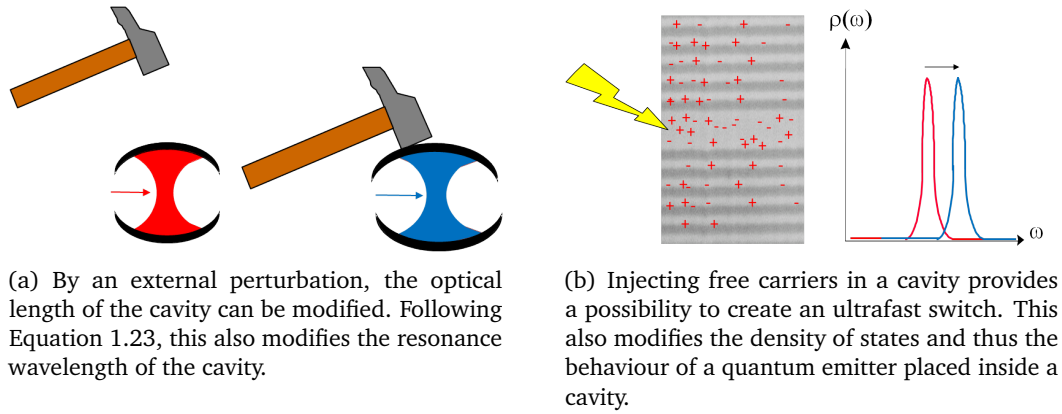


**Figure 1.21** Principle, result and possible experimental realization of cavity switching.

However, this is impossible for a monolithic solid-state cavity whose length is imposed by its design and cannot be modified significantly after fabrication.

That is why the only remaining parameter that can be tuned to switch the resonance frequency of the cavity is to change its refractive index. The modification of the resonance wavelength is given by

$$d\lambda_m = \frac{dn}{n} \lambda_m \quad (1.24)$$

Two main approaches exist for changing the refractive index of a semiconductor material in an ultrafast and reversible way.

### 1.3.1.1 Switching by free carrier injection

The presence of free carriers decreases the refractive index of a semiconductor material. The Drude model for free carrier dispersion [80] states that the amplitude of the modification is given by:

$$\Delta n = -\frac{e^2}{2n_0\epsilon_0\omega_{pump}^2} \left( \frac{\Delta N_e}{m_e^*} + \frac{\Delta N_h}{m_h^*} \right) \quad (1.25)$$

where  $e$  is the elementary charge,  $n_0$  the unperturbed refractive index of the material,  $\epsilon_0$  the vacuum permittivity,  $\omega_{pump}$  the frequency of the exciting laser,  $\Delta N_e$  ( $\Delta N_h$ ) the density of electrons/holes injected into the material and  $m_e^*$  ( $m_h^*$ ) their effective mass.

From that, we deduce that the refractive index difference  $\Delta n \propto -N_{eh}$  ( $N_{eh}$ : number of electron-hole-pairs).

Free carriers can be injected electrically [120] and optically [60].

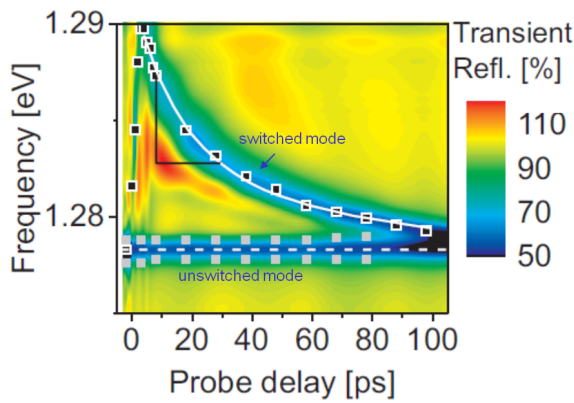
Switching by electrical injection of free carriers in a micrometer-sized cavity [120] is relatively slow and takes several nanoseconds. The reason for this is the relatively slow transfer of electrons based on charge effects which are on the time scale of a few nanoseconds.

On the contrary, switching by optical injection of free carriers, which was first reported in 1989 by Jewell [52], is faster. Switching times of few picoseconds are attainable, and much shorter than those obtained under electrical injection.

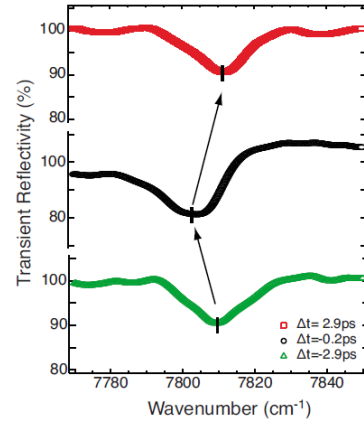
The high speed of all-optical switching is a result of the short duration of laser pulses which is of the order of picoseconds or even hundreds of femtoseconds and the fast response of the semiconductor material. When a laser pulse with photons above the energy bandgap hits a semiconductor, the photons of the pulse are absorbed and generate free carriers in the material, as sketched in Figure 1.21(b). These carriers relax within a few picoseconds towards the extrema of the conduction and valence band.

Through injection of free carriers, the refractive index of a semiconductor material changes and, following Equation 1.24, the mode frequency of the cavity is blueshifted.

On a larger timescale, free carriers will recombine non-radiatively or radiatively and the mode will return to its initial frequency. The recombination speed defines the duration of a complete switching cycle (on-off-on) and depends on the nature



(a) Switching of a cavity via injection of free carriers. The change of reflectivity indicates a change of the cavity mode position [45].



(b) Switching due to the Kerr effect. An ultrafast shift of the of the cavity frequency is observed [21].

**Figure 1.22** Cavity switching of planar GaAs/AlAs cavities.

of the semiconductor material. The quality of the material and the geometry of the structure also play an important role. For bulk GaAs, the recombination time can vary from less than 1 ps for low-temperature grown layers [106] up to a few nanoseconds for high quality material. In microcavities, surface recombination on sidewalls can become a dominant process. The spectral return is controlled by the propagation of the free carriers in the material and the recombination dynamics.

Figure 1.22(a) shows the frequency of a mode as a function of time and the typical behaviour of a switch induced by free carriers. Here, the switching behaviour is studied using a pump-probe approach. After a blueshift of 120 meV (corresponds to 15 linewidths of the cavity mode) which takes a few picoseconds, the cavity mode returns to its initial position following an exponential law. Figure 1.22(a) shows a fast decay with a characteristic time of approximately 50 ps. These results show that ultrafast switching of the cavity modes is possible on a very short timescale.

### 1.3.1.2 Kerr switching

Kerr switching is based on non-linear optics and a refractive index shift which appears in transparent material submitted to an intense optical beam. The electronic Kerr effect is a third order non-linear process whose magnitude depends linearly on the intensity of the pump pulse:  $\Delta n \propto n_2 I$  ( $I$ : intensity of the pump beam,  $n_2$ : Kerr coefficient, specific for every material). Only materials with a significant  $n_2$  can be used for Kerr switching. Semiconductors provide  $n_2$  values of the order of

$10^{-10}$  to  $10^{-2}$  [93]. In order to observe Kerr switching and avoid the dominant contribution of free carrier switching, the wavelength of the pump pulse has to be increased to  $\lambda_{\text{pulse}} > 2\lambda_g$  ( $\lambda_g$ : bandgap wavelength of the switched material) to avoid two-photon-absorption.

The great advantage of Kerr switching is its virtually instantaneous appearance and disappearance. As can be seen on Figure 1.22(b), an off-on-off cycle takes only 5.9 ps [21]. E. Yüce et al. were even able to push the duration of one cycle beyond one picosecond [128]. This means that terahertz switching rates are possible — this is more than 100 times faster than state-of-the-art switching speeds in electronic chips.

### 1.3.2 Applications of ultrafast switching

**Free-carrier switching** Ultrafast switching has different potential applications. First, switching was studied for telecommunication and optical computing [52, 60]. The advantage compared to electronic switching is the higher speed. However, the high power consumption of all-optical switching prevented a widespread use of all-optical switches in telecom systems or in computers.

Nevertheless, free-carriers can be used in photonic devices. Q. Xu et al. injected free carriers via a *p-i-n* junction into silicon and demonstrated electro-optic modulation in silicon [120]. This is of major importance for controlling and reconfiguring photonic circuits. However, the reported switching times are of the order of nanoseconds, i.e. much longer than for optical switching.

Because of the fast speed of the free-carrier injection, this technique became appealing for color change experiments where the wavelength of light stored in a cavity is converted by switching the cavity resonance. This was realized by Preble on silicon microrings [85] and Tanabe on photonic crystals [110]. In the frame of this PhD thesis, color-change by the injection of free carriers was demonstrated on planar cavities (see chapter 3).

From a fundamental research point of view, free carrier switching could be used to dynamically control the emitter mode detuning. Considering a cavity containing a QD, it would be possible to switch the cavity mode, and thus the Purcell effect, on a time scale much shorter than the QD exciton lifetime. An ultrafast modulation of spontaneous emission would thus be possible [111]. Recently, dynamic control of the spontaneous emission of QDs has been experimentally demonstrated for a

collection of QDs in this work (see chapter 4), as well as for a single QD by Fiore et al. [54]

The control of spontaneous emission of a single emitter could also be used for pulse shaping [55]. By carefully tuning the resonance of a cavity mode in time, the exponential-time envelope of a spontaneously emitted photon could be turned into a Gaussian or even an inverted exponential shape [82]. This prospect is particularly appealing in the context of photonic quantum engineering.

**Kerr switching** Due to its fast modulation speed, Kerr switching seems to be the ultimate solution for high speed switching. However, Kerr switching has a big drawback: Very high intensities are required even for small switching amplitudes. Figure 1.22(b) shows a switching amplitude below the linewidth of the cavity for a switching energy of  $20 \text{ pJ}/\mu\text{m}^2$  per pulse, which is 20000 times larger than for a CMOS operation and still 20 times higher than for free carrier optical switching.

Another possible application would be time-modulated CQED experiments with strongly-coupled emitter cavity systems [56, 21]. Because of its fast speed, it would be possible to change the light-matter interaction on a timescale smaller than a Rabi oscillation period, which is of the order of a few picoseconds [84].

## 1.4 Conclusion

In this chapter, I introduced the concept of optical cavities and described the most important figures of merit of a cavity. I presented different optical microcavities fabricated of semiconductor III-V-material. I also gave an overview over their state-of-the-art figures of merit  $Q$  and  $V_{\text{eff}}$ .

In the following, three types of cavities are used for experiments: planar cavities, micropillars and ring cavities based on a semiconductor waveguide. For reasons of clarity, I give a detailed overview over modes and other specific properties in the corresponding chapters.

Microcavities are an essential part of CQED experiments with solid state systems. An introduction of the concept of CQED has been given to the reader as well and different cavity-emitter regimes have been explained. I furthermore presented QDs as solid state quantum emitters which can be easily integrated in solid state devices. I gave a brief overview over CQED experiments performed with solid state cavities with QDs as integrated emitters.

Two applications seem particularly appealing for further use of QDs in the future: Single photon sources and microlasers. Operating principle and current performance of these devices were explained as well as potential drawbacks and future research directions.

All-optical cavity switching was discussed. This method enables an ultrafast spectral shift of the cavity resonances, either by the injection of free carriers, or by exploiting the electronic Kerr effect. Free carrier switching is an important effect on which rely many experiments of this PhD thesis.

In the following chapter, I will explain how to grow high-quality semiconductor cavities and how to structure these to build three-dimensional cavities. An overview over the experimental setups which have been used in this work is given as well.



# Experimental methods for sample fabrication and characterization

After having introduced the physical concepts which are compulsory for understanding the experiments of this PhD thesis, the fabrication processes of samples and their characterization are now described.

Different fabrication steps are required to create microcavities. First, the semiconductor structures are grown by molecular beam epitaxy which already defines the vertical composition of the samples.

For creating cavities which confine light in three dimensions, clean room processing is required. I present the fabrication steps including lithography and etching which define the final structure and properties of micropillars and oval ring resonators.

In the second part, I present principles of photoluminescence measurements of solid state devices at low temperature. The corresponding experimental setup is also described. Finally, the operation principle of the streak camera, which enables us to measure photoluminescence with a picosecond-resolution, is explained.

## 2.1 Fabrication of the different samples

Modern fabrication technologies allow precise control of size and position of nanoobjects. Fabrication is a crucial step for the functionalities of microcavities. Indeed, the quality of the fabrication process determines important figures of merit. The emission properties of the QDs depend on the growth. The quality factor of cavities and their modal structure depend on the cleanroom fabrication processes.

In this section, I present the basics of semiconductor growth by molecular beam epitaxy and different growth regimes. I describe how cavities are fabricated from the planar samples yielded after the growth.

## 2.1.1 Molecular beam epitaxy

A method which provides a precise way to produce semiconductor structures with a low defect concentration is molecular beam epitaxy (MBE). The principle of molecular beam epitaxy consists of depositing one layer of semiconductor material after the other. Thereby, the thickness of each layer can be controlled up to a single molecular layer.

Epitaxy always starts with a semiconductor substrate with a defined crystalline order. The substrate transfers the crystalline order to the thin layer which is grown by letting a flux of atoms and molecules interact with the substrate surface.

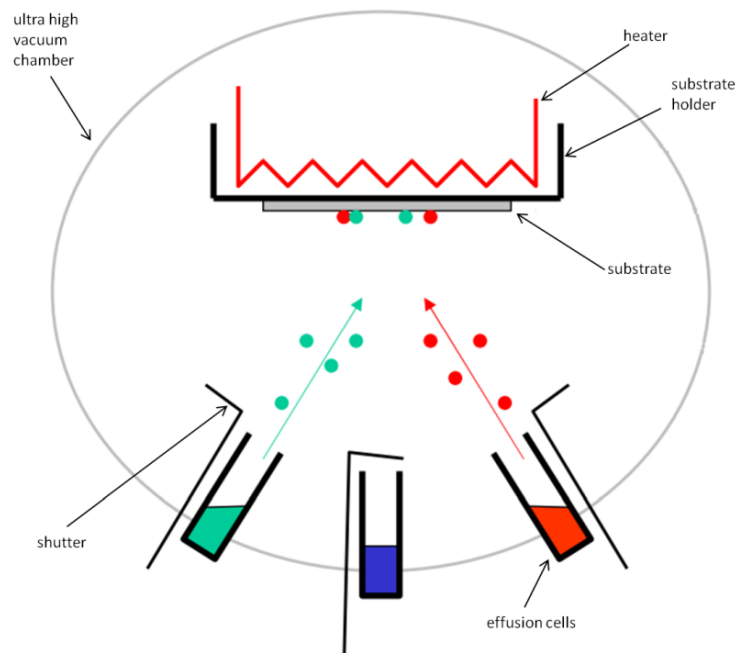


**Figure 2.1** Setup for epitaxial growth via MBE.

Figure 2.1 shows a schematic plan of a MBE chamber. Epitaxy has to be performed under ultra-high-vacuum conditions to avoid contamination by impurities. The incorporation of other elements causes undesired doping of the material. This affects the optical and electrical properties of the material. For this reason, the residual background pressure is  $10^{-9}$  mbar. The pressure is maintained by a combination of turbo-molecular pump and a titanium sublimator which work complementary. The growth chamber is also cooled down with liquid nitrogen to avoid evaporation of materials from its inner surfaces.

The substrate is placed on heatable substrate holder. Two mechanisms exist to fix the substrate to the holder and to provide a precise temperature control: The first

mechanism is based on glueing the substrate with indium onto the holder. This provides a very precise temperature control, but the indium on the backside of the sample can react chemically with the substrates. This is the case for GaAs wafers which results in a high degree of roughness of their back surface and degrades the mechanical and optical properties. This is a drawback for experiments based on transmission which require flat and transparent sample back surfaces.

The other method is clipping the sample into a frame and putting the sample directly in contact with the temperature control, which provides a less precise temperature control. Though, it is more important to keep the wafer free from indium contaminations and for this reason, the latter method was used.

The substrate holder is rotated by a motor around the wafer axis to ensure a homogeneous growth of the material despite the non-homogeneous flux of the atoms.

The growth is performed under As-rich conditions. Arsenic is provided by a high capacity cell in form of  $As_4$  molecules. For growing a III-V material, the stoichiometric condition has to be fulfilled. In practice, the growth speed is controlled by the flux of the metals (Ga, Al, In).  $As_4$  is provided in excess from the high capacity cell and, furthermore, extra arsenic is desorbed from the surface.

The flux results of heatable crucibles which provide a precise control of the temperature of the used material. The crucibles are filled with one single, ultrapure element. Each crucible can be opened separately with a precision of 0.1 s. The composition of the material and the growth rate can be regulated by its temperature: the more a crucible is heated up, the higher the flux will be. Monitoring of growth rate and time provides a precise control of the thickness of the deposited layers.

Only arsenide-structures were produced with the MBE machine used during this thesis. AlAs, GaAs, InAs and ternary combinations of AlGaAs were grown on (100)-oriented GaAs wafers. These materials exhibit a zinc-blende crystalline structure when grown epitaxially on GaAs.

#### **2.1.1.1 Regimes of epitaxial growth of III-As-materials**

Generally speaking, three different growth modes can be distinguished. These different regimes are depicted schematically on Figure 2.2 [49].

**Frank-van der Merwe growth** This growth is predominant if the lattice constants are nearly equal. This is the case for growth of the same material, but it is also possible for different materials. An example for this are GaAs (0.565325 nm) and AlAs (0.56605 nm). In this case, the layers are grown layer by layer onto each other. This enables the easy growth of Bragg reflectors for planar cavities.

**Stranski-Krastanov growth** Stranski-Krastanov (SK) growth appears for a big lattice mismatch between two different grown materials and a high interaction strength between ad-atom and the growth surface. The lattice mismatched material proceeds layer by layer at the beginning. At a critical thickness of this layer, self-assembled islands begin to form. At this point, the energy to form self-assembled islands is lower than that of a strained, planar wetting layer.

This results in small islands of a thickness of few atomic layers on top of a wetting layer of the same material. The bottom-up fabricated QDs are fabricated by this approach, which can be implemented for both MBE and CVD growth techniques.

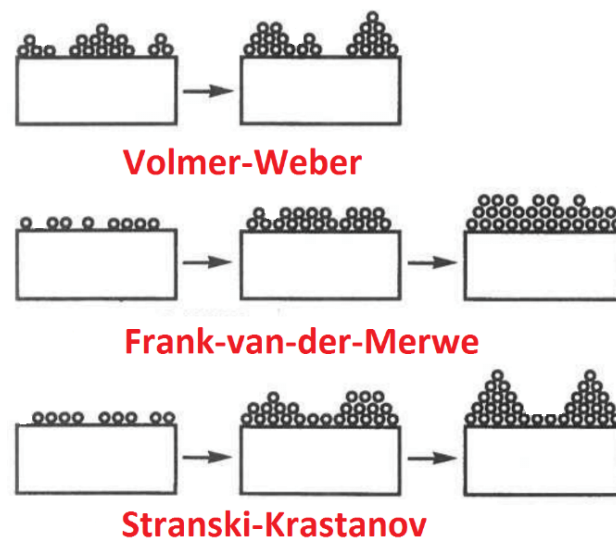


**Figure 2.2** Different growth regimes depending on the lattice constants and the interaction strength of ad-atom and growth surface.

**Volmer-Weber growth** Volmer-Weber growth appears for big lattice mismatches and low interaction strengths between ad-atom and the growth surface. Self-assembled islands are formed immediately without the presence of a wetting layer.

**Growth conditions used in this PhD thesis** The growth regime of the materials used in this PhD thesis depends thus on the lattice mismatch of the different used materials. GaAs (0.565325 nm), AlAs (0.56605 nm) and their ternary alloy  $\text{Al}_x\text{Ga}_{1-x}\text{As}$  (lattice constant between that of GaAs and AlAs linearly depending on  $x$ ). For these materials, the mismatch is at most 0.2 % and Frank-van der Merwe growth takes place.

To grow QDs, the lattice mismatch of InAs (0.60583 nm) to AlAs/GaAs systems of 7 % is exploited. The resulting growth scheme is the SK growth. Thus, a wetting layer is formed with randomly distributed self-assembled InAs islands on its top [18]. This layer is then capped by GaAs.

### 2.1.1.2 Experimental growth conditions

The growth takes place in a vacuum chamber. The processes are observed by an in-situ method called Reflection High Energy Electron Diffraction (RHEED). More information on RHEED can be found in [49]. During growth, the sample is rotated at a constant angular velocity in order to improve the thickness uniformity.

“Epi-ready”, commercially available GaAs-wafers do not need further chemical treatments before starting the growth. For substrate temperatures  $T_{\text{subst}}$  higher than 400 °C, arsenic starts to evaporate from the structure. Therefore, it is important to work under arsenic atmosphere at these temperatures. The arsenic flux from the cell compensates the evaporated As from the wafer and replaces As atoms immediately.

A desoxidation before the growth, which is performed in the chamber at a temperature of  $T_{\text{ox}} \approx 590$  °C is the only required step before starting the growth. At  $T_{\text{ox}}$ , the native oxide desorbs. This can also be used to calibrate the substrate temperature.

To guarantee a complete desorption of native oxide residuals, the wafer is heated up to  $T_{\text{ox}} + 20$  °C during 15 min.

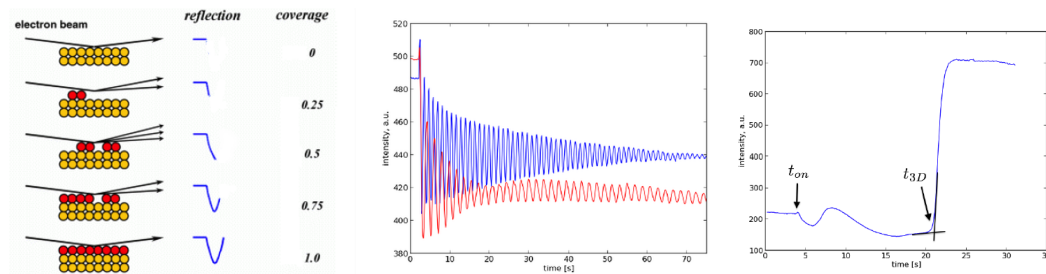
**Growth of planar structures** The growth temperature is kept at  $T_{\text{ox}} + 10$  °C. It is also possible to grow at lower temperatures. However, low temperature growth leads to an increased formation of punctual defects such as vacancies and antisite defects which degrade electrical and optical properties.

The desorption of group-III-materials from the surface can be neglected at these temperatures. The growth is always done under As-rich conditions which means that the flux of arsenide exceeds the flux of gallium and aluminum. Thus, the flux of

the group-III-materials is the decisive factor for the growth speed. It is determined by the temperature of the cells.

For a high precision, it is important to precisely calibrate the flux rates of the different materials. This is done before the growth using the RHEED technique on a test sample.

At a perfectly planar surface, the electron beam is diffracted onto a phosphor screen following crystallographic rules. One of these diffraction spots is selected and its intensity is observed (see also Figure 2.3(a)). When a new molecular layer (ML) is grown, the surface becomes rougher, the RHEED intensity decreases. Maximal roughness is obtained when 50% of the ML is grown and this results in an intensity minimum. Then, the layer is completed and the RHEED increases to its maximum which indicates the completion of this new ML.



(a) Surface structure of the grown material and the corresponding intensities of the RHEED signal. This results in oscillations. (b) RHEED oscillations of two materials grown at different growth speed. Blue: GaAs, 0.9 ML/s. Red: AlAs, 0.5 ML/s. (c) RHEED pattern of the growth of QDs. The arrows correspond to the start of the deposition of InAs and to the onset of the 3D growth mode.

**Figure 2.3** Principle of RHEED and corresponding intensities for bulk material and QDs. Images taken from [82].

One period of the RHEED oscillations corresponds thus to the growth of a monolayer. By this way, it is possible to precisely calibrate the growth rates of different materials, which depend on the corresponding cell temperatures. Figure 2.3(b) shows growth rates of GaAs (0.9 monolayer/s) and AlAs (0.5 monolayer/s). This procedure enables a precise control over thickness and composition of the grown  $\text{Al}_x\text{Ga}_{1-x}\text{As}$  material.

Before the growth, a 500 nm thick buffer of GaAs has to be deposited on the wafer. This creates a perfectly planar surface onto which further layers are grown.

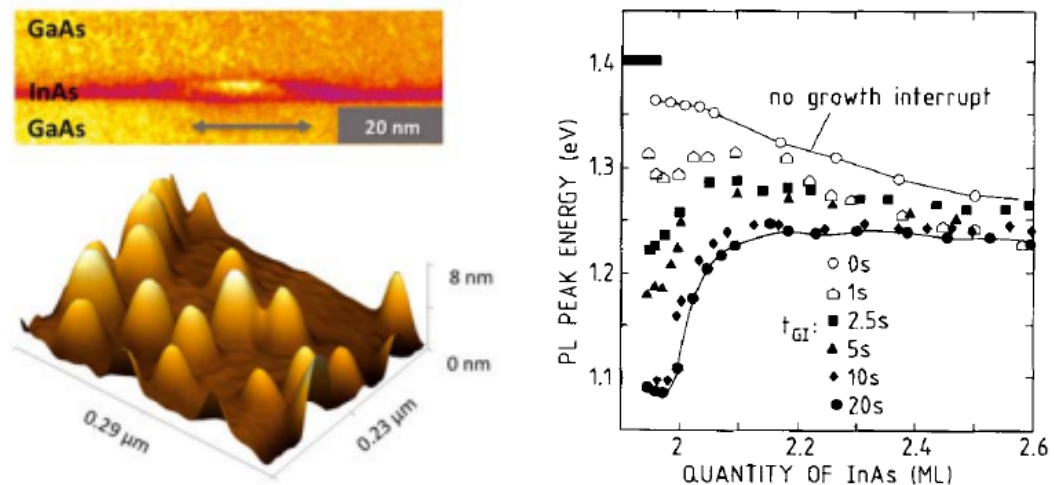
**Growth of InAs quantum dots** Self-assembled QDs as described in subsection 1.2.1 are also grown by MBE. QDs consist of small InAs islands with a typical lateral size

of 20 nm and a height of 3 nm embedded in a matrix of GaAs. TEM and AFM images of an epitaxially growth QD are shown on Figure 2.4(a).

The calibration of QD growth is done with the RHEED technique as well. Figure 2.3(c) shows a typical RHEED behaviour in the case of growth of QDs for a growth rate of 0.1 ML/s for InAs. At  $t = 4$  s, the intensity decreases. At this moment, the In cell is opened and the flux arrives on the sample. Then, one oscillation is observed followed by a long intensity minimum. At  $t = 21$  s, three dimensional islands start to appear and the intensity increases drastically. At this level, the deposited layer thickness is 1.7 ML and InAs-islands nucleate and begin to grow on the surface. At  $t = 24$  s, the intensity stays at a constant level. At this point the islands are well formed and just increase their size.

It is possible to observe these islands with atomic force microscopy (AFM). This allows studying their size and density. A typical AFM image is shown on the lower part of Figure 2.4(a).

For the creation of QDs, the islands have to be covered by GaAs in order to fabricate inclusions with a small bandgap (InAs), buried in a membrane of surrounding material of a higher bandgap (GaAs).



(a) (top) TEM image of a QD. (bottom) AFM image of self-assembled InAs islands grown on GaAs in the SK regime. Note the randomly distributed size of the islands (image taken from [100]).

(b) PL energy of QDs fabricated with different growth conditions. To achieve high emission energies, the growth should not be interrupted after the deposition of 1.8 ML of InAs (taken from [35]).

**Figure 2.4** Shape of quantum dots and overview over growth conditions.

For embedding QDs into the GaAs structure, the growth of GaAs has to be interrupted. Because of the precise knowledge of growth speed of GaAs, the vertical position of QDs in the GaAs layer can be determined with a high precision.

For growing InAs-QDs, the growth temperature has to be decreased to  $T_{\text{subst}} = 540$  °C. For higher temperatures, InAs would evaporate and no QDs are formed.

The upper part of Figure 2.4(a) shows a transmission electron microscope (TEM) image of the QDs. It confirms the formation of QDs and reveals that no defects such as dislocations are formed during the growth [40].

It is possible to tailor QD properties which depend on the growth sequence. Figure 2.4(b) shows the QD bandgap for different quantities of deposited InAs and time intervals before subsequent overgrowth by GaAs. QDs are only formed if the quantity of InAs is larger than 1.7 monolayers. At this point, SK growth becomes energetically possible. At lower quantities, a thin quantum well of InAs is grown.

Because of the higher sensitivity of our detectors at higher energies, it is desirable that QDs have a minimal size. This results in a higher bandgap of QDs and higher energies of emitted photons. As shown on Figure 2.4(b), these properties can be achieved by fulfilling two conditions: only 1.8 ML of InAs have to be deposited and the InAs islands have to be encapsulated immediately by GaAs. This prevents an extension of their lateral size.

Because of the lowered temperature of the substrate and the immediate restart of GaAs growth, the GaAs layers are grown at  $540$  °C  $< T_{\text{subst}} < 600$  °C. This results in a lower crystalline quality of the GaAs layers covering the InAs islands compared to the layers grown at  $T_{\text{subst}} = 600$  °C. Therefore, we increase the growth temperature back to 600°C as soon as the RHEED pattern confirms the recovery of a twodimensional growth mode of the GaAs layer.

## 2.1.2 Cleanroom fabrication of the samples

To observe CQED effects, it is important to integrate the emitter into cavities which confine light in three dimensions. Samples grown by MBE only provide one-dimensional confinement. Therefore, it is necessary to define a structure which traps photons in three dimensions. This is done by structuring the epitaxial layers in different steps in order to achieve the final shape of the resonators.

The rapid progress which has been made on nanofabrication during the last decades provides a precise control of the device size and position down to 5 nm. Respecting

high standards of cleanliness during processing, fabrication of high quality resonators is possible.

The fabrication sequence is identical for micropillars and oval ring resonators. The procedure is depicted on Figure 2.5.

The upper part of Figure 2.5 pictures how a hard mask is defined on the substrate. The second part of the fabrication consists of structuring the substrate by etching of the sample (lower part of Figure 2.5).

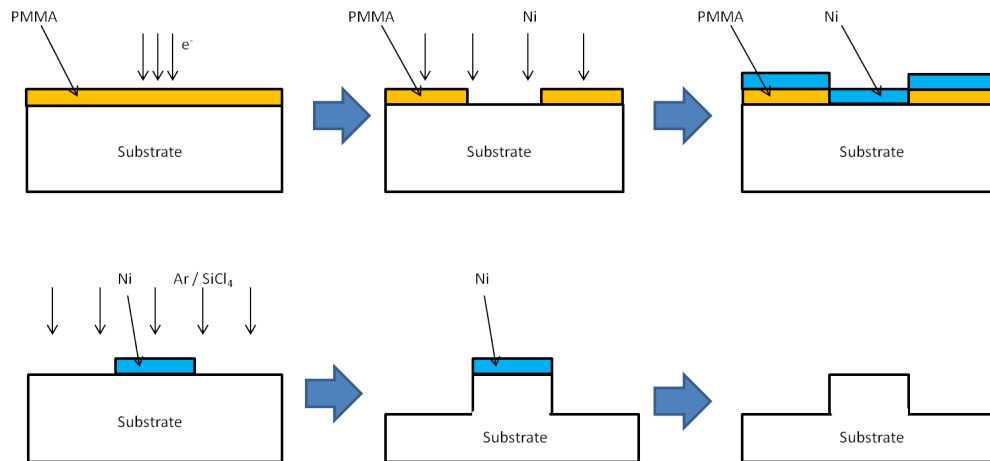


**Figure 2.5** Different steps of the microfabrication of the sample: Electron beam lithography, developing, evaporation of a Ni-mask, lift-off, reactive ion etching and removing the of Ni-etching-mask.

### 2.1.2.1 Defining a hard mask with Electron Beam Lithography

To define the microstructures on the wafer, a mask has to be deposited before the etching procedure. The shape of the mask is written by lithography onto a photoresist.

Due to the size and shape of structures (required resolution 50 nm) which is beyond the abilities of optical lithography systems available in our cleanroom (minimum resolution  $\approx 800$  nm), Electron Beam Lithography (EBL) was used to write the mask onto the photoresist.

**Cleaning and resist spin-coating** After the growth, the substrate is rinsed with acetone, isopropyl alcohol (IPA) and ethanol. It is dried after with clean  $N_2$ .

In a next step, the substrate is coated by a 250 nm thick layer of PMMA-4 %. This is done by spin-coating: a droplet of PMMA is deposited on the substrate and the

corresponding thickness is reached through the centrifugal force of the rotation. The wafer is rotated with a speed  $\omega = 4000$  rpm (acceleration: 4000 rpm/s) during 40 s. This results in a typical thickness of 300 nm.

**Electron beam lithography and development** The EBL system used for the patterning (JEOL 6300 FS) provides a resolution of 10 nm. The electron beam is focussed by electromagnetic lenses onto the sample. Because of the relatively slow variation of magnetic fields, the beam is deflected by an electric field to write individual pixels onto the photoresist.

The corresponding design patterns were defined using a commercially available software (L-EDIT by Tanner EDA). The acceleration voltage was 100 kV and the typical electron dose was  $2000 \mu\text{C}/\text{cm}^2$ . The dose depends on the size of the written pattern and the proximity to other patterns.

Exposed parts of the photoresist are removed after the lithography. This is done by dipping the exposed substrate into a MIBK-IPA solvent (1:3 volume ratio) during 30 s. The substrate is then dipped into two other beakers filled with IPA during 5 s respective 30 s for a final cleaning.

**Evaporation of the Ni-mask and lift-off** Subsequently, a Ni layer is deposited by electron-beam evaporation onto the substrate and the remaining pieces of the PMMA-photoresist. The thickness of the layer depends on the used etching process. Generally, the deeper the etch is, the thicker the Ni layer has to be. Its precise value is controlled with a calibration quartz.

In a next step, remaining parts of the e-beam resist are removed by acetone. This subsequently lifts off the Ni which was evaporated on the photoresist. The Ni-layer attached onto the substrate is not lifted by the acetone and remains. It serves as a hard mask for the reactive ion etching step.

In the case of oval ring resonators, the part of the mask at the inside of the resonator cannot be lifted off easily. For this reason, a different experimental procedure was used: the substrate is put 210 minutes in acetone, then 30 minutes on an oscillating magnet, 20 minutes warmed up to 40 °C and then 30 seconds in an ultrasound bath (without removing the substrate from the acetone bath). To clean the sample after the lift-off, it is put in a bath of clean acetone. The result of this lift-off process is shown on Figure 2.6. It is indeed possible to properly lift parts of the metal mask despite its difficult accessibility for the solvent.

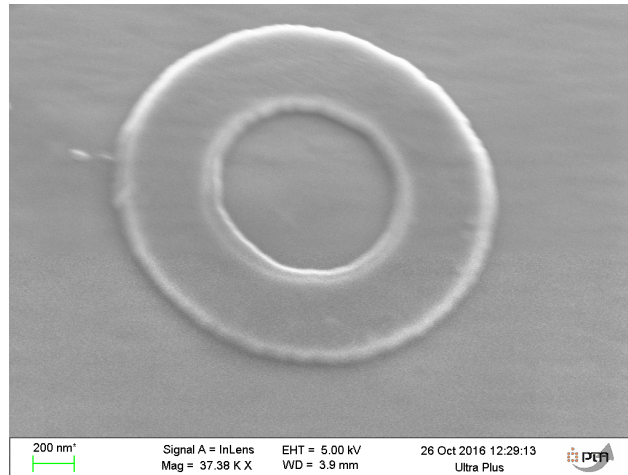


**Figure 2.6** SEM image of the Ni-mask after the lift-off. Even parts of small dimensions which are difficult to be impacted by the acetone are lifted in a clean way.

### 2.1.2.2 Defining the structure via etching

After having created a mask, the next step is to transfer the pattern by etching. It consists of etching the parts which are not protected by the mask, whereas parts covered with the mask remain untouched. Etching of the structure is a crucial part of fabrication because it defines the sidewall roughness of the structures. A high degree of sidewall roughness scatters light which is confined in the cavity and consequently degrades the quality factor of the cavity. For the targeted applications, an ideal etching process provides vertical and smooth sidewalls.

We employ dry plasma etching. Its principle consists of accelerating charged ions towards the substrate where a reaction takes place.

The ions are created by exciting a gas with microwaves oscillating at a frequency of 13.56 MHz. These waves ionize the gas and stripe off electrons of the atoms/molecules of the gas. The free electrons and positively charged ions form a plasma.

The lighter electrons are then accelerated towards the wafer or the top of the reactor. The latter is grounded, which leads to the creation of an electric field between the negatively charged substrate and the upper electrode of the reactor. This leads to the acceleration of positively charged ions towards the substrate [72]. At the substrate surface, two different etching mechanisms can take place:

**Chemical etching** Chemical etching is done by a chemical reaction between the etching ions and the etched material. The reaction products are vaporized and evacuated. Chemical etching is very selective and has the advantage of creating

smooth surfaces. However, its isotropic (not unidirectional) nature is a serious drawback.

In the case of etching GaAs and its alloys, chlorine molecules are used. They react with gallium and remove it from the crystal. Consequently, the arsenide evaporates.

**Physical etching** Physical etching occurs when the accelerated ions hit the surface of the etched materials at high speeds and sputter surface atoms. The process is not selective and, compared to chemical etching, creates rougher sidewalls. This can be reduced by adding a material to the etching gas which forms a passivation layer on the already etched sidewalls in order to protect them. In the case of GaAs and its alloys,  $\text{SiCl}_4$  is used as an etching gas. Si atoms combine with residual oxygen present in the etching chamber to form a thin  $\text{SiO}_2$ -rich layer on the sidewall, which prevents further etching in this direction.

The advantage of physical etching is the anisotropy of the process.

A combination of chemical and physical etching leads generally to a vertical profile because of sidewall passivation which protects already etched sidewalls from further etching. This combination is used in the performed processes.

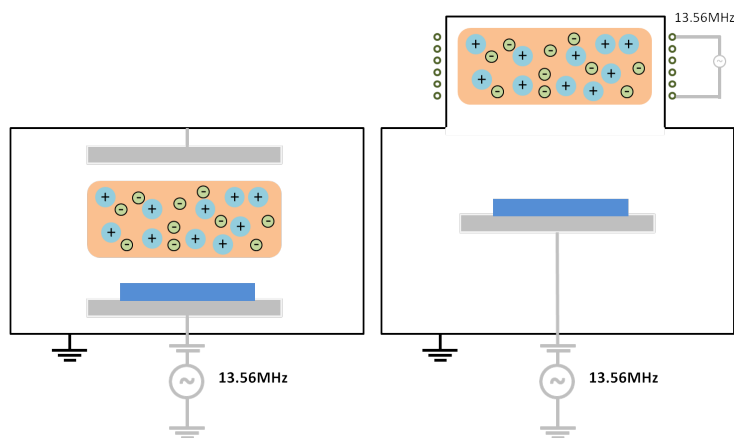


**Figure 2.7** Sketch of the reactor used for RIE and RIE-ICP. The basic difference between the two technologies is the external creation of the etching plasma in the case of ICP.

The etching reactor (Oxford PlasmaLab100) allows two different etching regimes: reactive ion etching (RIE) and inductively coupled plasma RIE (ICP-RIE) (cf. Figure 2.7).

In the case of the RIE mode, the power of the microwaves defines the density and consequently the reactivity of the plasma. The acceleration voltage of the ions is

also defined by the intensity: the higher the plasma density, the higher the tension between substrate and top-electrode will be.

ICP-RIE allows to adjust the kinetic energy of the ions and the plasma reactivity independently. This is achieved by creating the plasma in a separate chamber by applying an oscillating magnetic field. The created ions are then accelerated towards the substrate by a voltage which is created by another electromagnetic wave generator.

The advantage of RIE is the good control over the ions at low etching speeds and the well understood etching process. At higher etching speeds, physical etching becomes more and more important due to the higher acceleration tension. This leads to increased sidewall roughness.

ICP allows an independent control of plasma reactivity and the acceleration voltage. High etching speeds can be achieved with this method. The problem of this method is the more difficult adjusting of the parameters and a less robust process.

For these reasons, I used ICP-RIE for an etching deepness  $> 4 \mu\text{m}$ , as for example for micropillars. For future applications beyond this thesis, deeply etched structures are required. Therefore, an effort was dedicated to the development of an ICP etching routine.

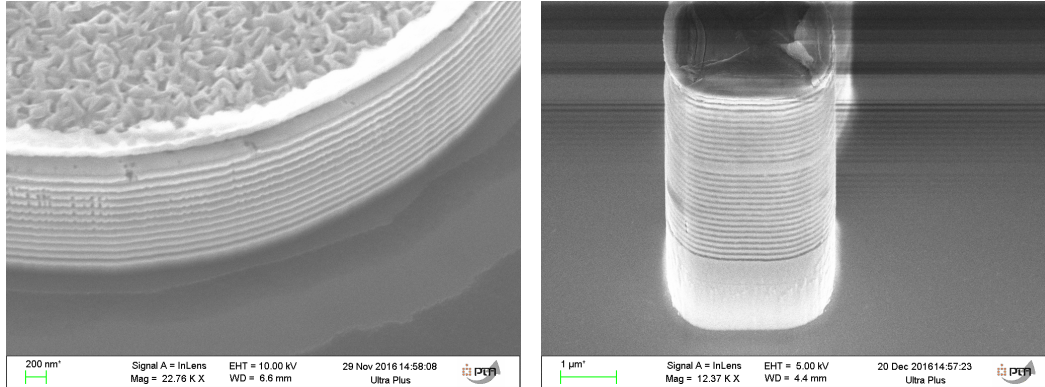
For other structures, I used the better understood RIE mode.

**Etching of micropillars** Micropillar etching was performed in the ICP mode. For future applications (see chapter 3),  $15 \mu\text{m}$  etching deepness has to be achieved and pure RIE would take several hours too long.

The sample is glued with **FOMBLIN** oil onto a  $\text{SiO}_2$  wafer in order to prevent an additional contribution of pure Si to the etching gas composition. As etching gas, a composition of  $\text{BCl}_3$ ,  $\text{SiCl}_4$  and Ar was used. This mixture is used to obtain a mix between physical and chemical etching. The chlorine atoms are reacting with Ga/Al, whereas boron and silicium serve for passivation. Figure 2.8(a) shows the importance of a passivation layer which prevents further attacking of the AlAs material of the sample.

Ar is used to vary the reactivity of the used gas. Ar ions created in the reactor only lead to physical etching. With an ICP power of 150 W and an RF power of 50 W, etching speeds of 160 nm/min were reached.

After etching, the remaining mask (see the grainy structure on Figure 2.8(a)) has to be removed because it degrades the optical properties of the microcavities. This is done by dipping the sample during one minute in 10 % diluted  $\text{HNO}_3$ . Figure 2.8(b) shows an SEM image of the result of the process.



(a) The surface of a micropillar before mask removal. Due to the absence of the passivation layer, the AlAs and GaAs layers are attacked differently which results in a rigged structure. The remaining parts of the mask are still visible on top.

(b) An etched micropillar after mask removal with a clean and passivated surface.

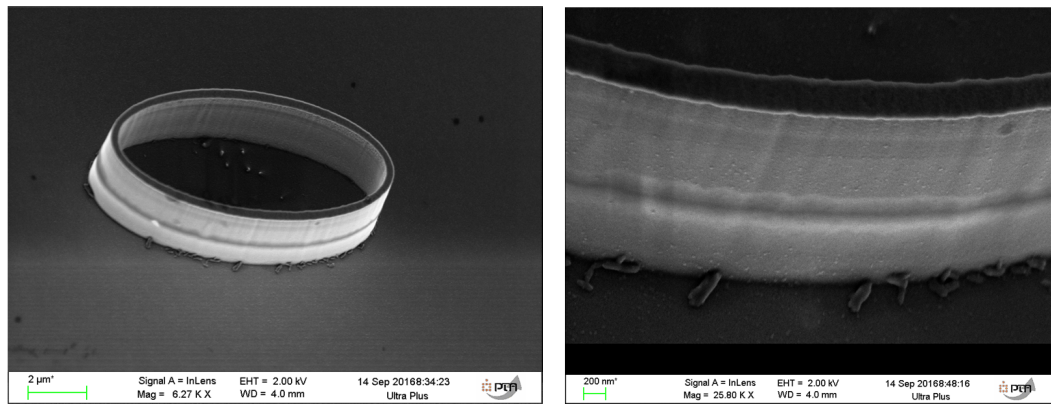
**Figure 2.8** SEM images of micropillars.

**Etching of ring resonators** Etching of ring resonators can be performed at slower speeds because of a maximum etching depth of  $5 \mu\text{m}$ . During this thesis, the RIE mode was used.

The sample is glued by **FOMBLIN** oil onto a Si wafer. An etching gas consisting of  $\text{SiCl}_4$  and Ar was used in order to create smooth surfaces. The RF power was 120 W. This results in an etching speed of 20 nm/min.

Similar to micropillars, the sample is dipped during one minute in 10 % diluted  $\text{HNO}_3$ .

The result of this procedure is shown on Figure 2.9(a). The rings are transferred with a high precision onto the wafer. A zoom onto the surface of the rings (Figure 2.9(b)) reveals punctual defects of the resonators which could degrade their optical performances. More information on the possible impact of such defects is given in chapter 5.



(a) Global view of a ring resonator which shows the precision of the process.

(b) A zoom onto the same ring reveals walls with slight roughness.

**Figure 2.9** SEM images of ring resonators.

## 2.2 Optical characterization of semiconductor microstructures

After the fabrication, the samples now must be analyzed and their properties must be evaluated. For these reasons, experiments with optics are conducted. Advanced experiments like cavity switching or color change experiments also require the use of optics.

In this section, I will present the optical techniques which were used in the frame of this PhD thesis. First, I explain the principles of photoluminescence and the required optical elements. The second part of this section is dedicated to a description of time-resolved PL.

### 2.2.1 Photoluminescence spectroscopy

Photoluminescence (PL) is defined as the emission of photons from any form of matter after absorption of light. The examined material is brought to its excited state by an incident laser beam with a defined wavelength. Then, it relaxes and emits light, whose spectrum is analyzed. Depending on its material properties and structure, the signal emitted by the sample varies. With the obtained spectra, one can conclude about the nature and properties of the sample.

In the case of semiconductors, electrons of the valence band are lifted to the conduction band by absorption of photons with an energy superior to the bandgap energy. If the electron-hole-pairs recombine radiatively, a photon is emitted.

Microphotoluminescence (micro-PL) is a PL experiment that allows a spatial resolution in the order of micrometers. The excitation beam is focused by a microscope objective onto the sample. This is decisive for a precise investigation of the microresonators, whose maximum size is  $10\ \mu\text{m}$ . The precise position of the sample is adjusted via micrometer screws which have a precision of  $\approx 100\ \text{nm}$ .

On the other hand, macrophotoluminescence (macro-PL) is used for non-structured materials in order to obtain information of their properties. An example would be the examination of a grown semiconductor structure with QDs and/or quantum wells as integrated emitters. Macro-PL can thus be used to easily obtain information over the success of a growth.

In the frame of this PhD thesis, photoluminescence was primarily performed in order to record the signal of QDs. As mentioned in chapter 1, photons are emitted when an electron recombines with a hole inside the QD.

Electrons and holes are created optically with a laser beam which is directed by an objective onto the structure containing the QDs. Optically created electrons and holes can be injected into QDs by different ways: through resonant excitation at the frequency of the QD, or by non-resonant excitation in the wetting layer or the surrounding material (GaAs). From there, they diffuse into the QDs and recombine. The emitted photons are then detected. Figure 2.10 shows the principle of QD spectroscopy.

The experiments are performed at cryogenic temperatures to avoid diffusion of the free carriers out of the QDs and resulting non-radiative recombination of excitons at etched sidewalls. For quantum optics experiments, low temperatures are also necessary to prevent spectral broadening of QD emission lines. The sample is cooled down in a cold-finger cryostat with a window which allows nearly lossfree excitation and detection. The temperature is measured in real-time.

**Detection of the emitted signal** The emitted signal is focused by a  $f = 75\ \text{mm}$ -lens on the entrance slit of a Jobin-Yvon Triax320 monochromator. It spatially separates the different spectral components of the signal with a grating. The resolution depends on the period of the grating and the maximum resolution which could be provided is  $0.1\ \text{nm}$ . The resulting signal is then detected with a CCD camera (Andor IDus) which is based on silicon.

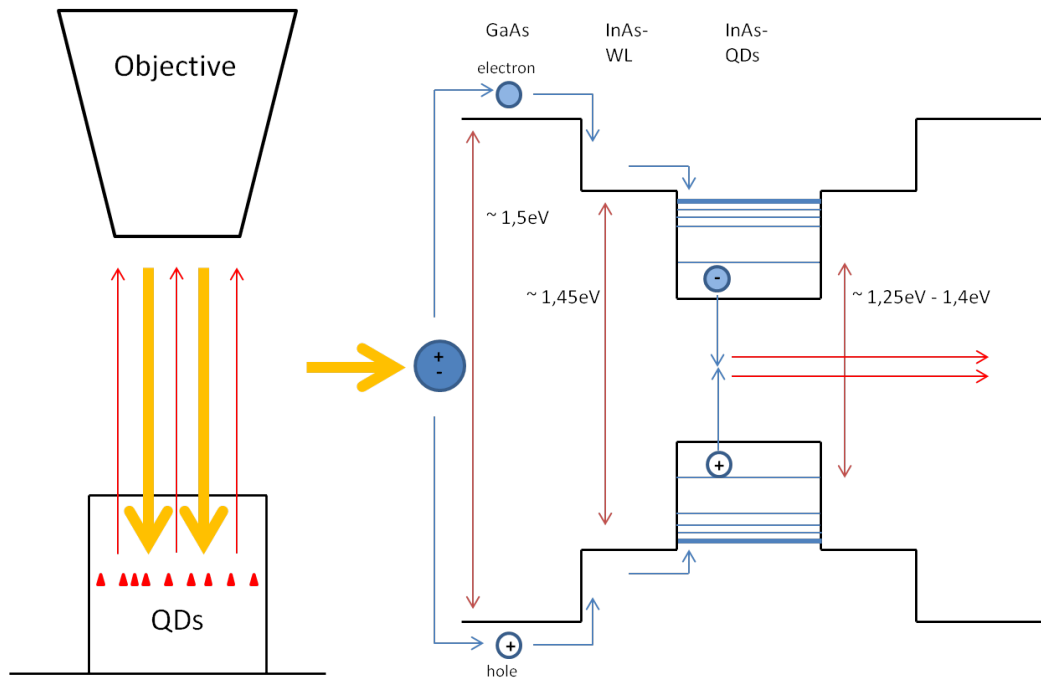


**Figure 2.10** Principle of photoluminescence measurements on QDs. Excitation and detection of the signal is provided by the same optical element. The free carriers which recombine in the QD are usually created in the surrounding semiconductor structure and are then captured by the QDs where recombination takes place.

## 2.2.2 Elements for time-resolved microphotoluminescence spectroscopy

It is crucial for cavity switching and color change experiments to resolve the PL-signal temporally and spectrally. The streak camera is an instrument that enables simultaneous spectral and temporal analysis of ultrafast events with a maximal temporal resolution of 0.9 ps. This allows a precise analysis of the temporal photoluminescence response of a semiconductor structure.

**The pulsed laser** To create these events, it is necessary to use a modulated light source. We use a CW-mode locked Ti:Sa laser for excitation.

A Nd-YAG-pumplaser emits light at a wavelength of 1064 nm. This light is frequency-doubled and used to pump a sapphire crystal doped with titanium. By tuning the cavity of the Ti:Sa-laser, one can adapt its wavelength continuously between 730 to 960 nm. The laser can work either in the pulsed mode, or in the continuous wave (CW) mode. The pulses are created by passive mode-locking and their lengths are  $\approx 200$  fs. The repetition rate is 76 MHz.

In order to avoid reflections which perturb the oscillations of the laser, the laser passes through an optical diode.

The power of the laser can be adjusted continuously via power attenuators based on two polarizers, which are situated at the exit of the Ti:Sa-cavity.

The light beam is then coupled into an optical fiber with a 10x-objective. This allows easier experimental handling concerning further applications.

**The streak camera** The streak camera has to be synchronized with the repetition rate of the laser. A small part of the emitted laser light is therefore sidlined by a tilted thin glass panel and directed onto a photodiode. The signal created by the photodiode has the same period as the laser and it is used for synchronization between streak and laser. The streak works at  $76 \pm 0.1$  MHz.

The photons of the PL signal have to be separated spectrally, before entering into the streak camera. This is assured by the Triax320 monochromator which contains two different blazed gratings: a 150-lines per mm and a 1200-lines/mm.

The first grating has a coarser spectral resolution compared to the second one, but creates a brighter signal in the streak camera. The reason for this is the much higher splitting of the different spectral components by the 1200-lines/mm grating. It reduces the number of photons impinging onto one pixel of the CCD camera.

Another difference between the two gratings is the resulting temporal resolution which is limited by three different factors: the number of lines of the grating onto which the signal impinges, the intrinsic resolution of the streak  $\Delta t_{\text{int}}$  and the duration of the laser pulse ( $\Delta t_{\text{pulse}}$ ).

Of the named factors, two are already determined:  $\Delta t_{\text{pulse}} = 2.9$  ps or 0.2 ps respective (whether a fiber is used or not) and  $\Delta t_{\text{int}} = 0.9$  ps

The first factor depends on the used grating and the size of the laser spot that arrives on the spectrometer. Between every line of the grating, a delay of one single  $\lambda$  appears. This time shift corresponds to  $\frac{\lambda}{c} \approx 3$  fs. The more grating lines are illuminated, the longer the shift between the light components coming from left and right sides of the spot. With a spotsize of 3 mm on the grating, which can be realised by positioning a small slit in front of the entrance of the monochromator,  $\Delta t_{\text{grating},150} = 1.4$  ps can be achieved. For the 1200-lines/mm grating, this would be  $t_{\text{grating},1200} = 10.8$  ps.

Adding up these errors, we obtain a maximal temporal resolution of

$$\Delta t = \sqrt{\Delta t_{pulse}^2 + \Delta t_{int}^2 + \Delta t_{grating}^2} \quad (2.1)$$

This results in a resolution of  $\Delta t_{150} = 1.7$  ps (without fiber) respective  $\Delta t_{150} = 3.3$  ps (with fiber) for the 150-lines/mm grating. For the 1200-lines/mm grating, the resolution is  $\Delta t_{1200} = 10.8$  ps respective  $\Delta t_{1200} = 11.2$  ps. Both of the gratings allow the detection of ultrafast all-optical switching processes.

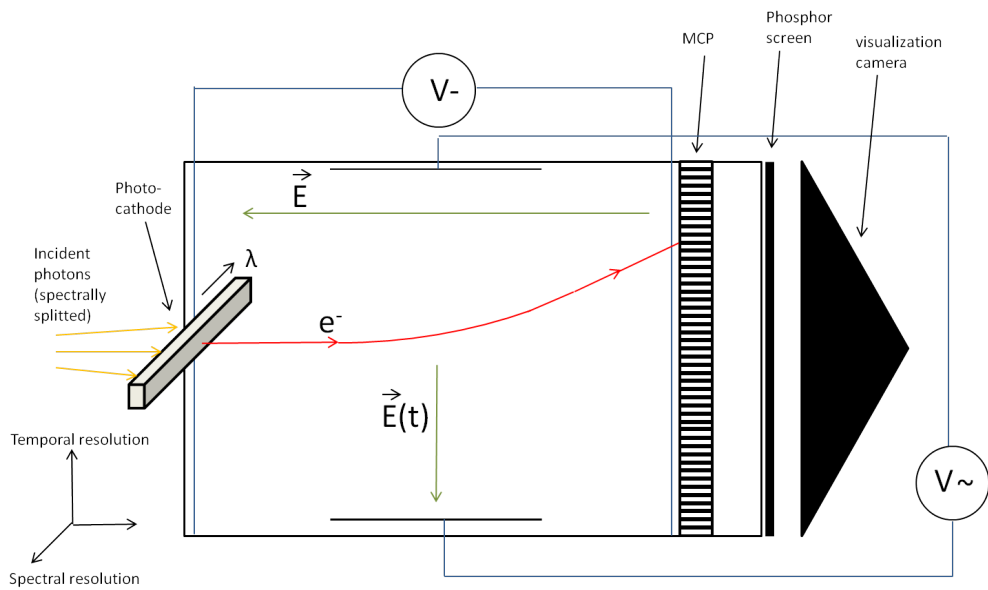


**Figure 2.11** Diagrammatic drawing of the streak camera. The caption on the axis symbol describes the direction of the electrons' deviations.

Figure 2.11 shows a schematic sketch of the streak setup. The spectrally resolved light signal arrives at a photo cathode which converts photons into electrons.

The electrons are now accelerated towards a multi channel plate (MCP) by an electric field in a vacuum tube. Another, time-dependent and oscillating electric field deviates the electrons transversally. This electric field is synchronized with the repetition rate of the pulsed laser and creates the time resolution of the streak camera.

Then, the spectrally and temporally resolved electrons impinge onto the MCP. There, the electron signal is amplified to obtain a detectable signal which is recorded by a phosphor screen.

## 2.3 Conclusion

This section dealt with the fabrication of optical microresonators. It includes the growth of samples and the cleanroom fabrication of resonators. I explained the principles of the used techniques and gave an overview over different used recipes and the resulting structures.

The first step is the epitaxial growth of the semiconductor samples which defines the microresonator structures in vertical direction and provides the integrated emitters. Due to the high precision of this method, the grown thicknesses are well defined and the emitters, QDs, show the required properties. These structures are then processed in a cleanroom microfabrication process. At the end of this process, micropillars and micro-resonators are obtained.

Characterization of the fabricated sample is performed by optical means. Different optical elements and detectors are required for time-resolved photoluminescence experiments. I explained these experiments in order to convey the basics which are required to understand the following chapters to the reader.

## Ultrafast color change experiments on planar cavities

By shifting the resonance frequency of a cavity, the wavelength of photons stored in it can be changed adiabatically. The conditions for this are a slow modification of the resonance compared to the time of one roundtrip of light in the cavity and a storage time exceeding the time needed for the frequency shift.

This effect does not depend on the intensity or photons statistics of the trapped light. Therefore, in a long term perspective, it is attractive in view of an application to frequency conversion of single photon pulses.

In this work, we have chosen to perform color change experiments with high Q planar cavities, which are well suited for a clean in- and out-coupling of light pulses. First, an overview of recent experimental works on color conversion is given. I also present properties and modes of planar cavities. In the second section, the cavity is characterized by PL- and ring-down experiments. Color change experiments performed during this PhD thesis are described and a quantitative analysis follows. We confirm in particular the adiabatic character of the frequency conversion process. The results are compared to FDTD simulations. At last, I give an overview of potential improvements of our experiment by using a different configuration.

### 3.1 Adiabatic color conversion and planar semiconductor cavities

This section gives a short overview over color conversion in general and the type of cavity that is used in this work: a planar cavity.

In the first part, results of color change experiments that have been achieved during the last decade are explained. Indeed, many different approaches, which are based on different physical effects, exist for converting the color of light. These recent

experiments are discussed and key numbers are given. The motivation of the present work is given, too.

Planar cavities are a well-known and explored medium. During decades, research was done on them and they are already integrated in devices of our daily life (e.g. VCSELs, spectral filtering); their fabrication and experimental handling are well mastered. I give a short description over their operation principle and the most important figures of merit in the second part.

### 3.1.1 Adiabatic color conversion: overview and basics

Wavelength conversion, or demonstratively spoken, color change of light is used in large-scale optical networks in order to switch between different data channels. It also increases capacity and flexibility of networks. On the macroscopic scale, it is a quite ordinary process and often used for wavelength-division multiplexing in telecommunication [126].

A huge number of publications and approaches exists on this research field. Because of the miniaturization trend, it is strongly desirable to be able to integrate wavelength conversion devices onto a chip platform. Consequently, I concentrate on approaches which fulfill two requirements: A micrometer scale device size and the potential to convert even single photons to other wavelengths.

A first possibility to convert the color of light is the use of non-linear effects in optical media. This method allows the conversion of light over large spectral ranges. In 2016, the research group of Srinivasan showed a high range frequency tuning (from several nm up to nearly 600 nm) by using four-wave mixing in a silicon ring resonator [63]. A conversion efficiency of 60 % was obtained with this approach.

Optomechanical tuning of vibrating waveguides can also be used for shifting the color of light [76]. Fan et al. demonstrated a frequency shifter capable of shifting single photons based on optomechanical methods [27, 59]. This method suffers from a complicated fabrication process and a wavelength shift below one nanometer.

Another approach is the frequency conversion of light stored in a cavity. Because of a confinement on small volumes, this allows an easy experimental handling. Light is converted by switching the resonance frequency of the cavity. The switching speeds need to take less time than the storage of photons in a cavity. This can be achieved by all-optical injection of free carriers into high Q-microcavities [46] or through Kerr switching [128].

In order to build the new technology on already existing standards, many research projects focus on wavelength conversion on silicon and operation at the telecom wavelength (around 1555 nm).

As a consequence, the first realization of a color change device on microscopic scale was achieved in 2007 by M. Lipson's research group. They demonstrated a change of wavelength up to 2.5 nm with an on-off conversion efficiency of 34 % at a wavelength in the telecom range [85]. They worked on a silicon chip and used a cavity coupled to a waveguide in order to perform a color change with photons in the telecom range.

Preble et al. repeated similar experiments on an approximated single photon level with wavelength changes up to 0.5 nm and 10 % efficiency [86].

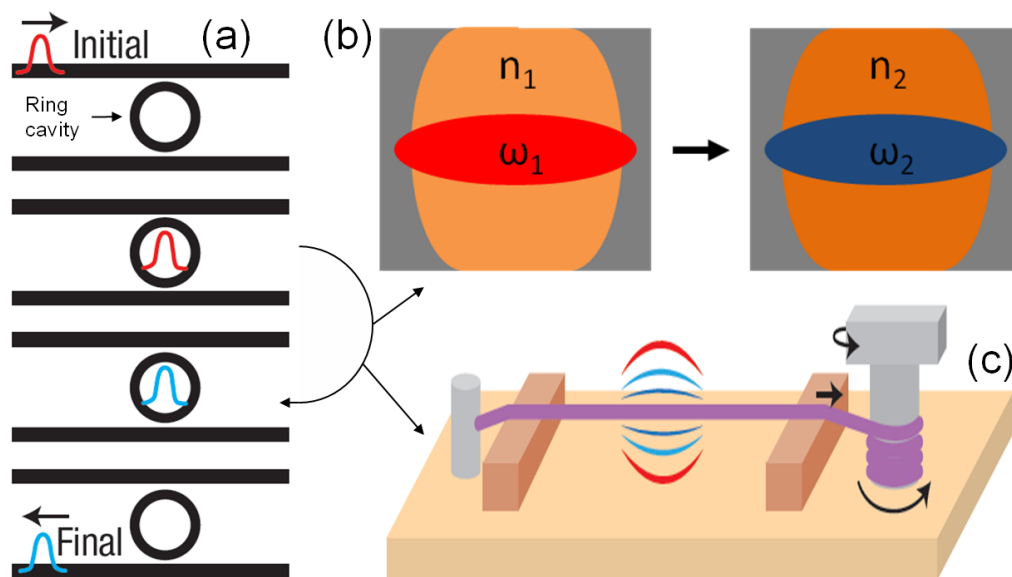


**Figure 3.1** Schematic representation of a color conversion experiment. Light of wavelength  $\lambda_1$  is stored in a cavity, converted to  $\lambda_2$  and then coupled out of the cavity (a). The conversion process itself consists in changing the optical length of the cavity by modifying its refractive index and forcing the light to adopt (b). This can be compared to tuning a recently plucked guitar string (c).

Both experiments use similar approaches: light is stored in a silicon ring resonator with a sufficiently high Q factor. After storing, the light is converted to another wavelength and coupled out of the resonator in order to be detected (see Figure 3.1(a)).

Storing of light in cavities and the subsequent outcoupling are steps that are very well controlled nowadays. The crucial step is the conversion of photons.

In 2006, Notomi described how the wavelength of light can be converted by simply tuning the refractive index of a photonic crystal cavity [75]. The conversion process is adiabatic, i.e. the light remains perfectly in the shifting cavity mode or, in other words, a transfer of the stored light towards other modes of the structure does not occur. This behaviour is observed, if the cavity shift is very slow compared to the shortest relevant timescale for trapped photons: one round trip in the cavity takes a few femtoseconds whereas the tuning of the cavity takes around few picoseconds.

Visually spoken, adiabatic color conversion can be compared to tuning a guitar: when a guitar string is plucked, it vibrates at its resonance frequency. If the length of a vibrating guitar string is changed by moving the finger clamping the end of the string, the resonance frequency is also changed. A change of the frequency of the sound appears (see Figure 3.1(c)).

An adiabatic conversion process is linear, independent from the initial light intensity and has a theoretical conversion efficiency of 100 % [75]. Furthermore, the statistics of the converted photons is conserved, which makes this process a promising candidate for single photon conversion and thus for more advanced quantum optics circuits.

Another application for an adiabatic frequency change could be in the frame of photonic memories. Electronics still has the advantage that the electron energy can be controlled with an external field. This enables a continuous manipulation of the electronic signal flow [109]. Until recently, the energy of a photon could not be efficiently changed. Adiabatic wavelength tuning makes this feature possible.

The experiments performed in [85] and [86] show that only a part of the initially injected light has been converted. Furthermore, the position of the cavity mode was not recorded. This arises questions whether the conversion process has been perfectly adiabatic.

Tanabe et al. were the first that performed adiabatic frequency tuning by free carrier injection on photonic crystals in 2009 and to overcome this limit. They also were able to observe the process in real time. By performing a pump probe experiment, they showed that the emitted light follows exactly the resonance of the cavity which is a clear indicator of an adiabatic behaviour [110].

However, in Tanabe's experimental work, the conversion efficiency was not estimated. Due to a rough temporal resolution, no exact observation of the color change process itself, which appears on a timescale of few picoseconds, could be made. Furthermore, the switching amplitude of only 0.15 nm was very small.

The physical effect, which Tanabe and Lipson used, is also applied to our cavity: by creating free carriers in the cavity, we shorten its optical length. The stored light adapts to the changing resonance frequency of the cavity and experiences a blueshift to shorter wavelengths (see Figure 3.1(b)).

The main difference of our approach with respect to previous experiments is related to the use of a planar cavity whose properties are described in the following chapter. Compared to photonic crystals, this structure is rather easy to fabricate and handle experimentally. It could play an important role in the efficient conversion of photons propagating in the free space.

### 3.1.2 An overview over planar cavities

Planar semiconductor cavities are always composed of two exactly parallel mirrors which reflect the light stored in the cavity and a guiding semiconductor medium where the photons can freely propagate between the mirrors. The structure is considered as infinitely extended in two dimensions. Generally, it can also be described as a Fabry-Pérot interferometer.

Due to its structure and the resulting interference effects, a planar cavity has resonances which are defined by the materials (or rather their complex refractive indexes) used for the sandwich, the reflectivity  $R$  of the mirrors and the distance  $d$  between them.

**The ideal case** In a first step, we consider the ideal and easiest configuration of a Fabry-Perot resonator: an isotropic layer of thickness  $d$  and refractive index  $n_c$  surrounded by two perfect mirrors ( $R = 1$ ). Because of interference effects, the photon momentum perpendicular to the mirrors  $k_z$  is quantized.

$$\left( \frac{\omega^2 n_c^2}{c^2} - k_{\parallel}^2 \right)^{\frac{1}{2}} d = k_z L_{cav} = N\pi \quad (3.1)$$

$L_{cav}$  is the physical length of the cavity.  $k_{\parallel}$  is associated to a photon momentum parallel to the cavity mirrors and acts as a number that can be continuously chosen. In this PhD thesis, we only work in perpendicular incidence and thus consider  $k_{\parallel} = 0$ .

We observe a discrete set of spectrally infinitely small states quantized by  $k_z$  which are allowed to exist in the cavity.

**The real case** In reality, perfect mirrors with a reflectivity  $R = 1$  do not exist. To create planar solid state cavities, it is important to use materials with a reflectivity close to unity.

Experimentally, two different realizations of planar cavities are possible. Their difference is the used mirror material.

**Metallic mirrors** Metallic mirrors usually consist of aluminum, gold or silver.

First of all, it is difficult to fabricate cavities with thicknesses of the order of few wavelengths and metal coatings on both sides (but it is possible).

However, the major drawback is the absorption of light in the metals at optical wavelengths: this leads to small storage times.

Metallic cavities also show relatively high reflectivities only if the metal layers are sufficiently thick ( $> 100$  nm, depending on the material). This leads to absorption of input and output beams due to the propagation through the mirror layer which is a drawback for the all-optical injection of free carriers as well as for the extraction of the frequency-converted light.

For these reasons metallic cavities have not been used until now for color conversion experiments.

### 3.1.2.1 Distributed Bragg reflectors

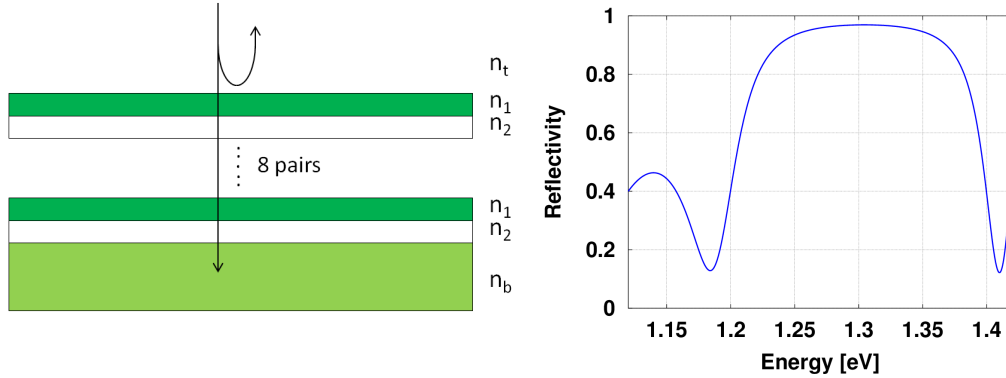
A more sophisticated approach to confine light in a planar cavity is the use of distributed Bragg reflectors (DBR). DBRs are designed for a central wavelength  $\lambda_B$  at which they show maximal reflectivity.

DBRs consist of alternating, isotropic layers with different refractive indices  $n_1$  and  $n_2$ . The thickness of each layer has to be  $\frac{\lambda_B}{4n_{1,2}}$ .

By stacking several pairs of DBRs, its reflectance  $R$  increases. For a Bragg mirror consisting of  $N$  pairs of alternating layers,  $R$  for  $\lambda_B$  is calculated as follows:

$$R = \left( \frac{1 - \frac{n_b}{n_t} \left( \frac{n_1}{n_2} \right)^{2N}}{1 + \frac{n_b}{n_t} \left( \frac{n_1}{n_2} \right)^{2N}} \right)^2, n_1 > n_2 \quad (3.2)$$

$n_b$  is the refractive index of the bottom layer,  $n_t$  of the top layer of the DBR (mostly substrate, spacer or air). Figure 3.2(a) sketches these different components of a Bragg mirror.



(a) Sketch of the construction of a DBR. Incident light from a medium with  $n_t$  impinges on the DBR consisting of periodic layers with  $n_1$  and  $n_2$  stacked on a bottom layer with  $n_b$ . (b) Plot of the reflectivity of a DBR consisting of 10 pairs (AlAs/GaAs) stacked onto a GaAs substrate at room temperature. The maximum reflectivity was fixed at 1.3eV.

**Figure 3.2** Composition and resulting reflectivity spectrum of a DBR.

Figure 3.2(b) shows a calculated reflectivity spectrum for the case of light impinging perpendicularly from the air onto a DBR consisting of 10 AlAs/GaAs pairs stacked on a GaAs substrate. The DBR thickness is designed for a maximal reflectivity at 1.3eV at room temperature ( $R = 97.3\%$ ).

Around the maximum, a spectral zone which is also highly reflective can be observed. This zone of high reflectivity is called the stopband and its width  $\Delta\lambda$  can be calculated as follows [88]:

$$\Delta\lambda = \frac{4\lambda_B}{\pi} \arcsin\left(\frac{n_1 - n_2}{n_1 + n_2}\right), n_1 > n_2 \quad (3.3)$$

Equation 3.3 states that the width of the stopband only depends of  $n_1$  and  $n_2$ . The material composition is thus crucial for the behaviour of the Bragg mirror.

### 3.1.2.2 Planar cavities based on Bragg mirrors

Semiconductor planar cavities based on Bragg mirrors consist of the following elements: (see also Figure 3.3)

- 1) a substrate onto which the actual structure is grown

- 2) a bottom DBR
- 3) a spacer where the photons are confined
- 4) a top DBR

This structure leads to a longitudinal confinement of light. Due to the infinite extensions of the planar cavity, light can still freely propagate perpendicular to the growth axis.

The condition for the thickness of the spacer  $L$  is given by

$$L = m^* \cdot \frac{\lambda_B}{n}, m^* \in \mathbb{N} \quad (3.4)$$

The optical thickness of the spacer also determines the number of the resonant modes in a specific wavelength range. For higher  $L$ , an increasing number of resonant modes in the stopband can be observed.

$L$  has an influence on the storage time of the light  $\tau$  in the cavity, too. The thicker the spacer is, the longer is the time which the photons need for a round trip. It is thus possible to increase  $\tau$  drastically by using a thicker spacer.

The other possibility to maximise  $\tau$  is to increase the reflectivity of the bottom and top Bragg mirror,  $R_B$  and  $R_T$ , by adding further Bragg stacks. A higher reflectivity increases the probability that photons do not leave the cavity and the storage time.

Based on these variables, the theoretical quality factor of the cavity can be calculated.

We first introduce the order of the cavity  $m$ :

$$m = m^* + 4 \cdot \frac{n_2}{n_1 - n_2} \quad (3.5)$$

The additional contribution results of the penetration depth of the photons into the DBRs.

The finesse  $\mathcal{F}$  of a Fabry Perot cavity is defined by [93]

$$\mathcal{F} = \frac{\pi \sqrt[4]{R_b R_t}}{1 - \sqrt{R_b R_t}} \quad (3.6)$$

The quality factor  $Q$  of a planar cavity can now be expressed by combining Equation 3.5 and Equation 3.6 [93]:

$$Q = m \cdot \mathcal{F} \quad (3.7)$$

This confirms that  $Q$  can be increased by using thicker cavities which allows larger values for  $m$  around a given wavelength range ( $\mathcal{F}$  depends only the number of Bragg pairs and the material composition).

It can be shown that the effective surface of a mode  $m$   $S_{\text{eff},m}$  of planar cavities is directly proportional to its quality factor [9].

$$S_{\text{eff},m} = \left(\frac{Q}{2}\right) \left(\frac{\lambda_m}{n}\right)^2 \quad (3.8)$$

The larger the quality factor of a mode, the larger is its spatial extension in the planar cavity.

## 3.2 Characteristics of the planar cavities used for frequency conversion and the experimental setup

This section is introduced by a short overview of the properties of planar cavities used for frequency conversion. I explain the design and fabrication of planar cavities. I also detail requirements for performing color change experiments successfully. In the second part of this section, the used experimental setup is shown and described.

### 3.2.1 Planar cavities designed for color change experiments

Our experimental setup imposes us to work in transmission. We are not using an internal light source like for example quantum dots as we do in other experiments described in this PhD thesis.

This has several advantages: Firstly, it enables us to perform a kind of dark field measurement which reduces signal artefacts of our measurement. In a reflection experiment, a big part of the light would be reflected before entering the cavity. This would create a very intense signal, completely saturate the detector and make

the observation of small effects impossible. In the transmission configuration, this problem can be avoided.

Furthermore, the transmission measurement allows us to reduce the optical elements in front of the detector to a minimum. By placing the visualization elements in front of the sample, we can precisely control position and size of our laser spot (see subsection 3.2.2).

Thus, our cavity has to be designed for having very low reflectivity values at its resonances to be able to work with our experimental setup. This is achieved by adding four additional pairs of AlAs/GaAs layers for the bottom mirrors. It compensates the asymmetry which appears on the bottom and top interface of the Bragg stack (air at the top, GaAs at the bottom).

Furthermore, it is a crucial requirement that the quality factor of the cavity is sufficiently high. For experiencing the color change due to free carriers, the light has to be stored long enough in the cavity. This can be obtained by “sandwiching” the cavity between a large number of Bragg pairs. Using a longer cavity is also a possibility to increase the storage time of light in the device. This strategy has been used in the present work to relax the constraints on the epitaxy of very high reflectivity Bragg stacks.

**Composition of the cavity** Figure 3.3 sketches the composition of the cavity used for our experiments. The bottom mirror of our cavity is composed of 20 pairs of  $\frac{\lambda}{4n}$  layers of GaAs and AlAs. Its nominal reflectivity is  $R_{\text{bottom}} = 0.9976$ .

Onto the bottom mirror, a  $27\frac{\lambda}{n}$  spacer is stacked. In the case of our cavity design, the thicker spacer increases the storage time of a photon by a factor of 8.44 compared to a cavity spacer of  $\frac{\lambda}{n}$  (in theory:  $Q_{27\lambda} = 65000$  versus  $Q_{\lambda} = 7700$ ).

The top mirror of the cavity consists of 16 pairs of  $\frac{\lambda}{4n}$  layers of GaAs and AlAs. This results in  $R_{\text{top}} = 0.9970$ . The difference of the number of Bragg pairs results from the fact that the bottom mirror is grown on a GaAs wafer ( $n = 3.5$ ), whereas the layer above the top mirror consists of air ( $n = 1$ ). The different refractive indices create the need for a different number of GaAs/AlAs pairs.

By choosing the central energy of the cavity  $E_{\text{central}} = 1.3$  eV, we also fix the actual length of the different layers.

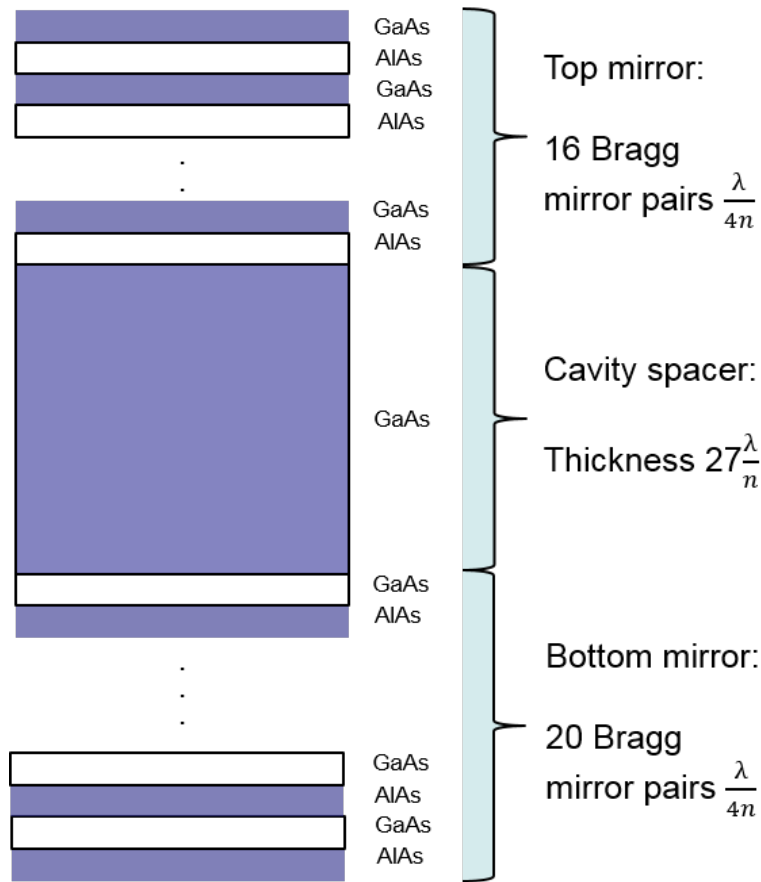


**Figure 3.3** The cavity which was used during the color change experiments. It is designed to fulfill several conditions: High transmissivity at resonance frequencies (nearly equal number of Bragg pairs) and long storage times (cavity length  $27\frac{\lambda}{n}$ , high number of Bragg mirrors). The structure is grown onto a GaAs wafer.

**Cavity fabrication** The cavity is fabricated by molecular beam epitaxy (MBE) to achieve a precise control over the composition of the different layers and also their thickness which is crucial for obtaining a high Q. A precise description is given in section 2.1. We also want to achieve a low density of defects. That is why the sample is grown at high temperatures. The sample was glued with indium on the sampleholder.

After the growth, the indium was removed by mechanical polishing of the backside of the sample in order to avoid scattering in the transmission experiments. The resulting roughness is then reduced by a mixed mechanical and chemical polishing (use of methanol and bromine). To reduce the reflection at the interface of the GaAs wafer and air, an antireflection coating made of SiN is deposited on the backside of the sample.

At the end of these fabrications steps, the sample has a thickness of around  $100 \mu\text{m}$ .

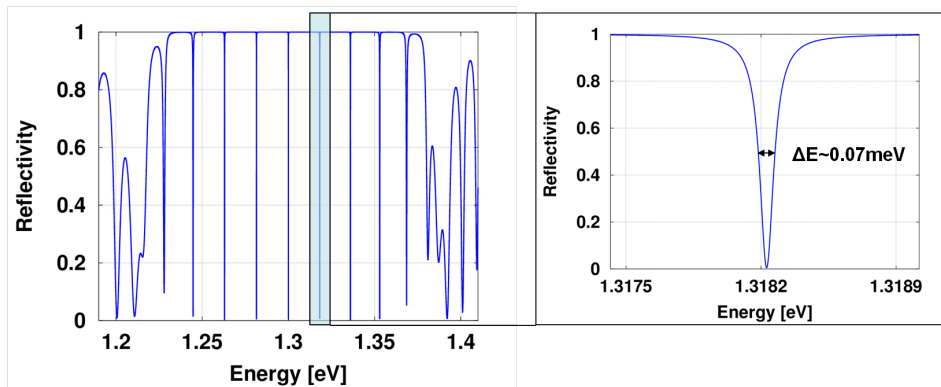


**Figure 3.4** Simulated reflectivity spectrum of the planar cavity. We observe a stopband width of 0.15 eV centered around 1.3 eV. The cavity has several discrete resonances which are expressed by deep dips in the reflectivity spectrum. The zoom of the resonance onto which this work was performed reveals a theoretical quality factor of 19000.

**Theoretical properties of the cavity** We now estimate the properties of our cavity theoretically. Therefore, we use the transfer matrix method (TMM) which is commonly used to model the propagation of electromagnetic waves through layered media. Further information on this method can be found in [125].

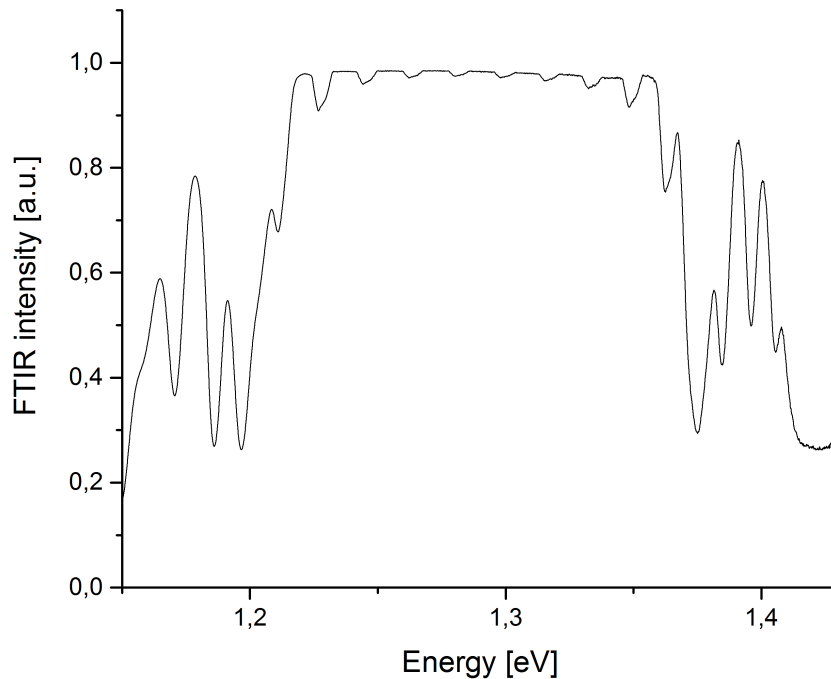
The result gives insight into several properties of the cavity, for example the width of the stopband with high reflectivities, the position of the resonances and their quality factor.

Figure 3.4 shows the result of a TMM simulation. On the left hand side, we can observe a reflectivity spectrum that shows a stopband width of 0.15 eV which is centered around 1.3 eV. In the stopband, several discrete, equally distanced dips appear. These are resonances of the cavity.

As we work with the cavity resonance on the right hand side of the central dips, a zoom onto this resonance can be seen on the right hand side of the image. The reflectivity is nearly zero at resonance, as expected for balanced top and bottom DBRs, while we observe a quality factor  $Q = 19000$  for this resonance. Due to the lower response of the streak camera detector at lower energies, we cannot work on the resonance around 1.3 eV which has a higher quality factor ( $Q = 65000$ ).

**Experimental spectra of the cavity** We are now interested in observing whether our cavity actually shows a similar behaviour as we predict theoretically. Therefore, we performed Fourier Transform Infrared (FTIR) spectroscopy on our sample. FTIR spectroscopy allows scanning the spectral properties of an object over a large range during a very short time. White light is sent through a Michelson interferometer and is modulated at a frequency proportional to its energy. After being reflected by the

sample, a detector measures its absorption. By applying a Fourier transformation, it can be concluded on the spectral properties of the measured sample.



**Figure 3.5** FTIR spectrum of the planar cavity. The hardly visible dips in the stopband highlight the resonances of the cavity. Compared to the simulation, the stopband is slightly shifted. Due to an insufficient spectral resolution, the deepness of the resonance dips and their spectral widths cannot be estimated.

A FTIR spectrum of the cavity can be seen on Figure 3.5. Compared to the simulation, the center of the stopband shows a 20 meV shift into the infrared. The stopband width is 0.14 eV which is similar to the simulated cavity.

The resonances of the cavity hardly appear on Figure 3.5. It is possible to determine their position but we cannot conclude on the quality factor. This is due to the small spectral widths of the resonances, which are beyond the resolution of the FTIR.

Nevertheless, two possibilities exist to measure the quality factors of our cavity experimentally.

The first possibility would be finely tuning a probe laser and analyse its intensity transmitted through the sample. This would take very long time because a large energy range needs to be scanned very finely [91, 3] and still a high spectral resolution of the detector is required.

The second and more precise method for high-Q cavities is performing a ring down experiment and directly measure the time that the light spends inside the cavity [3]. I will present results of such a “ring-down” experiment in subsection 3.2.3.

### 3.2.2 Experimental setup

As already mentioned in subsection 3.2.1, the color change experiment is done in a transmission configuration. In this section, I describe the used experimental setup, its characteristics, its advantages and limitations.

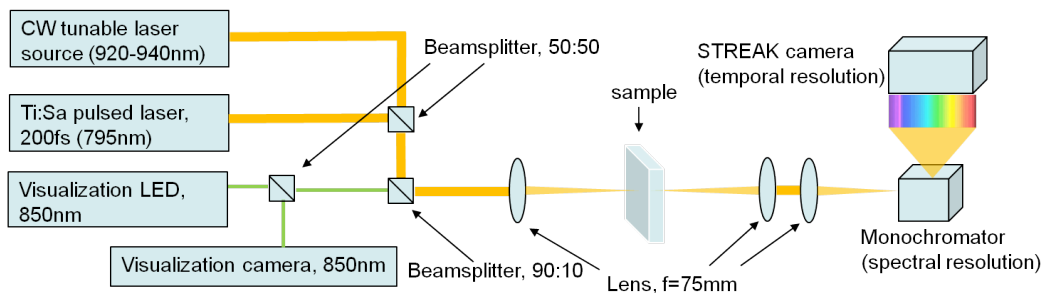


**Figure 3.6** Sketch of the experimental setup. Camera and LED are used to visualize the sample and ensure similar spotsizes and positions of the lasers. The two lasers are required for the pump-probe-experiment whereas the monochromator-streak-camera-combination is needed for resolving the signal spectrally and temporally.

Figure 3.6 sketches the experimental setup which was used for the experiment.

In order to perform a pump-probe experiment, we have to use two superposed laser beams.

The pump beam frequency has to be tuned above the band gap energy of GaAs at room temperature (1.424 eV) in order to inject free carriers. Furthermore, it must deliver laser pulses with a pulse length significantly below the storage time of our cavity. The used modelocked Ti:Sa laser used during the experiment fulfills these conditions with pulses of 200 fs length (confirmed by autocorrelator measurements) and a widely tunable wavelength range (from 795 nm to 935 nm).

The probe beam is provided by a tunable laser diode (Toptica DL100) which emits a CW beam. It can be finely tuned over the 920 nm to 940 nm wavelength range.

Both lasers are coupled into optical fibers in order to direct them onto the optical setup. A disadvantage of this configuration is a chirped pulsed laser which extends the pulse duration up to 2.9 ps (for more details see Figure 3.7). However, the fiber enables us to decouple the cavity of the Ti:Sa laser from the optical elements

in front of sample and detector. This allows to fix the laser spot on one given point of the sample even in the case of the modification of the laser wavelength. Another big advantage is the possibility to optimize one optical path for wavelengths around 800 nm and the other for 930 nm. This allows compensation of chromatic aberration at the lens focussing the beam onto the sample. It also allows successive measurements of ring down (pulsed laser operates at 930 nm) and color change (pulsed laser operates at 800 nm).

The two lasers are superposed at a 50:50 beamsplitter and then superposed with the visualization path at a 90:10 beamsplitter. The use of a 90:10 beamsplitter is crucial for the experiment, because we need high powers for pumping and probing our cavity, while low intensities are sufficient for imaging.

The light beams are focussed on the sample by a  $f = 75$  mm lens because it provides a good tradeoff between a spot size corresponding to  $S_{\text{eff,m}}$  and a small angle of incidence of the focalized beam. The latter prevents an excitation of lateral modes and ensures a light beam propagating as perpendicular as possible to the Bragg mirrors.

In order to cut off the remaining pump signal, a 830 nm-lowpass filter is used after the cavity. The outgoing signal is collected and refocussed onto the entrance of the monochromator which provides the spectral resolution. Finally, the photons are detected and temporally resolved by the streak camera.

For visualizing the sample and position and size of the two laser beams properly, we use a LED (emitting around 850 nm) and visualization camera. This is crucial for the experiment, because both of the laser spots must have a size which corresponds to  $S_{\text{eff,m}}$  when they impinge onto the sample. These light beams are superposed by a 50:50 beamsplitter.

### 3.2.3 Determining the quality factor of the cavity with a ring down experiment

Due to the limited resolution of our spectrometers, we cannot determine the quality factor of the cavity experimentally in the spectral domain. The streak camera provides a direct possibility to measure  $Q$  in the temporal domain by performing an experiment called ring-down measurement.

It consists of injecting light of a pulsed laser with a shorter duration than  $\tau_{cav}$  in the cavity and measuring the decay signal of the stored photons. From the detected behaviour, it is possible to conclude on the quality factor (see chapter 1).

**Examining the laser pulses** We perform this experiment by using the pulsed laser at a wavelength which lies in the stopband of the cavity and covers potential mode positions. In a first step, it is important to confirm the length of the laser pulses and a sufficiently high temporal resolution of the streak camera. The decay time can only be measured if a modification of the duration of the detected signal appears due to the cavity.

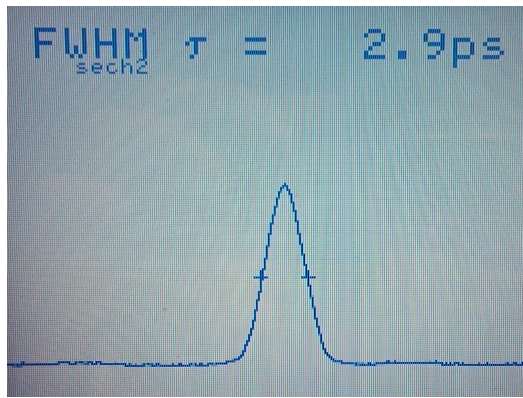
The sample is removed from the optical path and the unperturbed propagating laser pulse is measured with the streak camera. We compare the pulse lengths measured with the streak camera to our autocorrelator measurements. In order to achieve the highest temporal resolution, the experiment was performed with the 150 lines/mm-grating.

Figure 3.7(a) shows an autocorrelator measurement of the pulse width before arriving on the samples surface. The originally 200 fs long laser pulse now exhibits a length of 2.9 ps. This appears due to the transmission through an optical fiber. The different spectral components of the laser exhibit dispersion in the fiber and thus need different times to cross the fiber. For this reason, the laser pulse is slightly chirped.

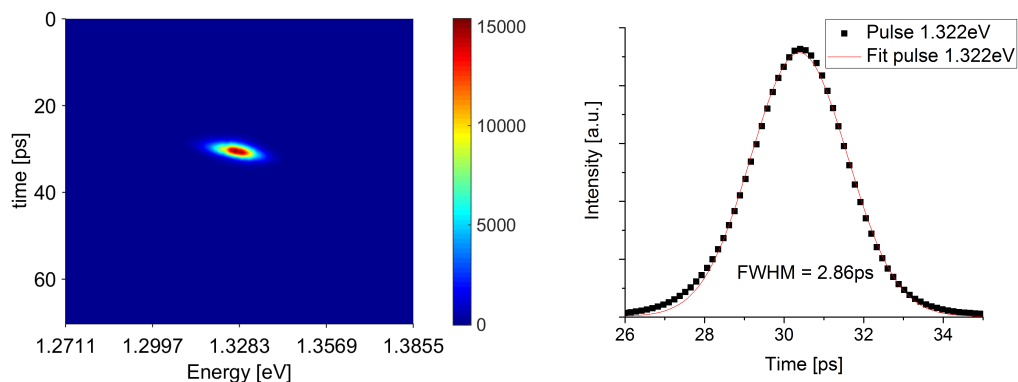
On Figure 3.7(b), the corresponding streak signal is shown and Figure 3.7(c) pictures the spectrally integrated intensities of the streak image (black points). Fitting a Gaussian curve to these points reveals a FWHM of 2.86 ps (red line).

The image reveals two major insights:

- There is a single pulse which is getting out of the fiber, no other signals are detected in the relevant spectral and temporal range.
- The streak measurement results in the same value as the autocorrelation measurement on an ultrafast timescale. It can thus be assumed that further measurements are also detected properly and that no further calibration is required. The resolution is also similar to the value deduced in section 2.2 which allows the detection of storage times  $\tau_{cav} > 2ps$ .



(a) Autocorrelator measurement of the pulse width.



(b) Streak image of the pulse.

(c) Temporal profile of the streak pulse.

**Figure 3.7** Determining the widths of pulses used for the ring-down measurements. Points: horizontal sum of the streak image; red line: Fitted Gaussian curve.

**The ring down experiment** With this knowledge, it is possible to perform the ring down experiment.

Ring down measurements provide a reliable possibility to measure the quality factor  $Q$  of a cavity directly in the time domain. In the past, ring down measurements have been performed in order to measure mainly  $Q$  of cavities that have an ultralong storage time in the nanosecond timerange such as silica microspheres or microtoroids [3] [114]. This enables a high precision of  $Q$ , whereas a measurement in the frequency domain is limited by the resolution of the spectrometer.

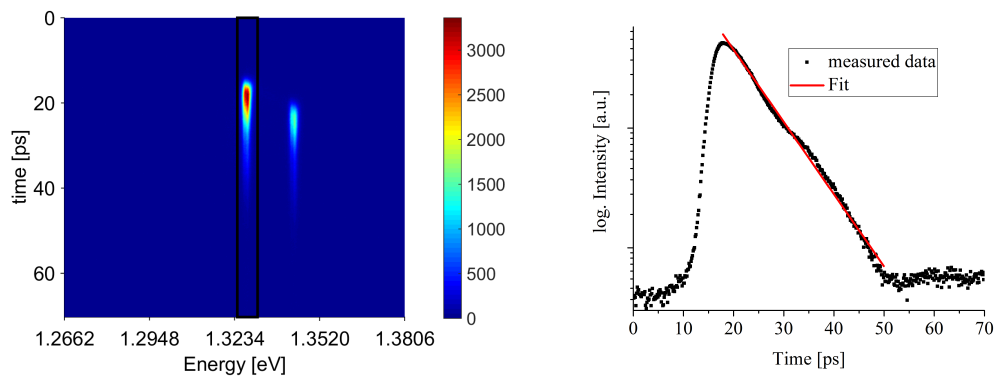
For a correct measurement, two conditions have to be fulfilled:

- The transmission through the cavity has to be large enough to allow the detection of the ring down signal.

- The storage time of the cavity must exceed the pulse length of the laser measured with the streak camera.

The used experimental configuration is shown on Figure 3.6 and a 150 lines/mm grating is used.

The pulsed laser acts as a kind of a white light source with a continuous bandwidth of  $\approx 10$  nm which serves for probing the cavity. Off-resonance, the cavity has a reflectivity of nearly 100 % whereas on resonances, it is significantly lower. Thus, only cavity modes are detected.



(a) Ring down experiment performed on the cavity. (b) Exponential plot of the temporal profile of the Two resonances allow a transmission through the left resonance (black frame) and its fit. the cavity.

**Figure 3.8** Ring down measurement of the cavity and the profile of the left resonance. The quality factor  $Q$  is 15000 for the resonance at lower energy with which the experiments were performed.

Figure 3.8(a) depicts the streak camera image of the ring down experiment. As expected, a discrete number of spots is observed, which correspond to the cavity resonances. The resonances are centered around 1.3278 eV and 1.3435 eV. A higher quality factor is expected for the mode with lower energy. That is why we work with this mode.

After horizontally integrating the signal of the left resonance (black framed area on Figure 3.8(a)), we obtain an exponential decay as shown on Figure 3.8(b). By fitting an exponential curve to the plotted points, we obtain a characteristic decay time  $\tau = 7.5$  ps. This corresponds to a quality factor  $Q = 15000$ . This shows a good agreement to the theoretically calculated  $Q = 19000$  of the TMM simulation.

The following experiments are performed with the mode centered around 1.3278 eV. It shows a very good trade-off between efficient signal detection by the streak camera

and a sufficiently large storage time ( $\tau = 7.5$  ps compared to a pulse duration of at most 2.9 ps).

Thus, the cavity exhibits a sufficiently high quality factor for performing color change experiments.

The quality factor is very sensitive to slight lateral displacements of the sample. It is crucial not to change the sample position and the laser spot after performing the ring down experiment.

**Lifetime of electron and holes in the sample** The lifetime of electrons and holes is a decisive factor for the color change experiment because the spectral position of the cavity mode is a function of the free carrier concentration in GaAs. The pump pulse injects a high concentration of free carriers into the cavity. The latter decay after a characteristic time and the mode returns to its initial position.

Therefore, the characteristic lifetimes of electrons and holes  $\tau_{e,h}$  determine the dynamics of the spectral return of a cavity mode to its unswitched value.

$\tau_{e,h}$  is the lifetime of electron-hole pairs in a semiconductor. It is an intrinsic property of the material and depends on different factors:

- 1) the temperature of sample
- 2) the growth quality of the bulk material
- 3) proximity to interfaces and surfaces to other materials

Different decay mechanisms of free carriers exist in semiconductor materials. The recombination rate of electrons and holes can be expressed as a function of the free carrier density  $N$  in the semiconductor material [122].

$$\frac{dN}{dt} = - \left( \frac{N}{\tau_{e,h}} + BN^2 + CN^3 \right) \quad (3.9)$$

$BN^2$  is the radiative recombination rate and  $C$  is the Auger recombination factor which is an intrinsic property of the material. Auger recombination is only significant for free carrier concentrations  $N > 2.5 \cdot 10^{19} \text{ cm}^{-3}$  [108] which is largely above the concentration at which we work (order of magnitude of max.  $10^{18} \text{ cm}^{-3}$ ).

In the literature,  $B$  is  $7.2 \cdot 10^{-10} \text{ cm}^2/\text{s}$  at room temperature for bulk GaAs [115]. In the following, I use this value in order to determine  $\tau_{e,h}$  from a measured PL decay.

Neglecting the last term of Equation 3.9, we can solve the differential equation and obtain the following expression:

$$N(t) = \frac{N(0)}{N(0)B\tau_{e,h}e^{t/\tau_{e,h}} - N(0)B\tau_{e,h} + e^{t/\tau_{e,h}}} \quad (3.10)$$

To measure  $\tau_{e,h}$ , it is necessary to use an experimental configuration based on reflection. The sample is too thick for performing a measurement in transmission; all emitted light from radiative free carrier recombination would be reabsorbed by the material. Thus, we use the experimental configuration explained in chapter 4. The only difference is that we do not use a cryostat because of measuring at room temperature. Furthermore, a  $f = 75$  mm lens was used in order to focalize the laser beam and to detect the PL emission. The excitation power was 11 mW at a wavelength of 750 nm.

The PL signal emitted due to radiative recombination is then recorded by the streak camera.

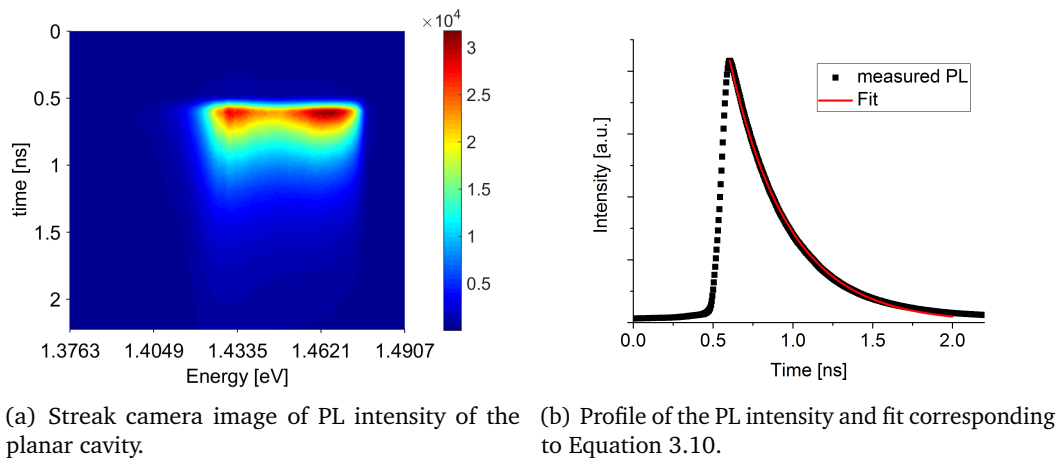


**Figure 3.9** Determination of  $\tau_{e,h}$ .

Figure 3.9(a) shows a streak camera image of the PL intensity due to radiative recombination. Figure 3.9(b) is the profile over the spectrally integrated PL signal.

The PL intensity starts with the arrival of the laser pulse. Then, a decay of the emitted signal is observed. This is a result of recombination: less and less free carriers exist in the material that contribute to radiative emission.

Spectrally, the PL signal is cut off from two sides. The low frequency limit results from the bandgap energy of GaAs of 1.424 eV at room temperature; below this limit,

no PL is emitted. The high energy contribution of the signal is cut off by a lowpass filter operating at 1.5 eV which protects the detector from transmitted laser light.

By fitting the decay from the PL signal peak up to  $t = 2$  ns with Equation 3.10 (at  $t > 2$  ns, noise contributions become important), we obtain  $\tau_{e,h} = 371 \pm 2$  ps which lies in the typical range of high quality GaAs grown at high temperature.

### 3.3 Changing the color of light in a planar cavity

FDTD simulations on color changing of light in planar cavities show promising results. A simulated streak image for such an experiment is shown on Figure 3.10. The simulation which calculates the electromagnetic field of laser light in a one-dimensional configuration identical to planar cavities involves two laser pulses: the first pulse is stored in the cavity and the second, stronger pulse arrives at  $t = 10$  ps and switches the cavity. The stored light is converted to a higher energy. During the return of the cavity resonance to its initial position, the light, which is stored, is emitted continuously. For this simulation, the following parameters were used:  $\tau_{\text{roundtrip}} = 173$  fs,  $Q = 87600$ ,  $\tau_{\text{cav}} = 43.9$  ps,  $\tau_{\text{switch}} = 6.8$  ps,  $\tau_{e,h} = 28$  ps and  $\Delta n = 1$  %.

The simulation shows that large switching amplitudes and an adiabatic behaviour can be expected. The black dots show the mode-position which was calculated for the corresponding free carrier densities with the TMM-approach. This approach is based on geometrical optics and models the experimental environment with matrices.

The positions of the mode resonances correspond exactly to the energies of the emitted photons. This indicates an adiabatic behaviour of frequency conversion in planar cavities for such a set of parameters, for which  $\tau_{\text{roundtrip}} \ll \tau_{\text{switch}} \ll \tau_{\text{cav}}$ .

In the next subsections, I show results of color change experiments obtained with a planar cavity showing similar parameters and a CW laser for probing the cavity. I compare these experiments to data obtained by FDTD simulations. I furthermore analyse the obtained data and conclude about the dynamics of the cavity and the efficiency of the color change. At last, I present results on the behaviour of the cavity on longer time scales and put these results into relation to experiments performed by other research groups in the past.

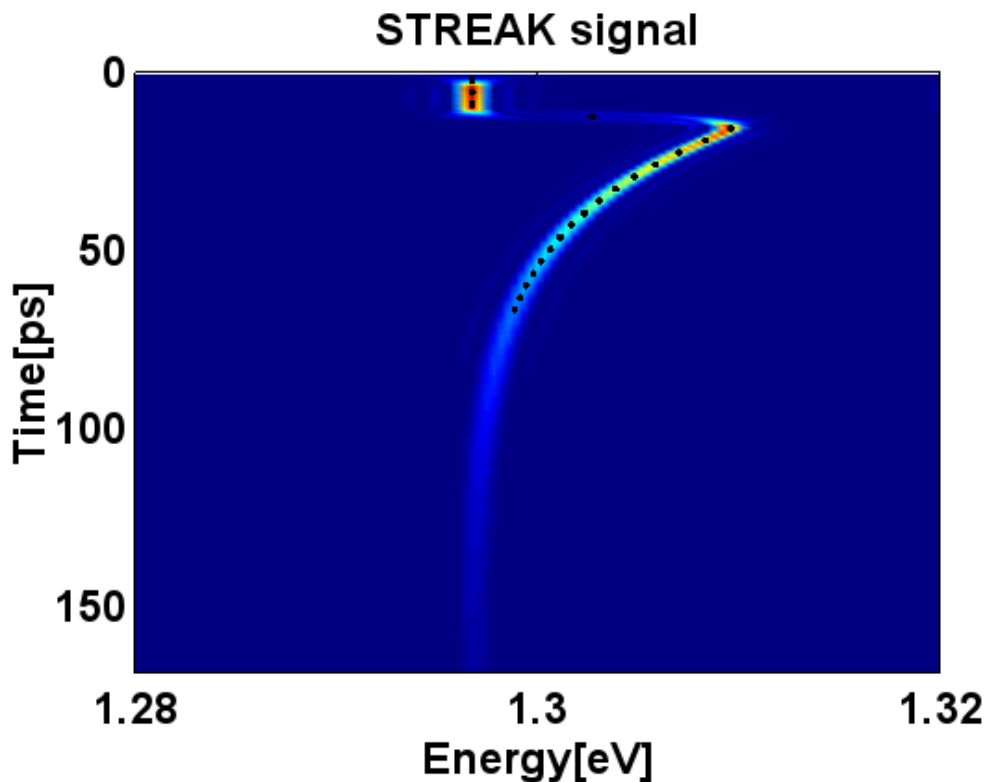


**Figure 3.10** FDTD simulation of converting the color of light stored in a planar cavity by all-optical injection of free carriers. The blue points show the resonance position of the cavity calculated by the TMM method for a defined distribution of free carriers. The agreement between the emitted light and the mode position indicates an adiabatic switching behaviour.

### 3.3.1 The color change experiment on a short time scale

The CW laser is tuned to the resonance of the cavity at 1.3278 eV in order to feed the cavity mode. The pulsed laser wavelength is shifted to 795 nm in order to be above the band gap and to inject a sufficient quantity of free carriers into the cavity.

It is important to record a streak measurement of the pump laser pulse in order to control its duration at the modified wavelength. Its duration must not exceed the duration of the pulse of the ring down measurement in order to avoid the emission of a large part of the stored electromagnetic field of the cavity before reaching the largest shift amplitude.

A streak camera image of the pump pulse is shown on Figure 3.11(a). Compared to the pulse used for the ring-down experiment, the pump pulse is spectrally narrower. This is due to the modification of the cavity of the Ti:Sa laser which is required for tuning to lower wavelengths. This results in the emission of otherwise shaped pulses.

Fitting the temporal profile of the streak image with a Gaussian curve reveals a FWHM of 2.22 ps. This means that the pulse is shorter than the storage time of the cavity and sufficiently short to perform color change experiments.

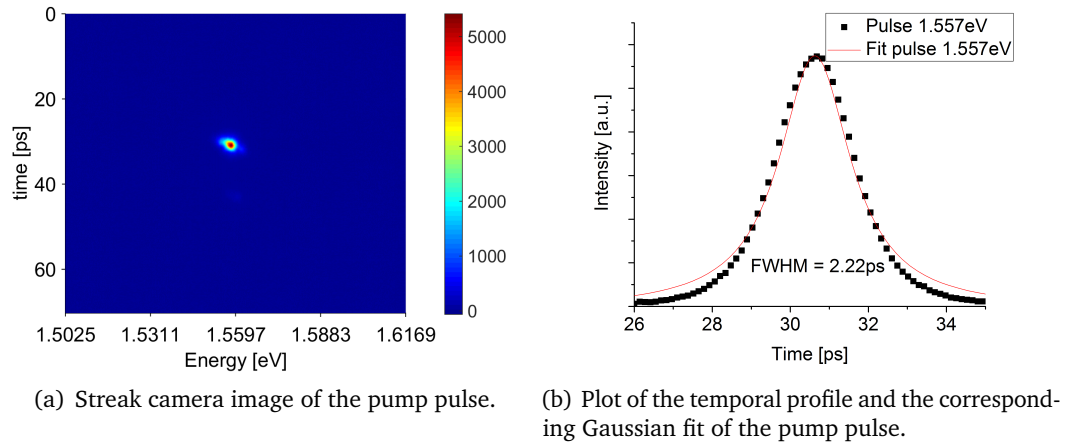


**Figure 3.11** Measurement of the length of the pump pulses.

Despite the high power of 110 mW of the pump laser, a small spectral shift of the cavity mode is expected because of a weak focalization by the lens. In order to ensure an observation of the color change, we use a monochromator grating with 1200 lines/mm.

The laser beams impinge exactly at the same spot on the sample as probed before. Above-bandgap-excitation heats up the sample. This creates a redshift of 4.2 meV which is measured by comparing the mode position of the ring down experiment (Figure 3.8) to the mode position before the switch ( $t = 0-20$  ps on Figure 3.12). This is an effect of an increasing refractive index due to higher temperatures. After absorption of several pump pulses, the sample is in a steady state where the input heating (laser pulses) is equal to the evacuated heat. By comparing the different resonance wavelengths, we can conclude on the temperature of the sample at the steady state:  $\Delta T = 32$  K

The result of the color change experiment is illustrated on Figure 3.12. For the color change experiment, the CW laser is tuned in resonance with the cavity mode at its modified frequency due to heating of the material but before the actual switch. During this time (from  $t = 0$  ps to  $t = 20$  ps), a strong CW laser signal can be observed. In this timerange, the CW laser is in resonance with the cavity, hence, it is transmitted.

At  $t = 20$  ps, two observations can be made:

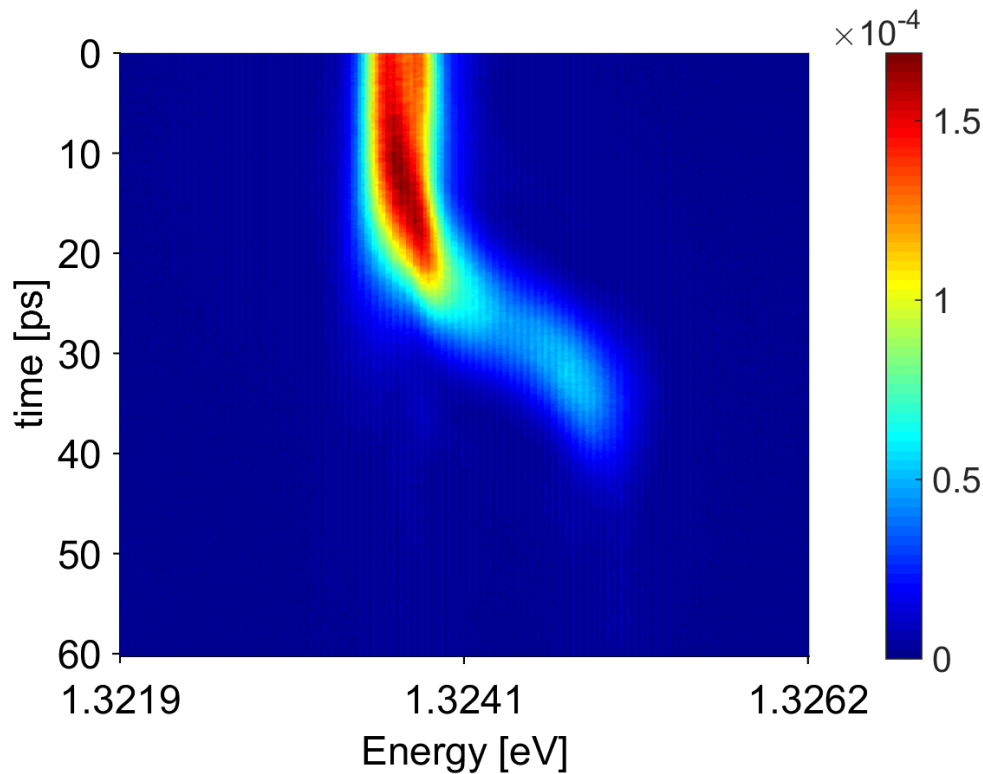


**Figure 3.12** Streak camera image a color change. At  $t = 20$  ps, a clear color shift into the blue of 1.5 meV can be observed. After 20 ps, the switched signal decreases and only a slight transmitted contribution of the CW laser which indicates its spectral position is still visible.

1) The signal exhibits a blueshift of 1.5 meV. Setting this into relation to the quality factor of the cavity which was measured before, it can be claimed that we observe a resonance shift as large as 17 linewidths.

2) The signal is getting weaker during  $\approx 20$  ps until it disappears.

From this streak camera image, several conclusions, which are discussed now, can be drawn.

**Heating of the sample** During the color change experiments, the sample was excited with a repetition rate of 76 MHz and a power of 110 mW at 795 nm. This means that each pulse contains an energy of 1.45 nJ. The pulse energy is 1.56 eV which is 0.14 eV above the bandgap of GaAs at room temperature.

Now, the heating of the sample depends on the ratio between radiative and non-radiative decay of the injected free carriers.

In the case of 100 % radiative decay, only this 0.14 eV extra energy per photon contributes to the heating.

By contrast, in the worst case scenario corresponding to 100 % non-radiative decay, the whole photon energy is used for heating up the sample. With a spot radius of 5  $\mu\text{m}$  (the intensity distribution is assumed to be constant) and a depth of 5.5  $\mu\text{m}$ , we obtain an upper limit for the heating of the sample of 1.94 K per pulse ( $\rho_{\text{GaAs}} = 5.315 \frac{\text{g}}{\text{cm}^3}$ ,  $c_{\text{GaAs}} = 0.325 \frac{\text{J}}{\text{g}\cdot\text{K}}$ ).<sup>1</sup>

Such a heating per pulse is not realistic, because the sample would be vaporized in less than one second. Dissipation of heat also takes place in the sample.

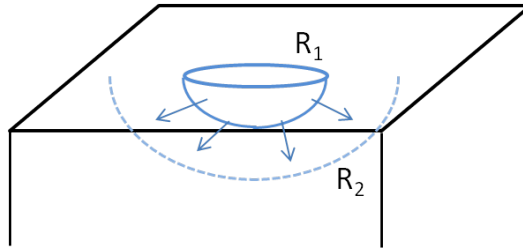


**Figure 3.13** Schematic description of the evacuation of the heat created by the laser spot (approximated by the circle with radius  $R_1$ ).

The principle of heat dissipation is depicted on Figure 3.13: The laser spot with a radius  $R_1$  impinges on the sample with a power of  $P$ . We consider thus the “heated spot” as a half sphere with radius  $R_1$ . Due to the big extension of the sample, we consider the heat transfer taking place to  $R_2 = \infty$ .

Fourier’s law states that the heat conduction without an internal source is given by

$$\frac{\partial T}{\partial t} = \alpha \Delta T \quad (3.11)$$

where  $\alpha$  is the thermal diffusivity and  $\Delta$  the Laplace operator.

In spherical coordinates, Equation 3.11 writes (assuming  $\partial_\varphi T = \partial_\theta T = 0$ )

$$\frac{\partial T}{\partial t} = \alpha \left( \frac{\partial^2 T}{\partial r^2} + \frac{2}{r} \frac{\partial T}{\partial r} \right) \quad (3.12)$$

We now use the Ansatz  $F(\vec{r}) = rT(\vec{r})$  and consider the system being in a stationary state  $\frac{\partial T}{\partial t} = 0$ .

<sup>1</sup>taken from Freiberger: Compound Materials

This leads to

$$\frac{\partial^2 F(\vec{r})}{\partial r^2} = 0 \quad (3.13)$$

which can be solved with the Ansatz  $F(\vec{r}) = A + Br$ . We define  $T_1 = \frac{A}{R_1} + B$  and  $T_2 = \frac{A}{R_2} + B$ .

By assuming  $R_2 = \infty$ , we can write  $T_2 = B$  and  $\Delta T = T_1 - T_2 = \frac{A}{R_1}$ .

The flux of heat (or also the dissipated power  $P$ ) can be written as

$$P(r = R_1) = -S\alpha \frac{\partial T(r = R_1)}{\partial r} = -2\pi R_1^2 \alpha \left(-\frac{A}{R_1^2}\right) \quad (3.14)$$

where  $S$  is the surface of the heat spot. By putting  $\Delta T = \frac{A}{R_1}$  into Equation 3.14, we obtain the following relation for the temperature difference:

$$\Delta T = \frac{P}{2\pi R_1 \alpha} \quad (3.15)$$

We assume an impinging power  $P = 72$  mW (35% of the incident power is reflected at the GaAs-air interface) and  $\alpha_{\text{GaAs}} = 55 \frac{\text{W}}{\text{m}\cdot\text{K}}$  [10] and  $\alpha_{\text{AlAs}} = 91 \frac{\text{W}}{\text{m}\cdot\text{K}}$  [6]. The contribution of the interface to the air can be neglected because of  $\alpha_{\text{air}} = 0.045 \frac{\text{W}}{\text{m}\cdot\text{K}}$ .

Averaging over  $\alpha_{\text{GaAs}}$  and  $\alpha_{\text{AlAs}}$  we obtain  $\Delta T = 62$  K for  $R_1 = 2.5 \mu\text{m}$ . This value, which has been obtained assuming fully non-radiative recombination, constitutes an upper bound for the temperature rise in our sample.

For determining the actual steady state temperature we compare the resonance energy just before the switch ( $E_1 = 1.3236$  eV) to the resonance measured during the ring-down experiment ( $E_2 = 1.3278$  eV).

The resonance condition

$$L_{\text{cav}} = 27 \frac{\lambda_1}{n_1} = 27 \frac{\lambda_2}{n_2} = \text{const.} \quad (3.16)$$

can be written as

$$E_1 \cdot n_1 = E_2 \cdot n_2 \quad (3.17)$$

Following an approach described in [32] for calculating the refractive index of GaAs, the shift of  $\Delta n = 0.0103$  corresponds to a 32 K warmer sample. This lower value could result from a high percentage of radiative recombination taking place because of the large concentration of free carriers after the pulse.

**Proof for the observation of a color change** From this streak image, we can conclude if we really observe a color change of stored light or if the signal results from other sources.

Firstly, the assumption could be made that despite the small bandwidth of the CW laser, we observe intensities stemming from this laser. The observed high energy signal would thus be a side band of the CW which is transmitted through the cavity.

There is one reason against this assumption: The spectrum of the CW laser clearly shows that the laser linewidth is too small to give a contribution to the shifted cavity. Despite not being able to determine the linewidth of the **switched** cavity (at the moment of its maximal blueshift), we know that the cavity returns to its steady state (due to  $\Delta T$ ) position 13.6 ns (duration corresponds to the repetition rate of 76 MHz of the pump laser) after the decay of the free carriers. In that case, it should be possible to observe the "assumed" broad CW laser following this resonance. In our case, the signal disappears. This is a clear sign that there is no contribution of the laser.

The pulsed pump-laser can also be excluded as a source for the signal, because it is filtered by a 830 nm-lowpass-filter and the monochromator grating.

Hence, we observe indeed a color change of light which was stored in a cavity.

**The dynamics of the color change** In order to properly observe the dynamics of the color change, we have a closer look in Figure 3.14 at the moment where the shift appears. A non-instantaneous color change is observed. Visibly, it takes 10 ps until the color of the photons is shifted by 1.5 meV. This delay seems nevertheless sensible because literature reports of a time span of  $\approx 5$  ps between the injection of free carriers and the full completion of the switch [46]. We also have to take into account the limited time resolution of the streak camera with the 1200 lines/mm grating which smoothes the actual switching time. This could explain the larger shift time.

In order to better conclude on the switching dynamics of our planar cavity, we perform further analysis of the streak image.

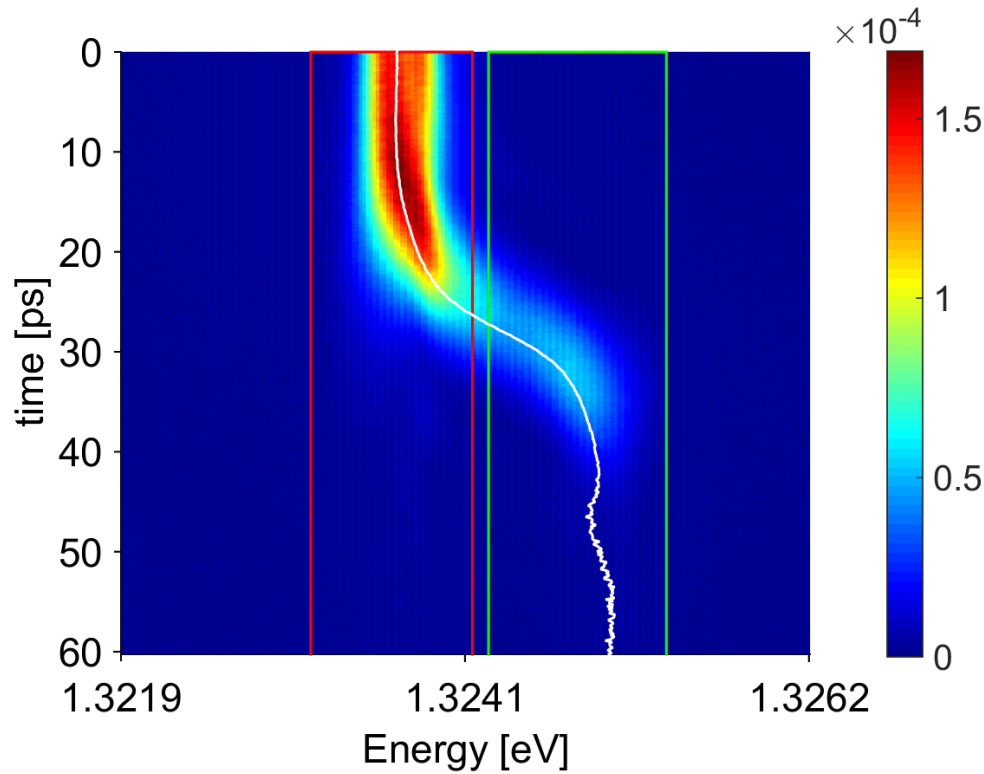


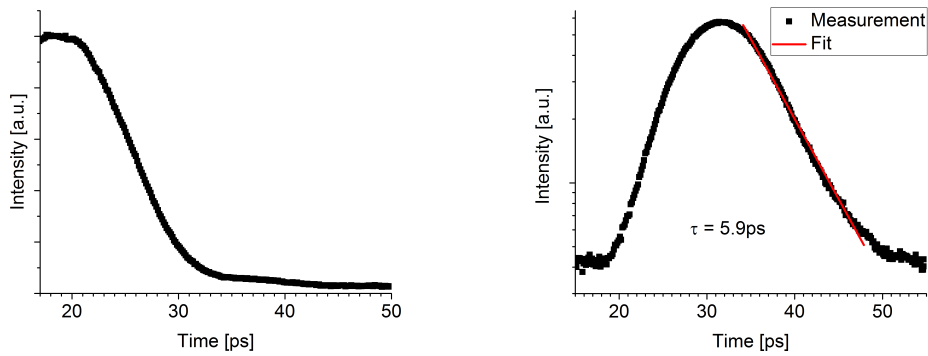
**Figure 3.14** Spectrograph of the color change in the highest temporal resolution ( $\approx 11$  ps). The white line indicates the position of the intensity maximum fitted by a Lorentzian. The red and green frame show the positions of the cut showed on Figure 3.15.

Cross sections along the time axis are taken (for indications on their localization see red and green frame on Figure 3.14) and their profiles are sketched on Figure 3.15.

On the cross cut taken around the initial frequency  $\omega_1$  (see Figure 3.15(a)), we observe a decay which starts at  $t = 22$  ps. The decay behaviour corresponds to the transmission of the CW through the cavity mode which is shifted into the blue at  $t = 20$  ps. That is why the laser transmission decreases and then drops to a low value.

It signifies that we observe blocking of the CW laser by the cavity, since no more transmission of the light is observed. It can thus be concluded that the number of photons which are coupled by the CW laser into the cavity decreases between  $t = 20$  ps and  $t = 30$  ps and becomes negligible then. It also enables us to conclude about the time that the free carriers need to relax before contributing to the switch. A time span of  $\approx 8$  ps corresponds well to the value given by Harding et al. [46].

From a cross cut at  $\omega_2$  we can conclude on the quality factor of the switched cavity. Indeed, once the cavity mode has reached its maximum value, photons which are



(a) Cross cut taken in temporal direction at the initial frequency  $\omega_1$ . (b) Logarithmic plot of the temporal profile at  $\omega_2$ . The curve is fitted with an exponential fit;  $\tau_{sw} = 5.9$  ps is derived.

**Figure 3.15** Temporal profiles of the STREAK camera image shown on Figure 3.14

shifted to  $\omega_2$  and confined in the cavity, leak out of it. In analogy to the ringdown experiment (described in subsection 3.2.3) we can now determine the storage time of the switched cavity. Figure 3.15(b) depicts a cross section taken at  $\omega_2$ . By fitting the decay with an exponential curve, we obtain a result of 5.9 ps. This value is reasonably close to the storage time of the unswitched cavity, measured in the ring down experiment (7.5 ps).

The lower storage time could be a result of photon absorption by free carriers which exist in great quantities in the cavity and/or degradation of the quality factor by non-symmetric switching of the GaAs parts of the top- and bottom-mirror.

### 3.3.2 Longterm behaviour of the planar cavity

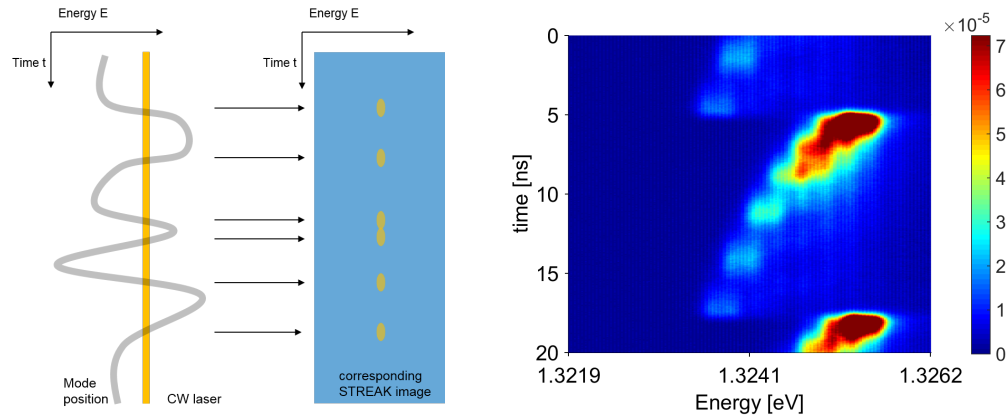
After having investigated the color change, it is now interesting to know how exactly the cavity behaves on the nanosecond timescale.

In the previous section, the CW laser was kept at  $\omega_1$ . Obviously, this works very well for observing the color change, but due to the storage time of few picoseconds, we cannot conclude on the longterm behaviour of the planar cavity.

However, it is possible to conclude with the used experimental setup on the position of the mode during the timespan between two pump pulses (13.6 ns). With a so-called pump-probe experiment, it is possible to track the spectral position of the mode at any given time.

This experiment makes use of two laser beams. The pulsed laser beam pumps the cavity (pump-beam) and triggers an ultrafast shift of the mode. The other beam, which is a CW laser in our case, (in many other experiments also a pulsed laser synchronized to the pump laser) is used to probe the spectral position of the cavity.

In the case of the planar cavity, photons only cross the sample and are detected if their energy corresponds to one of the resonances of the cavity. Otherwise, photons are reflected and not detected (see Figure 3.16(a)).



(a) Sketch of the basic idea of a pump-probe experiment with a planar cavity. Only light which is on resonance with the planar cavity is able to cross it and to be detected by the streak camera. By tuning the CW laser spectrally, it is possible to derive the mode position over a large spectral range.

(b) Superposition of several streak images taken with the pump-probe configuration. The cavity dynamics is spectrally revealed on a longer timerange. The periodic behaviour results of the fact that every 13.6 ns, a new pulse switches the cavity.

**Figure 3.16** Principle of a pump-probe measurement.

By performing a single pump-probe measurement, we can detect at which time  $t$  the cavity resonance is at a given frequency  $\omega$ . To obtain a complete spectral and temporal resolution of the resonances, it is necessary to cover a broad frequency range. This can be achieved by scanning the CW laser by sufficiently fine steps over the spectral interval of interest. Consequently, the experiment provides information over the mode position at any given time; the whole cavity dynamics can be studied. We visualize this by superposing the different datasets which have been obtained from pump probe experiments. Figure 3.16(b) shows the outcome of the study.

The mode positions correspond quite well to the results that we have obtained with the color change configuration. Note that the pulsed laser has a repetition rate of 76 MHz which corresponds to a replication of switching every 13.6 ns.

At the end of each period, ( $t = 4.5$  ns,  $t = 18$  ns) the cavity is at its initial energy  $E = 1.3236$  eV. This corresponds to the observations made in the color change configuration. At these moments, when the pulsed laser arrives, the cavity experiences a blueshift. The translation of the mode is 1.7 meV. After this event, the resonance returns exponentially to its initial energy.

This image provides us with a surprising information. In contrast to the measurement on the lifetime of the free carriers, (see Figure 3.9) where a lifetime of electron hole pairs  $\tau_{e,h} = 371 \pm 2$  ps was measured, we observe a much slower return time of the mode to its initial position. We deduce from the measurement a decay time of  $7.97 \pm 0.12$  ns.

This drastically higher value could be a result of different experimental conditions. The lifetime measurement was performed with a much lower excitation wavelength. This leads to a free carrier distribution which is very dense and only localized in the upper GaAs layers of the top Bragg stack. Because of the proximity to surfaces and interfaces, the recombination could be accelerated compared to recombination in bulk material.

We see that the decay time (7.97 ns) is of the same order of magnitude than the repetition rate (13.6 ns). Therefore, it is expected that some electron-hole pairs are already present before the switching pulse. A consequence of this observation is that the actual temperature of the substrate might be higher than 332 K. Indeed, this background density of electron-hole pairs slightly shifts the resonance frequency of the cavity to higher energies and compensates a part of the redshift created by the heating of the sample.

### 3.3.3 Conversion efficiency

For further applications, it is important to obtain information about the conversion efficiency of our process. Especially, when using the system for up-conversion of single photons, the conversion efficiency is a figure of merit which is crucial for practical applications.

We define the conversion efficiency  $\eta$  as the ratio between the energy of the stored light  $E_{\text{stored}}$  (at  $\omega_1$ ) and the energy of the color-converted pulse  $E_{\text{conv}}$  (at  $\omega_2$ ).

$$\eta = \frac{E_{\text{conv}}}{E_{\text{stored}}} \quad (3.18)$$

### Estimating the conversion efficiency of a planar cavity

To be able to estimate  $\eta$ , it is crucial to understand the processes which take place in a planar cavity. Therefore, FDTD simulations are performed. In view of the comparison with experiments, we simulate streak camera images. Such images are calculated using a 12 ps long sliding Hamming-window, on which a Fourier transformation was performed. The duration of the window was chosen in order to obtain a similar temporal resolution as in the experiments.

We start by simulating an easy example: a CW laser is switched on at  $t = 0$  and starts to impinge on the cavity which has similar parameters as our cavity (symmetric reflectivities of both Bragg mirrors) apart from a longer storage time  $\tau_{\text{cav}} = 13.3$  ps. The higher storage time in the simulation allows a more precise conclusion on the switching efficiency. The top-mirror of the planar cavity is oriented towards the laser source as in the experiment.

At  $t = 120$  ps, the CW laser is switched off. The corresponding streak camera image is shown on Figure 3.18(a).

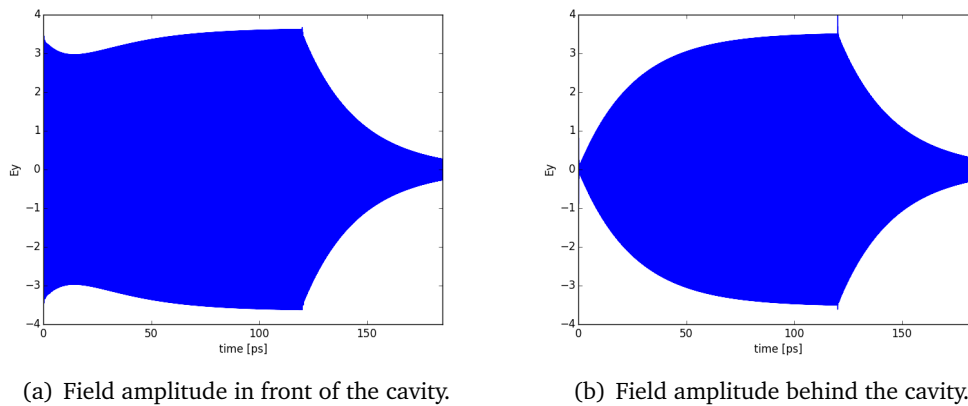


**Figure 3.17** Field amplitudes calculated with a one-dimensional FDTD simulation for both sides of the cavity. A CW laser is switched on at  $t = 0$  and switched off at  $t = 120$  ps and the resulting field amplitudes are estimated. The peaks at  $t = 120$  ps are artefacts of the simulation due to the abrupt switch-off of the CW laser.

Figure 3.17(b) shows the field at the bottom surface of the planar cavity. We observe an asymptotic rise of the intensity; the cavity is loaded and approaches a stationary state where light injection and light escape perfectly compensate each other. At  $t = 120$  ps, the CW laser is switched off and no more photons are fed into the cavity. The electromagnetic energy which is stored in the cavity decays exponentially with the characteristic time  $\tau_{\text{cav}}$ .

In front of the planar cavity (cf. Figure 3.17(a)) we observe a different behaviour for  $0 < t < 120$  ps. The intensity at  $t < 120$  ps is a result of the superposition of reflected light (the cavity is not yet completely loaded) and the incoming CW laser. The light of the CW laser interferes with the light which is reflected/reemitted on this side of the cavity. Because of interferences, no light is reflected on this side once the cavity is in the steady state, i.e. completely loaded. Therefore, only the field of the incoming CW laser can be observed at this point. The amplitude of the incoming CW laser is similar to the amplitude on the output side of the cavity as expected for the steady-state regime.

In the steady state the top mirror behaves effectively as a perfectly reflecting mirror for the light which is stored in the cavity mode.

For reflectivities close to unity, Equation 3.6 can be approximated in combination with Equation 3.7 as

$$Q = m \cdot \frac{2\pi}{2 - R_b - R_t} \quad (3.19)$$

Assuming  $R_b = R_t$  for a non-loaded cavity, we can conclude that the storage time of light doubles if, and only if, the cavity is in a steady state and constantly pumped by a CW laser (since then  $R_t = 1$ ).

For  $t > 120$  ps, the CW laser is switched off and no more interference takes place at the top mirror. The stored light energy decays exponentially with  $\tau_{\text{cav}}$ . The same field intensity and decay behaviour as on the exit side of the cavity is detected.

From this simulation, we learn that after the conversion, the photon population stored in the cavity experiences an exponential decay. Due to the symmetric structure of the cavity (see subsection 3.2.1), light outcoupling will be equally distributed on both sides of the cavity. As a consequence of the position of the streak camera on one side, our experimental setup only detects 50% of the converted light:  $E_{\text{conv}} = 2 \cdot E_{\text{detected}}$ .

$E_{\text{stored}}$  can be defined by assuming that the cavity is in an equilibrium state before the switch: the CW laser loads the cavity with the same number of photons as it reemits because of its decay. Since  $R_t = 1$  under steady state CW laser pumping, we have to double  $\tau_{\text{cav}}$  in this regime.

$$\frac{dE_{\text{stored}}}{dt} = g - \frac{E_{\text{stored}}}{2\tau_{\text{cav}}} = 0 \quad (3.20)$$

$g$  is the flux of incoming photons. We thus deduce  $E_{\text{stored}} = 2g \cdot \tau_{\text{cav}}$  in the case of a steady state pumping.

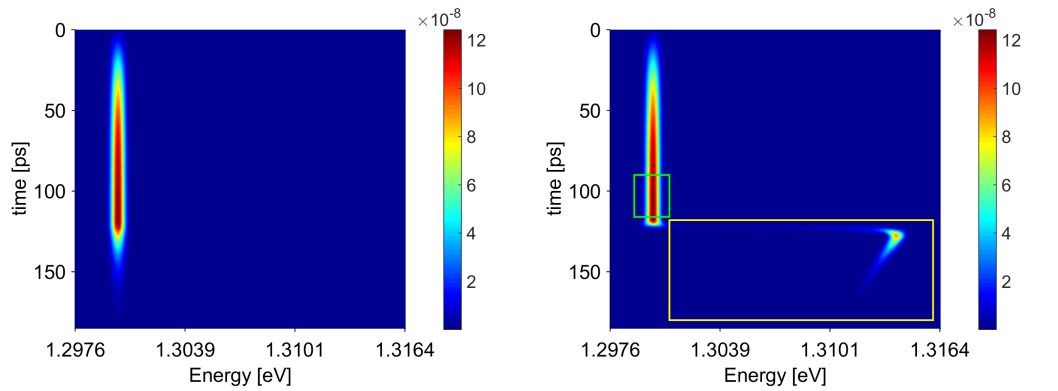
This leads to the final expression for  $\eta$ :

$$\eta = \frac{E_{\text{detected}}}{g \cdot \tau_{\text{cav}}} \quad (3.21)$$

Interestingly, all quantities which appear in Equation 3.21 can be deduced experimentally from measurements using the streak camera.  $\tau_{\text{cav}}$  is deduced from a ring-down experiment while  $g$  and  $E_{\text{detected}}$  are obtained from the switching experiment performed on the cavity, which is charged using CW pumping.

### Conversion efficiency estimation using FDTD simulations

We now apply this analysis method to a FDTD simulation of the switching of a loaded cavity.



(a) Ring-down experiment with a CW laser which is switched off at  $t = 120$  ps. (b) Color change experiment with a CW laser and a free-carrier switch taking place at  $t = 120$  ps.

**Figure 3.18** Simulated streak camera images of experiments with planar cavities.

Figure 3.18(a) shows a streak camera image of a FDTD simulation of a planar cavity with an impinging CW laser which is switched off at  $t = 120$  ps. It corresponds to the case of Figure 3.17. We deduce from this ring-down experiment a storage time  $\tau_{\text{cav}} = 13.3$  ps.

For the simulated case shown on Figure 3.18(b) the CW laser is not switched off. At  $t = 120$  ps, the cavity is shifted by 15 meV within 4 ps. This mimics some kind of ideal switching experiment: a cavity with a high quality factor is switched over a fairly large spectral range, within few ps.

This simulation allows us to validate the developed approach for the case of a switched cavity.  $E_{\text{detected}}$  is estimated by integrating over the whole space of the converted light (in order to cover the whole emission of the converted photons, we extend the yellow frame to a larger temporal range), whereas  $E_{\text{stored}}$  is obtained by integrating the intensity before the switch during  $\tau_{\text{cav}}$ . On Figure 3.18(b), these quantities are indicated by the yellow ( $E_{\text{detected}}$ ) and green ( $E_{\text{stored}}$ ) frames. We obtain  $\eta = 1$  and conclude that FDTD predicts a perfectly efficient conversion of the stored light from frequency  $\omega_1$  towards frequency  $\omega_2$ . Let us note that our FDTD simulations do not include at this stage absorption losses, due to free carriers for instance. Nevertheless, this study validates the approach, which we propose, to estimate  $\eta$  from combined time-resolved experiments using the streak camera.

### FDTD-simulation of the experiment

We now simulate a color change with more realistic parameters which we have deduced from our experiment: shift of 1.5 meV, storage time  $\tau = 7.5$  ps, recombination time of the cavity: 7.97 ns,  $Q = 15000$ , switching time 4 ps.

The result of the simulation is shown on Figure 3.19.

We know from the previous simulations that the conversion efficiency is 100 % when absorption losses are neglected. The present simulation should also lead to  $\eta = 1$ . Since the Hamming window smoothes the actual switch of the cavity mode both spectrally and temporally, it is difficult to know exactly where to place the yellow frame.

Because the switching time is comparable to the cavity storage time, Figure 3.19 is qualitatively different from Figure 3.10. Indeed, a significant peak of the stored light is released during the switch. To estimate accurately the total conversion efficiency, our yellow frame must include the full frequency range that is swept during the switch. This choice induces however a potential problem, since some light fed into the cavity after the switch could provide additional signal in our yellow frame. It is important to estimate this spurious contribution. For that, we first determine the spectral position of the cavity during the switch. We assume a constant switching speed. With the used parameters, the cavity shifts with a speed of 0.375 meV/ps. Since  $\Delta\omega_{\text{cav}} = 0.08$  meV, we know that few hundreds of femtoseconds after the switch, no more laser light is coupled into the cavity mode. Therefore, we see that injection of CW laser light after the switch can be neglected. Nearly all photons which exit the cavity after the start of the switch have actually been loaded into the cavity before the switch.

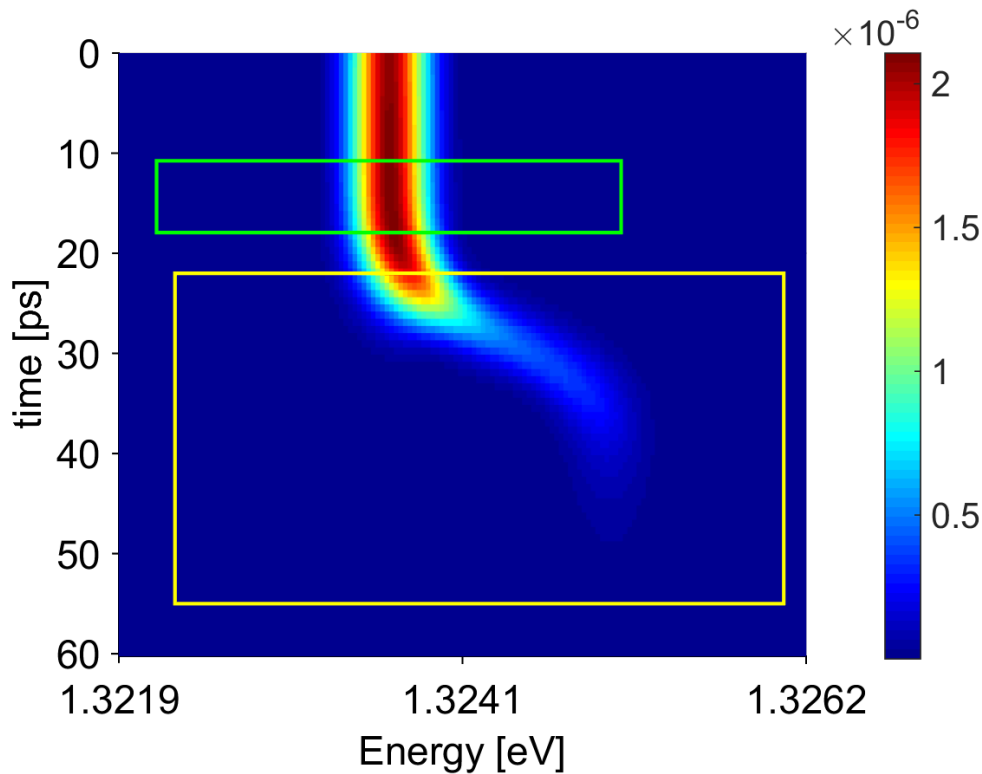


**Figure 3.19** FDTD simulation of a frequency conversion in a planar cavity performed with the same parameters as the experiment. A very similar behaviour as in the experiment is observed. The color frames show the integration areas for calculating the efficiency.

Because of the smoothing by Hamming windows, it is not obvious to define in Figure 3.20 the onset of the switch. Knowing that 100 % conversion efficiency is expected, we adjust finely the vertical position of the yellow frame in order to obtain 100 % efficiency in our numerical experiment. We are going to use now the same frame position to analyse our experiment.

### Estimate of the conversion efficiency in our experiment

The streak camera image used for the estimation is shown on Figure 3.20.

From this integration, we obtain a value of  $\eta = 1.3$  which seems unrealistic at first sight.

Several factors can explain this result:

- There could be a deviation of the storage time: It is possible that the laser spot slightly moved after the ring-down experiment. Its high sensitivity to lateral positioning on the sample could entail small variations of  $Q$  from one experiment to the other. Furthermore, we have estimated an uncertainty

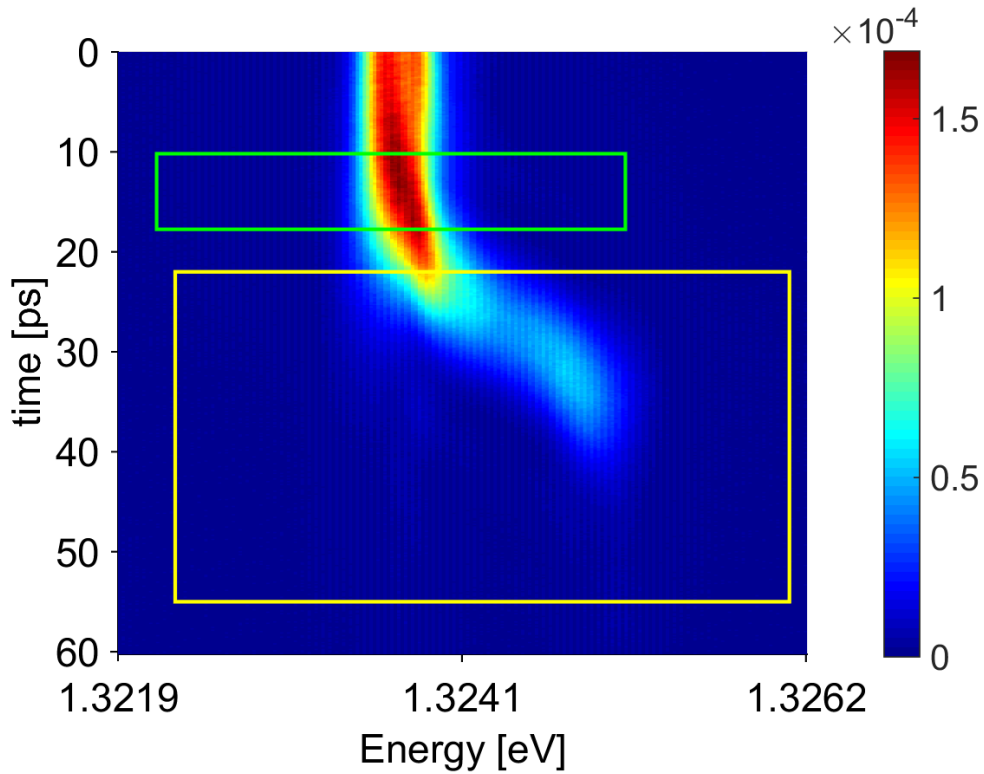


**Figure 3.20** Normalized spectrograph of the color change in the highest temporal resolution. The integrals of the green and yellow frame are used for the efficiency calculations.

around  $\pm 1.5$  ps for the ring-down experiment. Applied to the experiment, we obtain  $\eta = 1.3 \pm 0.25$ .

- In the simulation, the frequency of the CW laser matches the resonance of the cavity exactly. In the experiment, it is in fact possible that this is not the case. If the laser frequency has a slight offset to higher energies, the cavity mode goes on being fed after the start of the switch. This could increase  $E_{\text{detected}}$  and would have an impact on  $\eta$ .

However, even taking into account these sources of uncertainty, we obtain a conversion efficiency close to unity. This is a significantly higher efficiency than the 34 % reported by Lipson et al. [85] (conversion of a pulsed laser) and similar to the 80 % reported by Tanabe et al. [110] Our result indicates that perfectly efficient frequency conversion can be achieved using cavity switching, provided that the used cavity ensures an efficient collection of the frequency-converted light.

### 3.3.4 Adiabaticity of the color change and comparison to simulations

In this subsection, we have a closer look at the question whether our process is adiabatic or not. As described in subsection 3.1.1, the adiabaticity of the color change is a criterion that is crucial for many other applications. To conclude on this question, we look at three criteria:

- 1) Does the light follow the resonator mode during the switch?
- 2) Is the conversion efficiency close to 100 %?
- 3) Do simulations of our experiment show adiabatic behaviour?

The first criterion can be examined by comparing the amplitude of the shift from Figure 3.14 to the mode amplitude obtained by the pump-probe experiment (Figure 3.16)(b). On Figure 3.14 the maximum deflection of the light is at  $1.3252 \pm 0.0001$  eV. The pump-probe experiment measures a value of  $1.3253 \pm 0.0001$  eV. The difference between the two measured values is thus 0.1 meV. Compared to the switch amplitude of 1.6 meV, this is a deviation of 6 %. It could also result from variation of the setup, like differences in the power output of the Ti:Sa laser. This lowers the pump power and triggers a smaller switch. From this, we conclude that the first condition is fulfilled.

In the previous section, we already calculated the switching efficiency. A value  $\eta$  close to unity was obtained. The second criterion can thus also be considered as fulfilled.

We also compare the obtained results to a FDTD simulation which relies on the parameters which we extracted from the experimental data (characteristic switch-on time: 4 ps, recombination time of the cavity: 7.97 ns,  $Q = 15000$ ).

The result of the simulation is shown on Figure 3.19. The simulated behaviour agrees well with the experimental result. Since FDTD calculations have confirmed an adiabatic behaviour (cf. Figure 3.10), this agreement reflects adiabaticity in our experiment.

### 3.3.5 Perspectives for color change using cavity switching

Despite the respectable results that have been obtained in the frame of this PhD thesis, there is still a lot of potential for further improvements left.

Having the same experimental configuration, it would be interesting to observe the switch with a pump laser with a pulse duration of several hundred femtoseconds. This would accelerate the switch and give a clearer image on the relaxation dynamics of free carriers in a planar cavity. However, in terms of experimental handling, this is more challenging because either a chirp compensation of the pump laser, or working without optical fiber would be required.

One step further would be the use of a pulsed laser as probe laser. This requires a synchronization of the two laser sources in order to tune the temporal delay. Obtaining an efficient conversion of laser pulses is obviously an appealing issue. This is not straightforward, because the pulse has first to be coupled into the cavity. Simulations show that it is necessary to equal the probe laser pulse duration and the storage time of the cavity [82]. Furthermore, it is crucial that free carriers are injected at the moment when the stored field of the probe laser in the cavity is maximal. This ensures that a maximum of stored light is converted.

Lipson et al. reported of a conversion efficiency of 34% for this kind of experimental configuration. Theoretical calculations on planar cavities [82] have been performed by E. Peinke for a planar cavity with  $Q_m = 65000$ ,  $\tau_{\text{storage}} = t_{\text{FWHM laser}} = 33$  ps and  $E_1 = 1.3$  eV and using a probe pulse with Gaussian shape:

48% of the input pulse are reflected at the cavity-air interface. 10.5% of the light are already emitted (transmitted) by the cavity before the switch during the time duration needed to load the cavity. 16.5% of the probe pulse arrive after the switch and are also reflected.

25% of the light is therefore converted to  $E_2$ . Half of the converted light is then transmitted and the other half reflected. Figure 3.21(a) shows the simulated streak camera image of the FDTD simulation and Figure 3.21(b) the distribution of light.

However, one should emphasize that 100% of the light stored in the cavity is converted. The losses result from three sources: cavity properties (48% of the light is reflected before even entering the cavity), the geometry of the cavity (emission of the converted light always in two different directions) and the pulse shape.

The first problem is a result of the high reflectivity of the cavity at non-resonant energies. It is not possible to entirely solve this problem, because a spectrally smaller pulse is longer. Longer pulses create a need for cavities with longer storage times and, hence, for smaller spectral widths and an increased reflection at off-resonant energies.

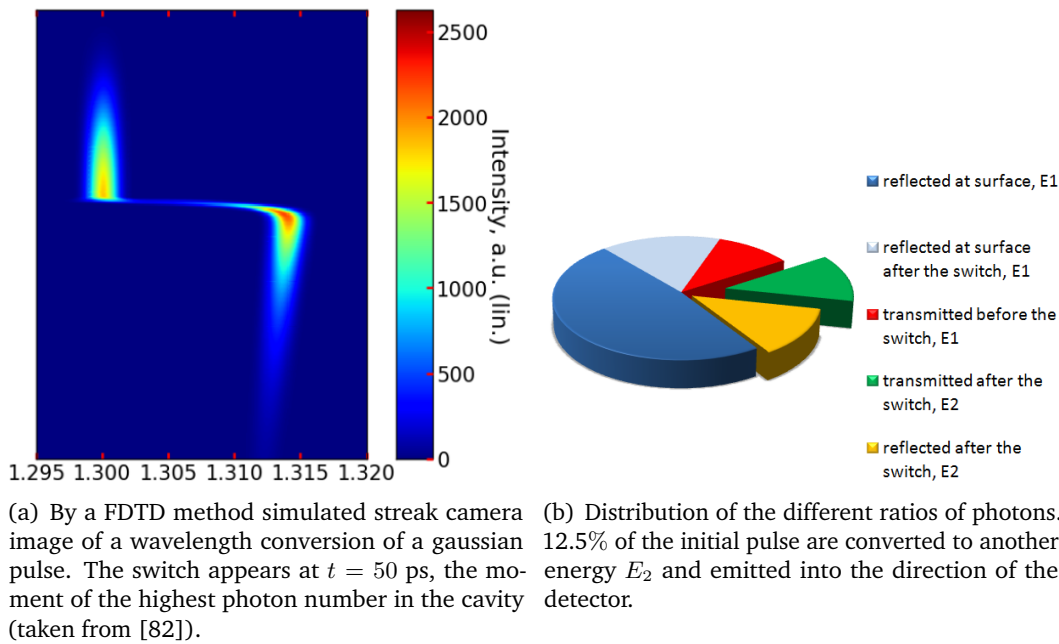


**Figure 3.21** Measurement of the length of the pump pulses.

The second problem could be resolved by working in a reflection geometry. By using a cavity with a very unequal number of Bragg mirrors and thus a much higher reflectivity for the bottom stack than for the top stack. As a consequence, stored light would only be emitted in one direction and the detected intensity of the converted light would be increased by a factor two. The drawback of this idea is the more complicated detection of the converted light. Especially in the case of a pulsed laser which is spectrally broad, it is difficult to separate spectrally the probe laser from the converted light. However, this approach works for large switching amplitudes  $\Delta\omega \gg \Delta\omega_{FWHM}$ . In this case, the probe laser contribution could easily be filtered.

The third problem can be addressed through a shaping of the temporal envelope of the probe pulse. Ideally, an exponentially rising pulse with  $\tau$  identical to the decay time of the cavity should be used. Using a time reversal argument, we see that such a pulse enters perfectly inside the cavity. This increases the ratio of light coupled into the cavity to 100%. However, this solution is demanding because of the difficulty to modulate light on ultrashort timescales by pulse shaping.

Finally, it is also possible to improve the switching amplitude of the cavity. The basic idea is confining light within a much smaller volume. This reduces the required light intensities for switching drastically. A possible idea which is experimentally quite close to planar cavities is the use of micropillars. These three dimensional cavities confine light on small volumes and decrease the switching energy drastically [53,

60]. For micropillars with diameters around  $1 \mu\text{m}$ , pulse energies of approximately 1 pJ would be enough to obtain switching amplitudes of 20 meV.

A higher switching amplitude would be important to convert large amounts of light to other wavelengths. In the case of our experiment, we could show that the total conversion efficiency is close to unity. However, large parts of the frequency-converted light leaves the cavity with a very small frequency shift. In the case of this experiment, we deduce from Figure 3.22 that only 57 % of photons are shifted by more than 0.8 meV (9 linewidths of the cavity).

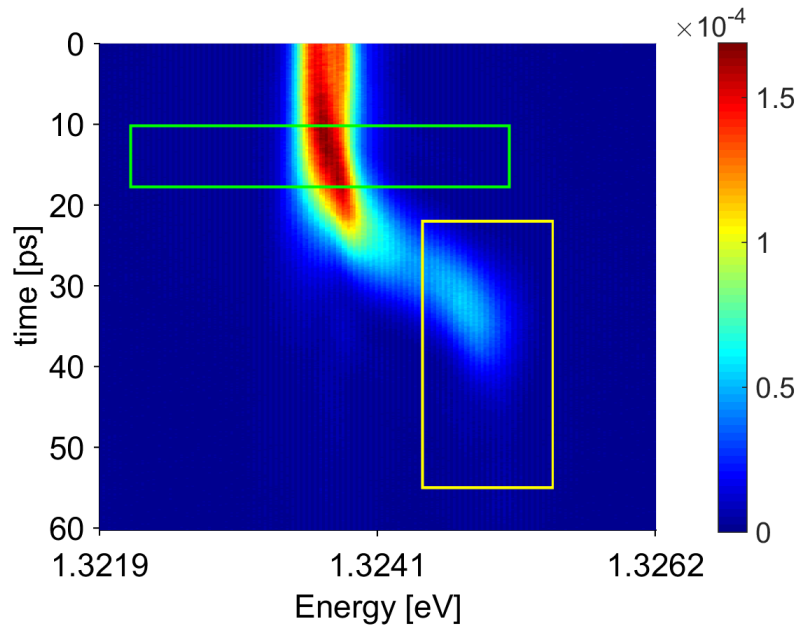


**Figure 3.22** Streak camera image of a color change experiments for determining an efficiency of 57 % for a frequency conversion over a range  $\geq 0.8$  meV.

The use of micropillars which enable a switching over a larger spectral range could lead to color conversion experiments similar to the simulated result shown on Figure 3.18(b).

## 3.4 Conclusion

In this chapter, we have presented results of a wavelength conversion experiment performed on a planar cavity with  $Q = 15000$  fabricated on the base of GaAs/AlAs-Bragg mirrors. By injecting free carriers into the material, it was possible to blueshift the resonator mode and the energy of the photons stored in the cavity by 1.5 meV at room temperature.

A new experimental approach which combines a ring-down experiment and a color change experiment with a CW laser was introduced for determining the efficiency of the conversion. The efficiency of our frequency conversion is close to 100%, in good agreement with the results of our FDTD simulations.

We have confirmed using combined TMM and FDTD simulations that one expects a perfectly adiabatic conversion process for our cavities which fulfill  $\tau_{\text{roundtrip}} \ll \tau_{\text{switch}} \ll \tau_{\text{cav}}$ . For our experiments, a good adiabaticity of the process was revealed by comparing simulations to the experimental values.

We have suggested possible improvements for achieving higher efficiencies and conversion amplitudes. Following these approaches, adiabatic color change in planar cavities is promising for future experiments on single photons, noticeably in the context of quantum engineering experiments.

## Differential mode switching in micropillar cavities

In this chapter, I describe the differential switching of micropillar modes on the picosecond timescale. The resonance frequencies of micropillar modes can be transiently changed on a picosecond timescale by all-optical injection of free carriers. By injecting an inhomogeneous distribution of free carriers, it is possible to exploit field distribution differences for obtaining mode-dependent switching behaviours. The spectral separation between modes changes during several tens of picoseconds before reestablishing a homogeneous distribution of free carriers. A real-time observation of this behaviour is possible by the use of an ensemble of QDs inserted in the micropillar.

In the first part of this chapter, a brief description of micropillar cavities which confine photons in all three dimensions is given as well as an overview over their modal structures. I furthermore describe how the spectral position of these modes can be probed on the picosecond timescale.

I describe our experimental approach which is based on an excitation of QDs by two consecutive laser pulses and subsequent analysis of the QD-micropillar photoluminescence by a streak camera.

Then, a section is dedicated to modelling of switching events in micropillars: it takes into account inhomogeneous free carrier injection, carrier diffusion and recombination. The model is used to calculate the free carriers distribution in a micropillar at different times with a FDTD simulation. Then, experimental results of differential switching, which have been achieved, are shown. At last, the obtained experimental data are analysed quantitatively by comparing them to results obtained by simulations.

## 4.1 Micropillar cavities - properties, modal structure and use of QDs as integrated probe

At the end of the 80ies, Jewell et al. proposed structuring planar cavities in order to confine light in all three dimensions. Firstly, this was done in the context of a use for ultrafast all-optical switches and for vertical-cavity surface-emitting lasers (VCSEL) [53].

Nowadays, micropillars are the backbone of many CQED applications and used in many research groups as promising devices for future use in quantum computing and communication (see chapter 1). The combination of micropillar cavities grown with III-V-materials (especially GaAs/AlAs systems) and InAs quantum dots (QDs) as emitter is for instance widely used to build high-efficiency single photon sources [69, 48, 103].

Enhanced spontaneous emission of an ensemble of QDs [36] or single QDs [69, 95] has been observed with these systems as well as strong emitter-cavity coupling [89].

Furthermore, micropillars are used as active components in micrometer scale systems. Electrical pumping of QDs implemented in high Q-micropillars has already been reported [12].

Generally, micropillars are defined from planar cavities using a highly anisotropic reactive ion etching (RIE) step which results in vertical sidewalls. For sake of convenience, for process and modelling, their cross section is often chosen as circular. Along the pillar axis, photons are confined by total internal reflection and guided like in a waveguide in this direction. Bragg reflectors on the top and the bottom of this waveguide confine the light vertically by reflection.

The spacer between the mirrors usually has a thickness of  $\frac{\lambda}{n}$ . A SEM image of such a micropillar is shown on Figure 4.1. In this case, the modal volume is kept at a low level and depends only on the radius of the micropillar. For the fundamental mode, it can be approximated by the product of the effective height ( $2\lambda/n$  for a spacer of thickness  $\lambda/n$ ) and the effective radius of a micropillar ( $\frac{r^2\pi}{4}$ ) [37]. This is important in view of applications in CQED experiments and microlasers.

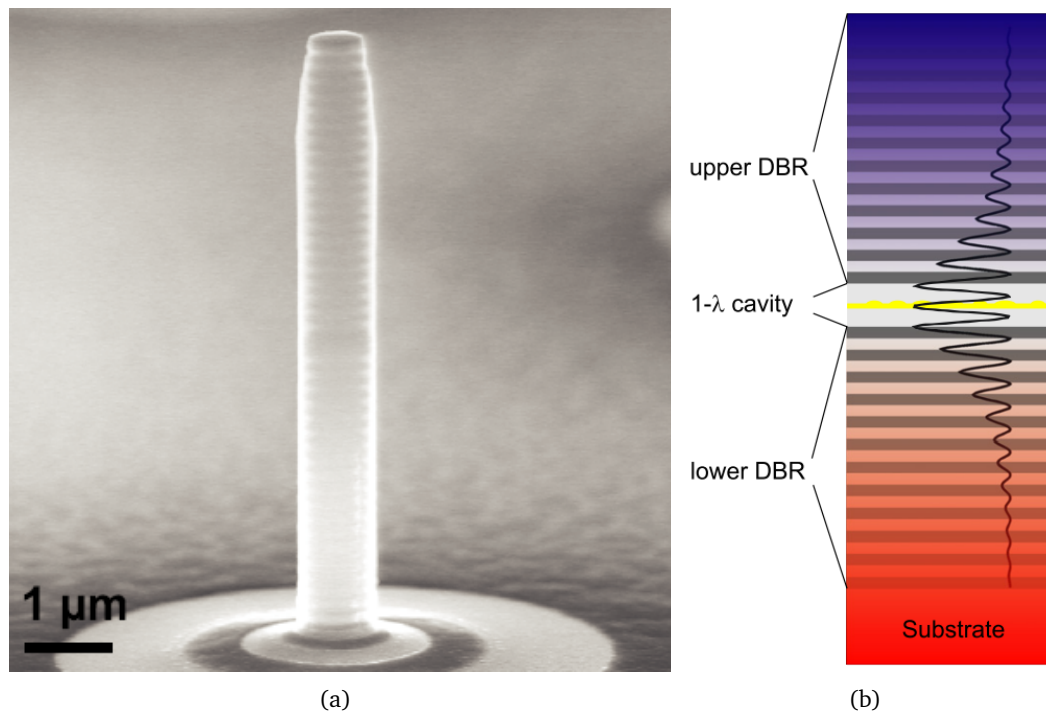


**Figure 4.1** SEM image of a micropillar showing very high  $Q$  (taken from [89]) and vertical distribution of the electric field (taken from [90]).

### 4.1.1 Modal structure

In a micropillar, light is guided along the pillar axis by total internal reflection and reflected back and forth by Bragg mirrors. This combination of effects leads to the formation of a set of discrete cavity modes, whose resonance frequency separations increase when the pillar radius is reduced.

The exact mode frequencies and quality factors can be obtained using Maxwell's equations which can only be solved numerically.

A good approximation of the micropillar mode energies is provided by calculating the modes of an infinite waveguide. Lateral confinement of light in a waveguide results in slight modifications of its propagation speed compared to bulk material. The modification of the propagation speed can be seen as a modification of the refractive index of the material. This concept is called the effective refractive index and is, visually spoken, a contribution of the cladding environment of an optical waveguide which is being "felt" by the light wave. By calculating the effective refractive index  $n_{\text{eff}}$ , the behaviour of the modes in  $z$ -direction is determined.

In a second step, the contribution of the vertical confinement by Bragg mirrors is taken into account by considering the resonance condition for each guided mode.

This simple two-step approach provides a very good estimate of micropillar mode frequencies [33]. More sophisticated models taking into account mode couplings upon reflection at interfaces must be used to predict accurately the quality factors of micropillar modes [61].

#### 4.1.1.1 Modes of an infinite waveguide

The calculation of modes of an infinite waveguide follows an approach described in [124].

We work in cylindrical coordinates and consider modes propagating in z-direction and constant refractive indices for both cladding and waveguide. We are interested in the modes propagating along the z-axis. We thus write the electric field  $\vec{E}$  (same counts for the magnetic field  $\vec{H}$ ):

$$\vec{E}(r, \theta, z, t) = \vec{E}(r, \theta)e^{i(\omega t - \beta z)} \quad (4.1)$$

$\vec{E} = (E_r, E_\theta, E_z)$  and  $\beta$  is the constant describing propagation in z-direction. It depends on the refractive indices of the waveguide and the surrounding material. It takes into account the distribution of the lightwave between cladding and waveguide material:

$$\frac{n_{\text{cladding}}\omega}{c} < \beta = \frac{n_{\text{eff}}\omega}{c} < \frac{n_{\text{waveguide}}\omega}{c} \quad (4.2)$$

$\omega$  is the resonance frequency of the cavity and  $c$  the speed of light.

By inserting Equation 4.1 into the wave equation, the wave equation along the z-axis reads:

$$\left(\Delta^2 + \left(\frac{n^2\omega^2}{c^2}\right)\right) \cdot E_z(r, \theta) = 0 \quad (4.3)$$

Because of the cylindrical symmetry, it is possible to write  $E_z(r, \theta) = \Psi(r)e^{il\theta}$ ,  $l \in Z$ . With the Laplacian in cylindrical coordinates, we obtain the Bessel type differential equation which describes the radial distribution of the micropillar modes:

$$\frac{\partial^2 \Psi(r)}{\partial r^2} + \frac{\partial \Psi(r)}{r \partial r} + \frac{n^2 \omega^2}{c^2} - \beta^2 - \frac{l^2}{r^2} = 0 \quad (4.4)$$

We solve Equation 4.4 by applying the correct boundary conditions, obtain  $\beta$  and can thus conclude on  $n_{\text{eff}}$  (see Equation 4.2). It is furthermore possible to calculate the other field components of  $\vec{E}$  and  $\vec{H}$  inside and outside of the waveguide.

Several solutions for each  $l$ , which are indexed by the letter  $n$ , can be found. Generally spoken, solutions of the infinite waveguide problem are never purely TE or TM waves (only in the case of  $l = 0$ ). That is why the classification of the solutions depends on the amplitudes of  $E_z$  and  $H_z$ . Solutions with  $E_z > H_z$  ( $E_z < H_z$ ) are more similar to TM (TE) modes and are written as  $\text{HE}_{l,n}$  ( $\text{EH}_{l,n}$ ) modes. The modes of a micropillar are named following this procedure.

#### 4.1.1.2 The micropillar mode approximation

We recall some of the characteristics of planar cavities which are described in more detail in subsection 3.1.2.

In the case of an ideal planar cavity with mirrors showing a reflectivity  $R_{\text{top}} = R_{\text{bottom}} = 1$  and a spacer thickness  $L_{\text{cav}} = \frac{\lambda_m}{n}$ , only one cavity mode can be observed for normal incidence propagation ( $k_{\parallel} = 0$ ), within the spectral window of the first stopband of the Bragg mirror.

Because GaAs and AlAs are both highly reflective materials, the field distribution of a given guided mode ( $\text{HE}_{m,n}$ ,  $\text{EH}_{p,q}$ ) is very similar in both materials for sufficiently large pillar diameters ( $> 1 \mu\text{m}$ ). It is thus possible to neglect intermode couplings at interfaces in micropillars in a first approximation and to build the  $\text{HE}_{m,n}/\text{EH}_{p,q}$  mode of pillars by using only the guided mode ( $\text{HE}_{m,n}$ ,  $\text{EH}_{p,q}$ ) in GaAs and AlAs. The field can then be calculated with a transfer matrix approach in the same way as we do it for planar cavities. A corresponding distribution is shown on Figure 4.1.

As mentioned before, the propagation of light in optical fibers can be described with  $n_{\text{eff}}$ . With a decreasing pillar diameter, optical modes  $m$  experience increasing transverse confinement and their effective refractive index  $n_{\text{eff},m}$  decreases.

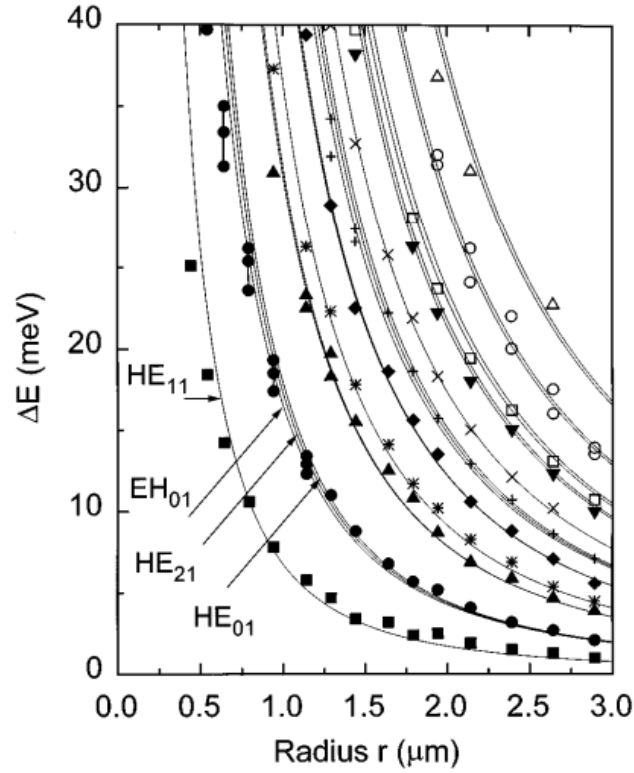


**Figure 4.2** Simulated (lines) and experimental values of  $\Delta E$  of different modes (HE11, EH01, HE21, HE01) as a function of the micropillar diameter. The reference energy of the shift corresponds to the energy of the planar cavity mode. A blue shift of every mode is observed (taken from [33]).

This leads to a blueshift of  $\Delta\lambda_m$  for the confined pillar mode versus the planar cavity resonance which can be calculated in first order by an approach following [33].

$$\frac{\lambda_{\text{planar}} - \Delta\lambda_m}{n_{\text{eff},m}} = \frac{\lambda_m}{n_{\text{eff},m}} = L_{\text{cav}} \quad (4.5)$$

$\lambda_{\text{planar}}$  is the resonance wavelength of the planar cavity and  $\Delta\lambda_m$  is the shift induced by the lateral confinement of the micropillar. The corresponding energy shift of different modes  $\Delta E_m = E_{\text{planar}} - E_m$  is depicted on Figure 4.2. Calculated and experimental values agree quite well and confirm the validity of this approach [33].

Figure 4.3 shows field intensity distributions of the first six modes of a micropillar with a radius  $R = 2.5 \mu\text{m}$ . The fundamental mode HE11 has a field maximum at the center of the micropillar, whereas the second mode family (EH01/EH21/EH01) is energetically close (see Figure 4.3) and has a donut-like shape. The modes EH11 and HE31 have very similar frequencies but different field distributions.

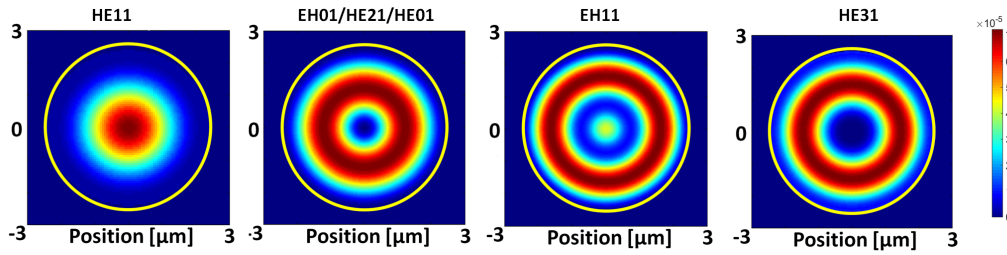


**Figure 4.3** Field intensity distribution of the mode families with the lowest energy of a micropillar with a radius of  $2.5 \mu\text{m}$ . The yellow circle indicates the sidewalls of the micropillars. The field of EH01 is similar to the field distribution of the modes HE21 and HE01 with which it forms an energetically close set of modes.

In the following, the different field distributions are used to differentially switch a micropillar.

It is important to note at this stage that pillars also possess a continuum of non-resonant modes, besides this discrete set of resonant modes. This continuum corresponds to modes for which light is either not guided vertically by the high index GaAs/AlAs cylinder, or guided but not reflected by the Bragg mirrors. Generally speaking, the spectral density of modes of a micropillar is therefore constituted by a set of discrete, high  $Q$  resonant modes sitting on the top of a relatively flat background of non-resonant modes.

#### 4.1.2 Probing micropillars with an internal light source

To understand all observed effects in CQED, it is crucial to have an exact knowledge of the mode positions of micropillars. In order to meet this requirement, the microcavity can be probed from outside or from inside.

Probing cavity modes from outside is mostly used for empty cavities, i.e. no emitters are implemented in the cavities. This can be done by detecting reflectivity and transmission. This approach is rather difficult because symmetry forbids coupling of external light waves with many confined modes and a correct spectral and spatial matching between probing laser and modes has to be achieved.

It is indeed possible to use spectrally broad, ultrashort laser pulses to detect the modes. This still requires focussing the probe laser on a spot smaller than the micropillar radius. Thus, this approach is only useful for bigger micropillars [20].

Studying micropillars from the inside with QDs often is a more convenient method to study the modal structure. A high number of QDs ( $> 10^3$ ) is implemented in a

micropillar cavity during the growth. These QDs have randomly distributed emission lines and overlap into a kind of white light source because of their large number. This provides a broadband source between 900 – 1000 nm. Furthermore, they have a random spatial distribution in the micropillar. This allows several QDs of the ensemble to couple to every mode.

Their emission into the respective mode is governed by the local amplitude of the electromagnetic field at their position. Their capability to confine free carriers on a very localized position reduces non-radiative recombination of free carriers at the sidewalls of the pillar.

Due to the small spatial extension of single QDs, which is much smaller than the typical extension of a mode, absorption of photons by QDs is small. This is important in order to not degrade the optical properties of a cavity and to avoid the so-called “Q-spoiling”. Only for micropillars showing  $Q > 5000$  or very dense QD ensembles, the absorption of QDs becomes important.

These properties favour QDs compared to QWs as an internal light source. Gérard et al. were the first to demonstrate these advantages experimentally in 1996 [33].

Let us also mention here that a single QD can be used to probe the spectral density of modes, provided its spectrum is broadened for instance by raising the temperature [69].

Going one step further, QDs also facilitate time resolved experiments. Due to their fast decay times  $\tau_{\text{QD}} \approx 1 \text{ ns}$ , QDs can be used to probe the temporal evolution of micropillar modes. This is particularly useful for switching experiments whose duration is on the picosecond timescale. That is why, micropillars with implemented QDs are a promising structure for studying light-matter interaction on a picosecond timescale. In addition to that, the detection of the created signal with a streak camera allows acquisition times of few minutes and an easy experimental handling.

For performing the same measurement, time resolved pump-probe experiments were done using the approach explained in [20], but the requirement of two synchronized lasers and long acquisition times are a significant drawback [112].

**Detection of the signal of a single QD placed in a micropillar** Let us first consider a single QD at the center of the micropillar. QDs generally emit into cavity modes and leaky modes. If the transition of a QD is spectrally off-resonant, only emission into leaky modes will take place. A QD which is in resonance with a cavity mode emits at a rate  $\gamma\Gamma_0$  into leaky modes and at a rate  $F_m\Gamma_0$  into a cavity mode (cf. chapter 1).

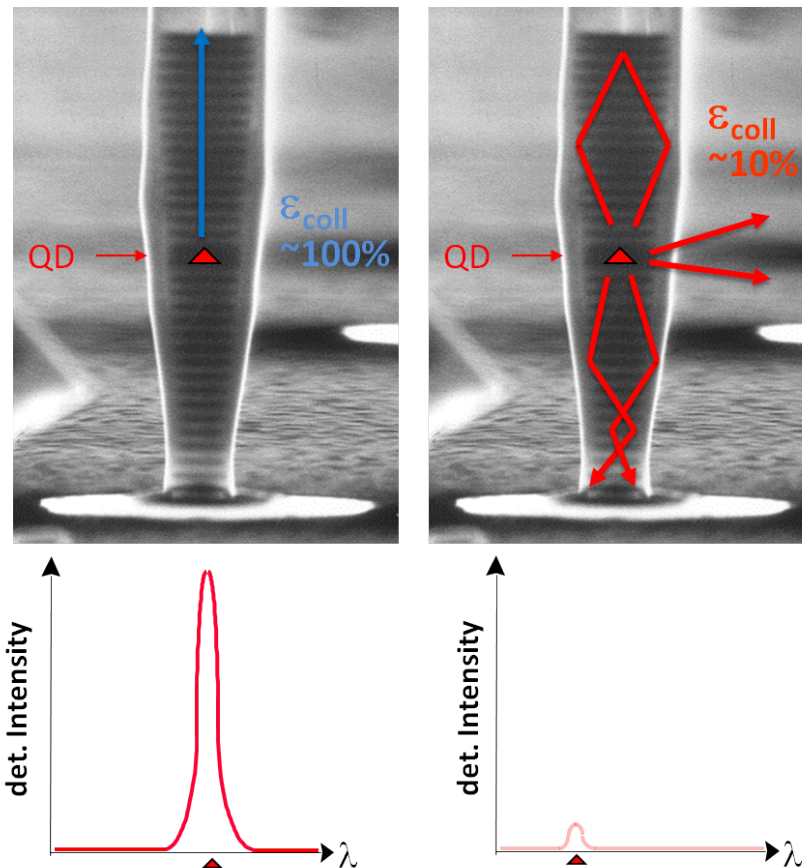


**Figure 4.4** Principle of probing of cavity modes with one single QD: If the emission line of the QD is on resonance with the cavity mode, its signal is guided into the detector. This behaviour is magnified in the case of emission enhancement of the resonant QD. In the case of a non-resonant QD, its emission is channeled into leaky modes which emit mostly through the bottom mirror. Only a small part of these photons is detected which results in a very weak signal.

The emission rate also depends whether the QD is at a position with a large field amplitude.

In the case of a photon emitted into a cavity mode, a high percentage of photons is detected because of the very directive emission diagram of micropillar modes, which is parallel to the micropillar axis. We suppose a collection efficiency  $\epsilon \approx 1$  (cf. Figure 4.4). The combination between potential spontaneous emission enhancement and the high collection efficiency creates a bright signal on the detector.

If a photon is emitted into a leaky mode, the detection probability is much lower. In the case of micropillars, we speak of leaky modes if the photons can be confined neither by the sidewall (total internal reflection) nor the Bragg mirrors. The greatest part of leaky modes is part of the second category. Visually spoken, a large part

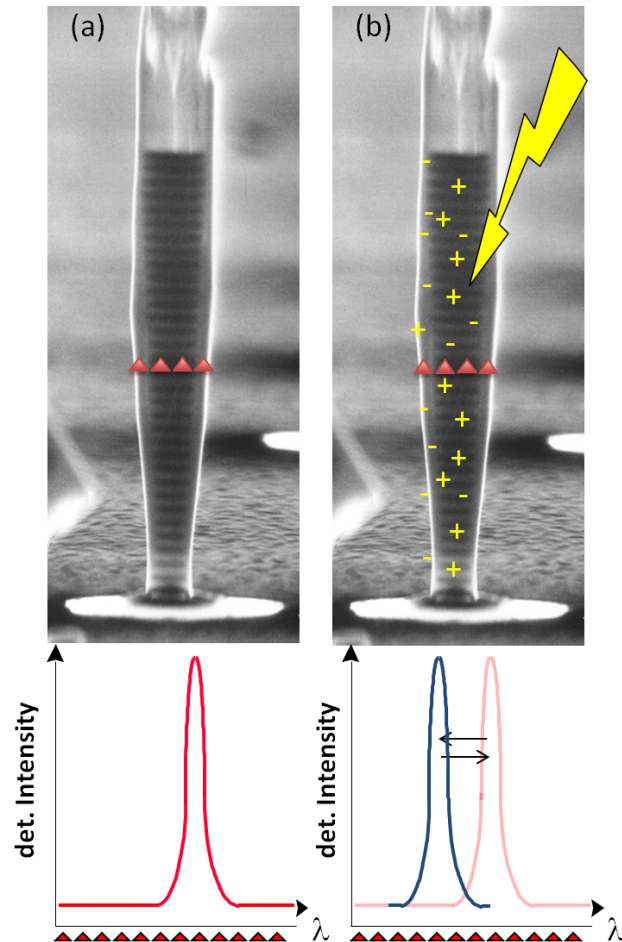


**Figure 4.5** Principle of probing cavity modes with an ensemble of QDs emitting at a large energy band. (a) The high number of QDs form a white light source and cover a broad spectral range. On-resonant QDs create a stronger signal on the detector than off-resonant QDs and reveal the modes of the micropillar at any moment. (b) In the case of shifting mode positions, emission of QDs reveals the mode positions if the detector presents a sufficient temporal resolution.

of these photons impinge with an incidence angle  $\neq 0$  onto the Bragg mirrors and propagate inside the mirrors instead of being confined by the mirror in the cavity. Then, a higher emission probability of these leaky modes appears at the bottom mirror due to the lower refractive index contrast between the Bragg mirror and the GaAs substrate (compared to air). Thus, only few leaky modes have an emission diagram parallel to the pillar axis and can subsequently be detected by the experimental setup. The resulting collection efficiency  $\eta < 0.1$  creates only a weak signal (cf. Figure 4.4).

**Detection of the signal of an ensemble of QDs placed in a micropillar** The micropillars being used in this work, contain large numbers of QDs. The high number of QDs covers a large spectral range due to their inhomogeneous size distribution and the resulting different transitions. This allows probing of different cavity modes at the same time.

The signal created by many different QDs is superposed. The previously described mechanisms lead to a higher detected intensity at resonance positions and a low intensity background contribution of photons emitted by non-resonant QDs (cf. Figure 4.5(a)).

**Use of QDs for probing cavity dynamics** QDs as an internal light source can also be used for the detection of ultrafast cavity dynamics. An excited QD emits its photons at a moment which is temporally not exactly defined. Neglecting for the moment modifications of the spontaneous emission rate, the emission behaviour for a QD is statistically described by an exponential curve with a specific time  $\tau_{\text{QD}}$ . A QD can thus be used to probe cavity dynamics which appear on a timescale similar or smaller than  $\tau_{\text{QD}}$ . In the performed experiments,  $\tau_{\text{QD}} \approx 1$  ns. This allows a detection of ultrafast switching events on the picosecond time scale.

The emission diagram (or, in the case of an important Purcell effect, emission dynamics) of a QD can thus be modified. An emitted photon from a QD which is brought into resonance for a short time interval has a much higher detection probability during this interval (cf. Figure 4.5(b)). Consequently, a brighter signal is detected at these moments. Averaging the resulting signal with a time-resolving detector provides precise information on the mode positions at any given time.

It is important to know at which energy the cavity mode is centered initially and to obtain information over the whole switching process. If we want to probe the whole switch, the emitters have to be charged before the switch.

In a previous work on the switching of micropillars [82], the dynamics of micropillars have been probed with one single pulse which injected free carriers into the cavity. The free carriers charge the QDs and switch the cavity at the same time. Though, the characteristic time for capturing of free carriers by the QDs and subsequent relaxation ( $\approx 20$  ps) is significantly longer than the switch-on time of the cavity ( $\approx 5$  ps [46]). This means that no QD signal is available to probe during this time and no insight on the beginning of the switching event is obtained.

For information on the initial position of the cavity mode and the beginning of the switch, the QDs have to be charged already before the switch.

## 4.2 The experimental configuration

This section is dedicated to a description of the experimental approach and setup which has been used to study the differential switching of micropillars. In its first part, I describe the micropillars which have been studied. In the second part, I explain how two successive laser pulses can be created and how the setup for the time-resolved PL measurement is built.

### 4.2.1 The Micropillar cavity

The micropillar cavity, which is used in the experiment (cf. Figure 4.6), is made of GaAs and AlAs and has a bottom DBR of 25 periods and a top DBR of 15 periods. The central layer has a thickness of one  $\lambda/n$  and gives rise to resonances between 1.38 eV and 1.4 eV.

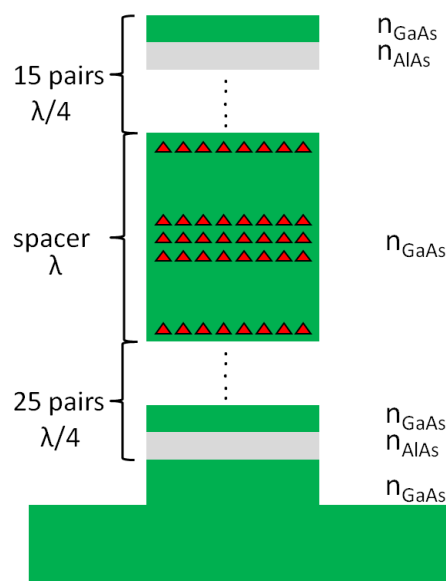


**Figure 4.6** Sketch of the vertical composition of the used micropillar.

Five layers of QDs are incorporated in the cavity. Three of these layers are grown around the middle of the spacer, the other two QD layers close to the bottom/top DBR stack. At these positions, the vertical field distribution of the cavity modes has antinodes. The QDs couple thus with a high probability to the cavity modes. The large number of layers provides an intense signal for probing the cavity.

Because of the higher reflectivity of the bottom mirror, light of the cavity modes essentially escapes through the top mirror and can easily be detected. In the following experiments, micropillars with diameters around  $5\ \mu\text{m}$  are probed.

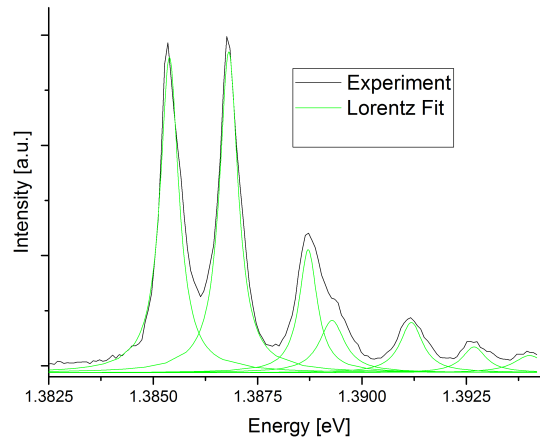


**Figure 4.7** Spectrum of an unperturbed micropillar with a diameter of  $5\ \mu\text{m}$  obtained under weak excitation power with a CW laser. The Lorentz curves (green) fit the different modes (from the left hand side: HE<sub>11</sub>, EH<sub>01</sub>/HE<sub>21</sub>/HE<sub>01</sub>, HE<sub>31</sub>/EH<sub>11</sub>, HE<sub>21</sub>, HE<sub>41</sub>/EH<sub>21</sub>, HE<sub>02</sub>/EH<sub>02</sub>/HE<sub>22</sub>).

A PL-spectrum obtained at 5 K is shown on Figure 4.7. The spectrum was obtained by exciting the QDs embedded in the micropillar with a CW laser (power:  $30\ \mu\text{W}$ , energy:  $1.56\ \text{eV}$ ). Because of the small and continuous excitation energy, small amounts of free carriers are injected and the mode positions are unperturbed. Seven different modes are observed in the spectral range of interest. The quality factors of the modes are between 1000 and 4000.

The unperturbed mode positions of the micropillar cavity can be measured with this system. This is important for comparing their position to those obtained from the time resolved setup.

## 4.2.2 Time-resolved microphotoluminescence using a two pulse system

Microphotoluminescence measurements of micropillars such as those used for observing the differential switching are performed with an optical path which is used for excitation as well as detection. The experiment requires a high precision of the positioning of the excitation beam and a high temporal and spectral resolution of

the detector. It furthermore requires two consecutive pulses in order to correctly probe the cavity before the switch.

#### 4.2.2.1 Creation of two successive laser pulses

In the frame of this work, a simple and reliable method to create two consecutive pulses was used. Because of its easy experimental handling, its stable behaviour and its compatibility with the experimental setup, a fiber solution was chosen.

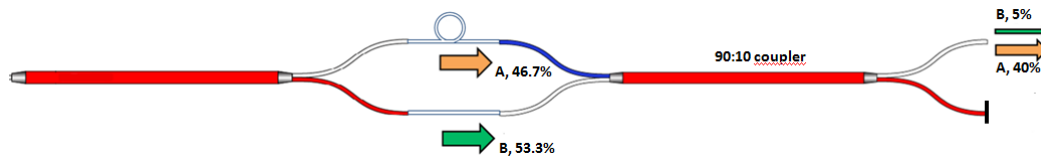


**Figure 4.8** Experimental configuration for creating two pulses by using coupled fibers. The initial beam is split, one of the parts is delayed and then the two beams are recombined. After splitting the two beams again, two pulses are generated.

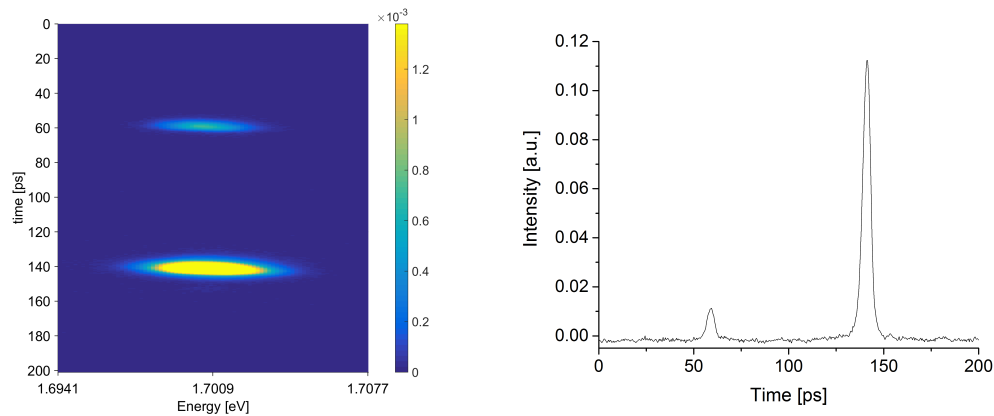
The functioning principle is depicted on Figure 4.8: a pulse propagating in a fiber is split by a wideband coupler into two components which travel through fibers of different lengths. The fiber guiding 46.7 % of the pulse energy is 1.6 cm (corresponding to a delay of 80 ps in the case of a fused silica fiber) shorter than the fiber guiding 53.3% of the pulse. The two pulses are recombined in a 2x2 coupler. At its exit, the train of two pulses is split again with a ratio of 90:10.

At the first exit of the coupler, the first pulse has a power of approximately 5 % of the incident pulse and the second pulse 40 % of the incident pulse (and vice-versa for the second exit of the coupler). We block this exit and use only the beam of the first exit.

Figure 4.9(a) shows a streak camera image of the two pulses with a central wavelength of 730 nm. Two clearly separated pulses centered around the same wavelength are observed at  $t = 60$  ps and  $t = 140$  ps. A horizontal integration of the streak image (cf. Figure 4.9(b)) reveals that the two pulses are separated by 80 ps. The integrated intensities also confirm the expected ratio between the two pulses.

#### 4.2.2.2 Microluminescence setup for probing and switching micropillars

Figure 4.10 schematizes the experimental setup used for studying spatially separated nanostructures and, in the frame of this work, for studying differential switching.



(a) Streak camera image of the pulsed laser centered around 730 nm.

(b) Horizontally integrated intensity distribution of the streak camera image.

**Figure 4.9** Output of the double pulse system.

The excitation of the microstructure and the collection of the subsequent photoluminescence signal is realised by a microscope objective with a high magnification (40x, NA = 0.6). The sample containing the micropillars is put inside a cold-finger cryostat which is cooled down to 5 K with liquid helium. The sample position can precisely be adjusted with micrometer screws. This allows a precise positioning of the incident laser beam which is crucial for the detection of differential switching processes.

The incident laser beam is created by the Ti:Sa laser and the double pulse fiber system.

For visualising the micropillars and the relative position of the laser spot, the sample is illuminated with a LED emitting around 850 nm. The visualisation of the sample is achieved with a CCD camera.

The PL signal is fed into a monochromator which resolves the signal spectrally before its detection with a Si-CCD camera. For performing temporally resolved PL-experiments, the signal can alternatively be guided onto a streak camera. A foldable mirror is used to provide an easy switch between the two experimental configurations.

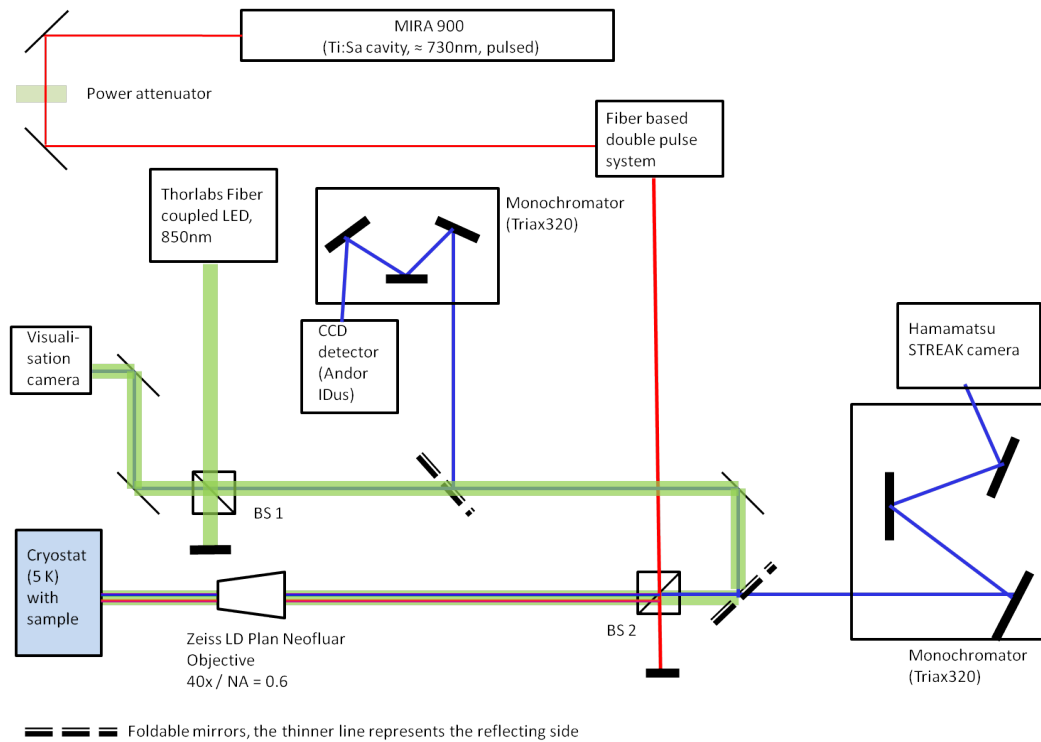


**Figure 4.10** Experimental setup used for the experiments with micropillars

## 4.3 Differential switching of micropillars

This section deals with the experiments that have been performed on differential switching of a micropillar.

For a better understanding, I will first introduce how switching events in a micropillar can be characterized and which processes take place in a micropillar after the injection of free carriers. These processes define the dynamics of the switch.

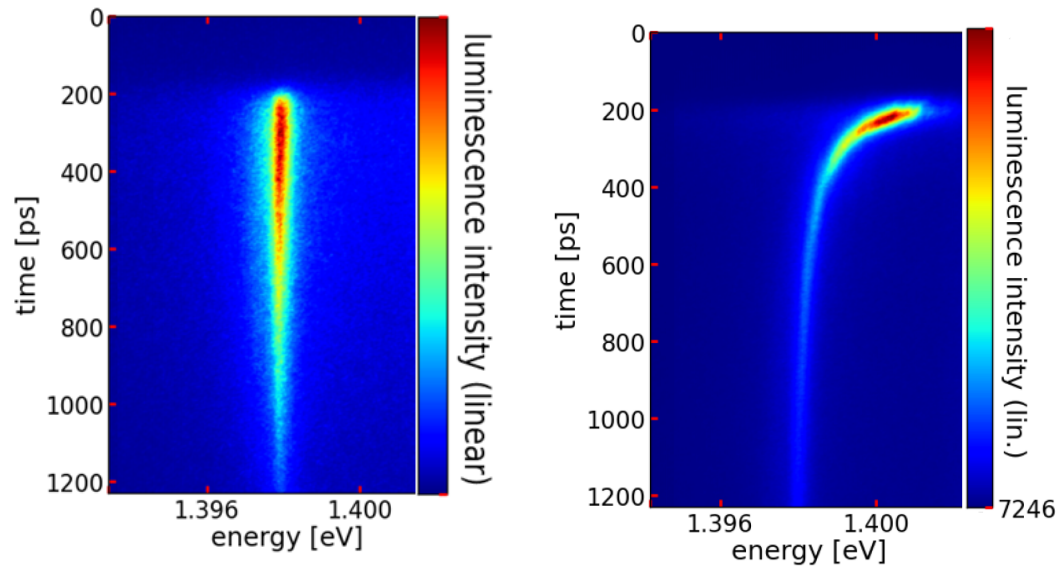
In the second part of this chapter, I will present results of differential switching. Two cases are presented for the injection of free carriers with a strongly focalized laser beam: at the center and at the border of the micropillar. These results are compared to FDTD simulations.

### 4.3.1 Characterization of switching events in micropillars

Figure 4.11(a) shows a streak camera image of the photoluminescence signal of QDs inserted into a micropillar. For this image, the QDs are excited with a single pulse at 830 nm (below the band gap of GaAs). Free carriers are only injected

into the QDs and their wetting layer. Because of the processes which are described in subsection 4.1.2, mostly the signal from QDs emitting into the cavity mode is detected.

An exponential decay of the QD signal after the excitation is observed. This shows the decay of excitons which are confined in the QD.



(a) Characterization of the QD behaviour. The QD is excited in the wetting layer with one laser pulse of an energy lower than the band gap of GaAs. The decay time of the QD can thus be deduced.

(b) Excitation of the micropillar with one single pulse at an energy above the band gap. We can conclude from this streak image on the switch-off behaviour, but no information on the switch-on process and the initial mode position are provided.

**Figure 4.11** Temporally resolved microphotoluminescence on a micropillar.

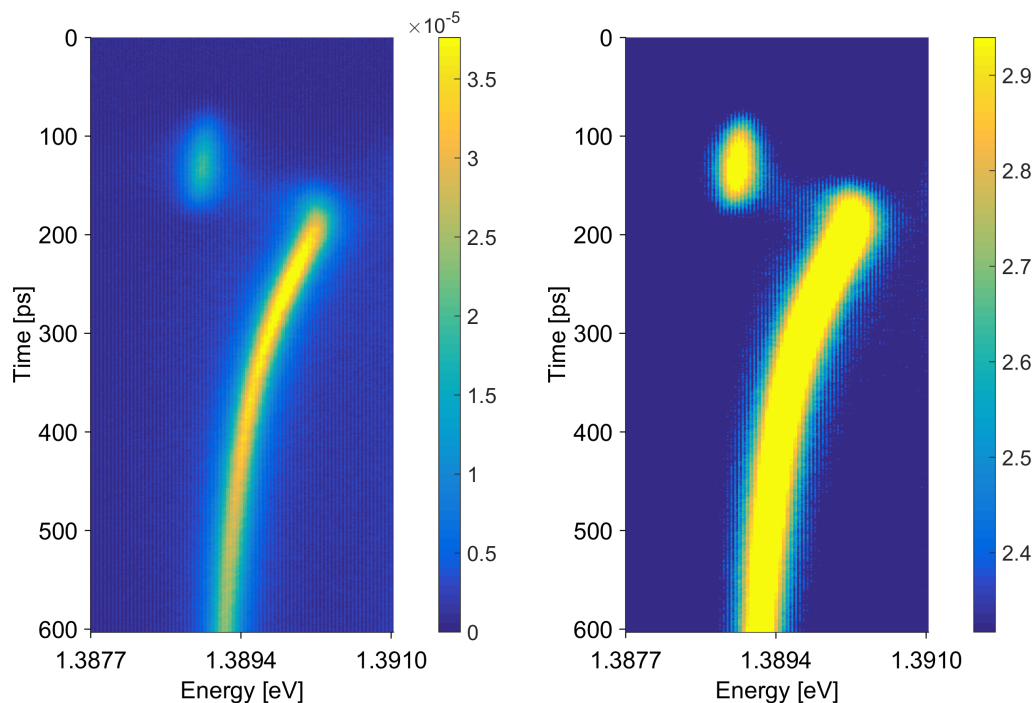
In order to switch the micropillar cavity, the frequency of the laser is tuned above the band gap of GaAs (1.519 eV). This excites free carriers in the GaAs layers of the micropillar. A part of the electron hole pairs is captured by the QDs which are thus also excited. Figure 4.11(b) shows a streak camera image of such an experiment which was performed with one single pulse.

This pulse injects free carriers into the GaAs layers which shift the resonance frequency of the cavity. Parts of these carriers are captured by QDs and relax to the lower energy levels of the QDs. This process takes around 20 ps which means that during this time, no photons are emitted by the QDs. The cavity is thus not probed by the QDs during this time interval which means that the switch-on process cannot be observed.

To overcome this limitation, we use the two pulse system. The first pulse injects a small number of free carriers into GaAs and, subsequently, into the QDs. Because of

the small quantity of free carriers injected by the first pulse, nearly no cavity switch can be observed [82]. Though, the resonance position of the unperturbed mode is determined. The first pulse arrives approximately 80 ps before the actual switch and enables an observation of the switch-on process.

The second pulse is eight times stronger and injects a sufficient quantity of free carriers to visibly shift the cavity mode to higher energies following Drude's law (Equation 1.25). A fast switch-on (shift to higher energies) appears. Luminescence of QDs which are resonant with the switched cavity mode is detected. The photoluminescence signal highlights the spectral return of the cavity mode energy to its initial position. A streak camera image of an experiment performed with the two pulse system on a micropillar with  $d = 5 \mu\text{m}$  and an excitation power of 500 mW is shown on Figure 4.12(a).



(a) Because of the two pulse system, the initial position of the mode can be deduced from the streak camera image.

(b) The same image plotted with a logarithmic scale. This allows a better insight of the switch-on process.

**Figure 4.12** Temporally resolved microphotoluminescence on a micropillar with the two pulse system.

**Switch-on process** The switch-on process is not instantaneous. Even if the laser pulse is considered to be infinitely short, it takes a few picoseconds to establish the switch. The duration corresponds to the time free carriers need to cool down through

phonon emission because the refractive index depends on the energy distribution of the free carriers following the Kramers-Kronig relation.

With the STREAK camera, E. Peinke measured a time of around 7 ps [82] on the micropillar used for this work in agreement with previous results obtained with GaAs/AlAs planar cavities by pump-probe spectroscopy [46].

We observe a similar switch-on time with the two pulse technique. Figure 4.12(b) shows a streak image which is plotted logarithmically for a obtaining a better insight of the switch-on process dynamics. Due to the fast switch-on, the QD signal is distributed over many pixels of the streak camera which creates a weaker signal. However, it is still sufficient to observe the switch-on.

**Spectral return of the mode** As explained in chapter 1, the position of a switched cavity mode relative to its initial position depends on the concentration of electron-hole pairs (cf. Equation 1.25).

The concentration of electron-hole pairs  $N$  is described by the following differential equation [122] (cf. subsection 3.2.3)

$$\frac{dN}{dt} = - \left( \frac{N}{\tau_{\text{NR}}} + BN^2 + CN^3 \right) \quad (4.6)$$

In the frame of this chapter, the quantity of free carriers is considered to be small (pump power 50 times smaller than in chapter 3) and the last two terms are neglected. A non-radiative, exponential decay with a characteristic time  $\tau_{\text{NR}}$  is expected to take place for the injected free carrier concentration and which redshifts the spectral position of the cavity.

The main contributions of  $\tau_{\text{NR}}$  are recombination in GaAs bulk material and recombination at the pillar surface [122]. For the total carrier population, this combination of effects leads to an exponential decay whose decay time  $\bar{\tau}_{\text{NR}}$  can be defined for simple geometries. Let us note that  $\bar{\tau}_{\text{NR}}$  also characterizes the relaxation dynamics of the cavity modes. E. Yablonovitch proposed for the case of a thin slab of thickness  $l$  the following expression [121]:

$$\frac{1}{\bar{\tau}_{\text{NR}}} = \frac{1}{\tau_{\text{bulk}}} + \frac{2S}{l} \quad (4.7)$$

where  $\tau_{\text{bulk}}$  is the characteristic recombination time in bulk material and  $S$  the surface recombination speed.

Defining  $\bar{\tau}_{NR}$  for a micropillar in a similar way, we obtain [82]

$$\frac{1}{\bar{\tau}_{NR}} = \frac{1}{\tau_{bulk}} + \alpha_S \frac{S}{R} \quad (4.8)$$

$\alpha_S$  is a dimensionless, geometry-dependent parameter and  $R$  the radius of the micropillar. At room temperature, H. Thyrestrup et al. obtained  $S = 2.8 \cdot 10^3$  m/s in a similar experiment [112].

Besides the total number of free carriers, it is important to know how the electrons and holes are distributed spatially. The amplitude of the shift of the cavity mode is a function of the overlap between the local number of free carriers and the local amplitude of the electromagnetic field of a mode.

For temporally simulating the behaviour of the cavity mode, precise knowledge of the distribution of free carriers is required at any moment. It can be obtained by establishing a model which is based on a defined initial free carrier distribution and takes into account the behaviour of free carriers in a micropillar.

The evolution of the free carrier distribution is governed by three processes: recombination in bulk material, recombination at the pillar surface and diffusion of the free carriers. This behaviour is also depicted on Figure 4.13.

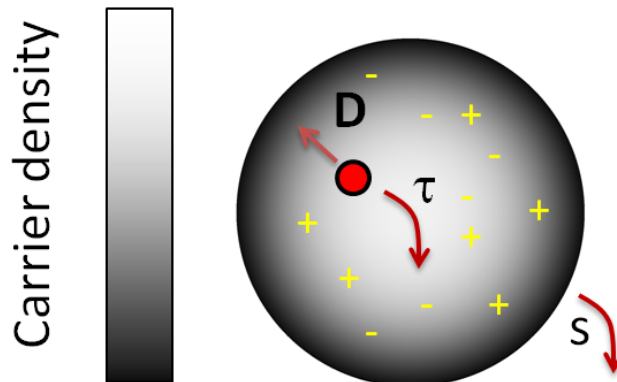


**Figure 4.13** Different processes taking place with free carriers which have been injected into a micropillar. Recombination can take place at the surface of micropillars (speed  $S$ ) and in bulk material (speed  $\tau$ ). If the carrier distribution is inhomogeneous, carriers diffuse in order to create an equilibrium. The diffusion constant  $D$  describes this behaviour.

The diffusion can be modelled with Fick's second law. The evolution of the free carriers is thus given by:

$$\frac{\partial N(\vec{r})}{\partial t} = D_a \Delta N(\vec{r}) - \frac{N(\vec{r})}{\tau_{e,h}(\vec{r})} \quad (4.9)$$

where  $\Delta$  is the Laplacian operator and  $D_a$  is the ambipolar diffusion coefficient which was experimentally determined by Zhao et al.:  $D_a = 170 \text{ cm}^2/\text{s}$  for bulk GaAs at 10 K and a free carrier concentration of  $10^{17} \text{ cm}^{-3}$ .

Using circular coordinates  $(r, \phi)$  and the assumption that  $\frac{\partial N}{\partial \phi} = 0$ , the Laplacian can be written as

$$\frac{\partial N(\vec{r})}{\partial t} = D_a \left( \frac{\partial^2}{\partial r^2} + \frac{1}{r} \frac{\partial}{\partial r} \right) N(\vec{r}) - \frac{N(\vec{r})}{\tau_{e,h}(\vec{r})} \quad (4.10)$$

The surface recombination can be expressed in terms of diffusion by Fick's first law:

$$\frac{\partial N}{\partial r} D_a = NS \quad (4.11)$$

For sake of simplicity, we replace the recombination at the surface by a thin layer close to the surface in which the recombination rate is strongly increased. Such a layer has the same effect as the strong recombination at the surface.

In the following simulations, the surface recombination is modelled in an area of thickness  $\Delta r_{\text{border}}$ . In the area  $\Delta r_{\text{border}} = 100 \text{ nm}$  situated around the sidewalls of the pillar, the recombination rate  $\tau_{\text{border}} = \frac{\Delta r_{\text{border}}}{S}$ . Elsewhere, the recombination rate corresponds to that of bulk material:  $\tau_{e,h} = \tau_{\text{bulk}}$ . At last, the boundary condition is supposed to show no flux of free carriers:

$$\frac{\partial N(r = \pm R)}{\partial r} = 0 \quad (4.12)$$

The result of the simulation is shown on Figure 4.14. It shows the radial free carrier distribution (and thus the refractive index profile) of a micropillar with a radius  $R = 2.5 \text{ }\mu\text{m}$  at different times (in ps) after an homogeneous injection at  $t = 0$ . The following values were used for the simulation:  $\tau_{\text{bulk}} = 385 \text{ ps}$ ,  $D_a = 198 \text{ cm}^2/\text{s}$  (following [92]:  $170 \text{ cm}^2/\text{s}$  at 10 K and interpolation to 5 K),  $S = 5 \cdot 10^3 \text{ m/s}$ ,

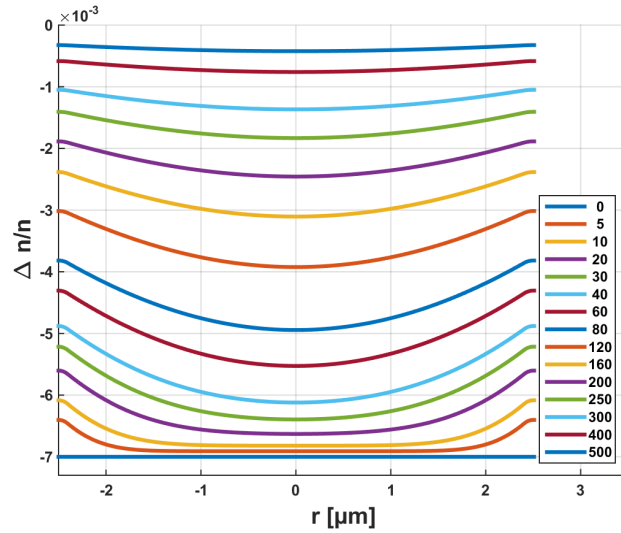
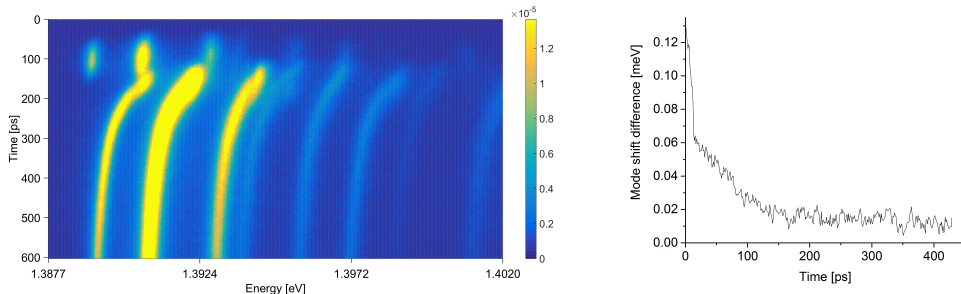


**Figure 4.14** Evolution of the refractive index profile of a micropillar with radius  $R = 2.5 \mu\text{m}$  taking into account surface and bulk recombination in the micropillar. The legend indicates the delay in ps.

amplitude of the initial switch  $\frac{\Delta n}{n_{\text{GaAs}}} = -0.007$ . Equation 4.10 was used to calculate the evolution of the refractive index distribution.



(a) Streak camera image of a homogeneous switch.

(b) Plot of the shift difference between the first two modes. A during the first 150 ps, the switch is slightly inhomogeneous.

**Figure 4.15** Temporally resolved microphotoluminescence on a micropillar with the two pulse system.

An experimental result of a homogeneous switch corresponding to the simulated distributions of Figure 4.14 is shown on Figure 4.15(a). The image was obtained by exciting a micropillar with  $d = 5 \mu\text{m}$  with a weakly focalised laserspot (waist  $w > 5 \mu\text{m}$ ) and a power of 1 mW. All modes behave in a similar way on the streak camera image.

A more detailed analysis of the first two modes (HE11 and EH01/HE21/HE01) reveals tiny differences: a plot of the shift difference (obtained by fitting a Lorentzian to the first two modes) of these modes is shown on Figure 4.15(b) and indicates an inhomogeneous shift for  $0 < t < 150$  ps. At  $t > 150$  ps, the modes behave equally.

This behaviour appears due to the different recombination speeds of surface material and bulk material. Because of the highly recombining surfaces at the border of the micropillar, the free carrier density decreases at a faster rate there than at the center of the micropillar. This creates an inhomogeneous distribution of the refractive index, especially during the first 150 ps after the injection of free carriers.

With the resulting refractive index profiles, the effective refractive index  $n_{\text{eff},m}$  of every mode  $m$  can be calculated. This also determines the resonance wavelengths  $\lambda_m$  of the cavity:  $\lambda_m = L_{\text{cav}} \cdot n_{\text{eff},m}$  ( $L_{\text{cav}}$ : physical length of the micropillar cavity).

The change of  $n_{\text{eff},m}$  due to index change could likely be estimated using first order perturbation theory. However, FEM simulations indicate that the index change also induces modifications of the field distribution of mode  $m$ . To take into account all these effects, we preferred to calculate  $n_{\text{eff},m}$  by solving Equation 4.3 for a calculated refractive index distribution with the FEM method by using the commercially available software **FEMSIM**. This allowed concluding on the resonance frequencies.

### 4.3.2 Differential switching of micropillars

The amplitude of the switch of different modes depends on the overlap between the field of the respective mode and the free carrier distribution in the micropillar. A given concentration of free carriers at a location of a field maximum induces a larger shift of the mode than at a location with a smaller field of a mode. Because of the different values of the electrical field of different modes, a non-uniform intensity profile of the pump laser leads to different shift amplitudes for different modes.

Consequently, two different kinds of switches can be observed: homogeneous and differential switches.

In the case of a homogeneous switch, the switching amplitude and time-evolution of the different modes are the same. Homogeneous switching can be achieved by a homogeneous free carrier distribution in the micropillar. As shown on Figure 4.14, perfectly homogeneous switching is difficult to achieve because of the large difference of recombination times of free carriers at the pillar surface and in bulk material.

Nevertheless, in many cases the behaviour of different modes is only slightly different as discussed in the previous section.

In this section, we inject on purpose a highly inhomogeneous population of free carriers in order to induce differential mode switching. Two experiments with different excitation spots were performed and compared to numerical simulations.

#### 4.3.2.1 Concept of differential switching

In the case of a differential switch, different modes have specific switching amplitudes and time evolutions. Such a behaviour can be induced by a non-homogeneous modification of the refractive index. This impacts the effective refractive index  $n_{\text{eff},m}$  of every mode  $m$  in a different way, because  $n_{\text{eff},m}$  describes the refractive index distribution which is “felt” by the field distribution of every mode. This creates a transient and reversible modification of the distances between the different mode families.

For example, a localized injection of free carriers at the center of a micropillar is expected to create a larger switch for the fundamental mode HE<sub>11</sub> (antinode at  $r = 0$ ) than for the mode family EH<sub>01</sub>/HE<sub>21</sub>/HE<sub>01</sub> (node at  $r = 0$ ). On a longer timescale  $> 100$  ps, a return to similar behaviour due to diffusion is expected. Indeed, due to the fast lateral diffusion of the free carriers, their spatial distribution is rather uniform at long time scales ( $> 250$  ps) except close to the sidewall as shown on Figure 4.14.

H. Thyrestrup et al. [112] investigated the differential switching behaviour of a micropillar. They used an experimental configuration based on a pump-probe laser system to determine the cavity resonance with reflection measurement.

In this work, the approach of probing the cavity from inside with QDs is used. Compared to Thyrestrup’s experiment, probing from inside allows an easier and much faster experimental handling and probing of all micropillar modes at the same time. Because of the exciton lifetimes of QDs being of the order 1 ns, the cavity resonances can be detected over a long time period, within a fast experiment.

The basic idea of this experiment is to inject a highly inhomogeneous free carrier distribution into the micropillar and consequently create a transient modification of the distances between the modes which can be detected with the streak camera.

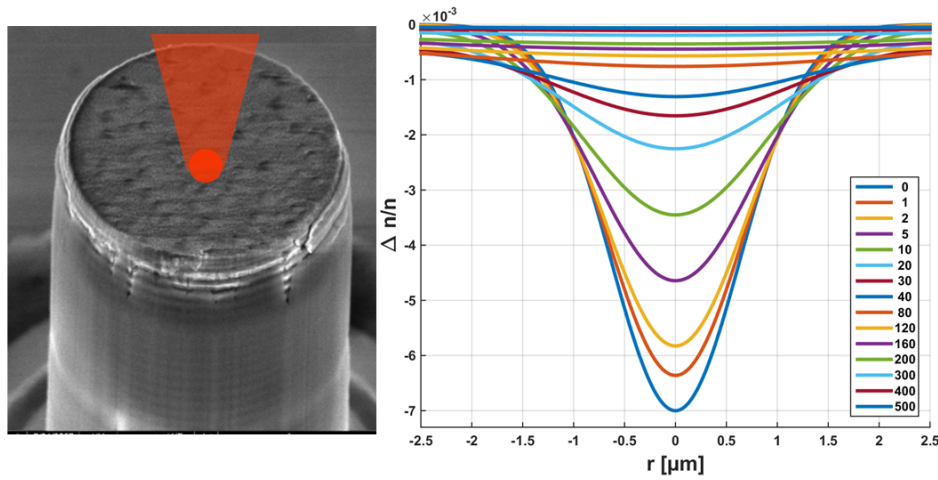


**Figure 4.16** Injection of free carriers at the center of the micropillar and the resulting free carrier distribution at different times (in ps) after the injection.

The inhomogeneous free carrier distribution is injected by a strongly focused laser which impinges on the micropillar at its central axis (cf. Figure 4.16). Its intensity profile is considered to be Gaussian. The spot size is  $1.5 \mu\text{m}$  at FWHM.

Figure 4.16 shows the modification of the refractive index  $\frac{\Delta n}{n}$  of a micropillar with  $d = 5 \mu\text{m}$  which is a result of the distribution of free carriers at different time delays (in ps) after the injection of electron-hole pairs. The profiles were calculated with  $D_a = 198 \text{ cm}^2/\text{s}$ ,  $\tau_{\text{bulk}} = 385 \text{ ps}$ ,  $\frac{\Delta n}{n}(t = 0) = -0.007$  and  $S = 5 \cdot 10^3 \text{ m/s}$ .

At  $t = 0$ , the shape of the modification is given by the intensity profile of the laser beam. At shorter times after the injection, the free carriers diffuse and the FWHM of the refractive index profile increases. The total number of free carriers changes slightly because only small concentrations are located close to the borders where they recombine at a fast speed. At a longer time range, the free carrier distribution becomes more uniform and the amplitude of  $\frac{\Delta n}{n}$  decreases.

The simulated impact of these free carrier distribution on the mode positions of a micropillar is shown on Figure 4.17. The free carriers are injected at  $t = 0$ . During the first 100 ps of the switch, the modes behave in a different way – the simulation shows a differential switch.

#### 4.3.2.2 Experimental study of differential switching by central excitation of a micropillar

The simulation shown on Figure 4.17 predicts that differential effects can be obtained. To confirm the theoretical predictions in an experiment, we use a strongly

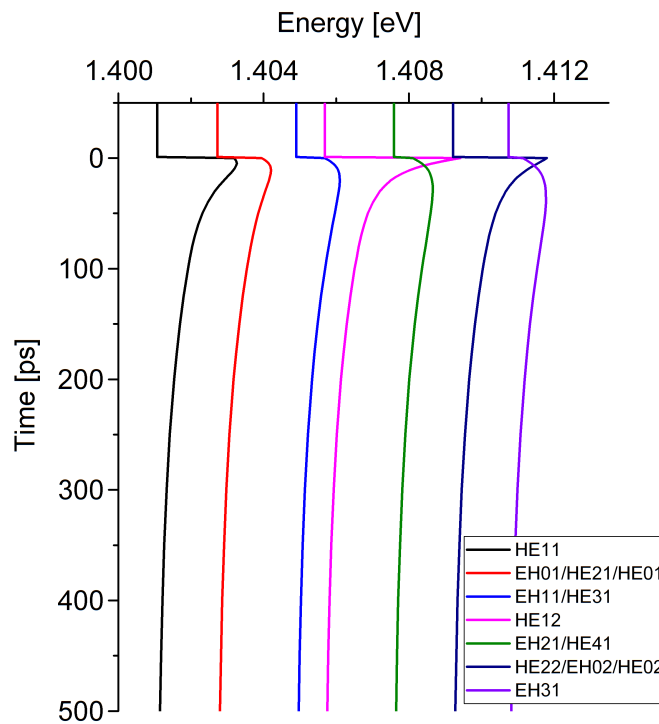


**Figure 4.17** Simulation of the mode positions of a micropillar ( $d = 5 \mu\text{m}$ ) with free carrier distributions as shown on Figure 4.16. The modes behave differently.

focalized beam for differentially switching a micropillar with a diameter  $d = 5 \mu\text{m}$ . The spectral spacings between the modes of this micropillar are small which allows to simultaneously observe a large number of modes with the streak camera. Furthermore, its big size compared to the laser spot allows a highly differential switching behaviour.

Figure 4.18 shows a streak camera image of a differential switch which was obtained with the experimental configuration shown on Figure 4.16. The micropillar was excited with the double pulse system with a total power of 1.3 mW.

The first pulse excites the QDs which probe the unperturbed positions of the modes. When the second, stronger pulse hits the micropillar at  $t = 120 \text{ ps}$ , all modes are blueshifted.

The seven mode families visible on the streak camera image have different switching amplitudes. The switch of the fundamental (HE11), fourth (HE12) and sixth mode

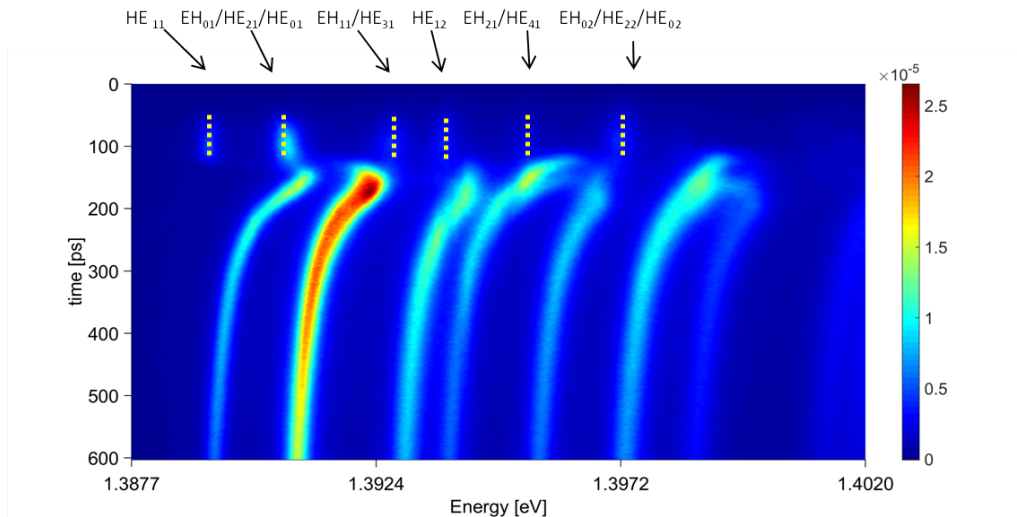


**Figure 4.18** Streak image of a differential switch of a micropillar with a diameter of  $5\mu\text{m}$  with central excitation. For a better visibility, the dotted points show the position of the unperturbed modes.

(HE22/EH02/HE02) is stronger than of the other modes. This is due to the fact that these modes have an antinode at the center of the micropillar and, hence, “feel” the carriers more strongly. After the switch, the mode position returns to lower energies.

The other modes (second (EH01/HE21/HE01), third (EH11/HE31), fifth (EH21/HE41) and seventh (EH31) have smaller switching amplitudes. Furthermore, the mode positions do not shift to lower energies immediately after the switch. During  $\approx 20$  ps, the mode stays at the same spectral position or still shifts to higher energies. This behaviour results from a small overlap of the mode field pattern and the injected free carriers at  $t = 120$  ps. At  $t > 120$  ps, the free carriers start to diffuse and higher concentrations reach the antinodes of these modes. In some cases, this effect is faster than the decay of free carriers. This leads to a further blueshift between  $t = 120$  ps and  $t = 140$  ps.

On a longer time scale, the decay behaviour of the shift is similar for all modes. An exponential decay, whose characteristic time corresponds to a combination of decay at the surface and in bulk material, is observed.

The simulated mode positions are compared to the experimentally obtained mode positions on Figure 4.19. The simulation agrees qualitatively very well to the experiment. The simulation predicts for the HE11, HE12 and HE02/EH02/HE22 modes a very high amplitude of the switch. This is experimentally observed as well as the contrary for the other mode.

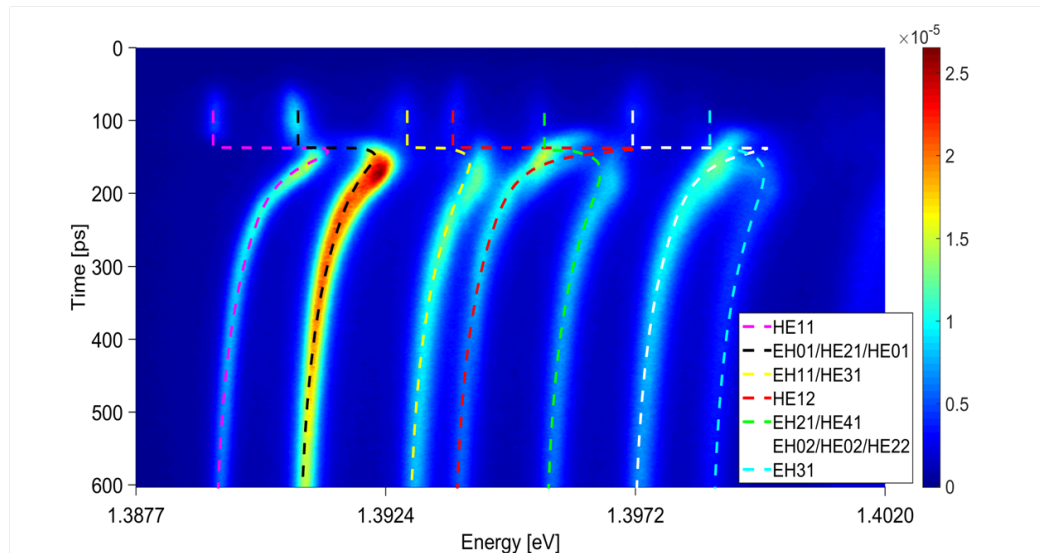


**Figure 4.19** Comparison between the simulation (lines) and the modes observed with the streak camera. It demonstrates that the used approach of an inhomogeneous free-carrier injection works for a high number of modes (in this case seven mode families) and that simulations agree with the actual mode positions.

Furthermore, at the beginning of the switch, a crossing between the HE12 (large switching amplitude) and the HE41/E21 modes (small switching amplitude) is predicted. The same prediction is made for the HE02/HE22/EH02 and the EH31 mode.

This crossing is difficult to see on the streak camera image, because during a short time range of  $\approx 10$  ps, the switch-on process also takes place and many different processes overlap. Nonetheless, the streak camera image shows clear indications for an actual existence of this behaviour.

We see that cavity switching using an inhomogeneous pumping beam enables to modify to a large extent the modal structure of a pillar microcavity.

In order to quantitatively analyse the switching behaviour of a micropillar and to illustrate the precision of the simulation, the mode positions of the first three modes are compared with the simulations on Figure 4.20.

The position of the modes were fitted by seven Lorentzian curves for every horizontal pixel line of the streak camera image. The positions of the peaks were compared to the positions of the unswitched modes. Because of a slight imprecision of the mode positions obtained with the first pulse, from this STREAK camera image only the unperturbed position of the fundamental mode was used as a reference point. The distance of the other modes to the HE11 was determined by the spectrum

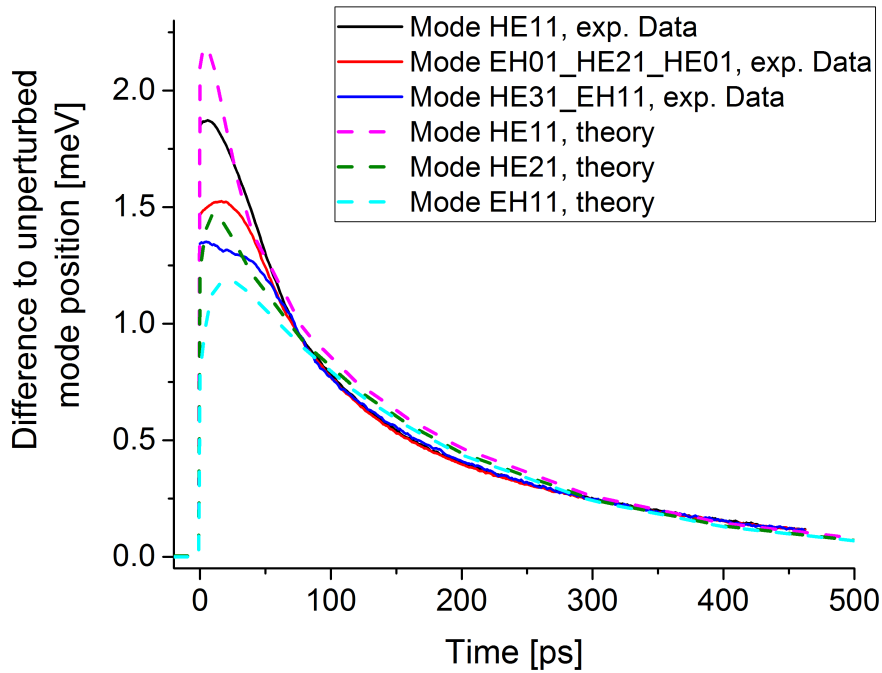


**Figure 4.20** Analysis of the position of the three low energy modes of the micropillar compared to the unperturbed resonance position.

obtained under CW laser excitation (cf. Figure 4.7). The values obtained are in good agreement with the mode positions of the prepulse.

In order to confirm the validity of this approach, the temporal evolution of every modes was fitted with an exponential curve. The position at  $t = \infty$  was the same as the position of the method described above.

The simulation of the long time behaviour of all three modes fits the experiment very well. During the first 50 ps, a significant deviation of 0.3 meV between the simulation and the experiment can be observed. This could result from the time resolution of the streak camera which is not good enough to correctly resolve the position of the mode. We use indeed for this experience the 1200 /mm grating with a temporal resolution of 11 ps. This results in an averaging over this timerange and a blurring of the mode position.

For the other two modes, the deviation of experiment and simulation is below 0.15 meV. This is close to the experimental uncertainty of 0.1 meV which results from a slight deviation of the position of the laser beam and the spectral resolution of the streak camera.

Overall, the simulation fits the experiment very well and confirms the assumptions which were made on the dynamics of free carriers and on the behaviour of differential switching.

#### 4.3.2.3 Differential switching by exciting close to the edge of the micropillar

Differential switching of a micropillar can also be performed with a laser spot which impinges on an off-axis position of a micropillar.

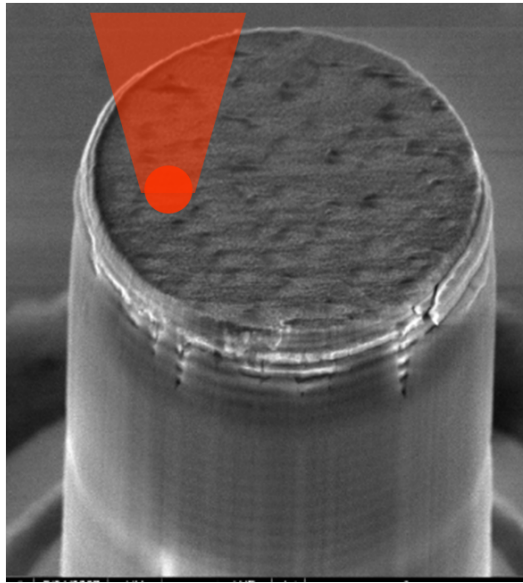


**Figure 4.21** Position of the pump laser beam in the case of an off-axis excitation experiment.

Figure 4.21 shows the laser spot position of such an experiment. With this experimental configuration, free carriers are injected far from the central axis of the micropillar and close to its border.

Consequently, different mode dynamics are expected: modes that have a maximal field intensity close to the border of the micropillar should experience a higher switching amplitude than modes with high intensities at the pillar axis. In order to probe this behaviour, only the position of the laser spot is changed. The other parameters of the experimental setup such as excitation power and laser spot size are the same as for the central excitation case which is presented above.

The result of an experiment based on an off-axis excitation is shown on Figure 4.22. In order to be able to better observe the position of the modes, the color scale of the streak camera was cut off at a lower value compared to the previous images.

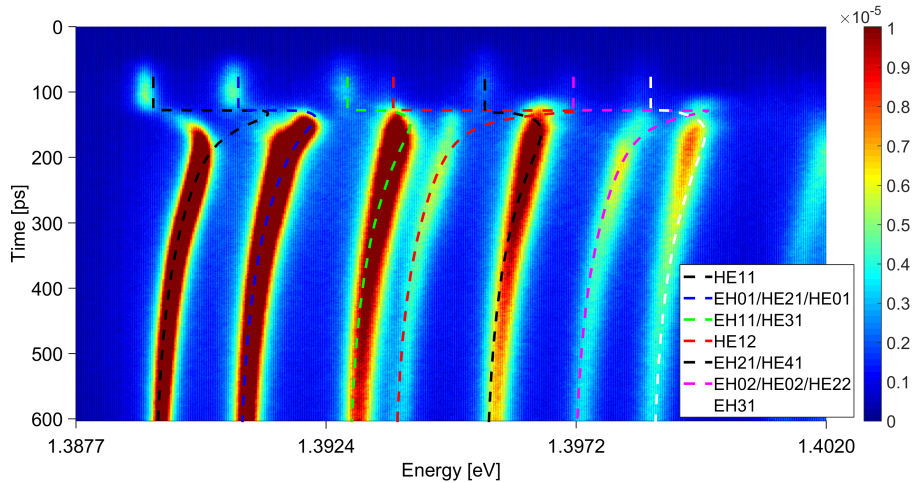


**Figure 4.22** Streak camera image of a micropillar excited with a pump laser spot position close to the border of the micropillar. Comparing the mode positions to those simulated for a central excitation (and thus also to the experimental results) reveals a drastically different behaviour during the first 50 ps of the switch.

The lines which are plotted in the image show the simulated position of the on-axis case. It is difficult to extract the experimental positions of the modes on Figure 4.18 because of the crossing of different modes. Since the simulation corresponds well to the experimental positions, they are used here as comparison for the off-axis experiment.

The switch takes place at  $t = 130$  ps. For all modes, the dynamics is similar to the one observed for on-axis excitation from  $t = 250$  ps on.

The fundamental mode (HE11) shows an exemplary behaviour for all modes with an antinode located at the pillar axis. It starts to shift into the blue nearly instantaneously, but takes about 50 ps to reach its maximum switching amplitude. After that, the same exponential decay behaviour as on Figure 4.18 takes place.

This indicates that immediately after the injection, the mode is not completely affected by the injected free carriers which are localized far from the mode antinode. Then, the free carriers diffuse and the concentration at the areas of high field intensity increases. This shifts the resonance frequency to higher energies. Approximately 50 ps after the switch, the concentration of the free carrier has reached a maximal overlap with the mode. From this moment on, the mode shifts to lower energies and shows a similar behaviour as in the case of central injection of free carriers. The maximal switching amplitude of 1.8 meV of the fundamental mode is significantly smaller than in the case of central excitation (3.2 meV). This is because of the decay of free carriers during the first 50 ps after the switch.

The modes which have a similar field intensity distribution (HE<sub>12</sub>, EH<sub>02</sub>/HE<sub>22</sub>/HE<sub>02</sub>) show a similar behaviour. Their maximal switching amplitude is significantly smaller than in the case of central excitation and is not immediately reached after the switch.

The second mode family (EH<sub>01</sub>/HE<sub>21</sub>/HE<sub>01</sub>) has its antinodes at approximately half distance between the border and the central axis (cf. Figure 4.3) which is closer to the laser spot than for the HE<sub>11</sub> mode. After the switch, the maximum is reached after a few picoseconds delay defined by carrier relaxation. The switching amplitude is as large as (but not larger than) in the case of an on-axis excitation. This results from the carrier distribution which does not match the whole region where the modes have a large field intensity.

A small bump is also visible at  $t = 150$  ps and indicates a splitting of a mode. Due to the circular symmetry of the pillar, the EH<sub>01</sub> has a twofold degeneracy. The localized, non-central injection of free carriers lifts the circular symmetry and triggers thus a splitting between the energy of this twofold degenerated mode.

Then, the resonance of this mode family shifts to lower energies. Similar behaviour is observed for the other mode families showing similar, donut-like field patterns (EH<sub>11</sub>/HE<sub>31</sub>, HE<sub>41</sub>/EH<sub>21</sub>, EH<sub>31</sub>).

The non-central injection of free carriers is a further qualitative proof for the predictions and models that have been presented in previous sections.

## 4.4 Conclusion

Results of differential switching of modes of a micropillar with diameter of 5  $\mu\text{m}$  have been shown in this chapter. An ensemble of embedded QDs allows probing of several micropillar modes at any given time and facilitates the experimental handling compared to pump-probe experiments drastically.

By injection of free carriers at well defined positions in the micropillars, the resonance position of all modes was shifted. The anisotropic injection of electrons and holes and the resulting different overlaps between the free carrier concentration and the mode field profile allows a strong variation of switching amplitudes and switch-on dynamics of different modes. Modifications of mode ordering can also occur for large switching amplitudes and strongly focalized pump beams. Consequently, it is possible to modify significantly the modal structure of a pillar microcavity during several tens of picoseconds, using this approach.

The resulting streak camera images are well explained by a model based on diffusion and different recombination speeds of free carriers in bulk material and at surfaces. Based on this model, FEM simulations were performed to calculate the resonances of the different cavity modes. The validity of our model is confirmed by an excellent agreement between simulation and experimental data and confirms the used modelization.

To sum it up, probing of cavity modes from inside by QDs can be seen as an attractive approach to detect cavity dynamics on picosecond time scales.

Besides that, differential switching is also promising for performing CQED experiments. It offers the possibility to precisely control the interaction time of a single QD or an ensemble of QDs and the cavity. Compared to homogeneous switching processes [96], the presented technique offers more flexibility.



# Oval ring cavities: properties, lasing, emission behaviour and switching

Microdisks are nowadays widely used resonator types. Despite their advantages such as high quality factors and low effective volumes, these circular structures based on whispering gallery modes (WGM) also present drawbacks such as an isotropic emission pattern.

By breaking the symmetry of these resonators, it is possible to influence their emission pattern and to make the emission more directional.

In this work, we investigate a novel cavity geometry: oval ring resonators. This cavity geometry seems promising to provide a more directive emission pattern without a significant decrease of the quality factor. Because of its large spatial extension, this cavity structure might also be useful for observing a real-time control of the Purcell effect.

In the first section, an overview of WGMs and our novel resonator geometry is given. Measurements of the basic properties of the resonator, such as the modal structure, the quality factor and the Purcell factor are described in the second section. At last, we investigate properties of active oval cavities. Lasing under optical pumping, a more directive emission behaviour and cavity switching are demonstrated in these experiments.

## 5.1 Principles of oval ring resonators

Oval ring resonators are inspired by a potential improvement compared to circular microdisks or microrings. These resonators are based on whispering gallery modes. I explain the properties of these modes and introduce the oval ring resonator shape in this section.

### 5.1.1 Whispering gallery modes

The expression “Whispering gallery modes” (WGM) originates from an acoustic phenomenon. It was known since a long time that in large circular buildings, people could talk at a large distance while whispering, provided that they did so close to the walls. This was properly explained at the end of the 19<sup>th</sup> century by Lord Rayleigh who discussed such a phenomenon that occurred on the cornice below the dome of Saint Paul’s cathedral in London. The effect originates from the propagation of acoustic waves close to the circular wall.

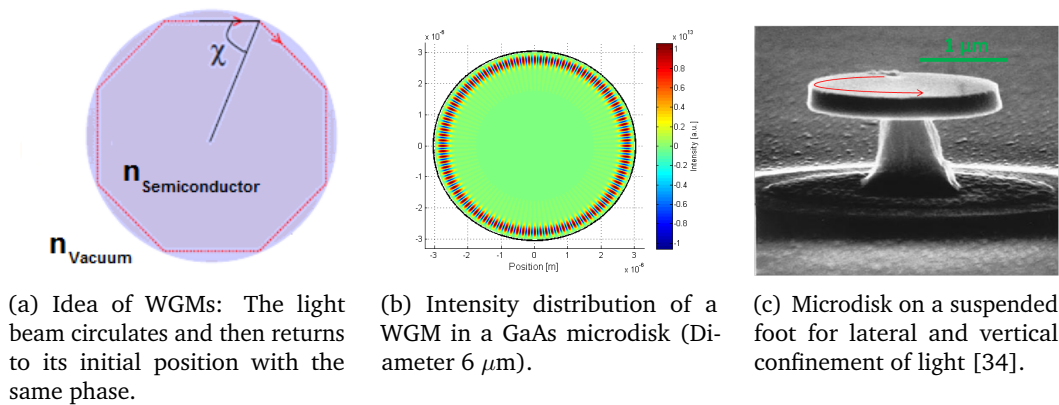


Figure 5.1 WGM patterns and experimental realization.

Optical WGMs are so called because of the analogy: In the geometric optics image, WGMs can be viewed as a light ray that propagates along the boundary of a circular cavity where it repeatedly hits the semiconductor/air interface at an incidence angle larger than the angle of total internal reflection. Thus, it is reflected again and again and the light is laterally confined in the cavity. If the light ray is phase-matched with itself after one roundtrip, it interferes constructively and a WGM is formed (cf. Figure 5.1(a)).

In the wave optics picture, standing waves appear. The field distribution, which is depicted on Figure 5.1(b), shows that the maxima of such a standing wave are well localized at the boundary of the disk. The mode is centrosymmetric, relative to the resonator axis.

An experimental realization of a WGM resonator is depicted on Figure 5.1(c): A several hundred nanometer-thick disk is held suspended on a pedestal. Both disk and pedestal consist of a semiconductor material that has a high refractive index. The light is confined both vertically between the disk plane faces and laterally by total internal reflection. Note that the pedestal dimension must be significantly

reduced compared to the disk radius in order to have the smallest possible influence on the confined modes of the microdisk. As can be seen in Figure 5.1(b), the field maxima are localized close to the edge of the disk and the field is vanishingly small close to the center of the disk. Hence, a sufficiently small pedestal does not influence the mode structure.

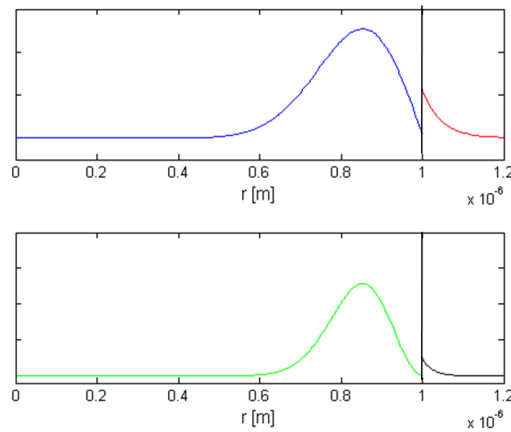


**Figure 5.2** WGM characteristics in circular microdisks: Electric field and intensity of a cavity mode.

The first experimental realization of a semiconductor microresonator which showed WGM behaviour was achieved by McCall et al. in 1992 [68]. They fabricated microdisks with a diameter of 3 to 10  $\mu\text{m}$  and thicknesses of 50 nm held on a pedestal. The material was the InP/InGaAsP system, where the integrated emitters were 10-nm thick InGaAs quantum wells, from which they obtained lasing.

The electromagnetic field structure in microdisks can be calculated following approaches described in [13, 64]. These calculations result in a radial field distribution as shown on Figure 5.2. As can be seen, a small, evanescent part of the field lies out of the microdisk, which is, combined with the curved character of the lateral sidewall of the disk, the cause for some intrinsic losses [29].

### 5.1.2 Ring microcavities

Even though microdisks on a pedestal offer very promising properties like high  $Q$  factors around  $10^5$  [105] and small effective volumes, they also present several drawbacks.

Firstly, electrical pumping is quite difficult because no charge carriers can be directly injected close to the circumference of the disk. Injecting carriers is possible only via

the pedestal which holds the center of the disk. Pumping emitters that are close to the sidewall of the disk is thus very difficult. This represents a drawback, because photon emission only in these zones would contribute significantly to WGMs.

The small pedestal is also the origin of another disadvantage of suspended microdisks: bad thermal properties. Heat, which is generated by non-radiative recombination of carriers, diffuses very slowly towards the substrate via the — thin — disk and the pedestal. This is a severe drawback for continuous-wave lasing at room temperature.

Munsch et al. [70] solved these problems in 2012 by using a microdisk without a pedestal, directly on the substrate. The increased contact surface of the resonator with the substrate improves heat sinking properties. By using a sandwich of doped confinement layers (AlGaAs) on the top and the bottom of the guiding layer (GaAs), injecting carriers and thus electrical pumping of emitters (InGaAlAs-quantum dots) was possible up to 300 K.

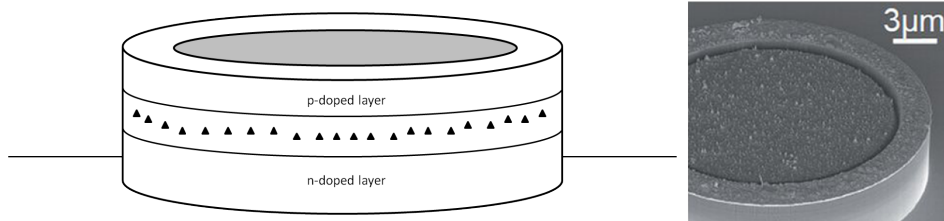


**Figure 5.3** Sketch of the micro-ring/disk cavity. The central, grey part is removed to obtain a microring. The triangles stand for the quantum dot emitters. The  $p$ - and  $n$ -doped layers allow injection of carriers. The central layer is the wave guiding layer. A SEM image [70] of this resonator is shown on the right side.

The authors also removed the inner part of the microdisk, thus transforming it into a microring.

With a full disk geometry, the light emitters in the center of the disk, which do not contribute to WGMs, can be regarded as parasitic recombination centers. In order to obtain a low lasing threshold, pumping of these emitters should therefore be avoided, hence the interest of the microring. Beside, the broader a ring resonator, the larger its lasing threshold.

Another advantage is the suppression of higher order radial modes. If the lateral extension of the ring is small enough, WGMs with field maxima at higher distances to the boundary will not exist anymore.

Figure 5.3 shows a sketch and a SEM image of a microring used by Munsch and coworkers. Compared to a microdisk, the central, grey area is removed in order to obtain the microring geometry.

With these devices (diameter  $\approx 10 - 100 \mu\text{m}$ ),  $Q$  factors of 60000 were realized, and optically and electrically pumped lasing at room temperature could be observed.

Despite of all these advantages, microrings also share one big disadvantage with microdisks: The non-directional emission of light. The emission into an azimuth angle of  $360^\circ$  causes difficulties to detect strong signals in quantum optics experiments. In the work of Munsch et al. [70], an optical fiber (placed at a distance of a few micrometers from the sidewall) had to be used to collect light and to measure the emission spectra.

In order to simplify experiments, a more directional emission is desirable. A directional lasing source could also be important for future optoelectronic applications.

### 5.1.3 Asymmetric microcavities

During the last decade, many efforts were made in order to make the emission of WGM microcavities more directional. Several different shapes were proposed, using different methods.

The general problem of directional emission is the need to remove the cylindrical symmetry of the resonators. If emission into a certain direction is required, the shape of the resonator has to be changed.

But the drawback of these changes is the resulting behaviour of these deformed disk cavities. Cavities that do not possess a circular or elliptical shape suffer from chaotic behaviour. This affects their mode spectra; clear, equally spaced and predictable peaks cannot be observed anymore. Other advantages of the microdisk resonators are affected as well: the quality factor decreases because of the uncontrolled outcoupling of photons, and the modal volume grows because modes are no longer confined close to the boundary. Nevertheless, different ways to obtain directional emission were proposed. A detailed review about chaotic microcavities is given by Cao and Wiersig [17].

One possible approach is the introduction of point-like defects in the resonator wall, where the size of the defects is of the same order of magnitude as that of the guided modes. The photons are deviated and leave the resonator directly (cf. Figure 5.4(a,b)).

This method provides high directivity, but suffers from relatively low quality factors as a result of these artificial defects.

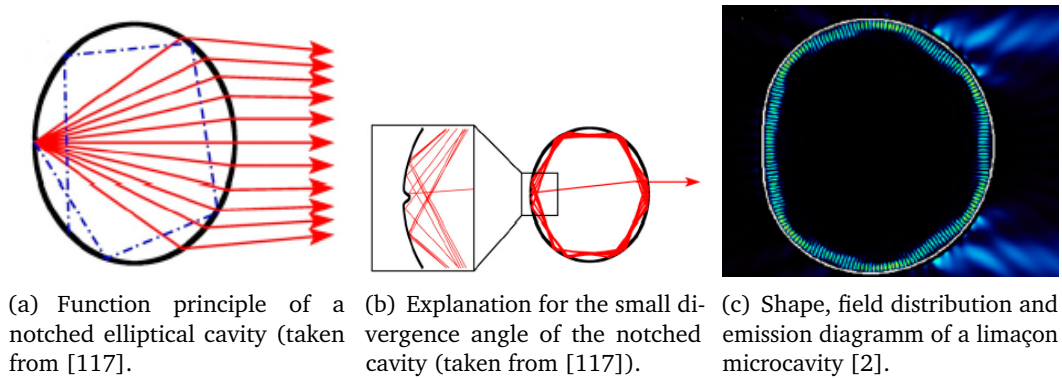


**Figure 5.4** Different resonator shapes for obtaining directional emission.

As an example, Wang et al. [117] achieved a beam divergence of  $6^\circ$  and lasing for a quantum cascade laser emitter. The shape of the cavity was elliptical and a little notch was etched on the sidewall. The measured  $Q$  factor was 1260, which is an acceptable value for these large wavelengths.

Another approach is the use of limaçon-shaped resonators, as was proposed by Wiersig and Hentschel in 2008 [118]. These have a slightly deformed circular shape which might provide chaotic behaviour as well (depicted on Figure 5.4(c)). Simulations showed that the combination of wave-localization and chaotic ray dynamics results in a mechanism that provides directional emission. It was also shown that the supported mode is confined close to the resonator wall despite of its chaotic behaviour.

This family of resonators has already been experimentally investigated: for a  $2\ \mu\text{m}$ -sized limaçon resonator that consisted of a GaAs disk with embedded InAs-quantum dots, Song et al. obtained an output beam divergence of  $30^\circ$  and a quality factor of 10000 [104].

Based on the same emitters, Albert et al. investigated micropillars with GaAs/AlAs mirrors. They achieved the same results concerning directionality, and a higher  $Q$  factor of about 40000 for  $10\ \mu\text{m}$ -sized resonators [2].

### 5.1.4 Oval microcavities

In the frame of this work, a different approach was used to obtain directional emission behaviour: The shape of an oval ring.

## Shape of the cavities

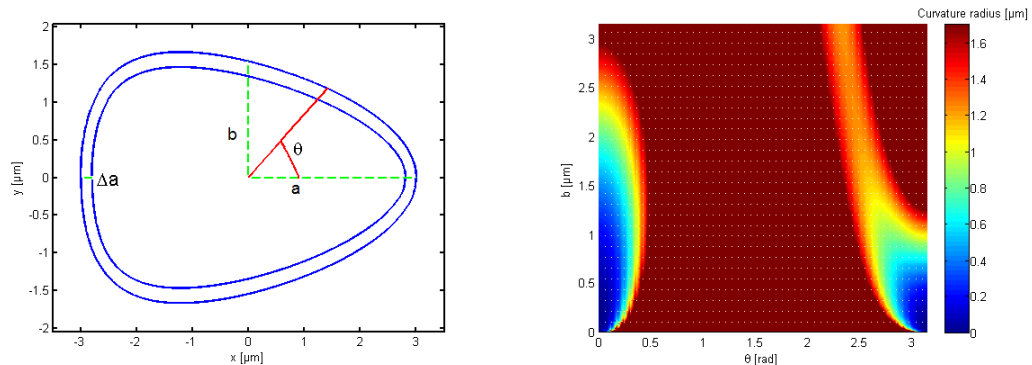
Like ellipses and limaçons, oval cavities have a varying curvature radius. The difference between them is their symmetry vs. the vertical and horizontal axis: An ellipse is symmetric with respect to both axes, whereas an oval is symmetric only with respect to the horizontal axis. The oval has a tip on one side and a blunt backside (see Figure 5.5(a)).

Now, we apply the same principles as in subsection 5.1.2: By removing the inner part of the resonator, and using a ring-shaped resonator with a lateral extension of the same order of magnitude as the wavelength, the resonator confines the photons in two dimensions, and guides them. As in the circular ring case, the pumping of emitters that do not contribute to the modes is prevented.

In the oval resonator, a second advantage of the ring structure takes place as well: chaotic behaviour, which is expected for non circular- or elliptical-shaped resonators, can be suppressed because of the guiding of light at the inner and outer wall of this waveguide-like structure.

The WGM properties are also expected to be preserved. The curvature radius of the resonator varies adiabatically, i.e., there is a continuous transition between its curvature radii, which leads to the smooth guiding of the photons in the resonator and thus to good quality factors. The small effective volume of the modes is also conserved.

Furthermore, one expects the oval to present a directional emission pattern, i.e., emit over a small azimuth angle.



(a) Shape of an oval ring resonator.  $a$ ,  $b$  and  $\Delta a$  are the dimensions of the resonator, whereas the position on the ring is defined by the angle  $\theta$

(b) Dependence of the curvature radius on angle  $\theta$  and parameter  $b$  ( $k = 0.7, a = 3 \mu\text{m}$ ).

**Figure 5.5** Shape and curvature radii of a resonator.

The shape of the oval is governed by the following equation:

$$\frac{x^2}{a^2} + \frac{y^2}{b^2} \left(1 + \frac{kx}{a}\right) = 1 \quad (5.1)$$

where  $2a$  is the size of the oval in the x-direction,  $2b$  the y-extension at  $x = 0$  and  $k$  is the factor that induces asymmetry and the “egg-shape” (cf. Figure 5.5(a)).  $\Delta a$  is the thickness of the ring. The values for  $k$  ranged between  $k = 0.5$  and  $k = 0.7$  for all of the resonators considered. These values provide an asymmetric shape and prevent triangular ovals (with small curvature radii).

The curvature radius at the tip of the resonator (usually the smallest curvature radius) is given by:

$$R_{\text{curvature tip}} = \frac{b^2}{a(1+k)} \quad (5.2)$$

Figure 5.5(b), where the curvature radii at different positions (depending on the angle  $\theta$ ) and for different  $b$  are depicted, shows that the conditions that we impose on the geometry of the ovals can be fulfilled. For  $b \approx 1.5 \mu\text{m}$  the curvature radius of the resonator is smaller than  $0.5 \mu\text{m}$  only at the tip of the resonator.

### Losses in oval ring resonators

In a semiconductor disk, three different kinds of energy/photon losses coexist: intrinsic, scattering and absorption losses.

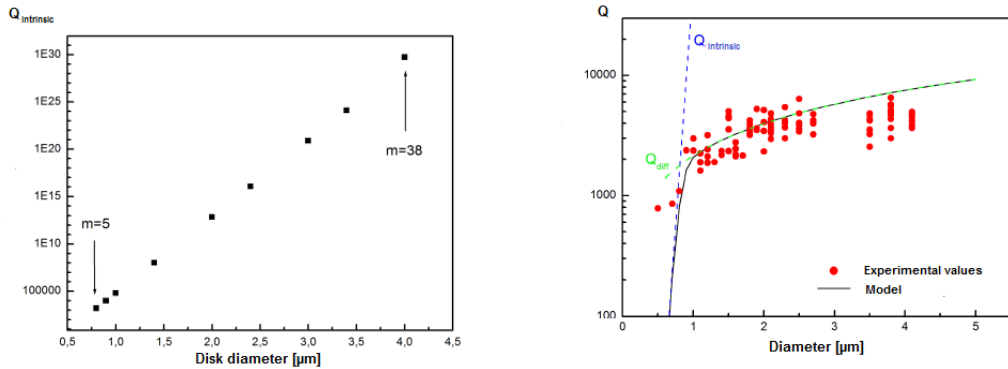
Let us consider working in the so-called low-loss regime of microdisks. In this regime, losses during one optical cycle are very small compared to the stored energy. Since the quality factor  $Q$  is inversely proportional to the total loss rate, one can write it as resulting from the different loss contributions as follows:

$$\frac{1}{Q} = \frac{1}{Q_{\text{intrinsic}}} + \frac{1}{Q_{\text{scattering}}} + \frac{1}{Q_{\text{absorption}}} \quad (5.3)$$

First, let us consider empty microcavities, i.e., cavities which do not contain emitters. The absorption losses can thus be neglected in a first step.

Intrinsic losses appear because of the curved boundary of the microdisk. They can be explained as tunneling of photons through the “potential barrier” (defined by the refractive index difference) of the microdisk wall (see Figure 5.2). The intrinsic

quality factor  $Q_{\text{intrinsic}}$  grows exponentially with the curvature radius of the microdisk (cf. Figure 5.6(a)).



(a) Exponential dependence of intrinsic losses of a microcavity on the radius (for WGMs in GaAs microdisks for energies close to  $E=1.3 \text{ eV}$ ).

(b) Combination of intrinsic and scattering losses in circular disk microcavities. For diameters above  $\approx 0.8 \mu\text{m}$ , scattering losses determine the  $Q$  factor, whereas below that limit, intrinsic losses dominate.

**Figure 5.6** Dependence of  $Q$  on the loss sources [77].

Hence, up from a radius of about  $0.8 \mu\text{m}$ ,  $Q_{\text{intrinsic}}$  becomes very large and the intrinsic loss contribution to  $Q$  becomes negligible.

From that curvature radius on, the second source of losses, scattering losses, becomes dominant. Scattering losses are the result of wall roughness, which originates from imperfections in the manufacturing process. The WGMs, which propagate close to the disk boundary, are thus suffering from losses because of scattering.

As can be seen on Figure 5.6(b), this contribution grows linearly with the radius. Nowicki-bringuier et al. [77] proposed for that an approximate approach, applied to circular microdisks:

$$Q_{\text{diff}}^{-1} = \epsilon I(R, \theta, 0) S \quad (5.4)$$

where  $S$  is the surface of the microdisk walls,  $\epsilon$  a coefficient that quantifies the quality of the surface and  $I$  the intensity at the boundary which has been normalized to the intensity distributed over the whole disk. We will use this to quantify the quality of our samples (cf. Figure 5.15).

The third origin of losses is the absorption of light by the materials forming the cavity, i.e., the waveguide material and the emitter material. Below its bandgap, the

waveguide material is transparent. In the case of a larger energy for pump photons, free carriers are created but quickly confined by the QDs.

By pumping below the bandgap of the waveguide material, at high intensities, one can make sure that the QD emitters are already in the excited state and cannot absorb photons any longer. Thus, for such experimental conditions, we can neglect the absorption by the QDs. However, at low intensities, even though the QD absorption is very small, it will be dominant if the quality factor  $Q$  of the empty cavity is sufficiently high.

## 5.2 Design, fabrication and optical characterization of oval cavities

The samples are fabricated taking into account the points given in the previous section.

First of all, the base material of the sample has to be produced. It consists of a substrate onto which different layers are epitaxially grown. An oval ring resonator should consist of layers of materials with different refractive indices in order to constitute a planar waveguide for the light.

Then, the sample is structured as detailed in section 2.1, and analysed with a microphotoluminescence setup.

### 5.2.1 Vertical structure of the substrate

In order to ensure the use of a low defect density, high quality material for the resonators, the growth of the sample is performed with MBE.

During this work, two different samples were used:

#### **Sample AS0157**

AS0157 consists of a  $\text{Al}_{0.8}\text{Ga}_{0.2}\text{As}$  bottom cladding (1250-nm thickness), onto which a 240-nm thick layer of GaAs (acting as the waveguide) is grown, with an embedded QD layer (cf. Figure 5.7(a)).

For the growth of the QDs, 1.9 monolayers of InAs were deposited on the sample. The density of the QDs is of the order of  $100 \text{ QD}/\mu\text{m}^2$ .

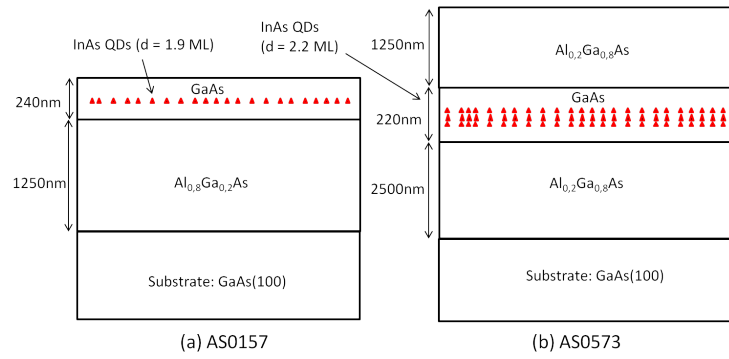


**Figure 5.7** Composition of the vertical structure of the different samples.

The position of the waveguide at the top of the resonator has the advantage of a better control over its shape. Under-etching processes are not as striking as for waveguides which are located deeper in the structures.

The disadvantage comes from the asymmetric confinement of the guided waves. The maximum of the wave is shifted from the position of the QD layer, which leads to a weaker coupling to the QDs.

### Sample AS0573

AS0573 is a sample with three embedded layers of InAs QDs (grown from 2.2 monolayers each), and thick  $\text{Al}_{0.2}\text{Ga}_{0.8}\text{As}$  claddings around a 220 nm-thick GaAs guiding layer (see Figure 5.7(b)). This guarantees that a large number of QDs couples to the cavity mode — which is required to get enough gain for lasing, and that the guided mode is centered on the waveguide. The outer QD layers are located at 85 nm from the  $\text{Al}_{0.2}\text{Ga}_{0.8}\text{As}/\text{GaAs}$  interfaces.

## 5.2.2 Setup for optical characterization

The work on oval ring resonators was performed with the experimental microphotoluminescence setup described in chapter 4.

The main difference between photoluminescence experiments with micropillars and with ring resonators is related to their drastically different emission patterns. In the case of micropillars, photons are mostly emitted along the pillar axis and are thus easily detectable.

In the case of oval ring resonators, the emission pattern is completely different. If a QD emits a photon into the cavity mode, one can distinguish between two different

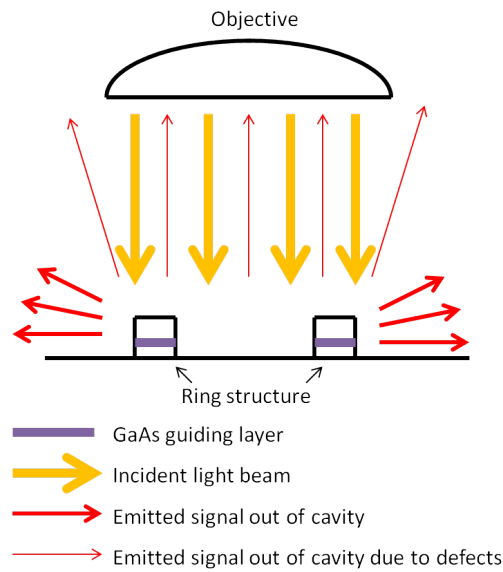


**Figure 5.8** Sketch of the emission direction of oval ring resonators. In this configuration, scattering by defects leads to the detection of modes.

regimes of emission of a photon out of the cavity mode. Photons propagate in the waveguide structure, which lies in the horizontal plane, orthogonal to the vertical growth axis of the structure. Most of the photons are emitted close to this waveguide plane via intrinsic and scattering losses (thick red arrows on Figure 5.8).

A much smaller part of the photons is scattered at large angles relative to this plane and leaves the waveguide close to the growth axis (fine red arrows).

The intensity ratio between these two emission “directions” is governed by the quality factor. The larger the quality factor, the more the radiation diagram shows intrinsic behaviour. For large  $Q$  factors, the scattering of photons towards the detector optics becomes less probable; it thus becomes more and more difficult to detect emission from high- $Q$  modes.

The spectrum of an ideal cavity with ultra-high  $Q$  would not show peaks. Because of the Purcell effect, all of the light emitted by the QDs that are in resonance with a cavity mode would be emitted into the cavity plane, where they cannot be detected. In this work, a minimal amount of scattering losses is needed in order to get some photons from the cavity modes sent in our detection optics with moderate NA ( $NA \leq 0.6$ ). As shown in subsection 5.3.2, additional scatterers can also be placed nearby the micro-ring to improve the collection of the ring emission by our setup.

## 5.2.3 Modal structure

In order to go further, and for future applications, we need to determine the modal structure of the devices.

### 5.2.3.1 Qualitative discussion of the spectra

Herein, I qualitatively discuss some of the spectra obtained on sample AS0157. Some representative examples are depicted in Figure 5.9. These spectra were taken in the pulsed mode of the excitation laser, with wavelength set at 800 nm and power at  $150 \mu\text{W}$ . Continuous wave excitation provides similar results.

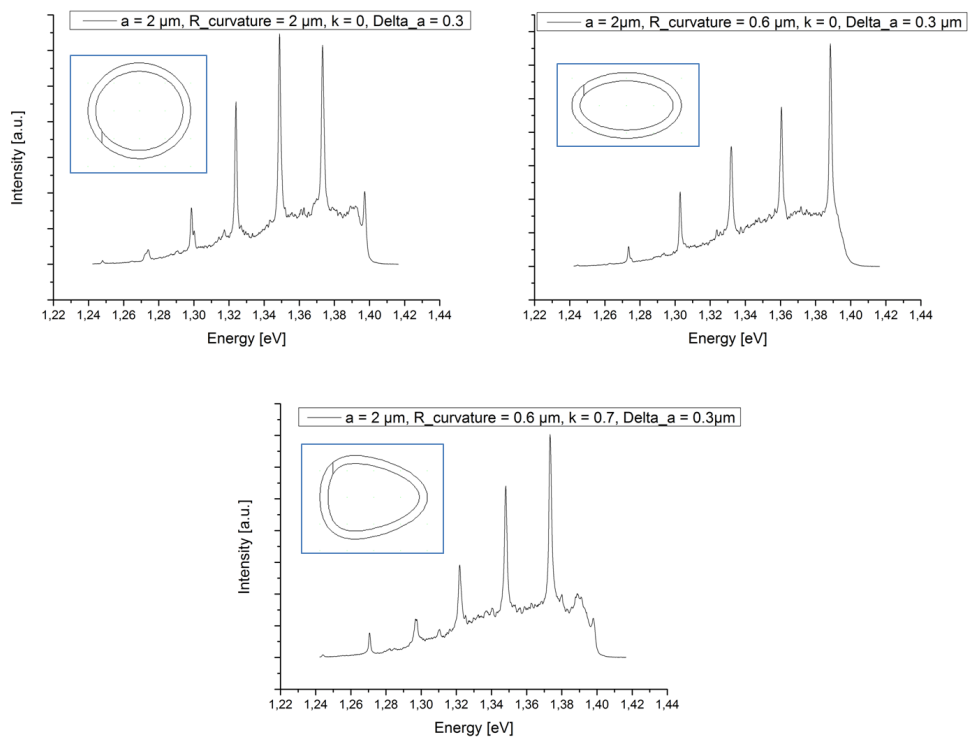


**Figure 5.9** Spectra of resonators with different forms: circle, ellipse and oval. The shape of the resonator is shown in the inset, the resonator data are described in the legend of the respective spectra. Measured intensities show the same behaviour: clearly separated, discrete mode peaks. The intensity background results from non-resonant emission of the QDs. The peaks indicate positions of resonance energies. The cutoff at 1.4 eV results from the use of a lowpass filter.

The spectra show the same qualitative behaviour for different resonator shapes. I measured PL spectra for a circle ( $R = 2 \mu\text{m}$ ), an ellipse ( $a = 2 \mu\text{m}$ ,  $b = 1.1 \mu\text{m}$ ) and an oval ( $a = 2 \mu\text{m}$ ,  $b = 1.6 \mu\text{m}$ ,  $k = 0.7$ ). The waveguide width  $\Delta a = 0.3 \mu\text{m}$  was the same for all structures.

First, we can observe a background signal that results from the emission of the QDs in the sample. The QD signal is inhomogeneously broadened and covers a large spectral range starting from 1.26 eV. A lowpass filter cuts off all signal at  $\approx 1.4$  eV. We also observe a comb of regularly spaced peaks on top of that background. The peaks' positions show the resonance energies. They have the same shape for different geometries and show a large intensity contrast relative to the background signal.

In the case of circular rings (cf. Figure 5.9), it is well known that the peaks stem from WGMs, and the background is created by the emission of the QD ensemble into the continuum of non-resonant modes [70]. The similarity of the spectra for different geometries is a first indicator that also the modes for elliptical and oval rings are WGMs.

One can also observe that, for a given structure, the Free Spectral Range (FSR, i.e., the energy spacing between two consecutive peaks) is nearly constant. This suggests that we observe a single family of WGMs.

In the case of our microstructures, the optical dipole of the QDs is oriented in the plane. Thus, only TE modes can be fed by the QDs.

Being vertically positioned at the center of the waveguide, only the waveguide fundamental mode couples to the QDs. Because of the vertical extension of the waveguide, only two modes should exist, but the second mode has a node on the QD layer, so the QD emission should not couple to that mode. In the radial direction, the resonator supports only the fundamental radial mode for  $\Delta a = 0.3 \mu\text{m}$ .

Simulations with **COMSOL**, a program based on the finite element method (FEM), confirm this qualitative behaviour. Figure 5.10 shows the computed electric field norm for different (circular, elliptical and oval) resonator shapes. The simulated resonators have the same dimensions as the resonators whose microphotoluminescence signal was measured. The electric field has the same WGM-like shape for all three simulated resonators.

In summary, the experiments and simulations confirm that WGMs can be observed in oval ring resonators. Figure 5.10(c) shows that the ring shape of the oval resonator suppresses chaotic behaviour of the resonator mode since a standing wave with well defined nodes and antinodes is observed in the oval ring resonator.

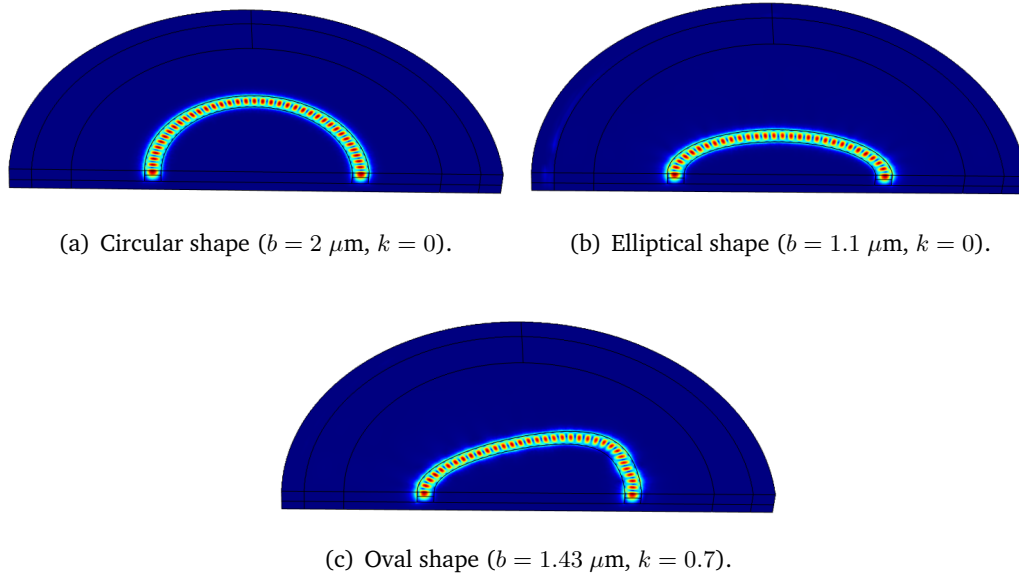


**Figure 5.10** COMSOL simulations showing the computed electric field norm for resonators of different shapes. The simulations were made for  $E \approx 1.3 \text{ eV}$ ,  $\Delta a = 0.3 \mu\text{m}$ ,  $a = 2 \mu\text{m}$ . Despite the different resonator shapes, the field patterns of the modes are similar.

### 5.2.3.2 Modal study as a function of the ring width

We investigate resonators with different lateral widths  $\Delta a$ , in order to confirm the assumption made on the radial extension of the higher order modes. For larger  $\Delta a$ , the maxima positions of these modes are inside the waveguide material.

Thus, several families of radial modes are expected to appear in the spectra of resonators with larger  $\Delta a$ .

The spectra shown on Figure 5.11 were measured on resonators with the following parameters:  $a = 3 \mu\text{m}$ ,  $R_{\text{c,tip}} = 0.7 \mu\text{m}$ ,  $k = 0.7$ ; the incident pulsed laser average power was  $150 \mu\text{W}$ .

We detected several smaller peaks between the principal resonance peaks for the resonator with  $\Delta a = 0.4 \mu\text{m}$ . This confirms that several radial mode series result in peaks of different heights, and ordered on ladders of different FSRs. The peak widths of these higher order radial modes are larger. They thus have smaller quality factors, which might be due to larger parts of these modes propagating close to the sidewall and outside the waveguide, therefore subject of larger scattering and intrinsic loss.

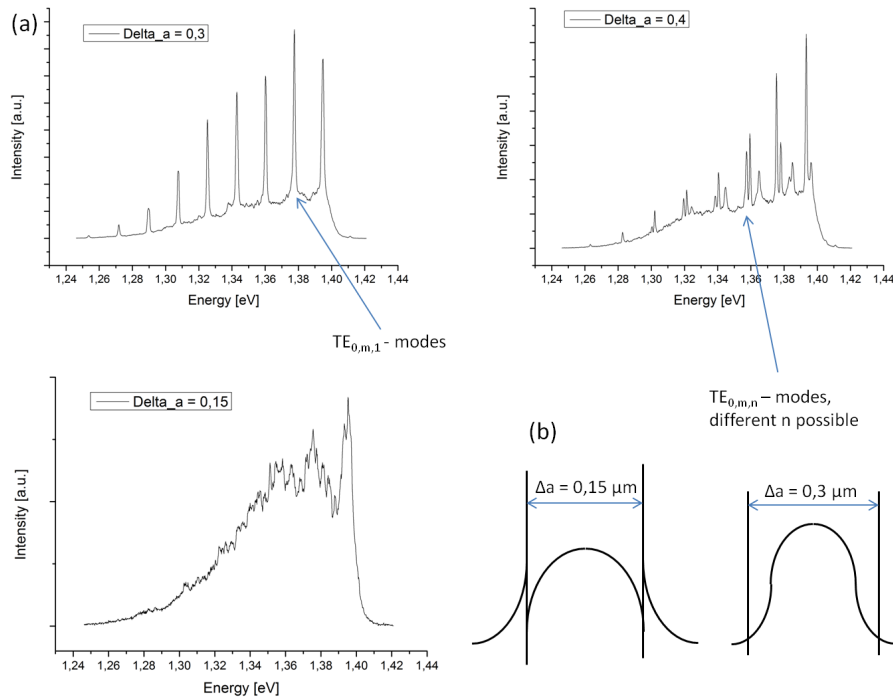


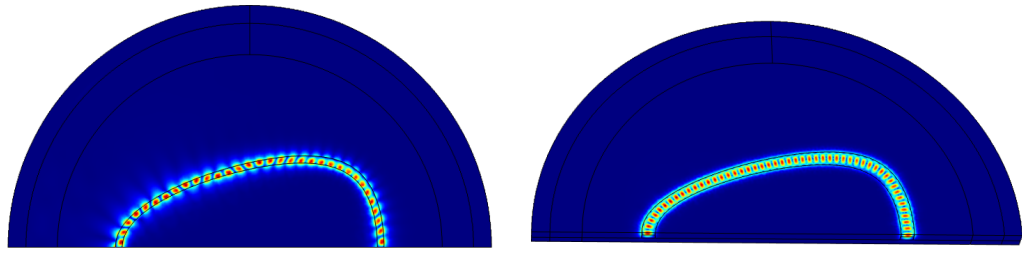
**Figure 5.11** (a) Spectra for samples with different  $\Delta a$ . We can observe several peaks of different families of radial modes for  $\Delta a = 0.4 \mu\text{m}$ . For  $\Delta a = 0.3 \mu\text{m}$ , there is only one family of peaks. For  $\Delta a = 0.15 \mu\text{m}$ , the clear peak structure disappears because of too large the FWHM of each resonance. An intuitive chart is sketched in (b), showing the fundamental radial mode field distributions for two  $\Delta a$  values.

A spectrum for  $\Delta a = 0.3 \mu\text{m}$  is also shown in Figure 5.11, in order to allow for a comparison. There, the FSR of the fundamental radial mode is the same as for  $\Delta a = 0.4 \mu\text{m}$ , which shows that changing the resonator thickness — in that range — has little influence on the fundamental radial mode.

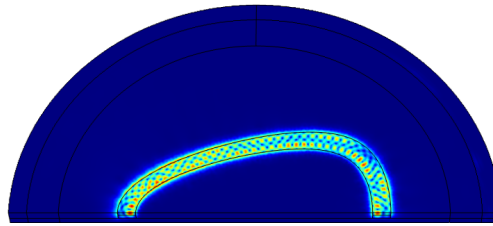
Still, the spectrum measured on the sample with  $\Delta a = 0.15 \mu\text{m}$  shows the limit on that property, as the clear peak structure of the broader rings completely disappeared.

If the waveguide width were approximately  $\lambda/n$  — which is the case for  $\Delta a = 0.3 \mu\text{m}$ , the largest part of the intensity would be confined in the guide, resulting in small optical losses. For  $\Delta a = 0.15 \mu\text{m}$ , in contrast, a large part of the wave propagates outside of the guide (cf. Figure 5.11(b)), which induces a higher loss rate of the mode energy. This higher loss rate equates with a smaller  $Q$ , and thus larger peak widths. The peaks become too broad to be resolved.

The computations shown in Figure 5.12 confirm this behaviour: there, I simulated oval cavities with (a)  $\Delta a = 0.15 \mu\text{m}$ , (b)  $\Delta a = 0.3 \mu\text{m}$ , and (c)  $\Delta a = 0.4 \mu\text{m}$



(a)  $\Delta a = 0.15 \mu\text{m}$ . A large part of the EM field for the fundamental radial mode leaks out of the resonator. (b)  $\Delta a = 0.3 \mu\text{m}$ . The fundamental radial mode is well confined within the resonator.



(c)  $\Delta a = 0.4 \mu\text{m}$ . A higher order radial mode in a resonator looks similar to higher order radial modes in microdisks, with the EM field leaking out of the resonator.

**Figure 5.12** COMSOL computations of the EM electric field norm, for resonators with different  $\Delta a$ .

( $a = 3 \mu\text{m}$ ,  $b = 1.89 \mu\text{m}$ ,  $k = 0.7$ ). (a) indicates that large parts of the EM electric field are outside of the resonator for  $\Delta a = 0.15 \mu\text{m}$ . Compared to the resonator with  $\Delta a = 0.3 \mu\text{m}$  (b), this results in much smaller computed quality factors:  $Q = 125000$  for  $\Delta a = 0.3 \mu\text{m}$ , whereas  $Q = 1550$  for  $\Delta a = 0.15 \mu\text{m}$ . In the experiment, the quality factors are significantly lower and the confined mode for  $\Delta a = 0.15 \mu\text{m}$  is not detected.

In Figure 5.12(c), we give a more detailed example of how a higher order radial mode looks like in an oval resonator. The computed  $Q$  factor is 17700.

## 5.2.4 Quality factor

After examining the modal structure of oval ring resonators, the quality factors of these objects were also measured. In this section, the validity of the  $Q$  measurements, using photoluminescence from QDs as an internal light source, is discussed. On the

basis of these results from the  $Q$  measurements as a function of different curvature radii, we show how promising oval rings can be designed.

#### 5.2.4.1 Operation of the quantum dots as internal light source

PL spectra such as the ones shown in Figure 5.9 provide information on the quality factor of the WGMs. However, these quality factors reflect the total losses of the system including the absorption by the QD active medium. Generally speaking, such experiments would reflect the  $Q$  of the empty cavity, if and only if the QD absorption losses were negligible compared to other losses.

In order to check whether the QD absorption losses are negligible or not, one can perform power dependent PL measurements. Through QD pumping, one can indeed saturate their absorption, so as to probe the “empty cavity”  $Q$ .

In photoluminescence experiments, we excite the samples with different laser power densities, in order to observe whether these power densities are large enough to saturate the QD emission. In the following, the parameters of the investigated resonator are  $a = 3 \mu\text{m}$ ,  $R_{\text{c,tip}} = 0.8 \mu\text{m}$ , and  $k = 0.7$ .

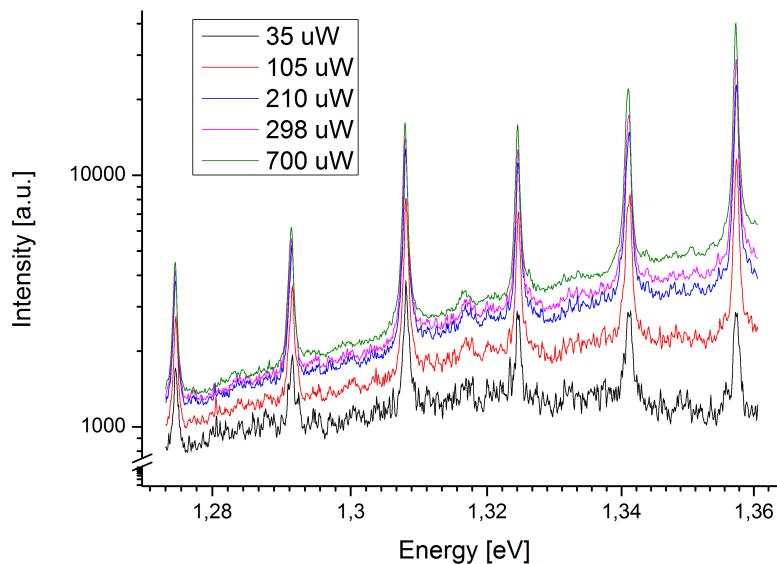


**Figure 5.13** PL spectra of an oval resonator ( $a = 3 \mu\text{m}$ ,  $R_{\text{c,tip}} = 0.8 \mu\text{m}$ ,  $k = 0.7$ ) for different pumping powers. The saturation of absorption threshold for the low energy modes of this resonator lies between  $210 \mu\text{W}$  (off resonance) and  $300 \mu\text{W}$  (on resonance). The available pumping power is therefore enough to suppress the contribution of the QD absorption loss on  $Q$ .

Figure 5.13 shows spectra for increasing pumping powers. At low intensities, we hardly see the WGMs, whereas a much better contrast is obtained for higher pumping powers.

At low photon energy (around 1.3 eV), the background intensity first increases linearly as a function of the incident power, then saturates for powers above 210  $\mu\text{W}$ . This behaviour is easily understood since the PL signal is proportional to the average number of excitons in the QDs. The saturation is reached when the first hole and electron levels are fully occupied (two excitons in each QD, because of spin degeneracy).

The same behaviour is observed for the WGMs. However, the saturation is reached for a larger pumping power, around 300  $\mu\text{W}$ .

From these observations, we can infer that :

- The saturation of the WGM intensity shows that lasing is not achieved for this microcavity: the gain provided by the ground states of the QDs is not large enough to overcome the losses of the empty cavity.
- The observation of a higher saturation power for the WGM intensity can very likely be attributed to the Purcell effect. The QDs that are coupled to the WGMs should experience a faster exciton recombination. After having emitted a photon, such QDs can capture an additional exciton from the reservoir (in this case: the wetting layer where excitons are generated by the pumping laser pulses) and emit another photon. This effect explains why the contrast from the WGMs to the background improves for higher pumping powers.
- This experiment enables us to estimate the power for which one exciton on average is captured in a QD ( $105 \pm 12 \mu\text{W}$ ). This is a very useful information, since it tells us for which pumping power the absorption of the QDs is bleached.

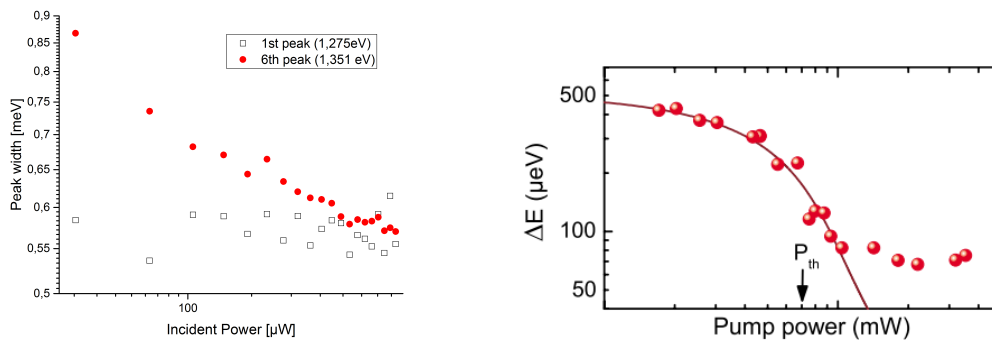
As a remark, we can add that resonant optical modes are only to be seen at energies smaller than the bandgap of the InAs wetting layer (at 1.46 eV), which lies below the bandgap of the bulk GaAs and AlGaAs layers, because we certainly cannot saturate the absorption of these large density of states layers for the power densities available on our experimental setup.

The absorption contribution from the QDs to  $Q$  can be written as:

$$\frac{1}{Q_{\text{absorption}}} = \frac{\alpha\lambda}{2\pi n_{\text{eff}}}(1 - \langle x \rangle) \quad (5.5)$$

where  $\langle x \rangle$  is the ratio between the QDs containing an exciton and the total number of QDs that present an absorption line at the mode energy, and  $\alpha$  the modal absorption coefficient. By filling all of the QDs that would absorb at this energy ( $\langle x \rangle \approx 1$ ), we can eliminate this contribution.

In order to estimate the contribution of  $Q_{\text{absorption}}^{-1}$ , we measure the  $Q$  factor of our microrings at different incident pump powers. When the saturation limit is reached,  $Q_{\text{absorption}}^{-1}$  tends to zero. We therefore expect larger experimental  $Q$  factors for larger excitation powers.



(a) Peak FWHM vs incident power. The FWHM — and the  $Q$  factor — of the first optical mode peak is nearly constant, at odds with the expected behaviour. The FWHMs of the other optical mode peaks go down, as expected.

(b) Expected behaviour of the optical mode FWHM for a QD microresonator based on WGMs. The inferred  $Q$  increases significantly, by a factor of about 5, before reaching the lasing threshold [51].

**Figure 5.14**  $Q$  factor variation: experimental results (a), and expected behaviour (b).

The measured peak FWHM values for the first optical mode (Figure 5.14(a), empty squares) do not show the expected behaviour as for example shown on Figure 5.14(b) where the peakwidth decreases from 0.45 meV to 0.08 meV. The peakwidth of the lower energy mode ( $\approx 1.275$  eV) decreases slightly with growing incident intensity.

In the case of the higher energy mode where excited states contribute to the intensity, a different behaviour is observed: the peak width decreases from 0.87 meV to 0.57 meV. From this, I conclude that the excited states are not completely filled.

Jaffrennou et al. [51] measured values that show a really significant change of the  $Q$  factor of around one order of magnitude, whereas the values measured in this PhD thesis almost stay constant for the peak of ground states (in this experiment, it was measured below the lasing threshold, in the spontaneous emission regime).

In Jaffrennou's case, the  $Q$  factors of the WGM modes are governed by the losses related to the absorption by QDs. This is due to the small magnitude of scattering losses ( $Q_{\text{scattering}} \approx 20000$ ,  $Q_{\text{abs}} \approx 8000 - 12000$ ).

It can thus be concluded that the absorption of the QDs in the resonators causes small losses. On the opposite, losses are dominated by scattering, which can be traced back to the sidewall roughness.

Here, absorption only gives a little contribution to the real  $Q$  factor which is dominated by diffusive and intrinsic losses. Thus, varying the incident intensity does not change the  $Q$  factor significantly.

#### 5.2.4.2 Dependencies of the quality factor

In this section, results of measurements of the  $Q$  factor as a function of the oval shape are presented:  $Q$  factors of different ovals are measured and the incident laser power is kept at a constant level. As shown in the above section, the contribution of the absorption to the  $Q$  factor can be neglected.

##### Measurements of the quality factor

The experiments were performed at a constant,  $I = 150 \mu\text{W}$  laser power, with the following, fixed parameters for the oval microrings:  $k = 0.7$ ,  $\Delta a = 0.3 \mu\text{m}$ , and  $a = 3 \mu\text{m}$ . We varied the curvature radius at the tip of the ovals as a parameter.

The results of the measurements and the predicted values of our model are depicted in Figure 5.15. Quality factors around 2000 were measured for resonators of different tip radii  $R_{\text{c,tip}}$ . The largest  $Q$  value was measured at 2400 for a structure with  $R_{\text{c,tip}} = 1 \mu\text{m}$ .

For fitting the measured values with Equation 5.4, two different  $\epsilon$  (average:  $\epsilon = \frac{1}{400}$ , or maximum:  $\epsilon = \frac{1}{550}$ ), which fit well the experimental data, were used. This quantifies the impact of the wall quality  $\epsilon$  on the  $Q$  values of the microring resonators.

The first observation from the measurements is the good qualitative and quantitative agreement to the predicted values of the model. The measured  $Q$  factors have the same slightly growing behaviour as those of the computed values. The two curves increase apparently with the same slope as a function of the curvature radius.

The measured microrings had a radius too big to enter the regime where intrinsic losses dominate. This is also caused by the rather small  $Q_{\text{scattering}}$ : the threshold

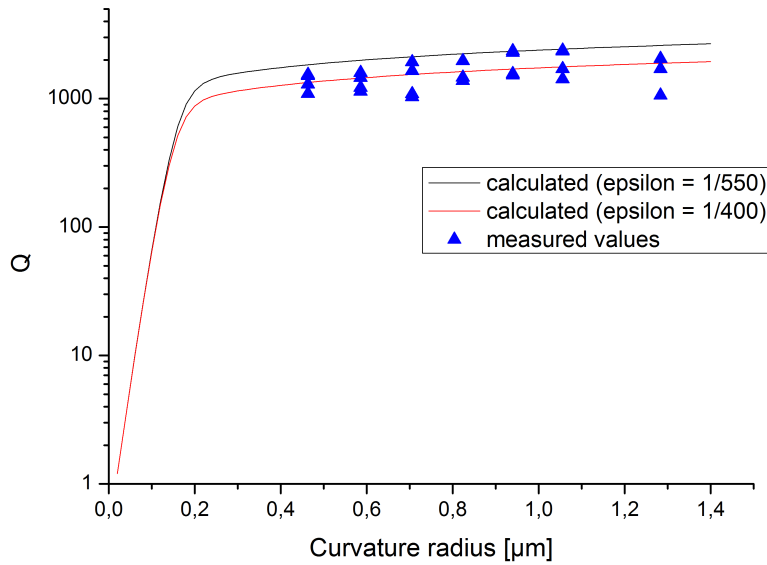


**Figure 5.15** Plot of  $Q$  vs.  $R_{c,\text{tip}}$ , and comparison of the measurements with modelling. The experimental average/maximum values fit well to theoretical values and show the same behaviour. The curvature radii of the fabricated structures are too large to enter the region where a rapid decrease of  $Q$  is expected from the intrinsic losses. The largest measured  $Q$  is 2400.

radius ( $\approx 0.2 \mu\text{m}$ ) between intrinsic and scattering loss regions is, as a result, shifted towards smaller curvature radii.

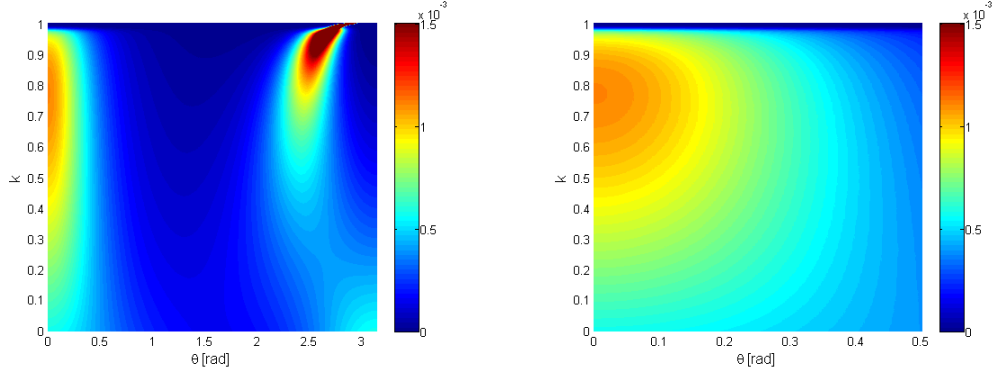
Experimentally, quality factors up to 2400 were observed. This is about two orders of magnitude smaller than the values computed with **COMSOL** for defect-free microrings. Hence, the quality factors are drastically limited by extrinsic losses in our structures.

Quality factors of several  $10^5$  have been realized by different research groups. For disk cavities,  $Q = 6000$  was already realized in our laboratory [77]. This value should also be within reach for oval microring cavities.

### Engineering of optical losses

Carefully choosing the parameter  $k$  allows controlling the different curvature radii and thus the position of losses. Based on the established model, calculations that predict the location of losses can be performed.

Figure 5.16(a) shows normalized loss rates for  $0 \leq k < 1$  along the different positions of the oval resonator ( $a = 3 \mu\text{m}$ ,  $b = 2.25 \mu\text{m}$ ,  $\epsilon = \frac{1}{400}$ ). We observe that losses can be well concentrated at the tip if  $0.2 < k < 0.7$ . For  $k < 0.2$  values, the



(a) Loss map for the whole oval structure. For large  $k$ s, the structure becomes more triangular-shaped and losses from other spots than the tip appear. The best  $k$  values lie in the range  $0.2 < k < 0.7$ .

(b) Loss map zoomed onto the tip of the resonator. We observe high loss rates at the tip for  $0.4 < k < 0.95$ .

**Figure 5.16** Normalized losses at different positions of an oval resonator ( $a = 3 \mu\text{m}$ ,  $b = 2.25 \mu\text{m}$ , perimeter  $P \approx 17 \mu\text{m}$ ) for varying  $k$ . For this model, I assumed  $\epsilon = \frac{1}{400}$  as extracted from our experiments.

ovals become too elliptical, and nearly equivalent losses occur at both ends; for  $k > 0.7$  values, the oval becomes too triangular. Both cases lead to emission at several spots (ellipse: backside tip, triangle: tips around  $\theta \approx 150^\circ$ ).

From Figure 5.16(b), we see that, for  $0.4 < k < 0.95$ , the tip of the resonator is where losses concentrate.

## 5.2.5 Purcell factors of oval ring resonators

Having obtained knowledge of the quality factors of oval microcavities, it is now possible to estimate the Purcell factor  $F_P$ .

### Determination of the effective volume of oval microcavities

It is not possible to describe the field patterns of oval ring resonators analytically. This means that an analytic calculation of the effective volume  $V_{\text{eff}}$  is not possible as well. It is nevertheless still possible to estimate  $V_{\text{eff}}$  with a good precision by using the simulations done with **COMSOL**.

Figure 5.17 shows results from effective volume calculations plotted as a function of the perimeter  $P$  ( $k = 0.7$ ) of the simulated structure. The plot shows that  $V_{\text{eff}}$  is approximately proportional to  $P$ , with slight deviations, which result from the different curvature radii of ring resonators with same perimeters but a different ratio

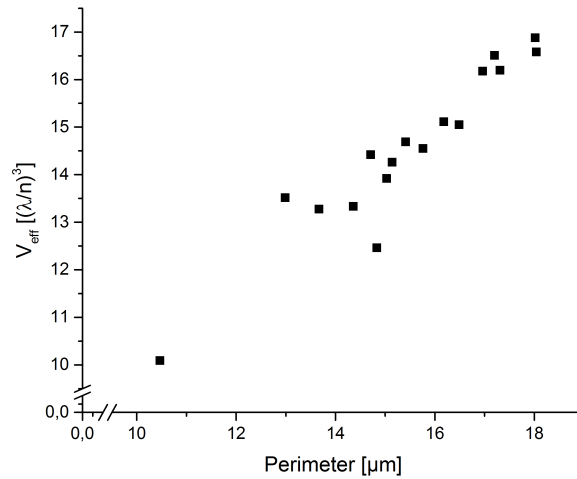


**Figure 5.17** COMSOL calculation of  $V_{\text{eff}}$  vs. perimeter for an oval microcavity. A linear dependence can be observed. The deviations result from different curvature radii that slightly change the position of modes in the resonator.

$\frac{a}{b}$ . This leads to a different shape of the resonators. Resonators with large  $\frac{a}{b}$  are more elongated and have thus smaller curvature radii at their tip. Hence, the mode maxima are located closer to the semiconductor-air-interface and larger parts of the EM wave are outside the waveguide which increases the modal volume.

### Theoretical and experimental Purcell factors - a figure of merit of the oval cavity

With these values, it is now possible to calculate the Purcell factors of the cavities.

The largest obtained  $Q$  factor in the simulations was around 200000 for a resonator with  $a = 3 \mu\text{m}$ ,  $b = 2.47 \mu\text{m}$ ,  $k = 0.7$ ,  $\Delta a = 0.3 \mu\text{m}$ . On that one, the computation gives  $V_{\text{eff}} = 16.88 (\lambda/n)^3$ , which leads to a Purcell factor  $F_P = 900$ .

This calculated  $F_P$  would be 30 times larger than the first value measured for a micropillar embedding a solid state emitter [36]. Compared to the other, state-of-the-art Purcell factors that were later reported in the literature on fabricated microcavities ( $F_p = 441$  for photonic crystal cavities, and  $F_p = 34$  for microdisks) [56], this value is still very large.

However, it is just a theoretical estimate, and such high quality factors have not yet been observed in the frame of our experiments. The largest measured  $Q$  factor was obtained on a resonator with  $a = 3 \mu\text{m}$ ,  $b = 2.25 \mu\text{m}$ ,  $k = 0.7$ , and  $\Delta a = 0.3 \mu\text{m}$ :

The corresponding Purcell factor was  $F_p = 11$ , obtained from the values  $Q = 2385$  and  $V_{\text{eff}} = 16.19 (\lambda/n)^3$ .

By using cavities with larger quality factors,  $F_p$  could be improved significantly.

Larger quality factors have already been reached at the NPSC laboratory ( $Q = 5000 - 6000$  for micropillars and microdisks [51], [77]). It is thus realistic to hope for similar quality factors by improving the fabrication process in the near future. The resulting  $F_p \approx 30$  would be sufficient for further applications.

## 5.3 Properties of active oval cavities

After studying the basic properties of oval cavities in the previous section, I will focus on the properties of active oval cavities in the following.

I first show reports of lasing in resonators with different emitters. Then I present measurements of the far-field pattern simulations and measurements. This section ends with the first results of cavity switching on oval microrings.

### 5.3.1 Lasing in oval ring resonators

A first step towards the fabrication of directional microlasers is the demonstration of lasing in oval microrings.

Lasing describes the behaviour of a resonator whose output comes from sustained stimulated emission rather than from spontaneous emission. This happens if, and only if, the gain, which is provided by the emitters within the cavity, exceeds all losses of the resonator due to absorption, scattering, and intrinsic losses, including the output.

Because of the large stimulated emission rates, a much larger number of photons is emitted into cavity modes when lasing. This leads to a strong amplification of the resonant, mode signal compared to non-lasing modes. In the case of QDs as emitters, which exhibit a spectrally wide ensemble emission, the optical modes that are covered by this wide emission can lase, as long as QDs provide large enough a gain on these modes.

The characterization of lasing can be obtained via different methods which take into account the changed emission behaviour of QDs.

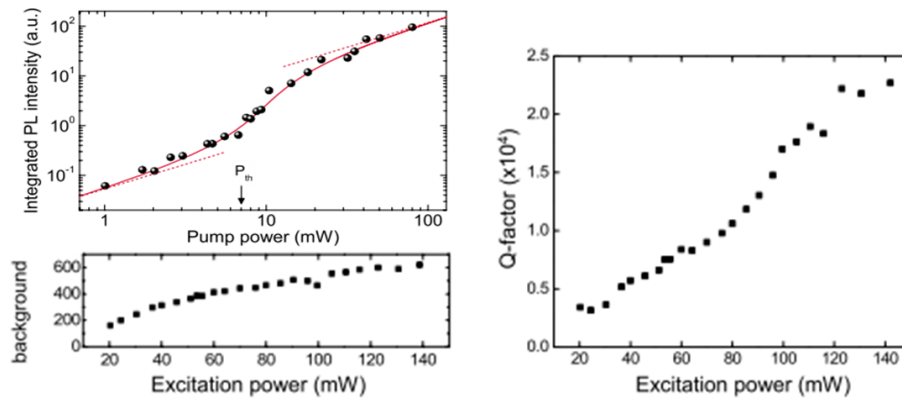


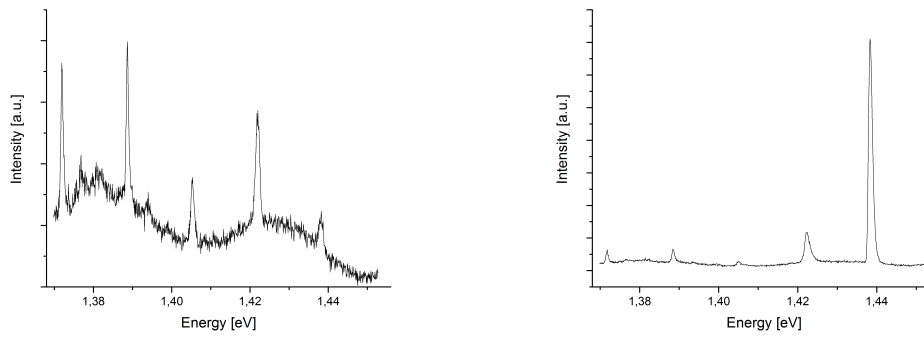
**Figure 5.18** Typical characteristics of lasing behaviour: In a log-log output- vs. pump-power plot, the slope of the output goes above 1, showing superlinearity, between the laser threshold and the gain saturation region. The quality factor of the mode increases with the excitation power (taken from [78, 51]).

- The integrated PL intensity of a resonance grows linearly, changes its slope and then grows superlinearly. A sign for this is the change of the slope of the output- vs. pump-power on the resonant mode in a log-log plot, whereas the off-resonance emission slope remains unchanged. This behaviour is depicted in the left side of Figure 5.18
- Lasing causes a significant decrease of the linewidth of resonances. Following the law of Schawlow-Townes [97] ( $\Delta E \propto 1/\bar{n}$ , where  $\Delta E$  is the linewidth, and  $\bar{n}$  is the average number of photons in the cavity), the linewidth (resp.  $Q$ ) should decrease (resp. increase) with increasing pump power (see Figure 5.18). However, as can be observed in Figure 5.14(b), this is not always the measured behaviour at incident powers beyond the lasing threshold for semiconductor microcavity lasers.

Other signatures of lasing are excess noise around threshold [66], and the clamping of the population of excited states in the stimulated emission regime (in spontaneous emission regime, the population grows with the pump power).

Figure 5.19 shows two spectra of an oval microring ( $a = 3 \mu\text{m}$ ,  $R_{c,\text{tip}} = 0.8 \mu\text{m}$ ,  $k = 0.7$  and  $\Delta a = 0.5 \mu\text{m}$ ) under pulsed excitation, set at a 800-nm wavelength, for pump powers of 350 and 1200  $\mu\text{W}$ .

At the lasing threshold (Figure 5.19(a)), the intensity of the lasing peak ( $\approx 1.438 \text{ eV}$ ) is of the same order of magnitude as the intensity of peaks at lower energies. At larger pump powers — in the lasing regime, (Figure 5.19(b)), the intensity of the



(a) Spectrum at  $350 \mu\text{W}$ , close to the lasing threshold. The spectrum is dominated by several peaks, with no clear lasing yet.

(b) Spectrum at  $1200 \mu\text{W}$ , largely over the lasing threshold. The lasing peak clearly dominates the spectrum, while the other peaks do not grow relative to the  $350 \mu\text{W}$  spectrum.

**Figure 5.19** Spectra from sample AS0157 under pulsed excitation at different pump intensities. The microring parameters are  $a = 3 \mu\text{m}$ ,  $R_{\text{c,tip}} = 0.8 \mu\text{m}$ ,  $k = 0.7$  and  $\Delta a = 0.5 \mu\text{m}$ .

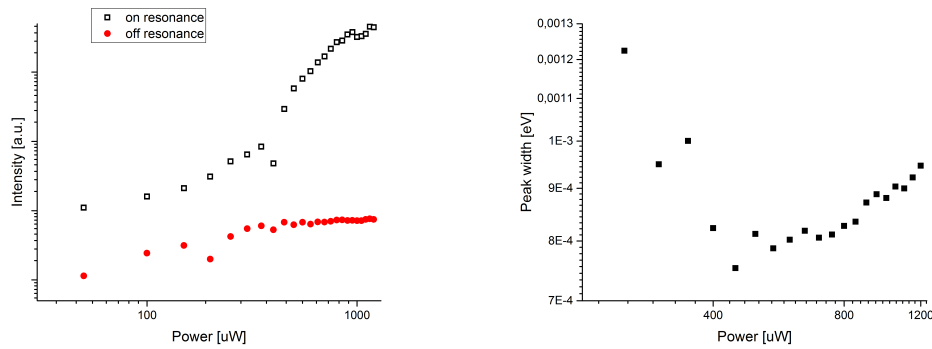
lasing peak clearly dominates the spectrum. Nearly all of the pumped electron-hole pairs feed the lasing mode.

The results underlining the lasing behaviour of the sample are also evaluated in Figure 5.20. For intensities below  $250 \mu\text{W}$ , no  $Q$  factor measurements could be performed because the peaks did not appear yet.

Figure 5.20(a) shows the same behaviour that was observed in Figure 5.18: A constantly growing background intensity and a faster growing on-resonance intensity. At the lasing threshold, the intensity of the peak changes its behaviour and grows steeper until pumping powers  $\approx 900 \mu\text{W}$ .

For the non-resonant emitters, a constant intensity is measured above the threshold. This is a signature of clamping, i.e. the population of these QDs stays constant.

In Figure 5.20(b), the peak FWHM of a lasing mode is plotted for different pump intensities. A behaviour similar to that on Figure 5.14(b) can be observed: At low pump powers, the peak width decreases and  $Q$  increases. The largest  $Q$  factors are reached at the lasing threshold. For stronger pumping intensities,  $Q$  slowly decreases. In [51], the decrease was attributed to heating of the cavities which might also be the reason in our case.



(a) Intensities of resonant energy emission (lasing peak) and non-resonant emission: At low incident pump power, both grow with similar slopes. At the lasing threshold ( $\approx 450 \mu\text{W}$ ), the on-resonance emission grows superlinearly, a sign of lasing behaviour. At large pump powers, the lasing mode saturates. For the non-resonant modes, clamping can be observed above the threshold.

(b) Lasing mode linewidth vs. excitation power. A significant decrease indicates that the absorption by QDs is bleached as it saturates. The increase at larger powers could be attributed to heating effects (similar results can be found in [51]).

**Figure 5.20** Lasing characteristics of a microring with QDs.

### 5.3.2 Localized, directional emission

One of the main motivations to introduce the oval shape of the resonators was to demonstrate directive emission. It could be an important achievement for further applications like microlasers and all-optical switching thanks to the improved collection of the emission that it would enable.

#### Mechanism of light emission

Geometrical optics forbids the emission of light of a resonator based on total internal reflection. However, due to the wave nature of light, photons can leak out of the resonator. The probability for this process taking place depends on the curvature radius of the resonator.

Tomes et al. performed experiments and simulations to measure the output of light from a circular silica micro-toroid resonator whose confinement is based on total internal reflection [113]. They showed that the propagation direction of the photons is conserved upon the leakage process.

This behaviour can also be applied to oval ring resonators. The main difference between a circular resonator and an oval resonator is the changing curvature radius, to exploit the fact that the smaller the curvature radii, the larger the emission probability is, which leads to emission localization.

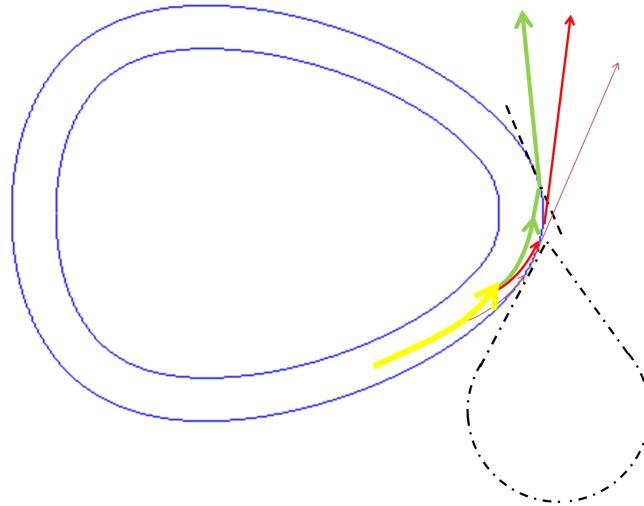


**Figure 5.21** Sketch of the mechanism of photon outcoupling in oval ring resonators. The largest part of the photons is outcoupled at the position with the smallest curvature radius, the emission from other positions is omitted (thicker arrows, higher photon numbers). For typical oval resonators, this position is at the tip of the ring. They are outcoupled there and emitted in the y-direction. This mechanism results in an emission pattern that has the form of the dashed-dotted lobe on the lower side of the resonator.

Figure 5.21 shows the emission mechanism of oval ring resonators. In that case, only losses which take place at the position with the smallest curvature radius (at the tip of the ring resonator) are taken into account.

There, the curvature radius also varies. The highest emission rate of photons can be observed at the position of the smallest curvature radius. The momentum vector of these photons is oriented in the y-direction. After tunneling through the potential barrier of the resonator, photons keep this direction, and propagate along the y-axis, creating the qualitative pattern depicted in Figure 5.21.

Emission can also occur from the backside of the oval which has a larger curvature radius than the tip. The fraction of photons that are emitted depends on the local confinement. Thus curvature radius and roughness of the waveguide material determine the quantity of light which is coupled out from the different areas of the resonator.

### 5.3.2.1 Results of far-field pattern simulations

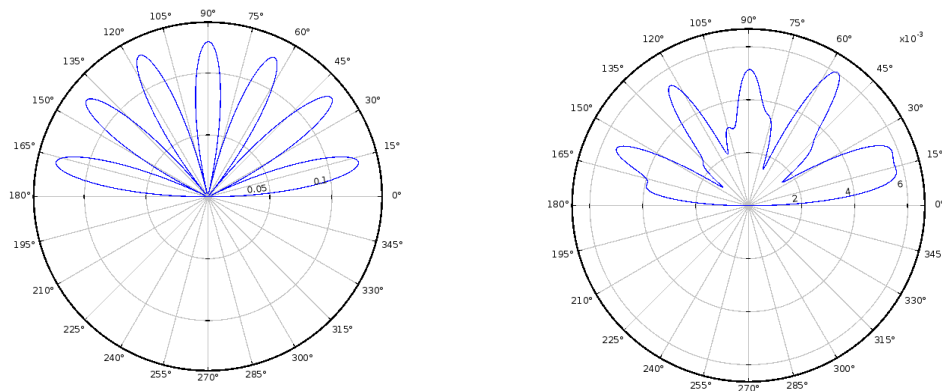
To calculate the far-field pattern, **COMSOL** uses data of the EM electric field impinging onto a surface which is situated a few  $\mu\text{m}$  away from the resonator.

Every resonator structure supports a large number of eigenmodes, and each eigenmode emits along a different far-field pattern. Thus, the field intensity values of the different far-field patterns from each mode which might be fed by InAs-QDs were summed up.

In the experiments, a single mode was spectrally filtered, in order to suppress the contributions from QDs emitting into non-resonant modes.

### Far-field pattern of circular objects

In order to examine the reliability of the simulations, it is important to compare simulations with results of predictable structures. A circular resonator presents a structure which is very easy to predict: because of its circular symmetry, an isotropic emission pattern is expected.



(a) Physically realistic far-field pattern of the resonator. The locations with zero far-field intensity result from interference effects. The  $Q$  factor of this structure is 25000.

(b) Physically unrealistic far-field pattern of a circular resonator. The intensities show deviations from the expected pattern.  $Q = 96000$ .

**Figure 5.22** Simulated far-field patterns for circular resonators with  $r = 0.5 \mu\text{m}$  (a) and  $r = 0.7 \mu\text{m}$  (b).

Results from simulations of circular rings are shown on Figure 5.22.

A ring with small radius ( $r = 0.5 \mu\text{m}$ ) behaves as physical intuition predicts: Its emission pattern possess circular symmetry, the lobes being a result of interference between the emitted photons (cf. Figure 5.22(a)).

For a ring with a larger radius ( $r \geq 0.7 \mu\text{m}$ ), the results strongly deviate from the predicted behaviour. Figure 5.22(b) indicates that the symmetry of the far-field pattern is broken.

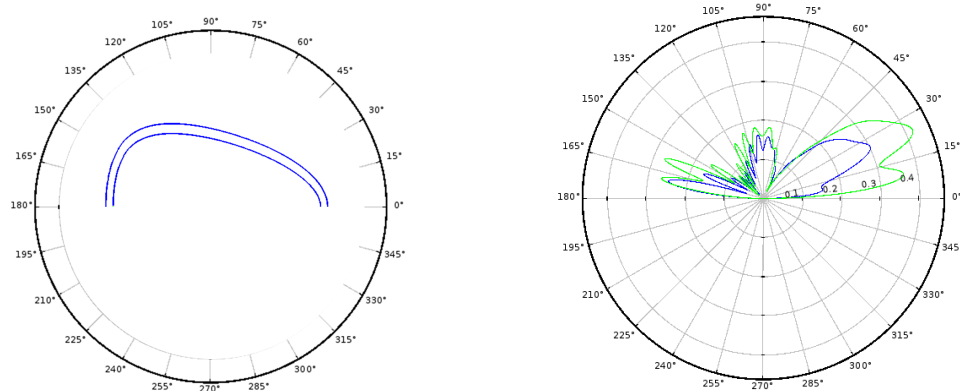
Two reasons for this are possible:

- Because of large  $Q$  factors, the structure only exhibits small amounts of losses. These small amounts could introduce numerical errors in **COMSOL** and might thus create errors in the far-field patterns.
- Structures showing a large  $Q$  factor have smaller resonance bandwidths and are thus more sensitive to errors. Small deviations of the calculated resonance energy can lead to unphysical behaviour because of the high precision that is required.

Consequently, the results from simulations of structures showing  $Q$  factors around or higher than  $10^5$  (as simulated) should be taken into account with much caution.

### Far-field pattern of oval objects

The simulated structures had the following parameters:  $a = 3 \mu\text{m}$ ,  $k = 0.7$  and  $\Delta a = 0.3 \mu\text{m}$ .  $a = 3 \mu\text{m}$  provides a good balance between reliability (the size of the structure is much larger than the wavelength of the light in GaAs) and reasonable calculation times.



(a) Positioning of the oval ring resonator in the **COMSOL** far-field simulation.

(b) Simulated far-field patterns for two consecutive resonant modes (order  $n = 60/61$ ) of an oval ring resonator, with parameters  $a = 3 \mu\text{m}$ ,  $b = 1.75 \mu\text{m}$ ,  $R_{c,\text{tip}} = 0.6 \mu\text{m}$ ,  $k = 0.6$  and  $\Delta a = 0.3 \mu\text{m}$ . Note the difference between the two patterns.

**Figure 5.23** Basics for understanding far-field experiments.

Figure 5.23(a) shows the position of the resonator in the far-field pattern.  $\theta$  ranges from  $0^\circ$  to  $180^\circ$  (to reduce the simulation time, only half of the structure is simulated). On Figure 5.23(b), I present the far-field patterns of two different eigenmodes of an oval microring with parameters  $a = 3 \mu\text{m}$ ,  $b = 1.75 \mu\text{m}$ ,  $R_{c,\text{tip}} = 0.6 \mu\text{m}$ ,  $k = 0.7$  and  $\Delta a = 0.3 \mu\text{m}$ .

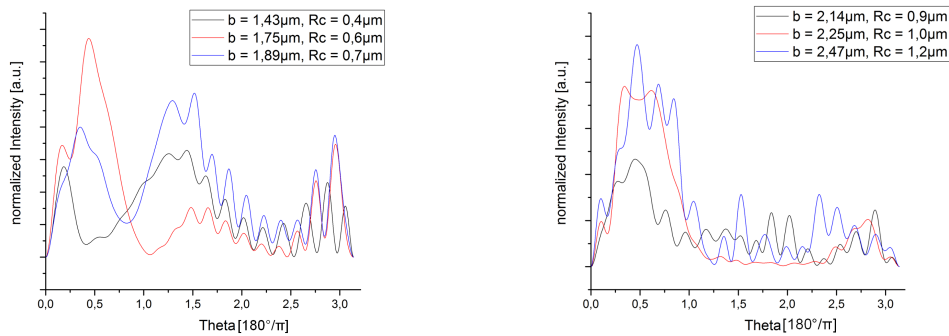
A rather directional emission pattern is observed: A large part of the emission goes into a cone between  $10^\circ$  and  $45^\circ$ . At angles close to  $0^\circ$  and  $180^\circ$ , we observe no intensity. This is a result of the chosen boundary conditions which suppress "light detection" in these areas.

A clear sign for the presence of interference are the fluctuations between neighbouring angles. A field amplitude which is half of the intensity maximum is observed at angles from  $75^\circ$  to  $120^\circ$  and from  $150^\circ$  to  $175^\circ$ .

Comparing the two modes, we observe that both emission patterns are qualitatively similar. The main emission areas stay the same. Quantitatively, the two patterns represent differences concerning the distribution of the emitted field.

### Emission pattern of different structures

Oval structures with different curvature radii at their tip were simulated. The aim of these simulations is to compare emission patterns of these structures and to conclude on the influence of different curvature radii.



(a) Far-field pattern of resonators with  $R_{c,tip} = 0.4, 0.6$  and  $0.7 \mu\text{m}$ . A significant part of the emission goes into an angular range between  $60^\circ$  and  $120^\circ$ .

(b) Far-field pattern of resonators with  $R_{c,tip} = 0.9, 1.0$  and  $1.2 \mu\text{m}$ . The largest part of the emission exits into an angle between  $10^\circ$  and  $60^\circ$ . Having high  $Q$  factor, this simulation could contain errors.

**Figure 5.24** Far-field plots of resonators with  $a = 3 \mu\text{m}$ ,  $k = 0.7$  and  $\Delta a = 0.3 \mu\text{m}$  (values obtained from simulation).

For large curvature radii at the tip ( $0.9 \mu\text{m}$ ,  $1.0 \mu\text{m}$ ,  $1.2 \mu\text{m}$ ), a relatively good directionality can be observed. Large parts of the field (56%, 82% and 69%) are emitted into an angle between  $10^\circ$  and  $60^\circ$  degree. However, small parts of the emission still go into other directions (cf. Figure 5.24(b)).

In the case of smaller curvature radii ( $0.4 \mu\text{m}$ ,  $0.6 \mu\text{m}$ ,  $0.7 \mu\text{m}$ ), the emission diagram changes (see Figure 5.24(a)).

The  $R_{c,tip} = 0.6 \mu\text{m}$  oval behaves differently. A highly directive emission diagram is observed: 65% of the field intensity is emitted in the angular range between  $10^\circ$  and  $60^\circ$ . This is a highly improved value over circular resonators that emit only 30% of their output into this angular range.

But this is not a general result. Indeed, the ovals with  $R_{c,tip} = 0.4 \mu\text{m}$  and  $R_{c,tip} = 0.7 \mu\text{m}$  emit only 30% and 33% into this angular range. Another emission maximum is observed for angles around  $90^\circ$ . This is approximately the same intensity in this angular range as the one that would be detected for an isotropic emitter. These ovals therefore present no advantage over circular devices.

Devices with larger curvature radii provide better properties for future applications. Compared to limaçon resonators, as investigated by Albert et al. [2], oval microcavities provide comparable properties. Albert et al. reported that 27% of the emission is emitted into an angle between  $0^\circ$  and  $20^\circ$ . The best simulated oval resonator ( $R_{c,tip} = 1 \mu\text{m}$ ) obtained a value of 19%. This is a significant progress compared to a circular waveguide which emits only 11% within the same angular range.

### 5.3.2.2 Experimental observation of directional emission

The direct detection of the emitted photons is not efficient with our experimental setup, because the emission patterns lie around the resonator waveguide plane.

So another concept was used, in order to redirect these photons to directions where they could be detected.

#### The diffuser structure

A semiconductor structure of the same height as the resonator and of a lateral size similar to the wavelength of the resonator modes is fabricated at a set distance around the resonator (see Figure 5.25(a)). This structure can easily be integrated onto the sample by designing it on the same etching mask that is used to fabricate the microrings.

We use this diffuser structure to scatter the emitted light along the vertical direction where it can be collected with the setup optics.

The emitted light propagates along the substrate plane and arrives at the diffuser structure. Two processes can then take place (cf. Figure 5.25):

- The light can scatter on the diffuser's edge towards the vertical direction.

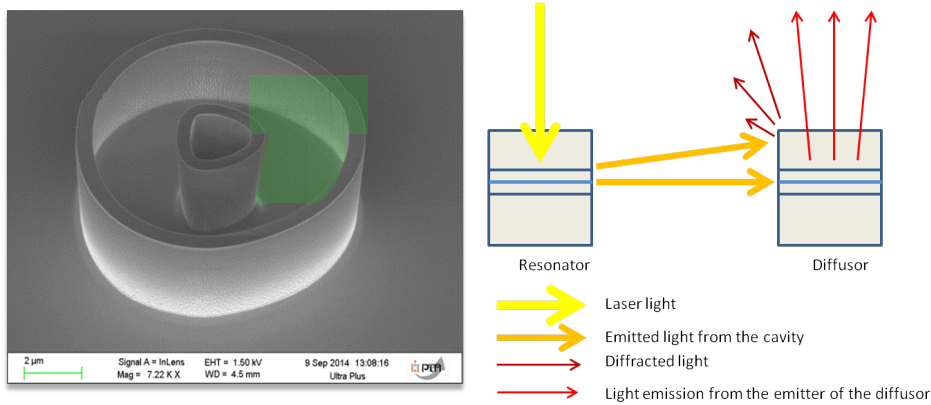


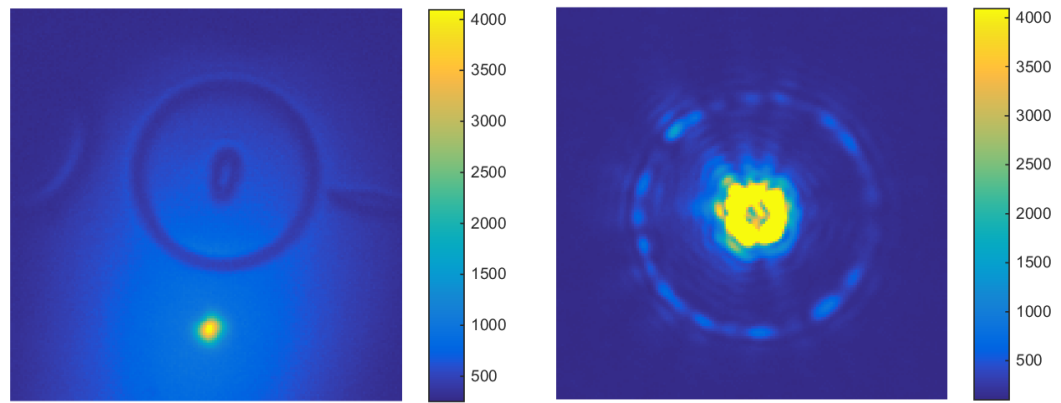
**Figure 5.25** Left side: SEM image of the diffuser structure which is located around the disk resonator. Right side: mechanisms that take place at the diffuser structure: pumping of integrated emitters, scattering at the edge. The cross section is taken at the green plane.

- The QD emitters located in the diffuser could absorb that light and subsequently re-emit photons off resonance towards the vertical. This second process is probably secondary.

To obtain clean emission signals, the following conditions have to be fulfilled:

- The resonator has to be excited as uniformly as possible. If we pump emitters in some zones more strongly than others, the then localized, off-resonant emission could wrongly affect the measurements. By uniformly pumping the resonator, the off-resonant emission will give a uniform background. A  $20\times$ -objective was used to create a sufficiently large and intense excitation spot to pump the whole resonator, without exciting the diffuser structure around it; For that to be possible, the distance between the resonator and the diffuser has been chosen around  $8\ \mu\text{m}$ .
- Pictures of the far-field diagram have to be taken while the resonator is lasing. In the stimulated emission regime, the intensity of the resonator optical modes is strongly increased relative to the background of off-resonant emission (cf. previous section). To further decrease detection of light which is not part of the lasing mode, we spectrally filter the non-resonant emission. This way, it can be ensured that the whole emission intensity originates from the lasing mode.

Figure 5.26 shows how to fulfill these conditions. On Figure 5.26(a), the size of the pump laser spot is depicted. It is  $\approx 4\ \mu\text{m}$ , which allows a rather uniform pumping for that structure. Nevertheless, it was not possible, on our setup, to create a laser spot that would have perfectly matched the oval shape.



(a) Image of the laser spot that excites the resonator inside the diffuser structure. Its size is approximately  $4 \mu\text{m}$ .

(b) Picture of a far-field diagram of circular structure, as observed on the diffuser. We get an “isotropic” emission with some randomly localized maxima and a weak modulation of the intensity on the diffuser.

**Figure 5.26** Detecting a far-field pattern with an  $20\times$ -objective and a  $850 \text{ nm}$ -lowpass filter.

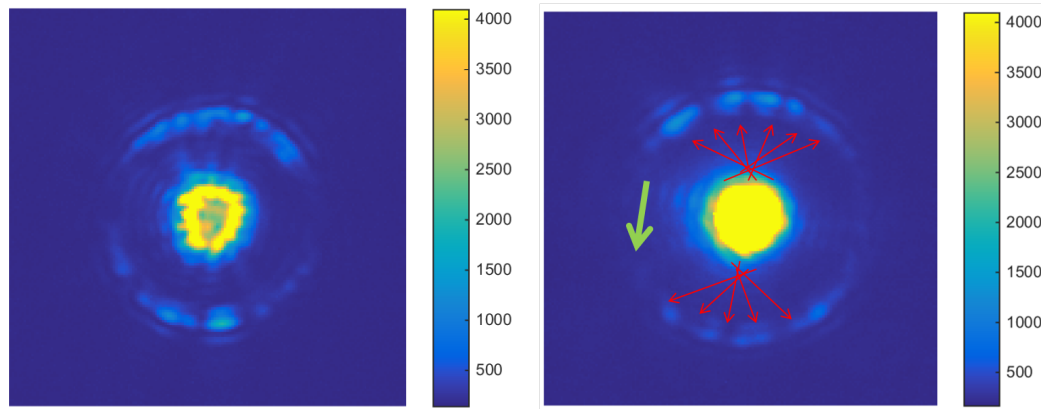
To get a homogeneous pumping as good as possible, we thus focus the laser spot inside the ring at its center and use the tails of that Gaussian beam to pump the resonator.

It is also important to check the results on easier-to-understand structures, before going on with more complicated structures. This is shown in Figure 5.26(b) with the far-field diagram from a circular microring with radius  $R = 5 \mu\text{m}$ . An asymmetric pattern would indicate that the experiment is not performed correctly. The bright, saturated spot at the center of the picture comes directly from the resonator structure. The asymmetry of that bright spot results from the roughness of the resonator, but we could consider that to be close to uniform excitation.

On the diffuser structure, we detect some azimuthal modulation on the signal, which we think is the result of interference effects, as it shows a behaviour similar to the simulation shown on Figure 5.22(a). A few brighter spots are distributed randomly over the whole structure. These probably result from roughness-related defects on some parts of the resonator which lead to a larger photon scattering.

This near-isotropic azimuthal pattern on the diffuser has been observed on a number of other circular structures, which confirms the capability of our diffuser structure to probe the far-field pattern of our microrings.

The same principle is now applied to oval microring resonators.



(a) Emission diagram of a resonator with a diffuser distance of  $8 \mu\text{m}$ . A pattern with maxima at angles between  $0^\circ$  and  $50^\circ$  and between  $140^\circ$  and  $180^\circ$  is observed.

(b) Emission diagram of a resonator with a diffuser distance of  $10 \mu\text{m}$ . The red arrows indicate the trajectories of the photons. The green arrow shows the orientation of the resonator. The tip of the resonator points in the same direction as the tip of the arrow.

**Figure 5.27** Far-field diagrams under pulsed excitation for resonator structures with parameters  $a = 3 \mu\text{m}$ ,  $R_{c,\text{tip}} = 1.2 \mu\text{m}$ ,  $k = 0.6$ , and  $\Delta a = 0.3 \mu\text{m}$ . The images were taken in the lasing regime.

Figure 5.27 shows images that were taken using a resonator with an oval shape and its diffuser located at different distances:  $8 \mu\text{m}$  (Figure 5.27(a)), and  $10 \mu\text{m}$  (Figure 5.27(b)).

Similar emission patterns are observed for both structures. The photoluminescence maxima can be observed on positions between  $0^\circ$  and  $50^\circ$  and between  $140^\circ$  and  $180^\circ$  ( $0^\circ$  is the direction of the green arrow). The signal on the diffuser for Figure 5.27(b) is weaker due to the larger distance between the resonator and the diffuser.

From the similarity of these images, we can infer that the photons come indeed from the microring parts with the lowest curvature radii (at the tip and backside of the oval). The signal is the strongest on the diffuser parts facing these low curvature parts of the ring.

This seems to confirm the prediction from the model established in the previous section (cf. Figure 5.21(b)).

However, both oval microrings with  $R_{c,\text{tip}} = 1.2 \mu\text{m}$  deviate from the emission pattern that is predicted by COMSOL (Figure 5.24(b)): In the experiments, large parts of the emission are emitted on the backside of the resonator and also along the growth direction, which is in strong contrast to the simulation that predicts that emission takes only place at the tip and in the resonator plane.

Different explanations for this behaviour are possible:

- As already mentioned in the previous subsection, predictions of **COMSOL** concerning far-field patterns of objects having high quality factors might be wrong and thus explain the deviation between simulation and experiment.
- In the simulation, losses are of intrinsic character and due to the curvature radius. These losses decrease exponentially with increasing curvature radius (cf. Figure 5.6(a)). As a consequence, the losses at the tip dominate largely.

In the experimental case, scattering losses due to the roughness of the waveguide are dominant. The decrease of losses with growing curvature radius does not behave exponentially (cf. Figure 5.6(b)). Thus, higher losses can be expected relative to the theoretical case.

Compared to isotropic emitters, like circular microdisks, the localized emission from parts with smaller curvature radius presents an advance in terms of directionality and of localized emission. However, state-of-the-art limaçon resonators provide better directional emission [2], as compared to the relatively large emission angle that we observe for oval ring resonators.

### 5.3.3 Cavity switching

In this section, I describe the first experiments for the cavity switching of oval ring resonators, which were performed during this work. These experiments provide a first test of the capability of oval resonators to be part of future cavity switching experiments. Throughout this section, the sample AS0157 was used for these experiments. The oval microring under consideration had the following parameters:  $a = 3 \mu\text{m}$ ,  $R_{\text{c,tip}} = 1 \mu\text{m}$ ,  $k = 0.7$  and  $\Delta a = 0.4 \mu\text{m}$ . The excitation was provided by the double pulse system (subsection 4.2.2) with a power of 10 mW at 1.56 eV.

Because most of the photons from a ring resonator mode are emitted into the plane, it is very complicated to detect a sufficiently strong signal from the cavity modes. Therefore, a resonator surrounded by diffuser structure is used for redirecting a sufficiently large number of photons which can be detected by the streak camera.

Figure 5.28 shows the resulting streak camera image of such an experiment. Because of the weak signal, a black line that approximately indicates the mode position was superposed to the image.

The first pulse pumps the QDs whose signal reveals the cavity mode position at 1.3793 eV. At  $t = 100$  ps, the second pulse hits the resonator and shifts the cavity

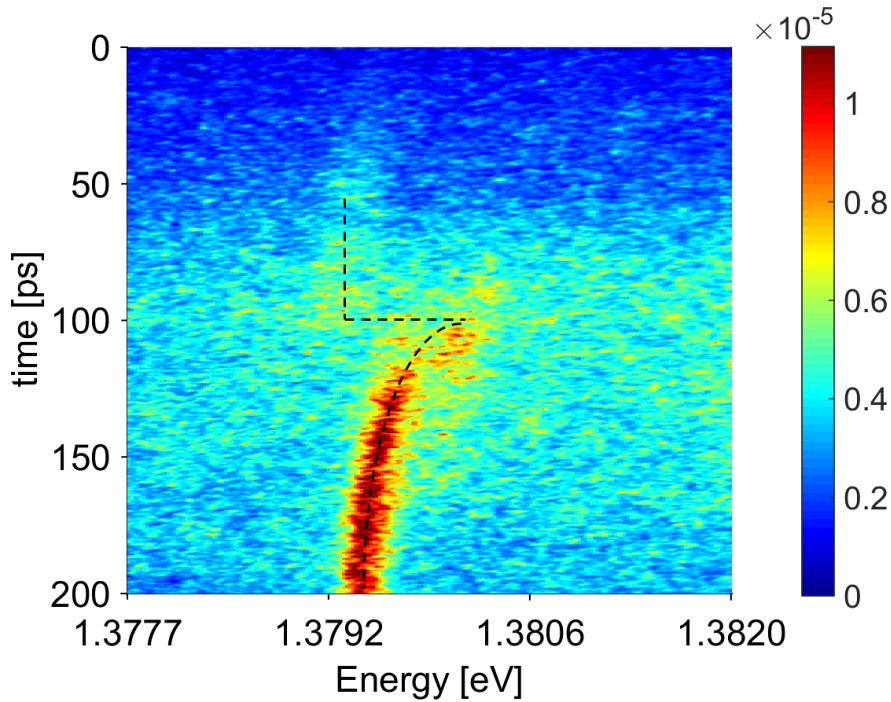


**Figure 5.28** Streak camera image of a switch of an oval ring resonator. The black line represents the mode position of the resonator.

mode by 1.1 meV. For  $t > 100$  ps, the mode goes back to its initial position, the initial shift decreasing exponentially with time.

The recombination time of the carriers is here much shorter than in the case of micropillars or planar cavities. Because of the small resonator width ( $\Delta a = 0.4 \mu\text{m}$ ), the carriers are always close to the sidewall surface, and surface recombination is therefore fast. This results in a short characteristic lifetime of free carriers  $\bar{\tau}_{\text{NR}} = 25.8$  ps. For micropillars and planar cavities, this lifetime was  $\bar{\tau}_{\text{NR}} \approx 370$  ps.

The relatively large intensity of off-resonant emission is remarkable in this experiment. As can be observed on Figure 5.28, off-resonant photons are detected over the whole spectral range. This makes ring resonators promising structures for performing experiments on the real time control of the Purcell effect [111].

Compared to micropillars, the switching amplitude of ring resonators is much smaller. This is a result of the larger spatial extension of the microrings. This large size and the required uniform pumping of the whole microring sets a stronger limit on the power density that is available from our setup, and it is the carrier density — proportional to the power density — that sets the switching amplitude.

## 5.4 Conclusion and outlook

This chapter has been dedicated to the study of a not yet explored optical resonator geometry — the oval ring resonator. One goal was to perform photoluminescence measurements to obtain insight into optical properties like the quality factor, the modal structure and the Purcell factor. Another aim was to explore the potential of that geometry in terms of optical switching experiments and directional microlasers.

Measurements concerning the modal structure have been performed: WGM-like behaviour was observed in circular, elliptical, and oval ring resonators. By choosing resonator widths and heights of the order of magnitude of  $\lambda/n$ , we were able to deal with a single family of vertical and radial modes, confined in the resonators.

Quality factors up to 2400 were measured. These quality factors are mainly limited by imperfections due to the fabrication process. Simulations with **COMSOL** indicate that much higher  $Q$ s could be reached. With improved fabrication processes, we should be able to reach  $Q$ s well above  $10^4$ .

By using **COMSOL** calculations for the effective volume and the measured quality factors, I estimated the Purcell factor  $F_p$  for empty oval cavities.  $F_p = 11$  was the best value I obtained. With structures showing expectable  $Q$ s, values of  $F_p > 100$  should be reached.

Lasing of resonators was achieved for quantum dots as emitters. In order to decrease the observed thresholds, it will be needed to increase the lifetime of photons in the cavity by using microrings exhibiting larger quality factors. Another mid-term challenge still is the fabrication of electrically pumped microlasers (see below).

Emission patterns were simulated and measured. Non-isotropic emission patterns were measured for oval microrings. I established a model that explains this pattern. The desirable, highly directional emission could not be obtained. However, improvements in directionality, compared to circular geometries, was observed.

First experiments to switch the cavity by all-optical means were performed. I succeeded in getting a cavity switch of 1.5 meV during  $\approx 35$  ps by optical injection of free carriers. For future experiments, like the real time control of the Purcell effect (see below), two major improvements are desirable: microcavities with larger Purcell factors, and larger signal intensity for the detection with the streak camera.

## Electrically pumped microlasers

A future target for oval ring resonators is the fabrication of electrically pumped microlasers.

It is indeed much easier to fabricate resonators which are pumped optically. However, in terms of future applications in planar photonic circuits, or as microlasers, it is highly desirable to inject the carriers via electrical pumping.

In the literature, many examples can be found that report on the use of electrically pumped microcavities [62, 30]. A recent example for electrically pumped ring resonators is given by Munsch et al. [70]. A sandwich structure of *n*- and *p*-doped AlGaAs claddings was used to inject the carriers into the waveguide layer.

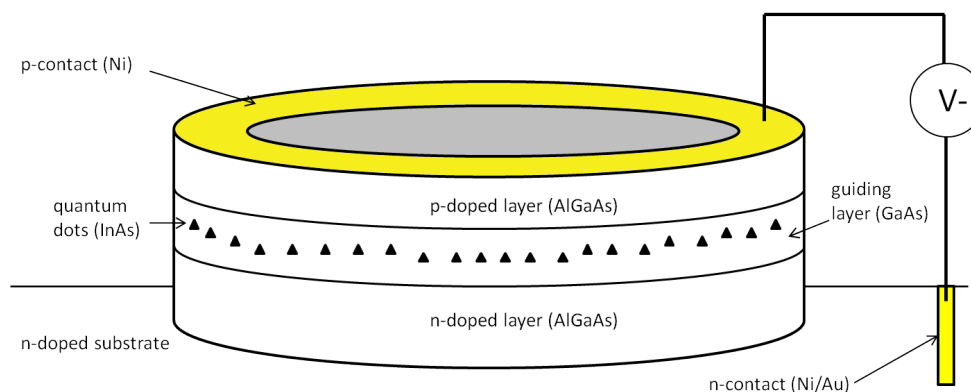


**Figure 5.29** Concept of an electrically pumped ring resonator with conductive claddings.

The same structure could be readily adapted for injection of carriers into oval microring resonators. First, the use of a *n*-doped GaAs substrate is necessary. To contact the substrate, a Ni-Au film is coated onto it. For cladding layers, it is easier to use a *n*-doped AlGaAs alloy as bottom cladding layer. The doping concentration must be reduced in the close proximity to the GaAs waveguide layer, to reduce absorption losses from this doped layer. The emitters, QDs or QWs, are embedded in the GaAs waveguide. A *p*-doped AlGaAs layer serves as the top cladding layer. Finally, a Ni metallic layer is deposited onto the structure in order to make contact with it (Figure 5.29).

### Real time control of the Purcell effect

Oval ring resonators also have very promising properties that could lead to the real time control of the Purcell effect.

Let us consider a ring cavity that contains QDs. The cavity is supposed to have a sufficiently high Purcell factor  $F_p$  to observe Purcell enhanced spontaneous emission.

The QDs in the resonator are lifted to their excited state by a laser pulse at  $t = 0$ .

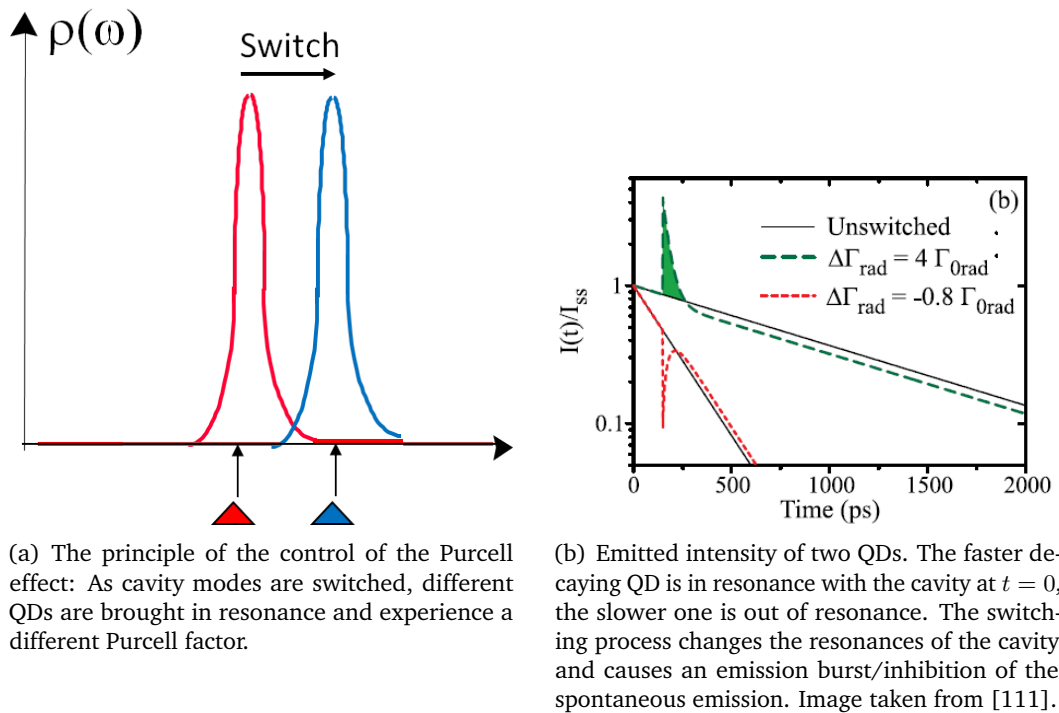


**Figure 5.30** Real time control of the Purcell effect: Principle and expected effect.

The ground state transitions of a few quantum dots are first in resonance with the cavity modes, while all the other quantum dots are not. This means that the resonant quantum dots will decay faster than the others.

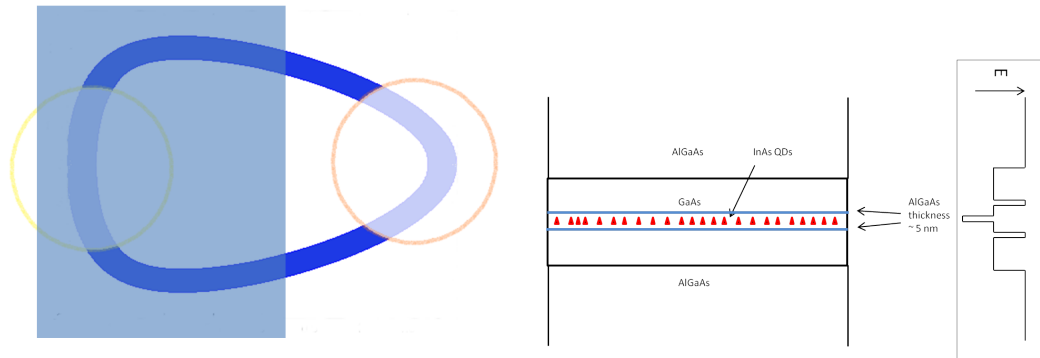
If the resonance energy of the cavity is switched by a laser pulse at time  $t = 0$ , these resonant QDs are brought out of resonance. This means that their decay time will increase, whereas the decay time of the other QDs that are then on resonance will decrease. This mechanism is depicted in Figure 5.30(a).

If the switch takes place during the spontaneous emission process, one can directly change the emission behaviour of a single QD on a time scale that is shorter than its radiative time for the emission of a single photon [111]. Ultimately, this effect could be used to shape in real time the temporal envelope of single photon pulses.

Putting QDs into resonance makes them decay faster, causing an emission burst, while pulling them out of resonance makes them decay slower, causing an emission dip. This behaviour can be seen in Figure 5.30(b).

By carefully controlling the switching pulse, one can precisely control the degree of influence of the Purcell effect on a QD.

One of the potential parasitic effects is the repumping of the QDs in the resonator via the switching pulse. These QDs also emit a photoluminescence signal that destroys the clear signature of the emission burst which is depicted in Figure 5.30(b). This could be the reason why we did not succeed in observing real time control of the Purcell effect in our micropillar cavities.



(a) The QDs in the blue-gray zone are inactive. The switching pulse (yellow circle) is focused on this zone in order not to induce undesired signal. The pump beam (orange circle) impinges on a zone with one or several active QDs and creates the emission that probes the effect.

(b) Required sample composition. The AlGaAs-QWs around the InAs-QDs are there to prevent diffusion of the free-carriers, that are required for the switching process, to the QDs.

**Figure 5.31** Real time control of the Purcell effect: Possible experimental realization with oval ring resonators.

With oval ring resonators with a  $10\text{-}\mu\text{m}$  size, it is possible to spatially separate the pumping and switching zones. Via implantation of ions, QDs can be de-activated through the generation of a high density of defects. The recombination processes that take place in these QDs are then non-radiative, and very fast. It can thus be ensured that no undesired signal disturbs the detection of the switching process, as these QDs will not emit photons. This future experimental realization is depicted in Figure 5.31(a).

To further improve the performance of the switching devices, it might be necessary to use a specially designed sample. Free carriers, which are triggering the switch, are quickly confined by the QDs and do not contribute any more to the switching process. This can be avoided with a modified sample composition, which is depicted in Figure 5.31(b): Two AlGaAs-layers serve as barriers that are centered around the active zone. The inset of Figure 5.31(b) shows the band structure of this sandwich. Diffusion of the carriers into the QDs can thus be suppressed. There will always be some carriers that are captured by the QDs and the wetting layer, but this design reduces their number significantly.

# Conclusion

The main subject of this PhD thesis was to study the all-optical switching of innovative cavity structures and geometries on the picoseconds timescale. This experimental technique enables us to observe manifold physical effects such as the frequency conversion of photons or differential switching of an ensemble of cavity modes, which are of great interest for future applications in solid state quantum optics experiments.

In the frame of this work, III-As semiconductor materials were used, namely GaAs, AlAs, the  $\text{Al}_x\text{Ga}_{1-x}\text{As}$  alloy and InAs-QDs. With these materials, planar structures confining light in one dimension by distributed Bragg reflectors were grown by molecular beam epitaxy. Noticeably we use a very thick cavity layer in order to increase the storage time of photons in the cavity and to lift the need for high quality Bragg reflectors which are very sensitive on the quality of the fabrication process.

Other planar structures with embedded InAs-QDs were structured via plasma etching in order to form micropillars, cavities which provide three-dimensional confinement of photons. To resolve the light emitted by cavities both spectrally and temporally, we use a combination of a monochromator and a streak camera for detection.

The switching of planar and micropillar cavities has already been studied in the early 90's. At that time, shifting of resonance frequencies by all-optical injection of carriers was developed for all-optical data processing and computing. Nowadays, one promising application is the adiabatic conversion of light stored in a resonator by all-optical means. This could be applied to tune the frequency of single photons. Such experiments have already been performed with ring-resonators and photonic crystals. In this work, we stored light in a high Q-planar cavity to shift its wavelength. Thanks to our "thick cavity" design, we measured a storage time of photons up to 7.5 ps in the cavity in a ring-down experiment.

During this experiment, we stored light with a pulsed laser in a cavity and measured its decay time with the streak camera. Having the confirmation that the storage time is longer than the switching time (5 ps), the condition for the color change experiment was fulfilled. We used a narrow CW laser to inject light into the cavity

which was then switched with a pulsed laser providing high intensities. With the streak camera, we could detect a color shift of 1.5 eV. The corresponding decay time of 5.9 ps is consistent with a value obtained by TMM simulations. We introduced an approach to estimate the switching efficiency of our process by comparing the detected intensities before and after the switch. Our experimental results are compatible with a conversion efficiency close to 100 % as predicted from FDTD modelling. We furthermore performed a pump-probe experiment which indicates the actual position of the resonance frequency of the cavity. The light shift matched the cavity shift with a precision of 10 %. These two experiments indicate that the frequency of the stored light follows adiabatically the shifting mode during the process. We have proposed possible ways to apply this effect to the frequency conversion of light pulses, with appealing prospects such as the frequency conversion of single photon pulses.

Micropillars can serve as a model system for a better understanding of switching dynamics of microcavities. An ensemble of QDs, which are embedded in a micropillar, serve as a white light source for probing the cavity from inside. This method provides a much easier experimental handling as pump-probe experiments and is able, in combination with the streak camera, to temporally resolve cavity dynamics with picosecond precision.

With this method, we investigated the differential switching of micropillar modes, i.e. every mode presents different switching dynamics. This behaviour can be triggered by all-optically injecting a strongly inhomogeneous distribution of free charge carriers into a circular micropillar. A strongly focused pulsed laser beam is used to inject electron-hole pairs.

We developed a model for the temporal and spatial evolution of a free carrier distribution, taking into account diffusion and recombination, either in bulk material or at the surface of the pillar. FDTD simulations, which are based on this model, enabled us to calculate refractive index profiles of the micropillar and the corresponding resonant energy at any time.

To judge the validity of these simulations, we performed a corresponding experiment. To obtain an insight into the entire mode dynamics, we used a system which splits a laser pulse into an intense and a weak fraction and delays the intense part of the pulse. We could thus already excite the QDs in the micropillar before the actual switch. This allows probing the unperturbed micropillar and the switch-on of the system which is a clear improvement compared to single pulse excitation schemes.

The experimental values match the theoretical predictions and confirm the validity of our model. In the case of an excitation along the central pillar axis, the experiment confirms that modes whose field intensity has a large overlap with the injected free carriers of the micropillar (HE<sub>11</sub>, HE<sub>12</sub>, EH<sub>02</sub>/HE<sub>02</sub>/HE<sub>22</sub>) show larger switching amplitudes than modes with a donut-like intensity pattern. Inverse behaviour is observed in the case of an experiment where the free charge carriers are excited close to the pillar surface.

Generally speaking, differential cavity switching enables to modify to a large extent the density of modes of an optical microcavity (mode spacings, mode degeneracies, mode ordering). It can also be used to control the interaction time between a mode and an emitter. Therefore, differential cavity switching appears as an attractive novel resource for solid state CQED, and noticeably in view of a dynamic control of CQED effects.

A cavity type which is considered to be able to advance significantly the field of CQED is the ring microresonator. The confinement of light in these resonators is based on total internal reflection at interfaces to dielectric materials and gives rise to waveguide/whispering gallery modes. Ring resonators show ultrahigh Q-factors combined with small modal volumes which results in high Purcell factors. The combination of these properties with the relatively large spatial extension of the cavities makes ring resonators a promising device for CQED experiments.

We studied a modified cavity type, the oval ring resonators. Besides the advantages of ring resonators, this geometry has a varying curvature radius and is able to concentrate the largest part of cavity losses at its tip and to provide more directional emission behaviour compared to the isotropic emission of circular ring resonator.

We probed the modal structure of these devices by exciting an ensemble of integrated QDs inside the resonator and by collecting their microphotoluminescence signal. These experiments reveal equally spaced modes independently of the shape of the fabricated resonators. Q factors up to 2400 have been measured which results in theoretical Purcell factors  $F_P$  up to 2.9 for an ensemble of integrated QDs.

Oval ring cavities can also serve as microlasers. Typical signatures of lasing behaviour were observed for resonators with integrated QDs for pulsed and continuous wave excitation of the QDs.

Lasing oval ring resonators have been used to study the radiation pattern of such cavities. We used scattering of emitted light by a microstructure which was built around the resonator. By filtering all other contributions of the signal besides one

single mode, the emission pattern of the resonators could be visualized with a CCD camera. The results show indeed emission at areas with low curvature radii. The measured pattern agreed qualitatively with those calculated by FEM simulations.

For future applications in time resolved CQED experiments, it is important to investigate the switching behaviour of the ring resonators. With the two-pulse system, which has also been used for observing the differential switching of micropillars, we performed first switching experiments. A shift of two linewidths was observed and, compared to micropillars, a much shorter recombination time. This effect appears because of the higher surface to volume ratio. In this case, free carriers are closer to surfaces and recombine faster.

In the future, improvement of the quality of etched microrings (e.g. of the smoothness of their sidewalls) will result in a significant increase of their quality factors. We have shown that such high  $Q$ , high  $F_P$  extended cavities are very interesting in view of a dynamic control of CQED effects using cavity switching.

# Bibliography

- [1] Igor Aharonovich, Dirk Englund, and Milos Toth. “Solid-state single-photon emitters”. In: *Nature Photonics* 10.10 (Sept. 2016), pp. 631–641. DOI: 10.1038/nphoton.2016.186. | cit. on p. 22
- [2] F. Albert, C. Hopfmann, A. Eberspächer, et al. “Directional whispering gallery mode emission from Limaçon-shaped electrically pumped quantum dot micropillar lasers”. en. In: *Applied Physics Letters* 101.2 (July 2012), p. 021116. DOI: 10.1063/1.4733726. | cit. on pp. 142, 169, 173
- [3] D. K. Armani, T. J. Kippenberg, S. M. Spillane, and K. J. Vahala. “Ultra-high-Q toroid microcavity on a chip”. en. In: *Nature* 421.6926 (Feb. 2003), pp. 925–928. DOI: 10.1038/nature01371. | cit. on pp. 73, 74, 77
- [4] Christophe Arnold, Vivien Loo, Aristide Lemaître, et al. “Optical bistability in a quantum dots/micropillar device with a quality factor exceeding 200 000”. en. In: *Applied Physics Letters* 100.11 (Mar. 2012), p. 111111. DOI: 10.1063/1.3694026. | cit. on p. 14
- [5] Antonio Badolato, Kevin Hennessy, Mete Atatüre, et al. “Deterministic Coupling of Single Quantum Dots to Single Nanocavity Modes”. en. In: *Science* 308.5725 (May 2005), pp. 1158–1161. DOI: 10.1126/science.1109815. | cit. on p. 16
- [6] Barin, Ihsan, Knacke, Ottmar, and Kubaschewski, Oswald. *Thermochemical properties of inorganic substances*. 1st. Aachen: Springer Berlin Heidelberg, 1977. | cit. on p. 86
- [7] M. Bayer, G. Ortner, O. Stern, et al. “Fine structure of neutral and charged excitons in self-assembled In(Ga)As/(Al)GaAs quantum dots”. In: *Physical Review B* 65.19 (May 2002), p. 195315. DOI: 10.1103/PhysRevB.65.195315. | cit. on p. 22
- [8] Benisty, Henri, Gérard, Jean-Michel, Houdre, Romuald, Rarity, John, and Weisbuch, Claude. *Confined Photon Systems: Fundamentals and Applications*. 1st. Palaiseau: Springer Berlin Heidelberg, 1999. | cit. on p. 19
- [9] Gunnar Björk, Henrich Heitmann, and Yoshihisa Yamamoto. “Spontaneous-emission coupling factor and mode characteristics of planar dielectric microcavity lasers”. In: *Physical Review A* 47.5 (1993), p. 4451. | cit. on p. 69
- [10] J. S. Blakemore. “Semiconducting and other major properties of gallium arsenide”. en. In: *Journal of Applied Physics* 53.10 (Oct. 1982), R123–R181. DOI: 10.1063/1.331665. | cit. on p. 86
- [11] Joël Bleuse, Julien Claudon, Megan Creasey, et al. “Inhibition, Enhancement, and Control of Spontaneous Emission in Photonic Nanowires”. en. In: *Physical Review Letters* 106.10 (Mar. 2011). DOI: 10.1103/PhysRevLett.106.103601. | cit. on pp. 25, 26

- [12]C. Böckler, S. Reitzenstein, C. Kistner, et al. “Electrically driven high-Q quantum dot-micropillar cavities”. en. In: *Applied Physics Letters* 92.9 (Mar. 2008), p. 091107. DOI: 10.1063/1.2890166. | cit. on p. 104
- [13]Matthew Borselli, Kartik Srinivasan, Paul E. Barclay, and Oskar Painter. “Rayleigh scattering, mode coupling, and optical loss in silicon microdisks”. en. In: *Applied Physics Letters* 85.17 (Oct. 2004), pp. 3693–3695. DOI: 10.1063/1.1811378. | cit. on pp. 14, 139
- [14]M. Brune, F. Schmidt-Kaler, A. Maali, et al. “Quantum Rabi oscillation: A direct test of field quantization in a cavity”. In: *Physical Review Letters* 76.11 (1996), p. 1800. | cit. on p. 18
- [15]Sonia Buckley, Kelley Rivoire, and Jelena Vučković. “Engineered quantum dot single-photon sources”. In: *Reports on Progress in Physics* 75.12 (Dec. 1, 2012), p. 126503. DOI: 10.1088/0034-4885/75/12/126503. | cit. on pp. 21, 23, 24, 26
- [16]Davide Cadeddu, Jean Teissier, Floris R. Braakman, et al. “A fiber-coupled quantum-dot on a photonic tip”. en. In: *Applied Physics Letters* 108.1 (Jan. 2016), p. 011112. DOI: 10.1063/1.4939264. | cit. on p. 30
- [17]Hui Cao and Jan Wiersig. “Dielectric microcavities: Model systems for wave chaos and non-Hermitian physics”. en. In: *Reviews of Modern Physics* 87.1 (Jan. 2015), pp. 61–111. DOI: 10.1103/RevModPhys.87.61. | cit. on p. 141
- [18]T. H. Chiu and W. T. Tsang. “Reflection high-energy electron diffraction studies on the molecular-beam-epitaxial growth of AlSb, GaSb, InAs, InAsSb, and GaInAsSb on GaSb”. en. In: *Journal of Applied Physics* 57.10 (May 1985), pp. 4572–4577. DOI: 10.1063/1.335362. | cit. on p. 45
- [19]Julien Claudon, Joël Bleuse, Nitin Singh Malik, et al. “A highly efficient single-photon source based on a quantum dot in a photonic nanowire”. In: *Nature Photonics* (Jan. 2010). DOI: 10.1038/nphoton.2009.287. | cit. on pp. 1, 28, 30
- [20]Georgios Ctistis, Alex Hartsuiker, Edwin van der Pol, et al. “Optical characterization and selective addressing of the resonant modes of a micropillar cavity with a white light beam”. en. In: *Physical Review B* 82.19 (Nov. 2010). DOI: 10.1103/PhysRevB.82.195330. | cit. on pp. 109, 110
- [21]Georgios Ctistis, Emre Yüce, Alex Hartsuiker, et al. “Ultimate fast optical switching of a planar microcavity in the telecom wavelength range”. en. In: *Applied Physics Letters* 98.16 (Apr. 2011), p. 161114. DOI: 10.1063/1.3580615. | cit. on pp. 36, 37, 38
- [22]Xing Ding, Yu He, Z.-C. Duan, et al. “On-Demand Single Photons with High Extraction Efficiency and Near-Unity Indistinguishability from a Resonantly Driven Quantum Dot in a Micropillar”. en. In: *Physical Review Letters* 116.2 (Jan. 2016). DOI: 10.1103/PhysRevLett.116.020401. | cit. on p. 29
- [23]A. Dousse, L. Lanco, J. Suffczyński, et al. “Controlled Light-Matter Coupling for a Single Quantum Dot Embedded in a Pillar Microcavity Using Far-Field Optical Lithography”. en. In: *Physical Review Letters* 101.26 (Dec. 2008). DOI: 10.1103/PhysRevLett.101.267404. | cit. on pp. 26, 29

- [24]Adrien Dousse, Jan Suffczyński, Alexios Beveratos, et al. “Ultrabright source of entangled photon pairs”. In: *Nature* 466.7303 (July 2010), pp. 217–220. DOI: 10.1038/nature09148. | cit. on p. 29
- [25]Bryan Ellis, Marie A. Mayer, Gary Shambat, et al. “Ultralow-threshold electrically pumped quantum-dot photonic-crystal nanocavity laser”. In: *Nature Photonics* 5.5 (May 2011), pp. 297–300. DOI: 10.1038/nphoton.2011.51. | cit. on p. 32
- [26]Dirk Englund, David Fattal, Edo Waks, et al. “Controlling the spontaneous emission rate of single quantum dots in a two-dimensional photonic crystal”. eng. In: *Physical Review Letters* 95.1 (July 2005), p. 013904. DOI: 10.1103/PhysRevLett.95.013904. | cit. on p. 26
- [27]Linran Fan, Chang-Ling Zou, Menno Poot, et al. “Integrated optomechanical single-photon frequency shifter”. In: *Nature Photonics* 10.12 (Oct. 2016), pp. 766–770. DOI: 10.1038/nphoton.2016.206. | cit. on p. 62
- [28]I. Favero, G. Cassabois, R. Ferreira, et al. “Acoustic phonon sidebands in the emission line of single InAs/GaAs quantum dots”. en. In: *Physical Review B* 68.23 (Dec. 2003). DOI: 10.1103/PhysRevB.68.233301. | cit. on p. 24
- [29]N. C. Frateschi and A. F. J. Levi. “Resonant modes and laser spectrum of microdisk lasers”. en. In: *Applied Physics Letters* 66.22 (May 1995), pp. 2932–2934. DOI: 10.1063/1.114233. | cit. on p. 139
- [30]Masayuki Fujita, Atsushi Sakai, and Toshihiko Baba. “Ultrasmall and ultralow threshold GaInAsP-InP microdisk injection lasers: design, fabrication, lasing characteristics, and spontaneous emission factor”. In: *IEEE Journal of selected topics in Quantum Electronics* 5.3 (1999), pp. 673–681. | cit. on p. 176
- [31]B. Gayral, J. M. Gérard, A. Lemaître, et al. “High-Q wet-etched GaAs microdisks containing InAs quantum boxes”. In: *Applied Physics Letters* 75.13 (Sept. 1999), pp. 1908–1910. DOI: 10.1063/1.124894. | cit. on p. 1
- [32]S. Gehrsitz, F. K. Reinhart, C. Gourgon, et al. “The refractive index of Al<sub>x</sub>Ga<sub>1-x</sub>As below the band gap: Accurate determination and empirical modeling”. en. In: *Journal of Applied Physics* 87.11 (June 2000), pp. 7825–7837. DOI: 10.1063/1.373462. | cit. on p. 87
- [33]J. M. Gérard, D. Barrier, J. Y. Marzin, et al. “Quantum boxes as active probes for photonic microstructures: The pillar microcavity case”. In: *Applied Physics Letters* 69.4 (1996), pp. 449–451. | cit. on pp. 24, 25, 106, 108, 110
- [34]J. M. Gérard and B. Gayral. “InAs quantum dots: artificial atoms for solid-state cavity-quantum electrodynamics”. In: *Physica E: Low-dimensional Systems and Nanostructures* 9.1 (2001), pp. 131–139. | cit. on pp. 14, 138
- [35]J. M. Gérard, J. B. Génin, J. Lefebvre, et al. “Optical investigation of the self-organized growth of InAs/GaAs quantum boxes”. In: *Journal of Crystal Growth* 150 (May 1995), pp. 351–356. DOI: 10.1016/0022-0248(95)80234-4. | cit. on p. 47

- [36]J. M. Gérard, B. Sermage, B. Gayral, et al. “Enhanced spontaneous emission by quantum boxes in a monolithic optical microcavity”. In: *Physical review letters* 81.5 (1998), p. 1110. | cit. on pp. 1, 22, 25, 26, 104, 160
- [37]Jean-Michel Gerard. “Solid-state cavity-quantum electrodynamics with self-assembled quantum dots”. In: *Single Quantum Dots* (2003), pp. 269–314. | cit. on p. 104
- [38]Nicolas Gisin, Grégoire Ribordy, Wolfgang Tittel, and Hugo Zbinden. “Quantum cryptography”. In: *Reviews of modern physics* 74.1 (2002), p. 145. | cit. on pp. 17, 27
- [39]Nicolas Gisin and Rob Thew. “Quantum communication”. In: *Nature photonics* 1.3 (2007), pp. 165–171. | cit. on p. 17
- [40]L. Goldstein, F. Glas, J. Y. Marzin, M. N. Charasse, and G. Le Roux. “Growth by molecular beam epitaxy and characterization of InAs/GaAs strained-layer superlattices”. In: *Applied Physics Letters* 47 (Nov. 1985), pp. 1099–1101. DOI: 10.1063/1.96342. | cit. on p. 48
- [41]P. L. Gourley. “Microstructured semiconductor lasers for high-speed information processing”. en. In: *Nature* 371.6498 (1994), pp. 571–577. DOI: 10.1038/371571a0. | cit. on p. 31
- [42]P. Goy, J. M. Raimond, M. Gross, and S. Haroche. “Observation of cavity-enhanced single-atom spontaneous emission”. In: *Physical review letters* 50.24 (1983), p. 1903. | cit. on pp. 1, 21
- [43]Thomas Grange, Gaston Hornecker, David Hunger, et al. “Cavity-Funneled Generation of Indistinguishable Single Photons from Strongly Dissipative Quantum Emitters”. en. In: *Physical Review Letters* 114.19 (May 2015). DOI: 10.1103/PhysRevLett.114.193601. | cit. on p. 24
- [44]Niels Gregersen, Dara P. S. McCutcheon, Jesper Mørk, Jean-Michel Gérard, and Julien Claudon. “A broadband tapered nanocavity for efficient nonclassical light emission”. en. In: *Optics Express* 24.18 (Sept. 2016), p. 20904. DOI: 10.1364/OE.24.020904. | cit. on p. 30
- [45]Philip J. Harding, Huib J. Bakker, Alex Hartsuiker, et al. “Observation of a stronger-than-adiabatic change of light trapped in an ultrafast switched GaAs-AlAs microcavity”. In: *JOSA B* 29.2 (2012), A1–A5. | cit. on p. 36
- [46]Philip J. Harding, Tijmen G. Euser, Yoanna-Reine Nowicki-Bringuier, Jean-Michel Gérard, and Willem L. Vos. “Dynamical ultrafast all-optical switching of planar GaAs/AlAs photonic microcavities”. en. In: *Applied Physics Letters* 91.11 (Sept. 2007), p. 111103. DOI: 10.1063/1.2779106. | cit. on pp. 62, 87, 88, 113, 121
- [47]Serge Haroche and Daniel Kleppner. “Cavity Quantum Electrodynamics”. en. In: *Physics Today* 42.1 (Jan. 1989), pp. 24–30. DOI: 10.1063/1.881201. | cit. on p. 16
- [48]Yu-Ming He, Yu He, Yu-Jia Wei, et al. “On-demand semiconductor single-photon source with near-unity indistinguishability”. en. In: *Nature Nanotechnology* 8.3 (Mar. 2013), pp. 213–217. DOI: 10.1038/nnano.2012.262. | cit. on p. 104

- [49]Marian A. Herman and Helmut Sitter. *Molecular beam epitaxy: fundamentals and current status*. 2nd, rev. and updated ed. Springer series in materials science 7. Berlin ; New York: Springer, 1996. | cit. on pp. 43, 45
- [50]Martin T. Hill and Malte C. Gather. “Advances in small lasers”. In: *Nature Photonics* 8.12 (Dec. 2014), pp. 908–918. | cit. on pp. 1, 33
- [51]P. Jaffrennou, J. Claudon, M. Bazin, et al. “Whispering gallery mode lasing in high quality GaAs/AlAs pillar microcavities”. en. In: *Applied Physics Letters* 96.7 (Feb. 2010), p. 071103. DOI: 10.1063/1.3315869. | cit. on pp. 156, 161, 162, 163, 164
- [52]J. L. Jewell, S. L. McCall, A. Scherer, et al. “Transverse modes, waveguide dispersion, and 30 ps recovery in submicron GaAs/AlAs microresonators”. en. In: *Applied Physics Letters* 55.1 (July 1989), pp. 22–24. DOI: 10.1063/1.101746. | cit. on pp. 35, 37
- [53]J. L. Jewell, A. Scherer, S. L. McCall, A. C. Gossard, and J. H. English. “GaAs/AlAs monolithic microresonator arrays”. en. In: *Applied Physics Letters* 51.2 (July 1987), pp. 94–96. DOI: 10.1063/1.98607. | cit. on pp. 100, 104
- [54]Chao-Yuan Jin, Robert Johne, Milo Y. Swinkels, et al. “Ultrafast non-local control of spontaneous emission”. In: *Nature Nanotechnology* 9.11 (Sept. 2014), pp. 886–890. DOI: 10.1038/nnano.2014.190. | cit. on pp. 1, 38
- [55]Robert Johne, Ron Schutjens, Chao-Yuan Jin, Andrea Fiore, et al. “Control of the electromagnetic environment of a quantum emitter by shaping the vacuum field in a coupled-cavity system”. In: *Physical Review A* 91.6 (2015), p. 063807. | cit. on p. 38
- [56]Galina Khitrova, H. M. Gibbs, M. Kira, Stephan W. Koch, and Axel Scherer. “Vacuum Rabi splitting in semiconductors”. In: *Nature Physics* 2.2 (2006), pp. 81–90. | cit. on pp. 38, 160
- [57]Emanuel Knill, Raymond Laflamme, and Gerald J. Milburn. “A scheme for efficient quantum computation with linear optics”. In: *nature* 409.6816 (2001), pp. 46–52. | cit. on p. 27
- [58]Thomas F. Krauss, Richard M. De La Rue, and Stuart Brand. “Two-dimensional photonic-bandgap structures operating at near-infrared wavelengths”. en. In: *Nature* 383.6602 (1996), pp. 699–702. DOI: 10.1038/383699a0. | cit. on p. 31
- [59]Eiichi Kuramochi and Masaya Notomi. “Optomechanics: Single-photon frequency shifting”. In: *Nature Photonics* 10.12 (2016), pp. 752–753. | cit. on p. 62
- [60]R. Kuszelewicz, J. L. Oudar, J. C. Michel, and R. Azoulay. “Monolithic GaAs/AlAs optical bistable etalons with improved switching characteristics”. en. In: *Applied Physics Letters* 53.22 (Nov. 1988), pp. 2138–2140. DOI: 10.1063/1.100298. | cit. on pp. 35, 37, 101
- [61]Ph. Lalanne, J. P. Hugonin, and J. M. Gérard. “Electromagnetic study of the quality factor of pillar microcavities in the small diameter limit”. In: *Applied Physics Letters* 84.23 (May 2004), pp. 4726–4728. DOI: 10.1063/1.1759375. | cit. on p. 106
- [62]A. F. J. Levi, R. E. Slusher, S. L. McCall, et al. “Room temperature operation of microdisc lasers with submilliamp threshold current”. In: *Electronics Letters* 28.11 (1992), pp. 1010–1012. | cit. on p. 176

- [63]Qing Li, Marcelo Davanço, and Kartik Srinivasan. “Efficient and low-noise single-photon-level frequency conversion interfaces using silicon nanophotonics”. In: *Nature Photonics* 10.6 (Apr. 2016), pp. 406–414. DOI: 10.1038/nphoton.2016.64.  
| cit. on p. 62
- [64]Brent E. Little and Sai T. Chu. “Estimating surface-roughness loss and output coupling in microdisk resonators”. In: *Optics letters* 21.17 (1996), pp. 1390–1392.  
| cit. on p. 139
- [65]Peter Lodahl, A. Floris Van Driel, Ivan S. Nikolaev, et al. “Controlling the dynamics of spontaneous emission from quantum dots by photonic crystals”. In: *Nature* 430.7000 (2004), pp. 654–657.  
| cit. on pp. 1, 26
- [66]F. Marin, Alberto Bramati, Elisabeth Giacobino, et al. “Squeezing and intermode correlations in laser diodes”. In: *Physical review letters* 75.25 (1995), p. 4606.  
| cit. on p. 162
- [67]J.-Y. Marzin, J.-M. Gérard, A. Izraël, D. Barrier, and G. Bastard. “Photoluminescence of single InAs quantum dots obtained by self-organized growth on GaAs”. In: *Physical Review Letters* 73.5 (1994), p. 716.  
| cit. on pp. 22, 23
- [68]S. L. McCall, A. F. J. Levi, R. E. Slusher, S. J. Pearton, and R. A. Logan. “Whispering-gallery mode microdisk lasers”. In: *Applied Physics Letters* 60.3 (Jan. 20, 1992), pp. 289–291. DOI: 10.1063/1.106688.  
| cit. on pp. 14, 31, 139
- [69]E. Moreau, I. Robert, J. M. Gérard, et al. “Single-mode solid-state single photon source based on isolated quantum dots in pillar microcavities”. In: *Applied Physics Letters* 79.18 (Oct. 2001), pp. 2865–2867. DOI: 10.1063/1.1415346.  
| cit. on pp. 29, 104, 110
- [70]M. Munsch, J. Claudon, N. S. Malik, et al. “Room temperature, continuous wave lasing in microcylinder and microring quantum dot laser diodes”. en. In: *Applied Physics Letters* 100.3 (Jan. 2012), p. 031111. DOI: 10.1063/1.3678031.  
| cit. on pp. 140, 141, 150, 176
- [71]Mathieu Munsch, Nitin S. Malik, Emmanuel Dupuy, et al. “Dielectric GaAs Antenna Ensuring an Efficient Broadband Coupling between an InAs Quantum Dot and a Gaussian Optical Beam”. en. In: *Physical Review Letters* 110.17 (Apr. 2013). DOI: 10.1103/PhysRevLett.110.177402.  
| cit. on pp. 29, 30
- [72]Nishi, Yoshio and Doering, Robert. *Handbook of Semiconductor Manufacturing Technology*. 2nd Edition. CRC Press, 2007.  
| cit. on p. 51
- [73]Susumu Noda. “Seeking the Ultimate Nanolaser”. en. In: *Science* 314.5797 (Oct. 2006), pp. 260–261. DOI: 10.1126/science.1131322.  
| cit. on p. 32
- [74]Susumu Noda, Masayuki Fujita, and Takashi Asano. “Spontaneous-emission control by photonic crystals and nanocavities”. In: *Nature photonics* 1.8 (2007), pp. 449–458.  
| cit. on pp. 1, 26
- [75]Masaya Notomi and Satoshi Mitsugi. “Wavelength conversion via dynamic refractive index tuning of a cavity”. en. In: *Physical Review A* 73.5 (May 2006). DOI: 10.1103/PhysRevA.73.051803.  
| cit. on p. 64

- [76]Masaya Notomi, Hideaki Taniyama, Satoshi Mitsugi, and Eiichi Kuramochi. “Optomechanical Wavelength and Energy Conversion in High- Q Double-Layer Cavities of Photonic Crystal Slabs”. en. In: *Physical Review Letters* 97.2 (July 2006). DOI: 10.1103/PhysRevLett.97.023903. | cit. on p. 62
- [77]Yoanna-Reine Nowicki-Bringuier. “Nouvelles géométries de confinement optique pour le contrôle de l’émission spontanée de boîtes quantiques semi-conductrices”. fr. PhD-Thesis. Université Joseph-Fourier - Grenoble I, June 2008. | cit. on pp. 15, 145, 158, 161
- [78]Y.-R. Nowicki-Bringuier, J. Claudon, C. Böckler, et al. “High Q whispering gallery modes in GaAs/AlAs pillar microcavities”. eng. In: *Optics Express* 15.25 (Dec. 2007), pp. 17291–17304. | cit. on p. 162
- [79]Jeremy L. O’Brien. “Optical quantum computing”. In: *Science* 318.5856 (2007), pp. 1567–1570. | cit. on p. 17
- [80]P. Drude. “Zur Elektronentheorie der Metalle”. In: *Annalen der Physik* 306.3 (1900), pp. 566–613. | cit. on p. 35
- [81]Jian-Wei Pan, Zeng-Bing Chen, Chao-Yang Lu, et al. “Multiphoton entanglement and interferometry”. en. In: *Reviews of Modern Physics* 84.2 (May 2012), pp. 777–838. DOI: 10.1103/RevModPhys.84.777. | cit. on p. 27
- [82]Emanuel Thomas Peinke. *Commutation tout optique ultra-rapide de micropiliers semi-conducteurs : propriétés fondamentales et applications dans le domaine de l’optique quantique*. Grenoble Alpes, Apr. 2016. | cit. on pp. 11, 38, 46, 99, 100, 113, 120, 121, 122
- [83]Matthew Pelton, Charles Santori, Jelena Vučković, et al. “Efficient Source of Single Photons: A Single Quantum Dot in a Micropost Microcavity”. In: *Physical Review Letters* 89.23 (Nov. 2002), p. 233602. DOI: 10.1103/PhysRevLett.89.233602. | cit. on p. 29
- [84]E. Peter, P. Senellart, D. Martrou, et al. “Exciton-Photon Strong-Coupling Regime for a Single Quantum Dot Embedded in a Microcavity”. en. In: *Physical Review Letters* 95.6 (Aug. 2005). DOI: 10.1103/PhysRevLett.95.067401. | cit. on pp. 1, 26, 38
- [85]Stefan F. Preble, Qianfan Xu, and Michal Lipson. “Changing the colour of light in a silicon resonator”. In: *Nature Photonics* 1.5 (May 2007), pp. 293–296. DOI: 10.1038/nphoton.2007.72. | cit. on pp. 2, 37, 63, 64, 97
- [86]Stefan Preble, Liang Cao, Ali Elshaari, Abdelsalam Aboketaf, and Donald Adams. “Single photon adiabatic wavelength conversion”. en. In: *Applied Physics Letters* 101.17 (Oct. 2012), p. 171110. DOI: 10.1063/1.4764068. | cit. on pp. 63, 64
- [87]E.M. Purcell. “Spontaneous emission probabilities at radio frequencies”. In: *Physical Review*. Vol. 69. 1946, p. 681. | cit. on pp. 1, 18
- [88]Rajeev J. Ram, D. I. Babid, Y. A. York, and John E. Bowers. “Spontaneous emission in microcavities with distributed mirrors”. In: *IEEE journal of quantum electronics* 31.2 (1995), pp. 399–410. | cit. on p. 67

- [89]J. P. Reithmaier, G. Sek, A. Löffler, et al. “Strong coupling in a single quantum dot semiconductor microcavity system”. In: *Nature* 432.7014 (2004), pp. 197–200.  
| cit. on pp. 1, 26, 104, 105
- [90]S Reitzenstein and A Forchel. “Quantum dot micropillars”. In: *Journal of Physics D: Applied Physics* 43.3 (Jan. 2010), p. 033001. DOI: 10.1088/0022-3727/43/3/033001.  
| cit. on p. 105
- [91]T. Rivera, J.-P. Debray, J. M. Gérard, et al. “Optical losses in plasma-etched AlGaAs microresonators using reflection spectroscopy”. en. In: *Applied Physics Letters* 74.7 (Feb. 1999), pp. 911–913. DOI: 10.1063/1.123407.  
| cit. on p. 73
- [92]Brian A. Ruzicka, Lalani K. Werake, Hassana Samassekou, and Hui Zhao. “Ambipolar diffusion of photoexcited carriers in bulk GaAs”. In: *Applied Physics Letters* 97.26 (Dec. 2010), p. 262119. DOI: 10.1063/1.3533664.  
| cit. on p. 123
- [93]Saleh, Bahaa E. A. and Teich, Malvin Carl. *Fundamentals of Photonics, 2nd Edition*. Wiley: 1991.  
| cit. on pp. 33, 37, 68, 69
- [94]Vea Sandoghdar, F. Treussart, J. Hare, et al. “Very low threshold whispering-gallery-mode microsphere laser”. In: *Physical Review A* 54.3 (1996), R1777. | cit. on p. 31
- [95]Charles Santori, Matthew Pelton, Glenn Solomon, Yseulte Dale, and Yoshihisa Yamamoto. “Triggered Single Photons from a Quantum Dot”. In: *Physical Review Letters* 86.8 (Feb. 2001), pp. 1502–1505. DOI: 10.1103/PhysRevLett.86.1502.  
| cit. on p. 104
- [96]T. Sattler, E. Peinke, J. Bleuse, et al. “Cavity switching: A novel resource for solid-state quantum optics”. In: *2017 19th International Conference on Transparent Optical Networks (ICTON)*. July 2017, pp. 1–4. DOI: 10.1109/ICTON.2017.8025177.  
| cit. on p. 135
- [97]Arthur L. Schawlow and Charles H. Townes. “Infrared and optical masers”. In: *Physical Review* 112.6 (1958), p. 1940.  
| cit. on p. 162
- [98]C. Schneider, P. Gold, S. Reitzenstein, S. Höfling, and M. Kamp. “Quantum dot micropillar cavities with quality factors exceeding 250,000”. en. In: *Applied Physics B* 122.1 (Jan. 2016). DOI: 10.1007/s00340-015-6283-x.  
| cit. on p. 14
- [99]Hiroshi Sekoguchi, Yasushi Takahashi, Takashi Asano, and Susumu Noda. “Photonic crystal nanocavity with a Q-factor of  $\sim 9$  million”. en. In: *Optics Express* 22.1 (Jan. 2014), p. 916. DOI: 10.1364/OE.22.000916.  
| cit. on p. 15
- [100]Pascale Senellart, Valérian Giesz, and Loïc Lanco. “Des sources de photons uniques...ultrabrillantes”. In: *Photoniques* 77 (July 2015), pp. 36–40. DOI: 10.1051/photon/20157736.  
| cit. on p. 47
- [101]Andrew J. Shields. “Semiconductor quantum light sources”. In: *Nature photonics* 1.4 (2007), pp. 215–223.  
| cit. on p. 27
- [102]G. S. Solomon, M. Pelton, and Y. Yamamoto. “Single-mode Spontaneous Emission from a Single Quantum Dot in a Three-Dimensional Microcavity”. en. In: *Physical Review Letters* 86.17 (Apr. 2001), pp. 3903–3906. DOI: 10.1103/PhysRevLett.86.3903.  
| cit. on p. 26

- [103]N. Somaschi, V. Giesz, L. De Santis, et al. “Near-optimal single-photon sources in the solid state”. In: *Nature Photonics* 10.5 (Mar. 2016), pp. 340–345. DOI: 10.1038/nphoton.2016.23. | cit. on pp. 1, 29, 30, 104
- [104]Q. H. Song, L. Ge, A. D. Stone, et al. “Directional Laser Emission from a Wavelength-Scale Chaotic Microcavity”. en. In: *Physical Review Letters* 105.10 (Aug. 2010). DOI: 10.1103/PhysRevLett.105.103902. | cit. on p. 142
- [105]Kartik Srinivasan, Matthew Borselli, Thomas J. Johnson, et al. “Optical loss and lasing characteristics of high-quality-factor AlGaAs microdisk resonators with embedded quantum dots”. en. In: *Applied Physics Letters* 86.15 (Apr. 2005), p. 151106. DOI: 10.1063/1.1901810. | cit. on pp. 14, 139
- [106]M. Stellmacher, J. Nagle, J. F. Lampin, et al. “Dependence of the carrier lifetime on acceptor concentration in GaAs grown at low-temperature under different growth and annealing conditions”. en. In: *Journal of Applied Physics* 88.10 (Nov. 2000), pp. 6026–6031. DOI: 10.1063/1.1285829. | cit. on p. 36
- [107]S. Strauf and F. Jahnke. “Single quantum dot nanolaser”. en. In: *Laser & Photonics Reviews* (Mar. 2011), pp. 607–633. DOI: 10.1002/lpor.201000039. | cit. on p. 32
- [108]U. Strauss, W. W. Rühle, and K. Köhler. “Auger recombination in intrinsic GaAs”. en. In: *Applied Physics Letters* 62.1 (Jan. 1993), pp. 55–57. DOI: 10.1063/1.108817. | cit. on p. 79
- [109]Takasumi Tanabe, Masaya Notomi, Eiichi Kuramochi, Akihiko Shinya, and Hideaki Taniyama. “Trapping and delaying photons for one nanosecond in an ultrasmall high-Q photonic-crystal nanocavity”. In: *Nature Photonics* 1.1 (Jan. 2007), pp. 49–52. DOI: 10.1038/nphoton.2006.51. | cit. on p. 64
- [110]Takasumi Tanabe, Masaya Notomi, Hideaki Taniyama, and Eiichi Kuramochi. “Dynamic Release of Trapped Light from an Ultrahigh-Q Nanocavity via Adiabatic Frequency Tuning”. en. In: *Physical Review Letters* 102.4 (Jan. 2009). DOI: 10.1103/PhysRevLett.102.043907. | cit. on pp. 2, 37, 64, 97
- [111]Henri Thyrrestrup, Alex Hartsuiker, Jean-Michel Gérard, and Willem L. Vos. “Non-exponential spontaneous emission dynamics for emitters in a time-dependent optical cavity”. en. In: *Optics Express* 21.20 (Oct. 2013), p. 23130. DOI: 10.1364/OE.21.023130. | cit. on pp. 1, 37, 174, 177
- [112]Henri Thyrrestrup, Emre Yüce, Georgios Ctistis, et al. “Differential ultrafast all-optical switching of the resonances of a micropillar cavity”. en. In: *Applied Physics Letters* 105.11 (Sept. 2014), p. 111115. DOI: 10.1063/1.4896160. | cit. on pp. 110, 122, 126
- [113]Mathew Tomes, Kerry J. Vahala, and Tal Carmon. “Direct imaging of tunneling from a potential well”. eng. In: *Optics Express* 17.21 (Oct. 2009), pp. 19160–19165. | cit. on p. 164
- [114]Kerry J. Vahala. “Optical microcavities”. en. In: *Nature* 424.6950 (Aug. 2003), pp. 839–846. DOI: 10.1038/nature01939. | cit. on pp. 1, 77

- [115]Y. P. Varshni. “Band-to-Band Radiative Recombination in Groups IV, VI, and III-V Semiconductors (I)”. en. In: *physica status solidi (b)* 19.2 (Jan. 1967), pp. 459–514. DOI: 10.1002/pssb.19670190202. | cit. on p. 79
- [116]Edo Waks, Kyo Inoue, Charles Santori, et al. “Secure communication: Quantum cryptography with a photon turnstile”. In: *Nature* 420.6917 (2002), pp. 762–762. | cit. on p. 27
- [117]Qi Jie Wang, Changling Yan, Nanfang Yu, et al. “Whispering-gallery mode resonators for highly unidirectional laser action”. In: *Proceedings of the National Academy of Sciences* 107.52 (2010), pp. 22407–22412. | cit. on p. 142
- [118]Jan Wiersig and Martina Hentschel. “Combining Directional Light Output and Ultralow Loss in Deformed Microdisks”. en. In: *Physical Review Letters* 100.3 (Jan. 2008). DOI: 10.1103/PhysRevLett.100.033901. | cit. on p. 142
- [119]Sanfeng Wu, Sonia Buckley, John R. Schaibley, et al. “Monolayer semiconductor nanocavity lasers with ultralow thresholds”. In: *Nature* 520.7545 (Mar. 2015), pp. 69–72. DOI: 10.1038/nature14290. | cit. on p. 33
- [120]Qianfan Xu, Bradley Schmidt, Sameer Pradhan, and Michal Lipson. “Micrometre-scale silicon electro-optic modulator”. In: *Nature* 435.7040 (May 2005), pp. 325–327. DOI: 10.1038/nature03569. | cit. on pp. 1, 35, 37
- [121]E. Yablonovitch, D. L. Allara, C. C. Chang, T. Gmitter, and T. B. Bright. “Unusually Low Surface-Recombination Velocity on Silicon and Germanium Surfaces”. In: *Physical Review Letters* 57.2 (July 1986), pp. 249–252. DOI: 10.1103/PhysRevLett.57.249. | cit. on p. 121
- [122]E. Yablonovitch, C. J. Sandroff, R. Bhat, and T. Gmitter. “Nearly ideal electronic properties of sulfide coated GaAs surfaces”. en. In: *Applied Physics Letters* 51.6 (Aug. 1987), pp. 439–441. DOI: 10.1063/1.98415. | cit. on pp. 79, 121
- [123]Eli Yablonovitch. “Photonic band-gap structures”. In: *JOSA B* 10.2 (1993), pp. 283–295. | cit. on p. 28
- [124]Yariv, Amnon. *Optical Electronics in Modern Communications*. 5th ed. Oxford University Press, 1997. | cit. on p. 106
- [125]Yeh, Pochi. *Optical Waves in Layered Media*. Wiley, 1988. | cit. on p. 72
- [126]SJ Ben Yoo. “Wavelength conversion technologies for WDM network applications”. In: *Journal of Lightwave Technology* 14.6 (1996), pp. 955–966. | cit. on p. 62
- [127]T. Yoshie, A. Scherer, J. Hendrickson, et al. “Vacuum Rabi splitting with a single quantum dot in a photonic crystal nanocavity”. en. In: *Nature* 432.7014 (Nov. 2004), pp. 200–203. DOI: 10.1038/nature03119. | cit. on pp. 1, 26
- [128]Emre Yüce, Georgios Ctistis, Julien Claudon, et al. “All-optical switching of a microcavity repeated at terahertz rates”. EN. In: *Optics Letters* 38.3 (Feb. 2013), pp. 374–376. DOI: 10.1364/OL.38.000374. | cit. on pp. 37, 62



# Abstract

The all-optical injection of free charge carriers into a semiconductor material can change the resonance frequency of an optical microcavity within few picoseconds and allows an ultrafast modulation of light-matter interaction. In this PhD thesis, we study the switching of different types of cavities based on GaAs/AlAs materials and explore possible applications. When the resonance wavelength of a cavity is shifted on a timescale shorter than its storage time, the frequency of the stored light is up-converted. In this work, we study this effect experimentally for high Q planar microcavities, able to store light during several tens of picoseconds. Upon ultrafast switching, we observe a large frequency shift (around 17 mode linewidths) of stored light. In agreement with numerical simulations, we evidence an adiabatic behaviour and an efficiency close to 100 % for this conversion process. When embedded in a cavity, quantum dots can serve as an internal light source for probing cavity modes and their switching dynamics. We use this approach to study two different kinds of microcavities. On one hand, we inject an inhomogeneous distribution of free charge carriers into micropillars, whose interest for quantum optics experiments is well recognized. We observe drastically different switching behaviors for their cavity modes, due to the different overlaps between free carriers and field intensity distributions. This behaviour is understood in a quantitative way on the basis of simulations taking into account the diffusion and recombination of electron-hole pairs. On the other hand, we explore the properties of a novel type of microcavity, oval ring resonators. We present a characterization of their optical properties, as well as first switching experiments. These objects offer appealing perspectives for the fabrication of microlasers, and for quantum optics experiments such as controlling the Purcell effect in real time.

---

# Résumé

L'injection toute-optique des porteurs de charge libres dans un matériau semi-conducteur peut changer la fréquence de résonance d'une cavité optique pendant quelques picosecondes et permet une modulation ultra-rapide de l'interaction lumière-matière. Dans cette thèse, nous étudions la commutation de différents types de cavités basés sur les matériaux GaAs/AlAs et explorons des applications possibles. Quand la longueur d'onde de résonance est changée sur une échelle de temps inférieure à son temps de stockage, la fréquence de la lumière stockée est poussée vers des énergies plus hautes. Dans ce travail, on étudie expérimentalement cet effet pour des microcavités planaires à hauts facteurs de qualité, étant capable de stocker la lumière pendant plusieurs dizaines de picosecondes. Dans le cadre de cette commutation, on observe un décalage important (environ 17 largeurs de raie) de la lumière stockée. Conformément à nos simulations numériques, nous mettons en évidence un comportement adiabatique et une efficacité proche de 100 % pour ce procédé de conversion. Etant placées au sein d'une cavité, des boîtes quantiques (BQ) peuvent servir comme source de lumière interne pour sonder les modes de la cavité et la dynamique de la commutation. Nous utilisons cette approche pour étudier deux différents types de cavités. D'un côté, nous injectons une distribution inhomogène de porteurs de charge libres dans des micropiliers, dont l'intérêt pour des expériences d'optique quantique est bien reconnu. A cause des recouvrements différents entre les distributions des porteurs libres et des intensités des champs, nous observons des comportements de la commutation des modes drastiquement différents. Ce comportement est compris quantitativement sur la base des simulations prenant en compte la diffusion et la recombinaison des paires électron-trou. D'un autre côté, nous explorons les propriétés d'un nouveau type de microcavité, des résonateurs en forme d'anneau ovale. Nous présentons une caractérisation de leurs propriétés optiques et premières expériences de commutation. Ces objets présentent des perspectives prometteuses pour la fabrication des microlasers et pour des expériences d'optique quantique comme contrôler l'effet Purcell en temps réel.